

Green Solvent Processable Conjugated Polymers for Organic Photovoltaics

by

Xun Pan

Thesis

Submitted to Flinders University

for the degree of

Doctor of Philosophy

College of Science and Engineering

27th November 2018

Table of Contents

Abstract	i
DECLARATION	ii
Acknowledgements	iii
Abbreviations and acronyms	iv
1. Chapter One - Introduction	1
1.1. Global energy overview	1
1.2. Alternative energy source	1
1.3. Solar energy	2
1.4. Organic photovoltaics (OPVs)	2
1.5. Pathway to the green fabrication of OPVs.....	3
1.6. Aim of thesis	4
1.7. References	5
2. Chapter Two - Organic Photovoltaics	8
2.1. Conjugated polymers.....	8
2.2. Acceptor materials.....	9
2.3. Photocurrent generation in OPVs.....	9
2.4. The development of OPVs	11
2.4.1. Single layer OPVs	11
2.4.2. Bilayer OPVs	11
2.4.3. Bulk-heterojunction (BHJ) OPVs	12
2.5. BHJ device architectures.....	12
2.5.1. Conventional device structure	13
2.5.2. Inverted device structure	13
2.6. Characterisation of OPVs	14
2.7. References	17
3. Chapter Three - Research Methodology	23
3.1. Introduction.....	23
3.2. Design of conjugated polymers for OPVs.....	23
3.2.1. Design of donor polymers	23
3.2.2. Design of water/ethanol soluble polymers.....	27
3.3. Synthesis of conjugated polymers for solar cells.....	28
3.4. Preparation of water dispersible nanoparticles for OPVs	30
3.4.1. Miniemulsion method	30
3.4.2. Precipitation method.....	33
3.4.3. Stabilisation of nanoparticles.....	34
3.5. Characterisation techniques	37
3.5.1. UV-Vis Spectroscopy	37
3.5.2. Photoluminescence (PL) spectroscopy	38
3.5.3. Cyclic voltammetry	38
3.5.4. Thermal gravimetric analysis (TGA).....	39
3.5.5. Differential scanning calorimetry (DSC)	40
3.5.6. Dynamic mechanical thermal analysis (DMTA).....	40
3.5.7. Scanning electron microscopy (SEM)	41
3.6. References	42
4. Chapter Four - Water/Ethanol Processable P-type Conjugated Polymers with Functional Side Groups for Organic Electronics	47

4.1.	Abstract	48
4.2.	Introduction	49
4.3.	Experimental.....	50
4.3.1.	Material characterisation	51
4.3.2.	Device fabrication.....	52
4.3.3.	Device characterisation	52
4.3.4.	Electron spectroscopy	52
4.4.	Results and discussion	53
4.4.1.	Material synthesis.....	53
4.4.2.	Optical properties and switchable solubility in green solvents.....	55
4.4.3.	Electrochemical properties	58
4.4.4.	Interfacial engineering.....	61
4.4.5.	Photovoltaic performance.....	63
4.4.6.	Active layer morphology	66
4.5.	Conclusions	69
4.6.	References	70
5.	Chapter Five - Green Solvent Soluble Conjugated Polymers Based on Side Chain Modification with Tertiary Amine, Pyridine and Oligoethylene Glycol	73
5.1.	Introduction.....	73
5.2.	Materials synthesis	75
5.2.1.	Amino polymers.....	75
5.2.2.	Pyridine and OEG polymers.....	75
5.2.3.	Influence of solvent polarity on molecular weight of pyridine functionalized polymer.....	77
5.3.	Material characterisation	79
5.3.1.	Optical and electrochemical properties	79
5.3.2.	Solubility in green solvents.....	81
5.3.3.	Thermal stability and property	82
5.4.	Photovoltaic performance of amino polymers	84
5.4.1.	Miscibility of the polymers and PC ₆₁ BM.....	86
5.4.2.	Morphology.....	87
5.4.3.	Surface energy	90
5.4.4.	Energy losses.....	91
5.5.	Photovoltaic performance of TQ1P3 and TQ-OEG	93
5.6.	Electrochromic Properties of amino polymers	94
5.6.1.	Spectroelectrochemistry	94
5.6.2.	Kinetic study	96
5.7.	Interface materials with amino side groups.	98
5.7.1.	Suzuki coupling polymerisation	98
5.7.2.	Optical and electrochemical properties	99
5.7.3.	Device performance	102
5.8.	Experimental.....	102
5.8.1.	Materials.....	102
5.8.2.	Material characterisation	103
5.8.3.	Device fabrication.....	104
5.8.4.	Device characterisation	105
5.9.	Conclusions	106
	Author contribution:	106
5.10.	References	107
6.	Chapter Six - Water Processable Conjugated Nanoparticles for OPVs.....	110
6.1.	Introduction.....	110
6.2.	Parameters in the preparation procedure and their influence in the particle size and photovoltaic performance	111
6.2.1.	The influence of initial SDS concentration on particle size.....	111
6.2.2.	The influence of shearing force on particle size	112

6.2.3.	The influence of solvent additive on the morphology and photovoltaic performance of NPs	112
6.2.4.	The influence of final concentration of surfactant in water dispersed NPs prepared from green solvent	117
6.2.5.	The influence of molecular weight of donor polymer on particle size	120
6.3.	Methods to coalesce NPs in the solid state	122
6.3.1.	Thermal annealing	122
6.3.2.	Solvent vapour annealing	125
6.3.3.	Solvent blend washing	127
6.4.	Synthesis of nanoparticles without additional surfactant	128
6.4.1.	SDS effect study	129
6.4.2.	Preparation of NPs using polymers with functionalized side groups	130
6.4.3.	NPs synthesised from TQ1 and PCSS	131
6.4.4.	Introduction SDS in the preparation of NPs for photovoltaic study	132
6.5.	NPs prepared with ammonium lauryl sulphate (ALS) surfactant	133
6.5.1.	Thermal property of ALS and ALS assisted NP formation	133
6.5.2.	Photovoltaic performance	134
6.6.	Possibility of substituting SDS	135
6.6.1.	Substituted surfactants	136
6.6.2.	SDS removal post preparation of NPs	138
6.7.	Precipitation method	140
6.7.1.	Different binary system using precipitation method	140
6.7.2.	Study of the experimental parameters in the preparation procedure	142
6.7.3.	Precipitation method assisted with non-ionic surfactant	144
6.7.4.	NPs containing functionalized conjugated polymers using precipitation method	145
6.8.	Experimental	146
6.8.1.	Materials	146
6.8.2.	Preparation of nanoparticles	147
6.8.3.	Characterisation of nanoparticles	148
6.8.4.	Device fabrication	150
6.8.5.	<i>J-V</i> characterisation	151
6.9.	Conclusions	152
6.10.	References	153

7. Chapter Seven - Environmentally Friendly Preparation of Nanoparticles for Organic

Photovoltaics	156	
7.1.	Abstract	157
7.2.	Introduction	158
7.3.	Experimental	159
7.3.1.	PTNT synthesis	159
7.3.2.	Nanoparticle preparation	160
7.3.3.	Nanoparticle characterisation	162
7.3.4.	Device fabrication	164
7.3.5.	<i>J-V</i> characterisation	165
7.4.	Results and discussion	165
7.4.1.	Properties of nanoparticles	165
7.4.2.	Optical properties of nanoparticles	171
7.4.3.	Photovoltaic characterisations	173
7.5.	Conclusions	179
7.6.	References	180
Conclusion	184	
Appendix A	187	
1.	Detailed synthesis procedure of small molecules	187
2.	Polymerisation procedure	190

2.1. Stille coupling polymerisation	190
2.2. Suzuki coupling polymerisation	193
Appendix B	195
NMR spectra of quinoxaline monomers and polymers presented in Chapter 4	195

Abstract

Organic photovoltaics (OPVs) have experienced rapid development during the past decade, showing great potential in the utilisation of renewable solar energy. To realise the commercially competitive manufacturing of OPVs, tremendous efforts have been put into the design of novel conjugated materials and device engineering. However, the fabrication of OPVs, especially the deposition of photoactive layer is mainly processed using halogenated solvents, which is counterproductive to the environmentally friendly goal of OPVs. The harmfulness of halogenated solvents is one of the hurdles to overcome before the high performing OPVs can be transferred from a lab-scale to an industrial scale fabrication. Hence, urgent development of green solvent processable conjugated systems is required to realise the environmentally benign fabrication of solar cells.

This thesis is dedicated primarily to the study of water/ethanol processable photoactive materials in two main methodologies:

1. Design, synthesis and characterisation of water/ethanol soluble p-type conjugated polymers based on side-chain engineering.
2. Design, preparation and characterisation of water-dispersed conjugated nanoparticles (NPs) from water-insoluble donor-acceptor active materials.

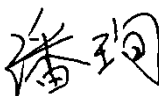
A series of new polymers were successfully synthesised utilising tertiary amine and pyridine substituents, presenting superb processibility using water/ethanol. The comprehensive characterisation of the functionalized polymers reveals the influence of side-chain properties and their content on the morphology of the bulk-heterojunction (BHJ) layer. The interaction between the functionalized polymers and fullerene derivative as well as polymer-anode interface was systematically studied. Among all the water/ethanol soluble p-type polymers, TQ1-50P4, which contains 50% of pyridine side groups, showed the most promising results, as 1.33% of PCE was achieved from TQ1-50P4 based OPVs.

In order to achieve water processibility for the deposition of active layers based on existing conjugated materials, water-dispersed NPs were prepared using two pre-established methods (miniemulsion and precipitation method). Efforts have been put into the elimination and replacement of the commonly used insulating surfactant, aiming to improve the efficiency of NP based OPVs. An environmentally friendly preparation of NPs was demonstrated, which eliminates the usage of halogenated solvent in both NP preparation and device fabrication, presenting promising photovoltaic performance (1.65% PCE). The results provide a guideline for developing green preparation of NPs for high performing OPVs.

Keywords: environment-friendly, conjugated polymers, side-chain engineering, water-dispersed nanoparticles.

DECLARATION

I certify that this thesis does not incorporate without acknowledgment any material previously submitted for a degree or diploma in any university; and that to the best of my knowledge and belief it does not contain any material previously published or written by another person except where due reference is made in the text.

Signed..........

Date.....27-November-2018.....

Acknowledgements

I would like to take this opportunity to thank the following people who helped me and shared all the beautiful memories during the last four-year PhD journey.

Prof. Mats R. Andersson, for accepting me as a PhD student 4 years ago and leading me to the world of OPV. You have always been an inspiring person and gave me tremendous help during my research. You are the best supervisor and mentor. It is a great and enjoyable experience working in your research group.

Anirudh Sharma, for generously sharing your knowledge and encouraging me. You are one of the best colleagues to work with. We all miss you here in Flinders University.

Renee Kroon, for the great supervision when I started my PhD and the continuous support even when you moved back to Sweden.

Desta Gedefaw, for being a knowledgeable person, and the help with organic synthesis and electrochemistry.

The people from our research group; Jonas Mattiasson Bjuggren, Petri Murto, Rajni Garg, Sait Elmas, for the caring discussion and collaboration. My PhD journey wouldn't be that wonderful without you. Special thanks to my co-supervisor, Prof. David Lewis, for all the excellent discussion about polymer chemistry and physics.

Prof. Gunther Andersson and Yanting Yin, for the great help and discussion in electron spectroscopy.

The people from Research Centre for Organic Electronics, University of Newcastle; Natalie Holmes, for the selfless instruction in the preparation and characterisation of nanoparticles. Prof. Paul Dastoor, for being an inspiring and knowledgeable person. Prof. Warwick Belcher, for being a great chemist and sharing your knowledge with me.

My mom and dad, for raising me with their entire deep love and constantly support wherever I am.

My husband Charlie, for being patient and loving me all the time even when I was a bit crazy after long day work. Thanks for supporting me through my emotional ups and downs. I love you so much!

Abbreviations and acronyms

ALS	Ammonium lauryl sulphate
AFM	Atomic force microscopy
BHJ	Bulk-heterojunction
CB	Chlorobenzene
CN	1-Chloronaphthalene
CV	Cyclic voltammetry
DIO	1,8-diiodooctane
DMTA	Dynamic mechanical thermal analysis
DSC	Differential scanning calorimetry
EA	Electron affinity
EDS	Energy-dispersive X-ray spectroscopy
EQE	External quantum efficiency
ETL	Electron transport layer
EtOH	Ethanol
FF	Fill factor
GPC	Gel permeation chromatography
HTL	Hole transport layer
HOMO	Highest occupied molecular orbital
IP	Ionization potential
ITO	Indium tin oxide
LUMO	Lowest unoccupied molecular orbital
LiF	Lithium fluoride

J_{SC}	Short-circuit current
MoO ₃ /MoO _x	Molybdenum (VI) oxide
NEXAFS	Near-edge X-ray absorption fine structure
NP	Nanoparticle
o-DCB	ortho-Dichlorobenzene
OEG	Oligoethylene glycol
OPV	Organic photovoltaic
PC ₆₁ BM	[6,6]-Phenyl-C ₆₁ -butyric acid methyl ester
PC ₇₁ BM	[6,6]-Phenyl-C ₇₁ -butyric acid methyl ester
PCE	Power conversion efficiency
PEDOT:PSS	Poly(3,4-ethylenedioxythiophene): poly(4-styrenesulfonate)
PEI	Poly(ethylenimine)
PEIE	Poly(ethylenimine ethoxylated)
PET	Polyethylene terephthalate
SDS	Sodium dodecyl sulphate
SEM	Scanning electron microscopy
STXM	Scanning transmission X-ray microscopy
TGA	Thermal gravimetric analysis
T_g	Glass transition temperature
TPD	N, N'-Bis(3-methylphenyl)-N,N'-bis(phenyl)-benzidine
UV-vis	Ultraviolet-visible
UHV	Ultra-high vacuum
UPS	Ultraviolet photoelectron spectroscopy
V_{OC}	Open-circuit voltage

ZnO

Zinc oxide

1. Chapter One - Introduction

1.1. Global energy overview

Fossil fuel has served as our main energy source over several centuries. With the process of world industrialization, the fossil fuel share of world primary energy increased from 76% to 82% during 1960-1985.¹ Due to its low cost and beneficial physicochemical properties, the fossil fuel can be applied to varieties of energy systems. In 2012, the world energy consumption percentage relied on fossil fuel (oil, coal and natural gas) was as high as 87% (**Figure 1.1**).

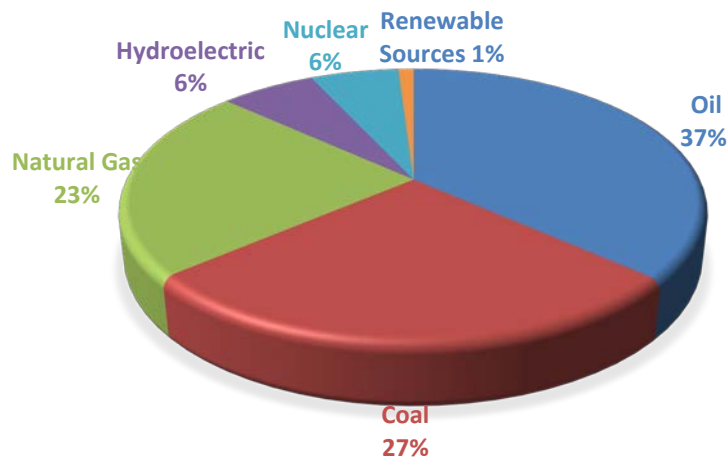


Figure 1.1 World energy consumption by sources 2012.

However, the fossil fuel depends on exhaustible resources that have already been showing signs of depletion, and it will take centuries before the supply is replenished. Moreover, the energy generating process of fossil fuel resources has a severe impact on the environment. Currently, billions of tons of fossil fuel emissions pollute our atmosphere, and the influence of these emissions are reflected on global warming, acid rain, smog, and increased occurrences of respiratory diseases.² One of the most concerning issue is the emission of greenhouse gases, especially carbon dioxide, which plays a vital role in global warming.³ It has been reported that global emission of carbon dioxide increased by 3% in the year 2011, reaching as high as 34 billion tons per year.⁴ Until so far, total flux of CO₂ related to human activities is around 30 gigatonnes, and total natural flux of CO₂ is around 770 gigatonnes. 90.5% of the total global CO₂ emissions (excluding naturally generated emissions) were attributed to fossil fuel combustion.⁵

1.2. Alternative energy source

The increased concentration of carbon dioxide to the earth's atmosphere, which is caused by the extensive use of fossil fuel, drives people to find alternative energy sources which are environmentally friendly and renewable.⁶⁻⁷ Renewable energy is defined as energy generated from

sources that can be naturally replenished on a human timescale.⁸ Since renewable energy resources do not contribute to the net increase of carbon dioxide and other kinds of greenhouse gases compared to fossil fuel, the global warming situation can be alleviated.⁷ Renewable energy sources can be of various kinds, such as wind, solar power, hydroelectricity, bioenergy and geothermal energy.⁹⁻¹⁰ A significant amount of research effort has been put in developing the technology to meet the increased demands of energy from renewable energy sources.⁹ The development in various research areas such as biotechnology and material science, all make great contribution to the renewable energy system. It is forecasted that the renewable energy share of fuels could reach nearly 25% by the year 2025 and dramatically rise to 40% by 2050.⁶

1.3. Solar energy

The majority of the biological processes and atmospheric processes on our planet is influenced directly or indirectly by various forms of solar energy input. Compared to other form of energy sources, solar energy is green and the process of the supply causes less pollution to our environment. More importantly, solar energy is an inexhaustible (at least for billions of years) and free source of energy. As our largest CO₂-neutral energy source, the energy produced from the sun in one hour could support all humans' activities in one year.⁷ The challenge is the utilisation of solar energy that reaches the earth, which needs to be in accordance with the aim of sustainable development.⁸

The exploration of solar energy has shown a substantial growth rate over the last few decades, however, the exploitation is still very limited.⁹ This situation indicates that the technology to explore solar power has high potential value.

Photovoltaic devices, which convert photon energy from the sun directly to electricity, have been widely used for the research in space exploration.¹¹ Nowadays, silicon based photovoltaics have been already recognised for decades and they are commercially available.¹²⁻¹³

1.4. Organic photovoltaics (OPVs)

Silicon is an excellent material to be used in photovoltaics due to its semiconducting properties. Silicon based photovoltaics, with the maximum theoretical power conversion efficiency (PCE) of 29.8%¹⁴ and commercial devices reaching PCE of over 23%,¹⁵ have covered most of the market of photovoltaics. However, the complexity of manufacturing process and high production cost of silicon based inorganic photovoltaics give people motivation to develop alternative photovoltaic techniques.

In the last three decades, tremendous efforts have been put into organic photovoltaic devices.¹⁶⁻¹⁸ An organic photovoltaic is defined as a photovoltaic that uses organic materials to generate electricity from incident light, in which the active materials are mainly semiconducting polymers. Compared to silicon based photovoltaics, OPVs enjoy some obvious advantages in terms of light-weight, low-cost

and facile fabrication. It has been reported that solar cell devices based on the bulk-heterojunction (BHJ) active layer have obtained a photo-conversion efficiency of more than 9%,¹⁹⁻²³ and an even higher PCE of 14.6% was reported recently.²⁴ Meanwhile, polymer tandem photovoltaics with two or more cells stacked on top of each other to absorb broader range of solar radiation²⁵ to further minimizing the thermalization loss of photon energy,²⁶⁻²⁷ reach a PCE over 17%.²⁸ However, the high PCEs were only obtained in small-scale laboratory devices and PCE in large arrays is still inferior compared to silicon-based counterparts, reaching a PCE of around 3%.²⁹⁻³⁰ This indicates that there is still significant potential for improving the OPV performance in the future.

1.5. Pathway to the green fabrication of OPVs

Currently the most employed technique to manufacture organic photovoltaics is spin-coating on small-scale rigid substrates^{18, 31-33}, which runs in the opposite direction of the low-cost, large-volume and flexibility target.³⁴ Furthermore, the preparation process of photoactive layers and interface layers are mainly based on the use of harmful halogenated solvents, which is incompatible with the environmentally friendly aim of organic solar devices.³⁵ In recent years, significant amount of research has been focussed on developing alternative OPV fabrication methods, which are scalable at low costs such as roll-to-roll printing.³⁶⁻³⁹ Roll-to-roll printing technique is under extensively developing and remarkable progress has been achieved in printing OPVs on flexible substrates.^{34, 40-41} However, most of the active materials used for printing are still processed from harmful halogenated solvents such as ortho-dichlorobenzene (o-DCB).⁴¹ The large amount of halogenated solvents being used is detrimental to the health and environment and increases the costs of large-scale fabrication, due to the necessity of using expensive solvent recovery system. It is thus urgent to develop green fabrication methods without introducing harmful solvents before lab-scale OPVs can be transferred to commercial products without causing negative influence to the environment during manufacturing.

To realise the green fabrication of organic photovoltaics, the use of harmful solvent during processing needs to be eliminated. Thus, innovative water/ethanol processable BHJ systems are crucial and need to be developed, considering water and ethanol have the least hazardous effect to organic lives. However, the presence of water in the OPV devices have been shown to be one of the major problems for long-term stability, and the diffusion of water into the underlying layer could affect the workfunction of the interlayer, further influence the device performance.⁴²⁻⁴³ In addition, aqueous processing requires high energy for water to evaporate during large-scale fabrication of OPVs using printing technique, which originates from the high heat capacity and low vapour pressure of water. A blend of water and ethanol as the processing solvent can potentially overcome this problem. However, to date only a limited number of publications have described green deposition of the active layer using truly green solvent, i.e. water and ethanol⁴⁴⁻⁴⁶, indicating that there is high potential in the exploration of new processing method and novel materials.

1.6. Aim of thesis

The studies presented in this thesis are mainly focused on the design, synthesis and characterisation of water/ethanol processable conjugated polymers that can be applied in polymer photovoltaics. One approach describes the synthesis of conjugated polymers based on side chain modification,⁴⁷ which exhibit water/ethanol solubility and could be potentially processed from aqueous solution for the application in organic electronics (Chapter 4 and 5). The influence of introduced functional side chains to the chemical and physical properties of the target polymers was systematically studied. The morphology between new p-type conjugated polymers and fullerene derivatives was carefully studied and correlated to the properties and loading of functional side chains, to understand its influence on the solar device performance.

Another approach to realise the green fabrication of OPVs is presented in Chapter 6 and 7, which describe the conversion from water-insoluble conjugated materials into water-dispersible conjugated nanoparticles (NPs) using two pre-established methods (mini-emulsion⁴⁸ and precipitation⁴⁹ method). The experimental parameters that could influence the size, stability and morphology of NPs have been thoroughly investigated, and OPVs fabricated using aqueous NP ink showed promising results. In order to replace or eliminate the commonly used stabilizing agent, which is an insulating and ionic surfactant, new polymers described in Chapter 4 and 5 have been introduced as conjugated polyelectrolytes to achieve surfactant-free NPs.

The water processable conjugated materials achieved from both approaches for the active layer in OPVs provide a pathway to realise the environmentally friendly fabrication of OPVs.

1.7. References

1. Newell, R. G.; Iler, S. *The global energy outlook*; National Bureau of Economic Research: 2013.
2. Nejat, P.; Jomehzadeh, F.; Taheri, M. M.; Gohari, M.; Abd. Majid, M. Z., A global review of energy consumption, CO₂ emissions and policy in the residential sector (with an overview of the top ten CO₂ emitting countries). *Renewable and Sustainable Energy Reviews* **2015**, *43*, 843-862.
3. Kalogirou, S. A., *Solar energy engineering: processes and systems*. Academic Press: 2013.
4. Olivier, J. G.; Janssens-Maenhout, G.; Peters, J. A., *Trends in global CO₂ emissions: 2012 report*. PBL Netherlands Environmental Assessment Agency: 2012.
5. Jos G.J. Olivier, G. J.-M.; Marilena Muntean, J. A. H. W. P. *Trends in Global CO₂ Emissions 2016 Report*; 103428; European Commission, Joint Research Centre, 2016.
6. Johansson, T. B.; Burnham, L., *Renewable energy: sources for fuels and electricity*. Island Press: 1993.
7. Eisenberg, R.; Nocera, D. G., Preface: Overview of the forum on solar and renewable energy. *Inorganic chemistry* **2005**, *44* (20), 6799-6801.
8. Herzog, A. V.; Lipman, T. E.; Kammen, D. M., Renewable energy sources. *Encyclopedia of Life Support Systems (EOLSS). Forerunner Volume-‘Perspectives and Overview of Life Support Systems and Sustainable Development* **2001**.
9. Luderer, G.; Krey, V.; Calvin, K.; Merrick, J.; Mima, S.; Pietzcker, R.; Van Vliet, J.; Wada, K., The role of renewable energy in climate stabilization: results from the EMF27 scenarios. *Climatic Change* **2014**, *123* (3-4), 427-441.
10. Armstead, H. C. H., *Geothermal energy: its past, present and future contributions to the energy needs of man*. London, E. & F.N. Spon, Ltd.; New York, Halsted Press, 1978. 382 p.: 1978.
11. Mori, M.; Kagawa, H.; Saito, Y., Summary of studies on space solar power systems of Japan Aerospace Exploration Agency (JAXA). *Acta Astronautica* **2006**, *59* (1), 132-138.
12. Turner, J. A., A realizable renewable energy future. *Science* **1999**, *285* (5428), 687-689.
13. Wenham, S.; Green, M., Silicon solar cells. *Progress in Photovoltaics: Research and Applications* **1996**, *4* (1), 3-33.
14. Tiedje, T.; Yablonovitch, E.; Cody, G. D.; Brooks, B. G., Limiting efficiency of silicon solar cells. *Electron Devices, IEEE Transactions on* **1984**, *31* (5), 711-716.
15. Blakers, A.; Zin, N.; McIntosh, K. R.; Fong, K., High Efficiency Silicon Solar Cells. *Energy Procedia* **2013**, *33*, 1-10.
16. Chamberlain, G., Organic solar cells: a review. *Solar Cells* **1983**, *8* (1), 47-83.
17. Nelson, J., Organic photovoltaic films. *Current Opinion in Solid State and Materials Science* **2002**, *6* (1), 87-95.
18. Zhou, Y.; Gu, K. L.; Gu, X.; Kurosawa, T.; Yan, H.; Guo, Y.; Koleilat, G. I.; Zhao, D.; Toney, M. F.; Bao, Z., All-Polymer Solar Cells Employing Non-Halogenated Solvent and Additive. *Chemistry of Materials* **2016**, *28* (14), 5037-5042.
19. He, Z.; Zhong, C.; Su, S.; Xu, M.; Wu, H.; Cao, Y., Enhanced power-conversion efficiency in polymer solar cells using an inverted device structure. *Nature Photonics* **2012**, *6* (9), 591-595.
20. Liang, Y.; Xu, Z.; Xia, J.; Tsai, S.-T.; Wu, Y.; Li, G.; Ray, C.; Yu, L., For the Bright Future—Bulk Heterojunction Polymer Solar Cells with Power Conversion Efficiency of 7.4%. *Advanced Materials* **2010**, *22* (20), E135-E138.
21. Son, H. J.; Lu, L.; Chen, W.; Xu, T.; Zheng, T.; Carsten, B.; Strzalka, J.; Darling, S. B.; Chen, L. X.; Yu, L., Synthesis and Photovoltaic Effect in Dithieno[2,3-d':2',3' -d']Benzo[1,2-b:4,5-b']dithiophene-Based Conjugated Polymers. *Advanced Materials* **2013**, *25* (6), 838-843.
22. Huang, Y.; Liu, F.; Guo, X.; Zhang, W.; Gu, Y.; Zhang, J.; Han, C. C.; Russell, T. P.; Hou, J., Manipulating Backbone Structure to Enhance Low Band Gap Polymer Photovoltaic Performance. *Advanced Energy Materials* **2013**, *3* (7), 930-937.
23. Zhao, W.; Li, S.; Yao, H.; Zhang, S.; Zhang, Y.; Yang, B.; Hou, J., Molecular Optimization Enables over 13% Efficiency in Organic Solar Cells. *Journal of the American Chemical Society* **2017**, *139* (21), 7148-7151.
24. Li, H.; Xiao, Z.; Ding, L.; Wang, J., Thermostable single-junction organic solar cells with a power conversion efficiency of 14.62%. *Science Bulletin* **2018**, *63* (6), 340-342.

25. Dou, L.; You, J.; Yang, J.; Chen, C.-C.; He, Y.; Murase, S.; Moriarty, T.; Emery, K.; Li, G.; Yang, Y., Tandem polymer solar cells featuring a spectrally matched low-bandgap polymer. *Nature Photonics* **2012**, *6* (3), 180-185.
26. Li, M.; Gao, K.; Wan, X.; Zhang, Q.; Kan, B.; Xia, R.; Liu, F.; Yang, X.; Feng, H.; Ni, W.; Wang, Y.; Peng, J.; Zhang, H.; Liang, Z.; Yip, H.-L.; Peng, X.; Cao, Y.; Chen, Y., Solution-processed organic tandem solar cells with power conversion efficiencies >12%. *Nature Photonics* **2016**, *11* (2), 85-90.
27. Zhang, Y.; Kan, B.; Sun, Y.; Wang, Y.; Xia, R.; Ke, X.; Yi, Y. Q.; Li, C.; Yip, H. L.; Wan, X.; Cao, Y.; Chen, Y., Nonfullerene Tandem Organic Solar Cells with High Performance of 14.11. *Advanced Materials* **2018**, e1707508.
28. Meng, L.; Zhang, Y.; Wan, X.; Li, C.; Zhang, X.; Wang, Y.; Ke, X.; Xiao, Z.; Ding, L.; Xia, R.; Yip, H.-L.; Cao, Y.; Chen, Y., Organic and solution-processed tandem solar cells with 17.3% efficiency. *Science* **2018**.
29. Li, N.; Kubis, P.; Forberich, K.; Ameri, T.; Krebs, F. C.; Brabec, C. J., Towards large-scale production of solution-processed organic tandem modules based on ternary composites: Design of the intermediate layer, device optimization and laser based module processing. *Solar Energy Materials and Solar Cells* **2014**, *120*, Part B (0), 701-708.
30. Shaheen, S. E.; Brabec, C. J.; Sariciftci, N. S.; Padinger, F.; Fromherz, T.; Hummelen, J. C., 2.5% efficient organic plastic solar cells. *Applied Physics Letters* **2001**, *78* (6), 841-843.
31. Mihailetschi, V. D.; Blom, P. W. M.; Hummelen, J. C.; Rispen, M. T., Cathode dependence of the open-circuit voltage of polymer:fullerene bulk heterojunction solar cells. *Journal of Applied Physics* **2003**, *94* (10), 6849-6854.
32. Gebeyehu, D.; Maennig, B.; Drechsel, J.; Leo, K.; Pfeiffer, M., Bulk-heterojunction photovoltaic devices based on donor-acceptor organic small molecule blends. *Solar energy materials and solar cells* **2003**, *79* (1), 81-92.
33. He, Z.; Zhong, C.; Su, S.; Xu, M.; Wu, H.; Cao, Y., Enhanced power-conversion efficiency in polymer solar cells using an inverted device structure. *Nat Photon* **2012**, *6* (9), 591-595.
34. Søndergaard, R.; Hösel, M.; Angmo, D.; Larsen-Olsen, T. T.; Krebs, F. C., Roll-to-roll fabrication of polymer solar cells. *Materials Today* **2012**, *15* (1-2), 36-49.
35. Søndergaard, R.; Helgesen, M.; Jørgensen, M.; Krebs, F. C., Fabrication of Polymer Solar Cells Using Aqueous Processing for All Layers Including the Metal Back Electrode. *Advanced Energy Materials* **2011**, *1* (1), 68-71.
36. Angmo, D.; Larsen-Olsen, T. T.; Jørgensen, M.; Søndergaard, R. R.; Krebs, F. C., Roll-to-Roll Inkjet Printing and Photonic Sintering of Electrodes for ITO Free Polymer Solar Cell Modules and Facile Product Integration. *Advanced Energy Materials* **2013**, *3* (2), 172-175.
37. Stapleton, A.; Vaughan, B.; Xue, B.; Sesa, E.; Burke, K.; Zhou, X.; Bryant, G.; Werzer, O.; Nelson, A.; David Kilcoyne, A. L.; Thomsen, L.; Wanless, E.; Belcher, W.; Dastoor, P., A multilayered approach to polyfluorene water-based organic photovoltaics. *Solar Energy Materials and Solar Cells* **2012**, *102*, 114-124.
38. Andersen, T. R.; Larsen-Olsen, T. T.; Andreasen, B.; Bottiger, A. P.; Carle, J. E.; Helgesen, M.; Bundgaard, E.; Norrman, K.; Andreasen, J. W.; Jørgensen, M., Aqueous processing of low-band-gap polymer solar cells using roll-to-roll methods. *ACS nano* **2011**, *5* (5), 4188-4196.
39. Krebs, F. C., Fabrication and processing of polymer solar cells: A review of printing and coating techniques. *Solar Energy Materials and Solar Cells* **2009**, *93* (4), 394-412.
40. Krebs, F. C.; Gevorgyan, S. A.; Alstrup, J., A roll-to-roll process to flexible polymer solar cells: model studies, manufacture and operational stability studies. *Journal of Materials Chemistry* **2009**, *19* (30), 5442.
41. Krebs, F. C.; Tromholt, T.; Jørgensen, M., Upscaling of polymer solar cell fabrication using full roll-to-roll processing. *Nanoscale* **2010**, *2* (6), 873-886.
42. Jørgensen, M.; Norrman, K.; Krebs, F. C., Stability/degradation of polymer solar cells. *Solar Energy Materials and Solar Cells* **2008**, *92* (7), 686-714.
43. Rafique, S.; Abdullah, S. M.; Sulaiman, K.; Iwamoto, M., Fundamentals of bulk heterojunction organic solar cells: An overview of stability/degradation issues and strategies for improvement. *Renewable and Sustainable Energy Reviews* **2018**, *84*, 43-53.
44. Darwis, D.; Holmes, N.; Elkington, D.; David Kilcoyne, A. L.; Bryant, G.; Zhou, X.; Dastoor, P.; Belcher, W., Surfactant-free nanoparticulate organic photovoltaics. *Solar Energy Materials and Solar Cells* **2014**, *121*, 99-107.

45. Nguyen, T. L.; Lee, C.; Kim, H.; Kim, Y.; Lee, W.; Oh, J. H.; Kim, B. J.; Woo, H. Y., Ethanol-Processable, Highly Crystalline Conjugated Polymers for Eco-Friendly Fabrication of Organic Transistors and Solar Cells. *Macromolecules* **2017**, *50* (11), 4415-4424.
46. Duan, C.; Cai, W.; Hsu, B. B. Y.; Zhong, C.; Zhang, K.; Liu, C.; Hu, Z.; Huang, F.; Bazan, G. C.; Heeger, A. J.; Cao, Y., Toward green solvent processable photovoltaic materials for polymer solar cells: the role of highly polar pendant groups in charge carrier transport and photovoltaic behavior. *Energy & Environmental Science* **2013**, *6* (10), 3022-3034.
47. Mei, J.; Bao, Z., Side Chain Engineering in Solution-Processable Conjugated Polymers. *Chemistry of Materials* **2013**, *26* (1), 604-615.
48. Landfester, K.; Montenegro, R.; Scherf, U.; GÜNTNER, R.; Asawapirom, U.; Patil, S.; Neher, D.; Kietzke, T., Semiconducting polymer nanospheres in aqueous dispersion prepared by a miniemulsion process. *Advanced Materials* **2002**, *14* (9), 651-655.
49. Darwis, D.; Elkington, D.; Sesa, E.; Cooling, N.; Bryant, G.; Zhou, X.; Belcher, W.; Dastoor, P.; Iskandar, F.; Abdullah, M. In *Surfactant Free P3HT / PCBM Nanoparticles for Organic Photovoltaics (OPV)*, AIP Conference Proceedings, 2011; pp 120-123.

2. Chapter Two - Organic Photovoltaics

This Chapter describes the development and the working principles of organic photovoltaics (OPVs).

2.1. Conjugated polymers

The development of OPVs is built on the foundation of the discovery of conjugated structures. Conjugated polymers, or often referred as semiconducting polymers, contain loosely bonded electrons in their backbones, which have attracted research effort during the last 40 years.¹⁻⁴ This field started to emerge since 1977 when Shirakawa, MacDiarmid, and Heeger demonstrated that the conductivity of conjugated polymers can be controlled by doping,⁵ for which they were awarded Noble Prize in Chemistry in 2000.^{1, 6-7}

Conjugated polymers exhibit alternating single bond-double bond structure of sp^2 -hybridized carbon atoms. The electrons in the p_z orbitals of each sp^2 -hybridized carbon atom form collectively the π band of the conjugated polymer. Due to the single-double bond alternation in the polymer backbone, conjugated polymers exhibit strong light absorption. Since the electrons in these delocalized systems are easily polarized by an external electric field such as that found in light, these type of polymers have also attracted interest for their nonlinear optical properties.⁸ **Figure 2.1** shows the structures of some well-known conjugated polymers.

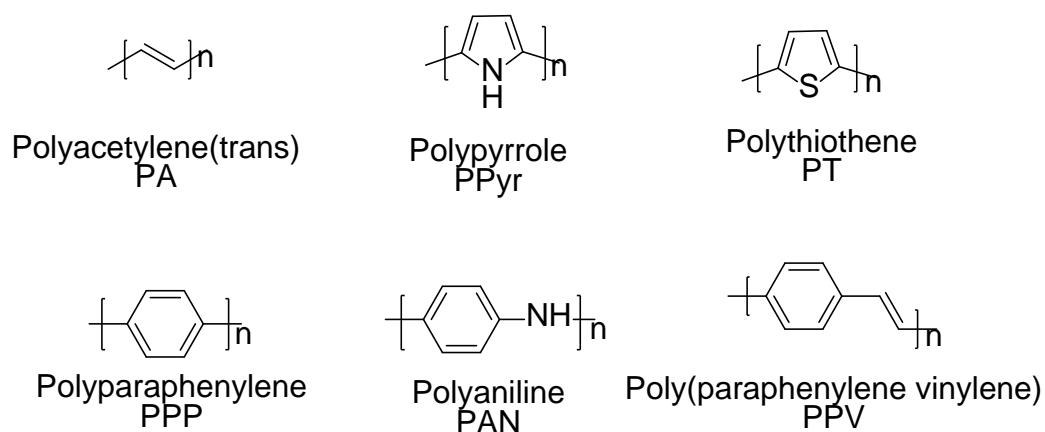


Figure 2.1 Chemical structure of several common conjugated polymers.

Upon light absorption of conjugated polymers, electrons may be excited from the ground states to the excited states. The absorption onset at low-energy region corresponds to the first optical excitation from the highest occupied molecular orbital (HOMO) to the lowest unoccupied molecular orbital (LUMO).⁹ The energy difference between the HOMO and LUMO energy levels is defined as the band gap or energy gap of a conjugated polymer. As the band gap of a conjugated system depends on the conjugation size,¹⁰ any disturbance of planarity of the conjugation along the polymer's backbone will change the local HOMO and LUMO positions.¹¹⁻¹² Due to the fact that

conjugated polymers have the immense advantages of facile tailoring to alter their band gaps, and their potential of providing environmentally friendly, lightweight, flexible and inexpensive electronics, they have attracted appreciable attention.¹³ Conjugated polymers have been widely studied and successfully used in organic light-emitting diodes (OLEDs)¹⁴⁻¹⁷ and organic photovoltaics (OPVs).¹⁸⁻¹⁹

TQ1, which is an easily synthesised quinoxaline-thiophene based conjugated polymers, has already been extensively studied in OPVs²⁰⁻²¹ and electrochromic devices.²² The synthesis work presented in this thesis discusses the modification of the side chain attached to the quinoxaline unit, aiming to achieve water/ethanol soluble TQ1 derivatives. The chemical structures of TQ1 and the quinoxaline unit are shown in **Figure 2.2**.

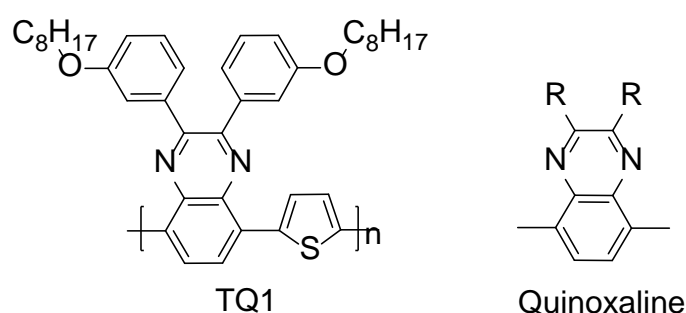


Figure 2.2 Chemical structure of TQ1 polymer and quinoxaline unit.

2.2. Acceptor materials

The first fullerene structure of C₆₀ was found by Harold Kroto et al. at 1985, for which they were awarded the 1996 Nobel Prize in Chemistry.²³ In 1992, Sariciftci et al. reported that photoinduced electron transfer from the excited state of a conjugated polymer onto C₆₀.²⁴ The high electron affinity of fullerenes makes fullerene derivatives great candidatures for electron acceptors in OPVs. To improve the solubility of fullerene, their derivatives are used for better solution-processibility. Thus, [6,6]-phenyl-C₆₁-butyric acid methyl ester (PC₆₁BM)²⁵ and [6,6]-phenyl-C₇₁-butyric acid methyl ester (PC₇₁BM)²⁶ were developed and well-studied.²⁷⁻²⁹ The commercial availability of PC₆₁BM and PC₇₁BM makes them the most commonly used small molecular acceptors with conjugated polymeric donors to fulfil photo-harvesting in OPVs. In single-junction polymer solar cells, PCE of over 10% was reported using PC₇₁BM as acceptor.³⁰⁻³¹

To further enhance the light absorption of photoactive layer and to improve the device performance of OPVs, conjugated non-fullerene small molecules have been developed as promising acceptors recently.³²⁻³⁴ Remarkably 13% PCE was reported using conjugated polymer donor with non-fullerene small molecule acceptor.³⁵

2.3. Photocurrent generation in OPVs

The process of the generation of photo-induced current in an OPV can be simplified in the following steps, shown in **Figure 2.3**. (a) After the absorption of a photon in the donor material (light can also be absorbed in the acceptor), an electron is excited from the HOMO into the LUMO, which leads to the creation of the bound electron-hole pair (singlet exciton); (b) Exciton diffuses from the donor polymer to the interface of the acceptor; (c) Exciton dissociation occurs by an electron transferring to the LUMO of the acceptor material, leaving a hole in the HOMO of the donor; (d) By virtue of the electric field or material disorder, the still Coulomb-bound electron-hole pair is separated, producing free charge carriers. The free charge carriers are transported through their phase respectively to the electrodes in order to be extracted. Possible recombination mechanisms are illustrated as (e) exciton decay, geminate recombination of bound electron-hole pairs, and (f) bimolecular recombination of free charge carriers. Finally, charge carriers are extracted from the device through two electrodes to generate photocurrent.

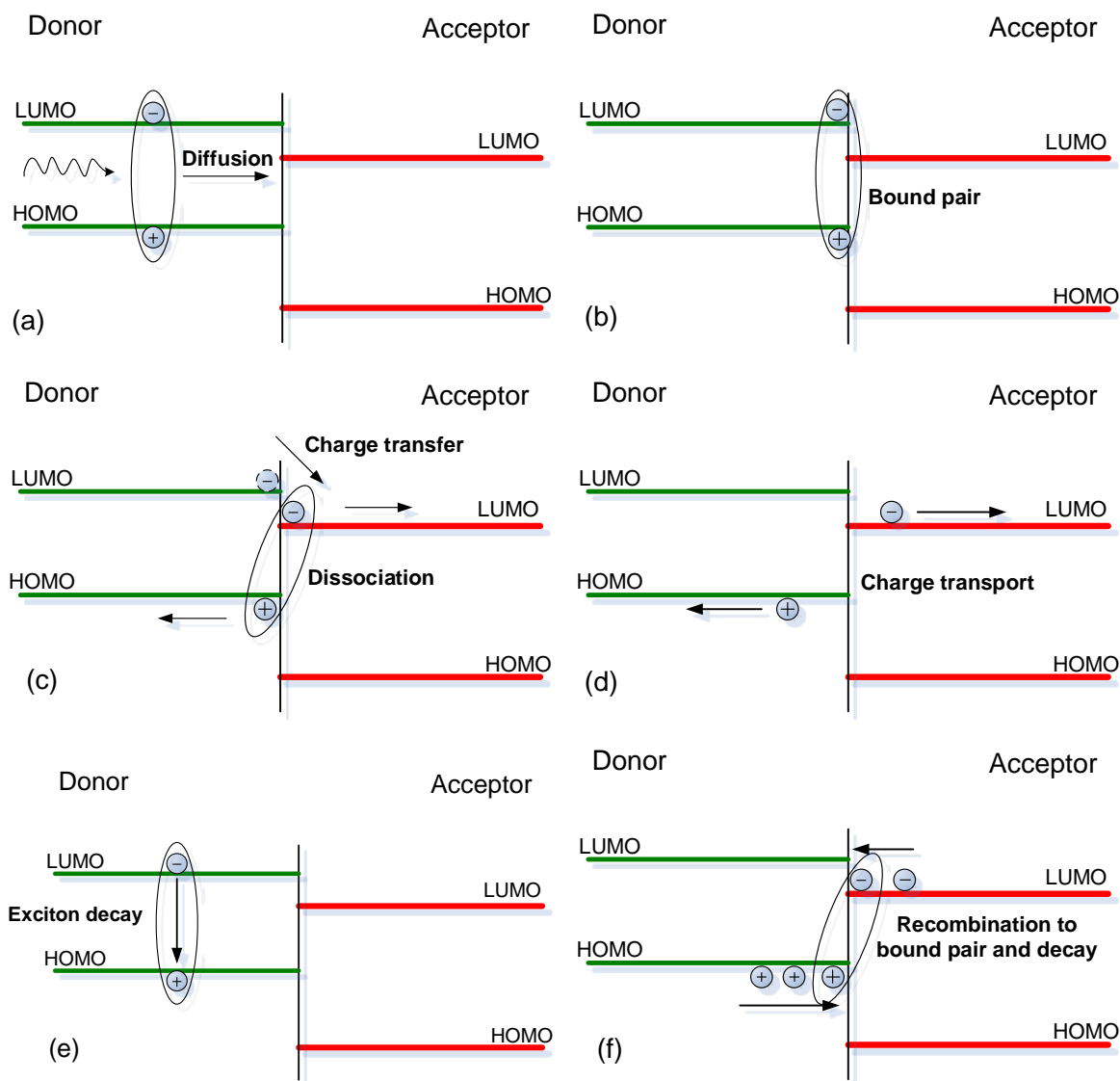


Figure 2.3 Schematic of photocurrent generation in OPVs.

To achieve efficient generation of photocurrent in OPVs, it is crucial to choose appropriate donor-acceptor pair for efficient exciton dissociation.³⁶

2.4. The development of OPVs

Currently, the photovoltaic techniques based on crystalline silicon are on the dominating position in the field of solar cells, showing the power conversion efficiencies (PCEs) of approximately 25%.³⁷ However, the high energy-demand, the complex production process and high manufacturing cost of these silicon solar cells requires the development of alternative photovoltaic technologies.³⁸ Compared to silicon solar cells, OPVs own the advantages of lightweight, flexibility, ease of manufacturing and less negative impact to the environment.³⁹ The main disadvantages of organic photovoltaic devices are that the PCE is not high enough compared to inorganic photovoltaic cells and the lifetime is limited by the stability of the active materials, which is related to the chemical and physical properties of conjugated molecules. Tremendous efforts have been putting into the design of novel materials^{21, 30, 34, 40-42} and optimisation of organic photovoltaic devices,⁴³⁻⁴⁶ accelerating the development of OPVs.

2.4.1. Single layer OPVs

The first generation of OPVs had the structure with one single active layer material between the anode and the cathode.⁴⁷ When the incident light is absorbed by the active layer, singlet excitons (strongly coulomb-bound electron-hole pairs) are created, which need to be separated to generate photocurrent. Hence overcoming the exciton binding energy is necessary in single layer OPVs. It can be accomplished by relying on the thermal energy or dissociating the exciton at the contacts of electrodes.⁴⁸ However, under the operating conditions of solar cells, the temperature is insufficient to dissociate the excitons. Furthermore, the thickness of the active layer is considerably higher compared to the diffusion length of excitons.⁴⁹ The difficulty of the diffusion and dissociation of excitons resulted in low PCEs of the single layer devices, which was far below 1%.⁴⁷ This highlights the advantage of having a donor-acceptor heterojunction in the active layer of an OPVs.⁵⁰

2.4.2. Bilayer OPVs

The second generation of solar cells are bilayer OPVs, which were first published by Tang in mid-1980s.⁵¹ In this type of device, two conjugated small molecules are sequentially stacked on top of each other. The donor material is usually a hole conducting small molecule such as phthalocyanine derivatives,⁵² while the acceptor material chosen was strongly electronegative.⁵³ In a bilayer device, the junction between donor and acceptor materials is planar.⁵² The photogenerated singlet excitons in a donor material diffuse towards the interface to an acceptor material, which provides the energy for the singlet exciton to be separated. After the dissociation of the exciton, the hole remains in the HOMO of donor whereas the electron moves to the LUMO of acceptor.⁴⁷

The PCE of bilayer OPV devices is about 1%,⁵⁴ which is mainly limited by the insufficient charge generation at the donor-acceptor interface.⁵⁵ In order to achieve a full absorption of the incident light, the thickness of the photoactive layer is around 100 nm, which is one order of magnitude higher than the diffusion length of the excitons (below 20 nm).^{19, 49, 56-57} Hence, only a small number of excitons could reach the donor-acceptor interface to dissociate into charge carrier pairs. Due to the low PCE of bilayer OPVs, the exploitation of the bilayer devices faced difficulty to move forward.

2.4.3. Bulk-heterojunction (BHJ) OPVs

The invention of the bulk-heterojunction for OPVs in the early 1990s¹⁸⁻¹⁹ overcame the exciton diffusion bottleneck and the generation of charge could be achieved efficiently in the whole volume of the active layer. The configuration of BHJ device is shown in **Figure 2.4**. In an active layer of BHJ device, donor and acceptor interpenetrate into each other; thus, the interface between two materials is spatially distributed instead of being planar. It can be achieved by co-evaporation of conjugated small molecules,^{53, 58} spin coating,⁵⁹⁻⁶⁰ spontaneous spreading⁶¹ or inkjet printing⁶²⁻⁶⁵ an donor-acceptor blend. Conjugated polymer-fullerene based solar cells were among the first to utilise this BHJ concept.^{18, 36, 66-67}

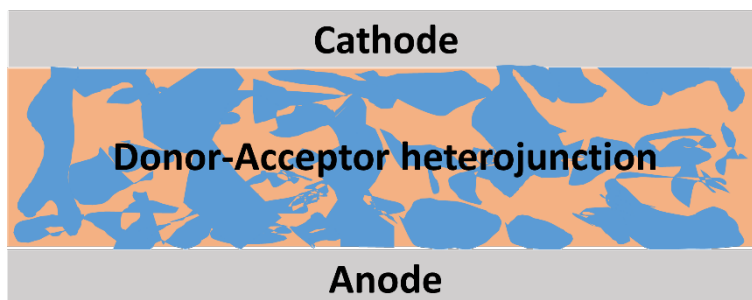


Figure 2.4 Sketch of a bulk heterojunction.

Since the generated exciton diffusion lengths are only approximate 10 nm⁶⁸ while the dissociation only occurs at the donor/acceptor interface, and the BHJ solar cells offer enormously increased (orders of magnitude) interfacial area,^{36, 47, 54} any absorbing site in the composite is ideally within a few nanometers of the interface.³⁶ This facilitates further enhanced quantum efficiency of charge separation,⁶⁹ which is the most remarkable advantage of BHJ device. Furthermore, the morphology of BHJ layer can be optimised utilising solvent additive⁷⁰ and annealing subsequently,^{44, 71-72} realising the feasible tuning of interface property.

2.5. BHJ device architectures

The general BHJ OPVs are fabricated in sandwich geometry,⁷³ the device structure of a conventional and an inverted BHJ solar cells are pictured in **Figure 2.5**. Glass or transparent polymer could be used as a substrate, upon which is commonly coated with ITO (indium tin oxide) acting as an electrode.⁷⁴ Due to its electrically non-blocking properties,⁴⁷ transparency and the commercially

availability of ITO coated glass/plastic substrate,⁶⁷ ITO has been widely used in both small-scale and roll-to-roll printed BHJ devices.⁷⁵⁻⁷⁶

2.5.1. Conventional device structure

In a conventional solar cell structure, ITO is used as the anode to collect holes. A layer of poly(3,4-ethylenedioxythiophene):poly(4-styrenesulfonate) (PEDOT:PSS) blend is commonly applied between the anode and the active layer,⁷⁷ modifying the work function of the anode. It serves as the hole-transporting layer (HTL) as well as smoothens out the ITO surface, and keeps anode electrode material from diffusing into the photoactive layer, which can lead to unwanted trap sites or create shorting.⁵⁰ The introduction of PEDOT:PSS has been reported to improve the performance of OPV.⁷⁸⁻⁸⁰ Prior to the deposition of BHJ layer, PEDOT:PSS undergoes thermal annealing to remove the moisture, and optimal annealing temperature has been reported to be essential to achieve high conductivity and photo-conversion efficiency.⁸¹

The BHJ layer is commonly processed by spin-coating active material blend on top of PEDOT:PSS. A low work function (compared to ITO) metal such as aluminium is applied as cathode to collect electrons. Between BHJ layer and cathode, a thin layer of material such as lithium fluoride (LiF) or calcium (Ca) is commonly used as a cathode buffer layer, which further enhances the device performance.⁸²

The conventional solar devices, in which PEDOT:PSS is commonly used as the HTL, have shown the problem of long-term stability due to the hygroscopic and acidic properties of PEDOT:PSS.⁸³⁻⁸⁴

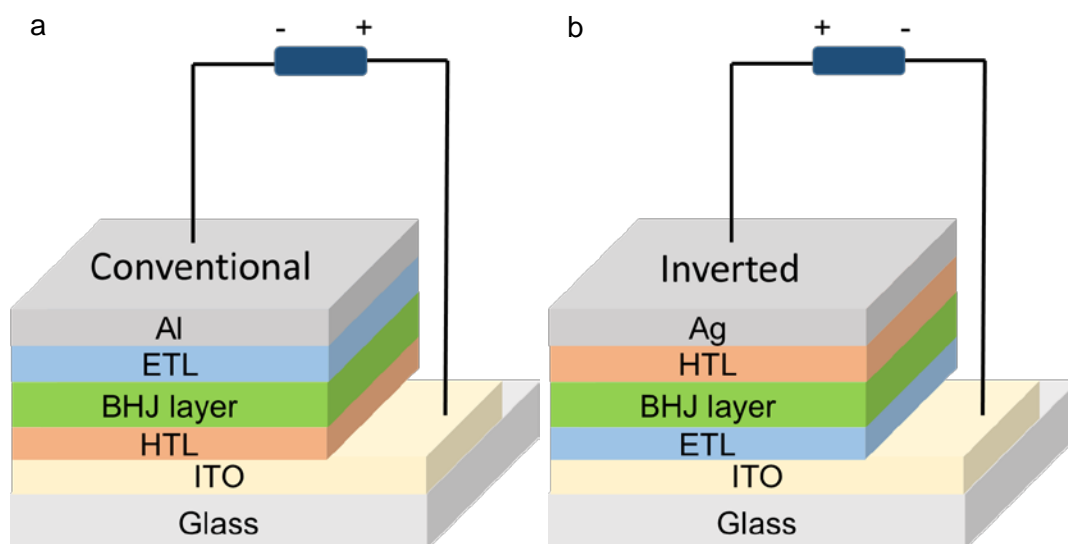


Figure 2.5 Schematic of a conventional and an inverted device structure.

2.5.2. Inverted device structure

Compared to conventional structure, inverted structure has shown to enhance the interfacial stability of devices in the absence of PEDOT:PSS layer.⁸⁵ An inverted device structure is presented in **Figure**

2.5b, in which Ag is often used as the anode due to its high work-function.⁸⁶ Meanwhile, high work-function transition metal oxides, such as molybdenum oxide (MoO_x) and vanadium pentoxide (V_2O_5), are applied to further improve the work-function of anode and serve as HTLs.⁸⁷⁻⁸⁸ On the opposite role of ITO in the conventional solar devices, ITO acts as the cathode in the inverted geometry. To lower down the work-function of ITO cathode, a thin layer of metal oxide, such as zinc oxide (ZnO),^{85, 89} cesium carbonate (Cs_2CO_3)⁹⁰ and titanium oxide (TiO_x),⁹¹ is used as a cathodic buffer layer/electron transport layer (ETL). The introduction of ETL plays a role in the enhancement of charge extractions and transportation of electrons from active layer to the cathode.⁹² The interlayer could, to some extent, change the surface and morphological properties.⁹³ There are various parameters that need to be taken into consideration when choosing materials used for the interfacial layer, such as surface energy, HOMO and LUMO energy level alignment with active materials as well as solvent processibility.⁹⁴⁻⁹⁶

2.6. Characterisation of OPVs

To evaluate the performance of OPVs, lab-scale fabricated OPVs are normally tested under a solar simulator lamp with a standardized air-mass coefficient (AM) of 1.5 solar irradiance spectrum, which corresponds to 100 mW/cm^2 .⁹⁷ The power conversion efficiency (PCE) is the ratio of maximum power converted into electricity (P_{max}) to the power of incident light on the device (P_{in}). Under the illumination of solar cells, P_{max} can be detected by plotting the photocurrent density versus voltage (J-V) and power versus voltage (PV curve) (**Figure 2.6**). The open-circuit voltage (V_{oc}), short-circuit current (J_{sc}) and fill factor (FF), which are key parameters to evaluate the solar cells, can be determined from the J-V characterisation.

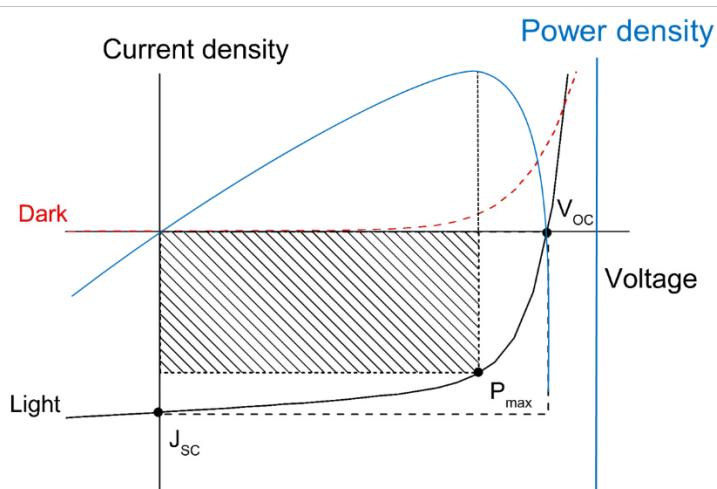


Figure 2.6 Current density-voltage curve of a solar cell under illumination (black solid line) and in the dark (red dashed line). Power density-voltage curve (blue solid line) illustrates the maximum power point. The rectangle with diagonal pattern represents maximum power from solar cell.

In OPVs, maximum V_{OC} is found to be linearly dependent on the charge transfer state (CTS) energy, which is related to the offset between the LUMO level of the acceptor and HOMO of the donor polymer.^{78, 98} Theoretically lower HOMO level of donor polymers leads to higher maximum V_{OC} . However, the LUMO level difference between donor and acceptor is desired to be at least 0.2-0.5 eV, which is necessary to dissociate exciton in the donor-acceptor interface.⁹⁹ The LUMO-LUMO offset inevitably results in a loss of V_{OC} , which could also be ascribed to the charge transfer (CT) state and local geometry.^{69, 100} There are also other factors that can significantly influence V_{OC} , such as non-radiative recombination loss between the donor and acceptor, built-in field and charge mobility.¹⁰¹ Optimisation of the electrode and interlayer materials based on appropriate tuning the work functions have been intensively investigated, leading to desirable built-in field, and have shown to improve the V_{OC} of OPVs.¹⁰² Nowadays, extensive research has been carried out to the suppression of recombination losses in order to achieve high V_{OC} .¹⁰³

The J_{SC} is the photocurrent that a solar cell with a defined area is able to generate at short circuit (zero bias). The J_{SC} was found to be highly dependent on the amount of photon absorption, which is affected by the energy gap of conjugated polymer and the thickness of active layer.^{42, 99} In order to enhance the light absorption, narrowing the energy gap of polymers is the first issue taken into consideration.^{57, 104} However, narrowing the bandgap of a donor could result in the decrease of V_{OC} , and eventually decrease the PCE. Moreover, narrowing energy gap alone is inadequate to achieve high J_{SC} , and it has already been shown that intermolecular interaction, active material packing and crystallinity all remarkably affect J_{SC} .¹⁰¹ Hence, chemical structure of conjugated materials used in the active layer should be carefully tuned to increase the solid state packing for efficient charge transfer. For a give donor-acceptor active system, to achieve high J_{SC} , efficient charge generation and extraction are required.¹⁰⁵⁻¹⁰⁶ Since the exciton dissociation only occurs at the interface between donor and acceptor materials, a good control of film morphology with nano-scale phase separation can significantly increase the J_{SC} , hence improving the device performance.¹⁰⁷

Fill factor (FF) is a parameter that is calculated by the ratio between maximum power (rectangular areas depicted in **Figure 2.6**) and the theoretical power that is the product of J_{SC} and V_{OC} .

$$FF = \frac{P_{max}}{J_{SC} \times V_{OC}}$$

Using these three parameters, the PCE is characterised as:

$$PCE = \frac{P_{max}}{P_{in}} = \frac{FF \times J_{SC} \times V_{OC}}{P_{in}}$$

FF is used to evaluate the quality of a solar cell, and represents the effectiveness of charge generation and collection.¹⁰⁸ In order to achieve highly efficient solar cells, the improvement is FF is also very important. However, FF can be affected by many factors, which adds the difficulty for the

improvement of it. In general, FF is mainly determined by the competition between charge exaction and recombination, both of which are highly influenced by the properties of active layer and interlayers.¹⁰⁹ Alternation of the active layer morphology is one strategy to enhance FF, which can be achieved by choosing appropriate processing solvent,¹¹⁰ thermal annealing¹¹¹ and solvent annealing.⁴⁴ Furthermore, optimisation of the interlayers to improve the charge extraction at the interface between active layer and interlayer is another strategy for the enhancement of FF.

2.7. References

1. Heeger, A. J., Semiconducting and Metallic Polymers: The Fourth Generation of Polymeric Materials (Nobel Lecture). *Angewandte Chemie International Edition* **2001**, *40* (14), 2591-2611.
2. McCulloch, I.; Heeney, M.; Bailey, C.; Genevicius, K.; MacDonald, I.; Shkunov, M.; Sparrowe, D.; Tierney, S.; Wagner, R.; Zhang, W., Liquid-crystalline semiconducting polymers with high charge-carrier mobility. *Nature materials* **2006**, *5* (4), 328.
3. Liang, Y.; Wu, Y.; Feng, D.; Tsai, S.-T.; Son, H.-J.; Li, G.; Yu, L., Development of new semiconducting polymers for high performance solar cells. *Journal of the American Chemical Society* **2008**, *131* (1), 56-57.
4. Hide, F.; Diaz-Garcia, M. A.; Schwartz, B. J.; Andersson, M. R.; Pei, Q.; Heeger, A. J., Semiconducting polymers: a new class of solid-state laser materials. *Science-AAAS-Weekly Paper Edition* **1996**, *273* (5283), 1833-1835.
5. Chiang, C. K.; Fincher, C. R., Jr.; Park, Y. W.; Heeger, A. J.; Shirakawa, H.; Louis, E. J.; Gau, S. C.; MacDiarmid, A. G., Electrical Conductivity in Doped Polyacetylene. *Physical Review Letters* **1977**, *39* (17), 1098-1101.
6. Shirakawa, H., The Discovery of Polyacetylene Film: The Dawning of an Era of Conducting Polymers (Nobel Lecture). *Angewandte Chemie International Edition* **2001**, *40* (14), 2574-2580.
7. MacDiarmid, A. G., "Synthetic Metals": A Novel Role for Organic Polymers (Nobel Lecture). *Angewandte Chemie International Edition* **2001**, *40* (14), 2581-2590.
8. Prasad, P. N.; Williams, D. J., *Introduction to nonlinear optical effects in molecules and polymers*. Wiley: 1991.
9. Streitwieser, A., Molecular orbital theory for organic chemists. In *Pioneers of Quantum Chemistry*, ACS Publications: 2013; pp 275-300.
10. Hoffmann, R.; Janiak, C.; Kollmar, C., A chemical approach to the orbitals of organic polymers. *Macromolecules* **1991**, *24* (13), 3725-3746.
11. Zade, S. S.; Bendikov, M., From oligomers to polymer: convergence in the HOMO- LUMO gaps of conjugated oligomers. *Organic letters* **2006**, *8* (23), 5243-5246.
12. Adachi, M.; Murata, Y.; Nakamura, S., Spectral similarity and difference of naphthalenetetracarboxylic dianhydride, perylenetetracarboxylic dianhydride, and their derivatives. *The Journal of Physical Chemistry* **1995**, *99* (39), 14240-14246.
13. Janssen, R., Introduction to polymer solar cells. *Eindhoven, Netherlands* **2005**.
14. Burroughes, J.; Bradley, D.; Brown, A.; Marks, R.; Mackay, K.; Friend, R.; Burns, P.; Holmes, A., Light-emitting diodes based on conjugated polymers. *Nature* **1990**, *347* (6293), 539-541.
15. Friend, R. H.; Gymer, R. W.; Holmes, A. B.; Burroughes, J. H.; Marks, R. N.; Taliani, C.; Bradley, D. D. C.; Santos, D. A. D.; Bredas, J. L.; Logdlund, M.; Salaneck, W. R., Electroluminescence in conjugated polymers. *Nature* **1999**, *397* (6715), 121-128.
16. Hu, Z.; Zhang, K.; Huang, F.; Cao, Y., Water/alcohol soluble conjugated polymers for the interface engineering of highly efficient polymer light-emitting diodes and polymer solar cells. *Chemical Communications* **2015**, *51* (26), 5572-85.
17. Li, Y.; Cao, Y.; Gao, J.; Wang, D.; Yu, G.; Heeger, A. J., Electrochemical properties of luminescent polymers and polymer light-emitting electrochemical cells. *Synthetic Metals* **1999**, *99* (3), 243-248.
18. Yu, G.; Gao, J.; Hummelen, J.; Wudl, F.; Heeger, A., Polymer photovoltaic cells: enhanced efficiencies via a network of internal donor-acceptor heterojunctions. *Science-AAAS-Weekly Paper Edition* **1995**, *270* (5243), 1789-1790.
19. Halls, J. J. M.; Walsh, C. A.; Greenham, N. C.; Marseglia, E. A.; Friend, R. H.; Moratti, S. C.; Holmes, A. B., Efficient photodiodes from interpenetrating polymer networks. *Nature* **1995**, *376* (6540), 498-500.
20. Wang, E.; Hou, L.; Wang, Z.; Hellstrom, S.; Zhang, F.; Inganäs, O.; Andersson, M. R., An easily synthesized blue polymer for high-performance polymer solar cells. *Advanced Materials* **2010**, *22* (46), 5240-4.
21. Gedefaw, D.; Prosa, M.; Bolognesi, M.; Seri, M.; Andersson, M. R., Recent Development of Quinoxaline Based Polymers/Small Molecules for Organic Photovoltaics. *Advanced Energy Materials* **2017**, 1700575.

22. Hellström, S.; Henriksson, P.; Kroon, R.; Wang, E.; Andersson, M. R., Blue-to-transmissive electrochromic switching of solution processable donor–acceptor polymers. *Organic Electronics* **2011**, *12* (8), 1406-1413.
23. Kroto, H. W.; Heath, J. R.; O'Brien, S. C.; Curl, R. F.; Smalley, R. E., C60: Buckminsterfullerene. *Nature* **1985**, *318* (6042), 162-163.
24. Sariciftci, N. S.; Smilowitz, L.; Heeger, A. J.; Wudl, F., Photoinduced Electron Transfer from a Conducting Polymer to Buckminsterfullerene. *Science* **1992**, *258* (5087), 1474-1476.
25. Hummelen, J. C.; Knight, B. W.; LePeq, F.; Wudl, F.; Yao, J.; Wilkins, C. L., Preparation and Characterization of Fulleroid and Methanofullerene Derivatives. *The Journal of Organic Chemistry* **1995**, *60* (3), 532-538.
26. Wienk, M. M.; Kroon, J. M.; Verhees, W. J.; Knol, J.; Hummelen, J. C.; van Hal, P. A.; Janssen, R. A., Efficient methano[70]fullerene/MDMO-PPV bulk heterojunction photovoltaic cells. *Angewandte Chemie International Edition* **2003**, *42* (29), 3371-5.
27. Hu, Z.; Gesquiere, A. J., PCBM concentration dependent morphology of P3HT in composite P3HT/PCBM nanoparticles. *Chemical Physics Letters* **2009**, *476* (1-3), 51-55.
28. Morita, S.; Kiyomatsu, S.; Yin, X. H.; Zakhidov, A. A.; Noguchi, T.; Ohnishi, T.; Yoshino, K., Doping effect of buckminsterfullerene in poly(2,5 - dialkoxy - p - phenylene vinylene). *Journal of Applied Physics* **1993**, *74* (4), 2860-2865.
29. Mihailetchi, V. D.; Blom, P. W. M.; Hummelen, J. C.; Rispen, M. T., Cathode dependence of the open-circuit voltage of polymer:fullerene bulk heterojunction solar cells. *Journal of Applied Physics* **2003**, *94* (10), 6849-6854.
30. Chen, J. D.; Cui, C.; Li, Y. Q.; Zhou, L.; Ou, Q. D.; Li, C.; Li, Y.; Tang, J. X., Single-junction polymer solar cells exceeding 10% power conversion efficiency. *Advanced Materials* **2015**, *27* (6), 1035-41.
31. Deng, D.; Zhang, Y.; Zhang, J.; Wang, Z.; Zhu, L.; Fang, J.; Xia, B.; Wang, Z.; Lu, K.; Ma, W.; Wei, Z., Fluorination-enabled optimal morphology leads to over 11% efficiency for inverted small-molecule organic solar cells. *Nature Communications* **2016**, *7*, 13740.
32. Nielsen, C. B.; Holliday, S.; Chen, H. Y.; Cryer, S. J.; McCulloch, I., Non-fullerene electron acceptors for use in organic solar cells. *Accounts of Chemical Research* **2015**, *48* (11), 2803-12.
33. Liu, J.; Chen, S.; Qian, D.; Gautam, B.; Yang, G.; Zhao, J.; Bergqvist, J.; Zhang, F.; Ma, W.; Ade, H.; Inganäs, O.; Gundogdu, K.; Gao, F.; Yan, H., Fast charge separation in a non-fullerene organic solar cell with a small driving force. *Nature Energy* **2016**, *1* (7), 16089.
34. Lin, Y.; Wang, J.; Zhang, Z. G.; Bai, H.; Li, Y.; Zhu, D.; Zhan, X., An electron acceptor challenging fullerenes for efficient polymer solar cells. *Advanced Materials* **2015**, *27* (7), 1170-4.
35. Zhao, W.; Li, S.; Yao, H.; Zhang, S.; Zhang, Y.; Yang, B.; Hou, J., Molecular Optimization Enables over 13% Efficiency in Organic Solar Cells. *Journal of the American Chemical Society* **2017**, *139* (21), 7148-7151.
36. Thompson, B. C.; Fréchet, J. M. J., Polymer–Fullerene Composite Solar Cells. *Angewandte Chemie International Edition* **2008**, *47* (1), 58-77.
37. Shah, A.; Torres, P.; Tscharnner, R.; Wyrsh, N.; Keppner, H., Photovoltaic technology: the case for thin-film solar cells. *Science* **1999**, *285* (5428), 692-698.
38. McEvoy, A. J.; Castaner, L.; Markvart, T., *Solar cells: materials, manufacture and operation*. Academic Press: 2012.
39. Chen, X.; Liu, X.; Burgers, M. A.; Huang, Y.; Bazan, G. C., Green-solvent-processed molecular solar cells. *Angewandte Chemie International Edition* **2014**, *53* (52), 14378-81.
40. Yang, Y.; Zhang, Z. G.; Bin, H.; Chen, S.; Gao, L.; Xue, L.; Yang, C.; Li, Y., Side-Chain Isomerization on an n-type Organic Semiconductor ITIC Acceptor Makes 11.77% High Efficiency Polymer Solar Cells. *Journal of the American Chemical Society* **2016**, *138* (45), 15011-15018.
41. Huang, Y.; Liu, F.; Guo, X.; Zhang, W.; Gu, Y.; Zhang, J.; Han, C. C.; Russell, T. P.; Hou, J., Manipulating Backbone Structure to Enhance Low Band Gap Polymer Photovoltaic Performance. *Advanced Energy Materials* **2013**, *3* (7), 930-937.
42. Kroon, R.; Diaz de Zerio Mendaza, A.; Himmelberger, S.; Bergqvist, J.; Bäcke, O.; Faria, G. C.; Gao, F.; Obaid, A.; Zhuang, W.; Gedefaw, D.; Olsson, E.; Inganäs, O.; Salleo, A.; Müller, C.; Andersson, M. R., A New Tetracyclic Lactam Building Block for Thick, Broad-Bandgap Photovoltaics. *Journal of the American Chemical Society* **2014**, *136* (33), 11578-11581.
43. He, Z.; Zhong, C.; Su, S.; Xu, M.; Wu, H.; Cao, Y., Enhanced power-conversion efficiency in polymer solar cells using an inverted device structure. *Nature Photonics* **2012**, *6* (9), 591-595.

44. Li, Z.; Xu, X.; Zhang, W.; Meng, X.; Ma, W.; Yartsev, A.; Inganäs, O.; Andersson, M. R.; Janssen, R. A.; Wang, E., High Performance All-Polymer Solar Cells by Synergistic Effects of Fine-Tuned Crystallinity and Solvent Annealing. *Journal of the American Chemical Society* **2016**, *138* (34), 10935-44.
45. Liu, Y.; Zhao, J.; Li, Z.; Mu, C.; Ma, W.; Hu, H.; Jiang, K.; Lin, H.; Ade, H.; Yan, H., Aggregation and morphology control enables multiple cases of high-efficiency polymer solar cells. *Nature Communications* **2014**, *5*, 5293.
46. Sharma, A.; Kroon, R.; Lewis, D. A.; Andersson, G. G.; Andersson, M. R., Poly(4-vinylpyridine): A New Interface Layer for Organic Solar Cells. *ACS Applied Materials & Interfaces* **2017**, *9* (12), 10929-10936.
47. Chamberlain, G. A., Organic solar cells: A review. *Solar Cells* **1983**, *8* (1), 47-83.
48. Hertel, D.; Bässler, H., Photoconduction in Amorphous Organic Solids. *ChemPhysChem* **2008**, *9* (5), 666-688.
49. Menke, S. M.; Holmes, R. J., Exciton diffusion in organic photovoltaic cells. *Energy & Environmental Science* **2014**, *7* (2), 499-512.
50. Benanti, T.; Venkataraman, D., Organic Solar Cells: An Overview Focusing on Active Layer Morphology. *Photosynth Res* **2006**, *87* (1), 73-81.
51. Tang, C. W., Two-layer organic photovoltaic cell. *Applied Physics Letters* **1986**, *48* (2), 183-185.
52. Gregg, B. A., Bilayer molecular solar cells on spin-coated TiO₂ substrates. *Chemical Physics Letters* **1996**, *258* (3), 376-380.
53. Petritsch, K.; Dittmer, J. J.; Marseglia, E. A.; Friend, R. H.; Lux, A.; Rozenberg, G. G.; Moratti, S. C.; Holmes, A. B., Dye-based donor/acceptor solar cells. *Solar Energy Materials and Solar Cells* **2000**, *61* (1), 63-72.
54. Hoppe, H.; Sariciftci, N. S., Organic solar cells: An overview. *Journal of Materials Research* **2004**, *19* (07), 1924-1945.
55. Friend, R. H.; Denton, G. J.; Halls, J. J. M.; Harrison, N. T.; Holmes, A. B.; Köhler, A.; Lux, A.; Moratti, S. C.; Pichler, K.; Tessler, N.; Towns, K.; Wittmann, H. F., Electronic excitations in luminescent conjugated polymers. *Solid State Communications* **1997**, *102* (2-3), 249-258.
56. Stubinger, T.; Brütting, W., Exciton diffusion and optical interference in organic donor-acceptor photovoltaic cells. *Journal of Applied Physics* **2001**, *90* (7), 3632-3641.
57. Winder, C.; Sariciftci, N. S., Low bandgap polymers for photon harvesting in bulk heterojunction solar cells. *Journal of Materials Chemistry* **2004**, *14* (7), 1077-1086.
58. Schmidt-Mende, L.; Fechtenkötter, A.; Müllen, K.; Moons, E.; Friend, R. H.; MacKenzie, J. D., Self-Organized Discotic Liquid Crystals for High-Efficiency Organic Photovoltaics. *Science* **2001**, *293* (5532), 1119-1122.
59. Zhou, J.; Wan, X.; Liu, Y.; Zuo, Y.; Li, Z.; He, G.; Long, G.; Ni, W.; Li, C.; Su, X.; Chen, Y., Small molecules based on benzo[1,2-b:4,5-b']dithiophene unit for high-performance solution-processed organic solar cells. *Journal of the American Chemical Society* **2012**, *134* (39), 16345-51.
60. Gedefaw, D.; Sharma, A.; Pan, X.; Bjuggren, J. M.; Kroon, R.; Gregoriou, V. G.; Chocho, C. L.; Andersson, M. R., Optimization of the power conversion efficiency in high bandgap pyridopyridinedithiophene-based conjugated polymers for organic photovoltaics by the random terpolymer approach. *European Polymer Journal* **2017**, *91*, 92-99.
61. Noh, J.; Jeong, S.; Lee, J. Y., Ultrafast formation of air-processable and high-quality polymer films on an aqueous substrate. *Nature Communications* **2016**, *7*, 12374.
62. Angmo, D.; Larsen-Olsen, T. T.; Jørgensen, M.; Søndergaard, R. R.; Krebs, F. C., Roll-to-Roll Inkjet Printing and Photonic Sintering of Electrodes for ITO Free Polymer Solar Cell Modules and Facile Product Integration. *Advanced Energy Materials* **2013**, *3* (2), 172-175.
63. Krebs, F. C.; Tromholt, T.; Jørgensen, M., Upscaling of polymer solar cell fabrication using full roll-to-roll processing. *Nanoscale* **2010**, *2* (6), 873-86.
64. Zhou, X.; Belcher, W.; Dastoor, P., Solar Paint: From Synthesis to Printing. *Polymers* **2014**, *6* (11), 2832-2844.
65. Krebs, F. C., Fabrication and processing of polymer solar cells: A review of printing and coating techniques. *Solar Energy Materials and Solar Cells* **2009**, *93* (4), 394-412.
66. Deibel, C.; Dyakonov, V., Polymer-fullerene bulk heterojunction solar cells. *Reports on Progress in Physics* **2010**, *73* (9), 096401.

67. Dennler, G.; Scharber, M. C.; Brabec, C. J., Polymer-Fullerene Bulk-Heterojunction Solar Cells. *Advanced Materials* **2009**, *21* (13), 1323-1338.
68. Hedley, G. J.; Ward, A. J.; Alekseev, A.; Howells, C. T.; Martins, E. R.; Serrano, L. A.; Cooke, G.; Ruseckas, A.; Samuel, I. D., Determining the optimum morphology in high-performance polymer-fullerene organic photovoltaic cells. *Nature Communications* **2013**, *4*, 2867.
69. Zheng, Z.; Tummala, N. R.; Fu, Y. T.; Coropceanu, V.; Bredas, J. L., Charge-Transfer States in Organic Solar Cells: Understanding the Impact of Polarization, Delocalization, and Disorder. *ACS Applied Materials & Interfaces* **2017**, *9* (21), 18095-18102.
70. Zhou, Y.; Gu, K. L.; Gu, X.; Kurosawa, T.; Yan, H.; Guo, Y.; Koleilat, G. I.; Zhao, D.; Toney, M. F.; Bao, Z., All-Polymer Solar Cells Employing Non-Halogenated Solvent and Additive. *Chemistry of Materials* **2016**, *28* (14), 5037-5042.
71. Nguyen, L. H.; Hoppe, H.; Erb, T.; Günes, S.; Gobsch, G.; Sariciftci, N. S., Effects of Annealing on the Nanomorphology and Performance of Poly(alkylthiophene):Fullerene Bulk-Heterojunction Solar Cells. *Advanced Functional Materials* **2007**, *17* (7), 1071-1078.
72. Holmes, N. P.; Burke, K. B.; Sista, P.; Barr, M.; Magurudeniya, H. D.; Stefan, M. C.; Kilcoyne, A. L. D.; Zhou, X.; Dastoor, P. C.; Belcher, W. J., Nano-domain behaviour in P3HT:PCBM nanoparticles, relating material properties to morphological changes. *Solar Energy Materials and Solar Cells* **2013**, *117*, 437-445.
73. Günes, S.; Neugebauer, H.; Sariciftci, N. S., Conjugated Polymer-Based Organic Solar Cells. *Chemical Reviews* **2007**, *107* (4), 1324-1338.
74. Cao, Y.; Yu, G.; Zhang, C.; Menon, R.; Heeger, A. J., Polymer light-emitting diodes with polyethylene dioxythiophene-polystyrene sulfonate as the transparent anode. *Synthetic Metals* **1997**, *87* (2), 171-174.
75. Dang, D.; Zhou, P.; Zhong, J.; Fan, J.; Wang, Z.; Wang, Y.; Pei, Y.; Bao, X.; Yang, R.; Hu, W.; Zhu, W., Novel wide band-gap polymer utilizing fused hetero-aromatic unit for efficient polymer solar cells and field-effect transistors. *Polymer* **2014**, *55* (26), 6708-6716.
76. Dang, D.; Chen, J.; Zhou, P.; Duan, L.; Bao, X.; Yang, R.; Chen, J.; Zhu, W., Tuning the fused aromatic rings to enhance photovoltaic performance in wide band-gap polymer solar cells. *Polymer* **2016**, *104*, 130-137.
77. Scott, J.; Carter, S.; Karg, S.; Angelopoulos, M., Polymeric anodes for organic light-emitting diodes. *Synthetic Metals* **1997**, *85* (1), 1197-1200.
78. Brabec, C. J.; Sariciftci, N. S.; Hummelen, J. C., Plastic solar cells. *Advanced Functional Materials* **2001**, *11* (1), 15-26.
79. Granström, M.; Petritsch, K.; Arias, A.; Lux, A.; Andersson, M.; Friend, R., Laminated fabrication of polymeric photovoltaic diodes. *Nature* **1998**, *395* (6699), 257-260.
80. Gebeyehu, D.; Maennig, B.; Drechsel, J.; Leo, K.; Pfeiffer, M., Bulk-heterojunction photovoltaic devices based on donor-acceptor organic small molecule blends. *Solar energy materials and solar cells* **2003**, *79* (1), 81-92.
81. Kim, Y.; Ballantyne, A.; Nelson, J.; Bradley, D., Effects of thickness and thermal annealing of the PEDOT:PSS layer on the performance of polymer solar cells. *Organic Electronics* **2009**, *10* (1), 205-209.
82. Brabec, C. J.; Shaheen, S. E.; Winder, C.; Sariciftci, N. S.; Denk, P., Effect of LiF/metal electrodes on the performance of plastic solar cells. *Applied Physics Letters* **2002**, *80* (7), 1288-1290.
83. de Jong, M. P.; van Ijzendoorn, L. J.; de Voigt, M. J. A., Stability of the interface between indium-tin-oxide and poly(3,4-ethylenedioxythiophene)/poly(styrenesulfonate) in polymer light-emitting diodes. *Applied Physics Letters* **2000**, *77* (14), 2255-2257.
84. Kawano, K.; Pacios, R.; Poplavskyy, D.; Nelson, J.; Bradley, D. D. C.; Durrant, J. R., Degradation of organic solar cells due to air exposure. *Solar Energy Materials and Solar Cells* **2006**, *90* (20), 3520-3530.
85. Sun, Y.; Seo, J. H.; Takacs, C. J.; Seifert, J.; Heeger, A. J., Inverted polymer solar cells integrated with a low-temperature-annealed sol-gel-derived ZnO Film as an electron transport layer. *Advanced Materials* **2011**, *23* (14), 1679-83.
86. White, M. S.; Olson, D. C.; Shaheen, S. E.; Kopidakis, N.; Ginley, D. S., Inverted bulk-heterojunction organic photovoltaic device using a solution-derived ZnO underlayer. *Applied Physics Letters* **2006**, *89* (14), 143517.

87. Shrotriya, V.; Li, G.; Yao, Y.; Chu, C.-W.; Yang, Y., Transition metal oxides as the buffer layer for polymer photovoltaic cells. *Applied Physics Letters* **2006**, *88* (7), 073508.
88. Hermerschmidt, F.; Savva, A.; Georgiou, E.; Tuladhar, S. M.; Durrant, J. R.; McCulloch, I.; Bradley, D. D. C.; Brabec, C. J.; Nelson, J.; Choulis, S. A., Influence of the Hole Transporting Layer on the Thermal Stability of Inverted Organic Photovoltaics Using Accelerated-Heat Lifetime Protocols. *ACS Applied Materials & Interfaces* **2017**, *9* (16), 14136-14144.
89. Sharma, A.; Franklin, J. B.; Singh, B.; Andersson, G. G.; Lewis, D. A., Electronic and chemical properties of ZnO in inverted organic photovoltaic devices. *Organic Electronics* **2015**, *24*, 131-136.
90. Li, G.; Chu, C. W.; Shrotriya, V.; Huang, J.; Yang, Y., Efficient inverted polymer solar cells. *Applied Physics Letters* **2006**, *88* (25), 253503.
91. Baek, W.-H.; Seo, I.; Yoon, T.-S.; Lee, H. H.; Yun, C. M.; Kim, Y.-S., Hybrid inverted bulk heterojunction solar cells with nanoimprinted TiO₂ nanopores. *Solar Energy Materials and Solar Cells* **2009**, *93* (9), 1587-1591.
92. Chueh, C.-C.; Li, C.-Z.; Jen, A. K. Y., Recent progress and perspective in solution-processed Interfacial materials for efficient and stable polymer and organometal perovskite solar cells. *Energy & Environmental Science* **2015**, *8* (4), 1160-1189.
93. Tang, Z.; Andersson, L. M.; George, Z.; Vandewal, K.; Tvingstedt, K.; Heriksson, P.; Kroon, R.; Andersson, M. R.; Inganäs, O., Interlayer for Modified Cathode in Highly Efficient Inverted ITO - Free Organic Solar Cells. *Advanced Materials* **2012**, *24* (4), 554-558.
94. Tang, Z.; Andersson, L. M.; George, Z.; Vandewal, K.; Tvingstedt, K.; Heriksson, P.; Kroon, R.; Andersson, M. R.; Inganäs, O., Interlayer for modified cathode in highly efficient inverted ITO-free organic solar cells. *Advanced Materials* **2012**, *24* (4), 554-8.
95. Wu, Z.; Sun, C.; Dong, S.; Jiang, X. F.; Wu, S.; Wu, H.; Yip, H. L.; Huang, F.; Cao, Y., n-Type Water/Alcohol-Soluble Naphthalene Diimide-Based Conjugated Polymers for High-Performance Polymer Solar Cells. *Journal of the American Chemical Society* **2016**, *138* (6), 2004-13.
96. Xu, B.; Zheng, Z.; Zhao, K.; Hou, J., A Bifunctional Interlayer Material for Modifying Both the Anode and Cathode in Highly Efficient Polymer Solar Cells. *Advanced Materials* **2016**, *28* (3), 434-9.
97. Gueymard, C. A.; Myers, D.; Emery, K., Proposed reference irradiance spectra for solar energy systems testing. *Solar Energy* **2002**, *73* (6), 443-467.
98. Mühlbacher, D.; Scharber, M.; Morana, M.; Zhu, Z.; Waller, D.; Gaudiana, R.; Brabec, C., High Photovoltaic Performance of a Low-Bandgap Polymer. *Advanced Materials* **2006**, *18* (21), 2884-2889.
99. Kroon, R.; Lenes, M.; Hummelen, J. C.; Blom, P. W.; De Boer, B., Small bandgap polymers for organic solar cells (polymer material development in the last 5 years). *Polymer Reviews* **2008**, *48* (3), 531-582.
100. Guan, Z.; Li, H.-W.; Cheng, Y.; Yang, Q.; Lo, M.-F.; Ng, T.-W.; Tsang, S.-W.; Lee, C.-S., Charge-Transfer State Energy and Its Relationship with Open-Circuit Voltage in an Organic Photovoltaic Device. *The Journal of Physical Chemistry C* **2016**, *120* (26), 14059-14068.
101. Li, G.; Zhu, R.; Yang, Y., Polymer solar cells. *Nature Photonics* **2012**, *6* (3), 153-161.
102. Zhou, Y.; Fuentes-Hernandez, C.; Shim, J.; Meyer, J.; Giordano, A. J.; Li, H.; Winget, P.; Papadopoulos, T.; Cheun, H.; Kim, J.; Fenoll, M.; Dindar, A.; Haske, W.; Najafabadi, E.; Khan, T. M.; Sojoudi, H.; Barlow, S.; Graham, S.; Brédas, J.-L.; Marder, S. R.; Kahn, A.; Kippelen, B., A Universal Method to Produce Low-Work Function Electrodes for Organic Electronics. *Science* **2012**, *336* (6079), 327.
103. Liu, X.; Du, X.; Wang, J.; Duan, C.; Tang, X.; Heumueller, T.; Liu, G.; Li, Y.; Wang, Z.; Wang, J.; Liu, F.; Li, N.; Brabec, C. J.; Huang, F.; Cao, Y., Efficient Organic Solar Cells with Extremely High Open-Circuit Voltages and Low Voltage Losses by Suppressing Nonradiative Recombination Losses. *Advanced Energy Materials* **2018**, 1801699.
104. Dou, L.; You, J.; Yang, J.; Chen, C.-C.; He, Y.; Murase, S.; Moriarty, T.; Emery, K.; Li, G.; Yang, Y., Tandem polymer solar cells featuring a spectrally matched low-bandgap polymer. *Nature Photonics* **2012**, *6* (3), 180-185.
105. Schwarz, K. N.; Farley, S. B.; Smith, T. A.; Ghiggino, K. P., Charge generation and morphology in P3HT:PCBM nanoparticles prepared by mini-emulsion and reprecipitation methods. *Nanoscale* **2015**, *7* (47), 19899-904.

106. Mihailetchi, V. D.; Xie, H. X.; de Boer, B.; Koster, L. J. A.; Blom, P. W. M., Charge Transport and Photocurrent Generation in Poly(3-hexylthiophene): Methanofullerene Bulk-Heterojunction Solar Cells. *Advanced Functional Materials* **2006**, *16* (5), 699-708.
107. Zhao, F.; Wang, C.; Zhan, X., Morphology Control in Organic Solar Cells. *Advanced Energy Materials* **2018**, 1703147.
108. Zheng, Z.; Hu, Q.; Zhang, S.; Zhang, D.; Wang, J.; Xie, S.; Wang, R.; Qin, Y.; Li, W.; Hong, L.; Liang, N.; Liu, F.; Zhang, Y.; Wei, Z.; Tang, Z.; Russell, T. P.; Hou, J.; Zhou, H., A Highly Efficient Non-Fullerene Organic Solar Cell with a Fill Factor over 0.80 Enabled by a Fine-Tuned Hole-Transporting Layer. *Advanced Materials* **2018**, e1801801.
109. Li, S.; Ye, L.; Zhao, W.; Liu, X.; Zhu, J.; Ade, H.; Hou, J., Design of a New Small-Molecule Electron Acceptor Enables Efficient Polymer Solar Cells with High Fill Factor. *Advanced Materials* **2017**, *29* (46).
110. McDowell, C.; Abdelsamie, M.; Toney, M. F.; Bazan, G. C., Solvent Additives: Key Morphology-Directing Agents for Solution-Processed Organic Solar Cells. *Advanced Materials* **2018**, e1707114.
111. Wang, T.; Lau, T.-K.; Lu, X.; Yuan, J.; Feng, L.; Jiang, L.; Deng, W.; Peng, H.; Li, Y.; Zou, Y., A Medium Bandgap D–A Copolymer Based on 4-Alkyl-3,5-difluorophenyl Substituted Quinoxaline Unit for High Performance Solar Cells. *Macromolecules* **2018**.

3. Chapter Three - Research Methodology

This chapter will provide the research methodology utilised to design and prepare water/alcohol processable conjugated materials for OPVs. Brief descriptions of the characterisation techniques employed by the candidate to characterise material properties will be presented in this chapter.

3.1. Introduction

During the last decade, intensive research has been progressed on the design and synthesis of photoactive materials for OPVs, achieving remarkably high efficiency in the last three years.¹⁻⁴ The design of donor materials is one of the most important area in the research of OPVs.

Fullerene derivatives, for example, PC₆₁BM and PC₇₁PM, are commonly used as electron acceptors for high efficiency BHJ solar cells due to their advantageous electron mobility as well as commercial availability.⁵⁻⁶ Their relatively low LUMO energy level makes PCBM thermodynamically favorable to accepting electrons from excited donor material.⁷ However they are not perfect due to that the commonly used fullerene derivatives typically have limited light absorption in the visual region,⁸⁻¹⁰ explaining the extensive efforts in exploring novel donor material which has a broad absorption spectrum. Furthermore, extensive use of harmful halogenated solvent to deposit active layer in OPVs is the one of the main hindrance for up-scaling. Hence, the study of green solvent processable conjugated materials presented in this thesis provides important guide for the further design of conjugated materials and the optimisation of OPV fabrication in an environment-friendly way.

3.2. Design of conjugated polymers for OPVs

3.2.1. Design of donor polymers

The desired properties of conjugated polymers for OPVs have been described above. One of the key steps in photon harvest is the absorption of incident light by active materials.¹¹ Most of the photons within the solar spectrum are located in the range of 400-1000 nm. Hence, to ensure the sufficient generation of exciton under illumination, low bandgap conjugated polymers have been widely used as the donor materials for OPVs.

The bandgap of conjugated polymers can significantly influence PCE of solar devices.¹² There are several structure factors that affects the modification of the band gap of a conjugated polymer (**Figure 3.1**). These factors work together instead of individually on the bandgap of a given polymer, which also have influence on other chemical and physical properties. One straightforward way to narrow the bandgap of a given polymer is to increase the conjugation length on the backbone, in other way, increasing the molecular weight (M_w). However, when the effective conjugated length reaches saturation value (number of repeating units goes above a certain value, approximate 6-10

aromatic rings), the bandgap reaches its threshold.⁷ That is to say, the bandgap could only get limited reduction through manipulating the molecular weight.

Substituents attached to the backbone, such as alkyl chains and alkoxy chains improve the solubility of polymers in solvents, which can lead to high molecular weight during polymerisation. What's more, substituents can alter the HOMO and LUMO energy level through inductive effect.¹³ For example, electron rich substituents raise the HOMO level while electron deficient ones attribute to the decrease of LUMO level.

The dihedral angle (θ), in other word, coplanarity (E_θ) of the backbone have strong effect on the conjugation length of polymers. With high coplanarity, the delocalization of electron along the conjugated backbone is enhanced, resulting in low bandgap. The coplanarity of polymers can be achieved via utilisation of fused units, which have shown to improve the charge generation and transfer.¹⁴⁻¹⁶ Alternatively, unsubstituted 5 member rings such as thiophene can be used.¹⁷

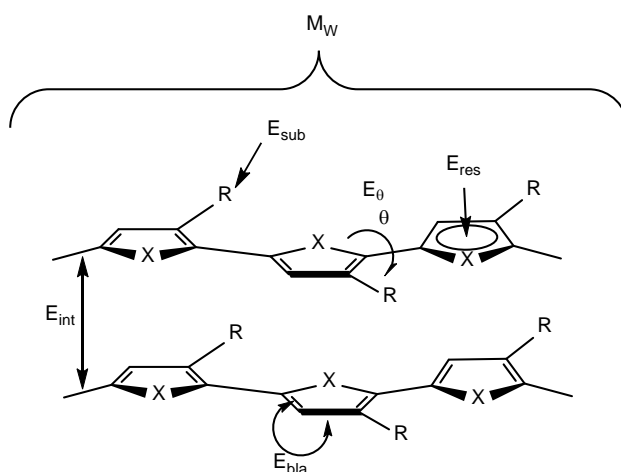


Figure 3.1 Parameters influencing the bandgap (E_g) of π -conjugated polymers: Molecular weight (M_w), intermolecular interaction (E_{int}), substituents (E_{sub}), dihedral angle (θ), coplanarity (E_θ), aromatic resonance energy (E_{res}) and bond length alternation (E_{bla}).

Intermolecular interaction (E_{int}) takes place between polymer chains. Through intermolecular interaction, the delocalizing of π -electron can be enhanced. The increased interaction occurs via aggregation and/or orderly π - π^* transitions in solid state, leading to a smaller bandgap. This could be reflected on the UV-vis spectra of polymer in solution and in solid state. A significant red-shifted absorption onset in solid state of polymer indicates lower optical bandgap obtained.¹⁸

The polymers used as donor materials for OPVs commonly consist of aromatic units. The aromatic resonance energy (E_{res}) is defined as the energy difference between aromatic structure with confined π -electron and delocalization of the π -electron along the conjugated chain.¹³ The difference in the length between adjacent single and double carbon-carbon bonds is depicted as the bond length alternation (E_{bla}). Delocalized electrons could be increased by suppressing the difference between

the length of single and double bonds. Therefore the bandgap could be control efficiently through the manipulation of E_{bla} .¹³

To manipulate the bond length between the aromatic units, the conversion between aromatic form and quinoidal form needs to be taken into account, which is shown in **Figure 3.2**. In the aromatic form, each benzene or thiophene unit maintains its aromaticity and π -electrons are restricted, while in the quinoidal form, π -electrons are delocalized along the conjugated backbones. Since establishing a quinoidal structure needs to decrease the aromaticity and the stabilization energy will decrease during this process, the quinoidal form of a polymer has a narrower bandgap.¹⁹ With the increasing ratio of aromatic form of a given polymer, the difference of bond length is increased accordingly. That is to say, increasing quinoidal character can effectively narrow the bandgap of a given polymer. It could be deduced that one approach to get low bandgap can be achieved via stabilizing the quinoidal form of conjugated polymers.²⁰

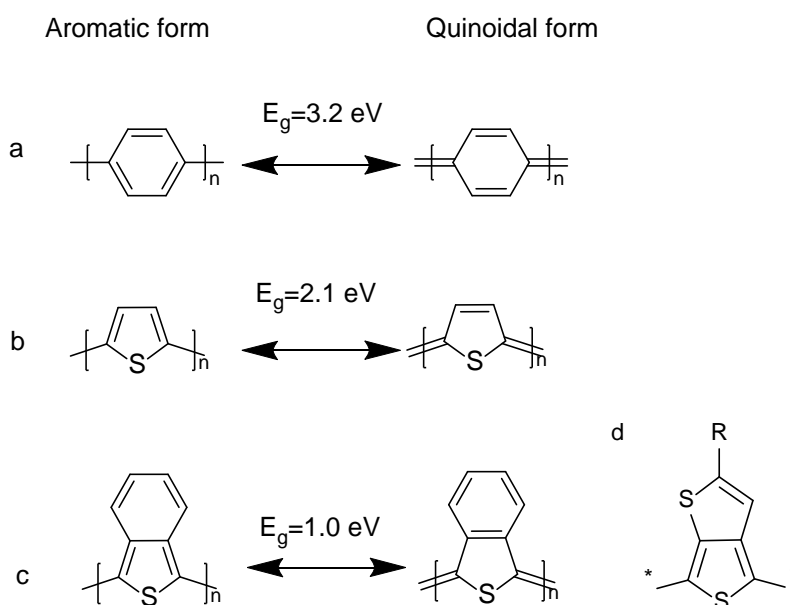


Figure 3.2 Aromatic and quinoidal resonance forms of (a) PPP, (b) PT, (c) PITN. (d) Chemical structure of thienothiophene moiety.

As shown in **Figure 3.2a**, the benzene ring has a high aromatic character and is twisted, which can be reflected from the high bandgap of polyphenylene (PPP). Compared to PPP, polythiophene (PT) is planer and easier to adopt a quinoidal resonance form due to the lower aromaticity of thiophene ring and, resulting in a lower bandgap of 2.1eV (**Figure 3.2b**). By fusing an aromatic benzene ring on the thiophene, a low bandgap polymer polyisothionaphthalene (PITN) is obtained (**Figure 3.2b**), which resulted from that aromatic resonance energy of benzene is much higher than that of thiophene. The backbone of PITN has high tendency to adopt the quinoidal form to preferentially keep the aromaticity of benzene ring. Based on the concept of quinoidal structure being stabilized by introducing thienothiophene moiety (**Figure 3.2d**), narrow bandgap donor material was designed, which gave high performance in OPVs.²⁰

Another methodology to achieve low bandgap conjugated polymer is so-called donor-acceptor (D-A) approach.²¹ The concept of D-A approach was first introduced by Havinga et al. in 1992.²² The principle of this concept is combining the electron-rich (donor) and electron-deficient (acceptor) moieties as repeat units, through which the intramolecular charge transfer (ICT) is created (Figure 3.3). The intramolecular charge transfer can result in a broadening of the valence and conduction bands, which is favorable to the reduction of bandgap.²³⁻²⁴

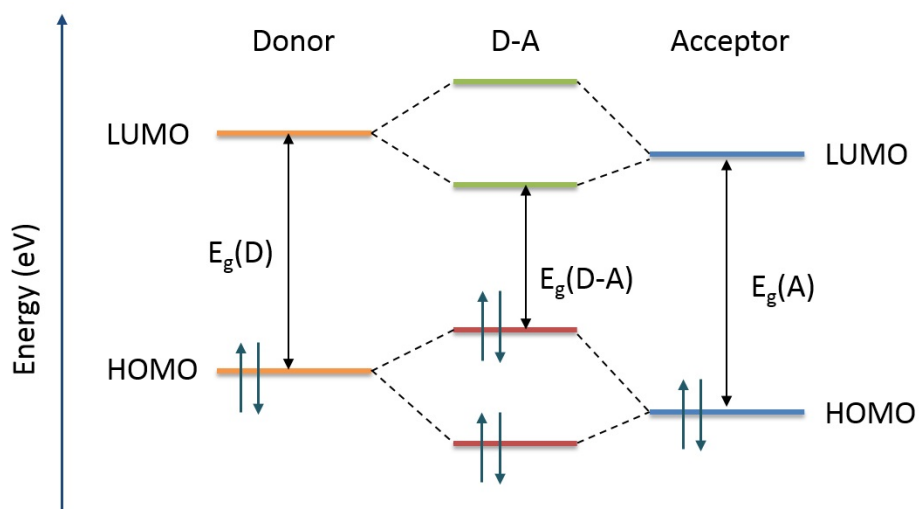


Figure 3.3 Simplified orbital interaction between donor and acceptor units and the obtained lower bandgap [$E_g(D-A)$].

As depicted in **Figure 3.3**, the HOMO of the donor unit and HOMO of the acceptor unit interact with each other and two new HOMOs are generated for the D-A polymer. Meanwhile two new LUMOs are generated in the same way. Then electrons reallocate from original orbitals to the hybridized orbitals of polymer, hence a lower LUMO and a higher HOMO are established, which results in small bandgap in D-A polymer.⁷

For D-A polymer, HOMO energy level is mainly governed by the donor moiety and the LUMO energy levels by the acceptor moiety. Theoretically we can easily tune the bandgap by choosing different donor and acceptor building blocks.²⁴ For example, a D-A polymer namely TQ1 with an optical bandgap of 1.7 eV had been designed and successfully synthesised utilising electron-rich thiophene unit and electron-deficient quinoxaline unit, which achieved the highest efficiency of 6% in OPVs when blended with PC₇₁BM.²⁵ The quinoxaline moiety has the advantages of the ease of structural modification and relatively uncomplicated synthetic procedure.¹⁷ Moreover, the low-lying HOMO energy level of polymers based on quinoxaline moieties enhances the stability against oxidation,²⁶ which is ideal for large-scale fabrication of OPVs in ambient condition. Hence, a range of quinoxaline based donor polymers was designed and have shown high photovoltaic performance.²⁷⁻²⁹ Another D-A polymer based on quinoxaline donor moiety was reported by Chen et al. in 2012,³⁰ through manipulating fluorine substitution on the benzene ring of quinoxaline. This so called PBDT-TFQ

donor polymer gave a high PCE of 8% with PC₇₁BM as acceptor in BHJ polymer solar cells. In 2016, a polymer (PBQ-4F) utilised benzodithiophene (BDT) and quinoxaline units was applied in BHJ solar cell, which achieved over 9% efficiency.³¹ The chemical structures of PBDT-TFQ and PBQ-4F are shown in **Figure 3.4**.

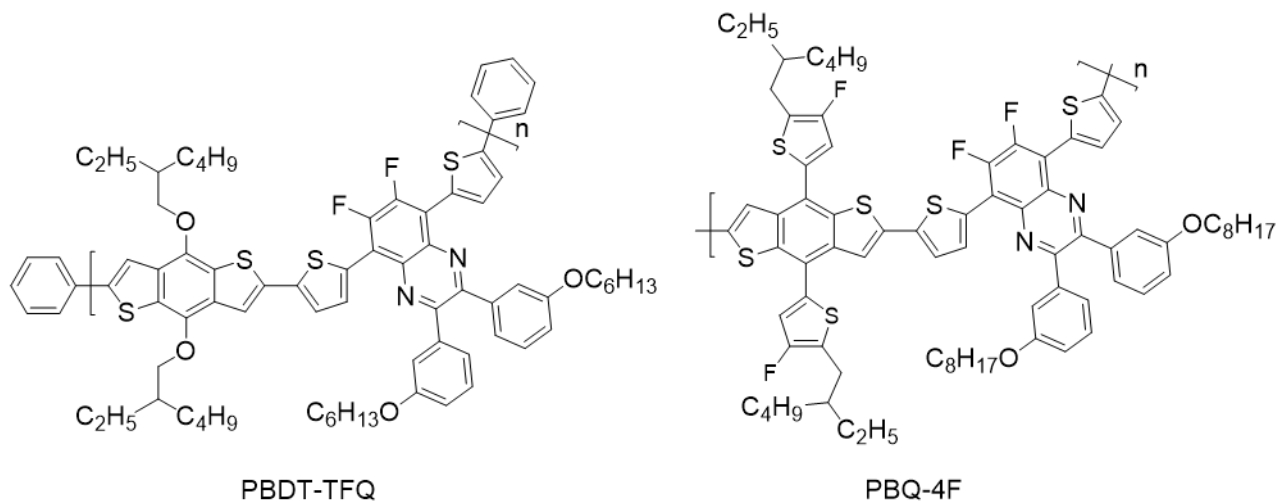


Figure 3.4 Chemical structure of PBDT-TFQ and PBQ-4F.

3.2.2. Design of water/ethanol soluble polymers

So far, highly efficient OPVs have been successfully achieved based on the development of interfacial and donor-acceptor materials as well as morphological control of the functional layers.^{1-2, 32-34} In spite of the great achievements in the area of OPVs, most of the reported BHJ layer in organic photovoltaic devices were possessed from non-environmentally friendly solvent, such as chlorobenzene (CB)³⁵ and *o*-DCB.³⁴ To fulfil the environmental-friendly target of OPVs, green fabrication of efficient and stable OPVs is the ultimate goal to reach. In 2011, a polymer solar cell fabricated using aqueous processing for all layers in ambient condition was reported,³⁶ which shows the possibility and potential of green fabrication.

One approach to realise the green fabrication of OPVs is based on the design of water soluble donor and acceptor materials. This method allow the active layer to be fabricated directly from aqueous solution. Due to the highly conjugated planar backbone and low polarity of p-type polymers, most of the materials used in solar cells can only be dissolved in halogenated and/or aromatic solvents. Since superior organic photovoltaic devices are highly dependent on the decent π -orbital interactions between donor and acceptor, the design strategy of water soluble photoactive materials should not interrupt the conjugation. As discussed above, one design rule to ensure the solubility of conjugated polymers in organic solvents is to attach substituents such as alkyl chain to the conjugated backbone. Hence, the technique to achieve water soluble conjugated polymers can be briefly described as side chain modification. By introducing highly polar and hydrophilic substituents to the conjugated polymer backbone instead of hydrophobic aliphatic alkyl chains, the solubility of targeting

polymers can be tuned without strongly impact to the π -conjugated system. Recently ethanol-soluble donor polymer and fullerene derivative acceptor have been reported, which introduced oligoethylene glycol (OEG) side chains to increase the polarity of active materials.³⁷ Based on OEG modified donor and acceptor, ethanol-processed photovoltaic devices achieved best PCE of 0.75%.

As mentioned earlier, quinoxaline moieties can be easily modified with different types of substituents and well established synthetic procedure exists.¹⁷ The design of water soluble conjugated polymers presented in this thesis was carried out by attaching side chains with polar pendant end groups, such as tertiary amine and pyridine, onto the quinoxaline monomers (**Figure 3.5**). The polymers were subsequently polymerised from modified quinoxaline monomer and another monomer with electron-rich unit, such as thiophene.

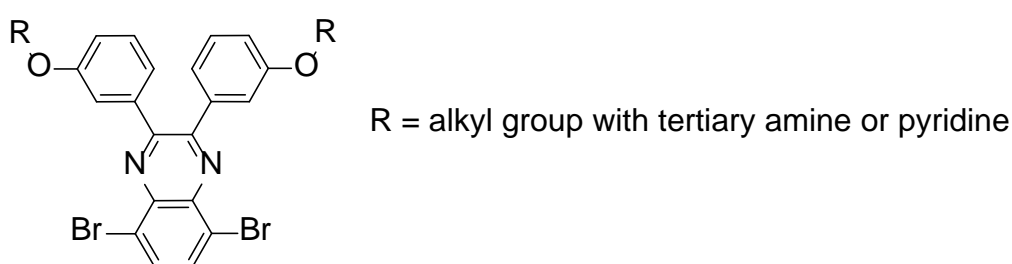


Figure 3.5 Structure of quinoxaline monomer with modified side chain.

In the neutral state, the polymers are not water soluble, which is beneficial for the subsequential purification. Due to the localization of the lone pair of electrons on the nitrogen atoms in the tertiary amine and pyridine ring, the polymers can be easily protonated by using volatile acid, such as acetic acid and formic acid (**Figure 3.6**). Hence, the polymer/molecules designed can be dissolved in water or alcohol in the presence of acid. Compared to pyridine, the quinoxaline unit exhibit much weaker basicity,³⁸ thus, the protonation cannot take effect on the polymer backbone. The active layer based on the materials with functional side chains could be processed from aqueous solution with trace amount of volatile acid. The protonated polymers/molecules in the thin active layer after deposition can be deprotonated by thermal annealing to offer their neutral precursors. Furthermore, the quaternization of the tertiary amine attached to the given polymer could be another option to fulfil water solubility of the polymers.³⁹

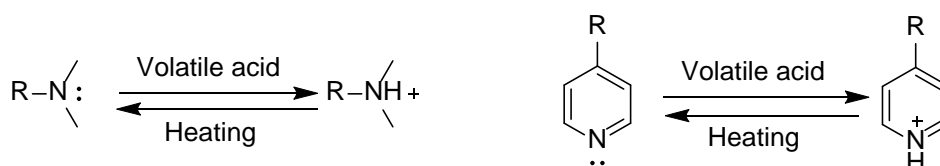


Figure 3.6 Protonation of tertiary amine and pyridine, and reversible deprotonation by heating.

3.3. Synthesis of conjugated polymers for solar cells

The synthesis of D-A conjugated polymers strongly depends on the formation of efficient carbon-carbon single bond between two unsaturated carbons in the donor and acceptor moieties.⁷ Since 1980s, powerful methods for the synthesis of π -conjugated polymers were developed based on electrochemical synthesis⁴⁰ and chemical oxidation polymerisation.⁴¹⁻⁴² In addition to these useful synthetic methods, transition-metal-catalyzed cross-coupling reactions provide an outstandingly efficient and powerful tool for Csp^2-Csp^2 and $Csp-Csp^2$ bond formation and experienced remarkable development over the last decades.⁴³ Palladium-based complexes are the most commonly utilised transition-metal catalysts for the polymerisation of conjugated polymers. A typical catalytic cycle of a transition-metal-catalyzed cross-coupling reaction is shown in **Figure 3.7**, which involves (a) oxidative addition reaction across carbon-halide bond of an electrophile to give an intermediate, (b) transmetalation with an organometallic nucleophile and (c) reductive elimination reaction to form single carbon-carbon bond coupled product and regenerate metal (0) catalyst. By consecutive transition of the catalytic cycle, conjugated length of a targeting polymer can be extended.

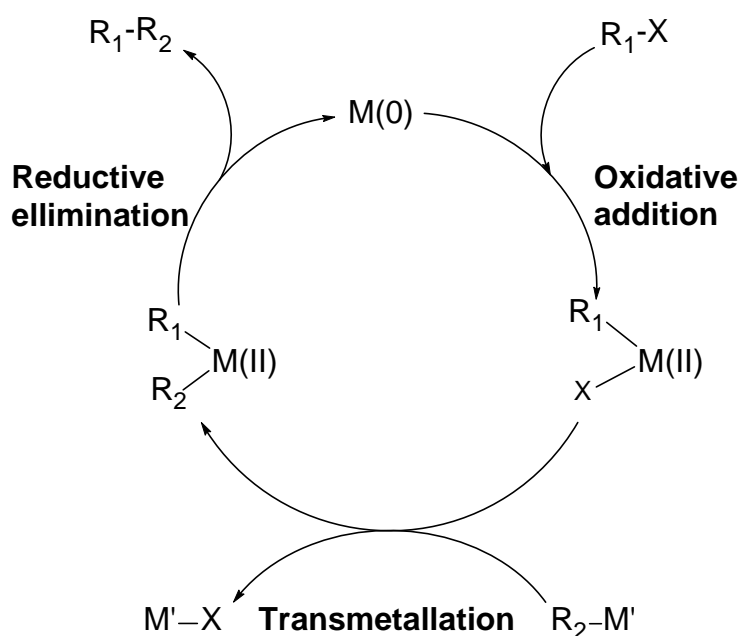


Figure 3.7 Typical catalytic cycle of a transition-metal-catalyzed cross-coupling reaction.

Due to the prominent advantages of mild reaction condition and high tolerance with many functional groups, transition-metal-catalyzed cross-coupling reactions enjoy the dominating roles in the synthesis of conjugated polymers for OPVs. Two types of palladium-catalyzed cross-coupling reactions employed to synthesis conjugated polymers presented in the thesis are Stille⁴⁴ and Suzuki⁴⁵ coupling reactions. Moreover, a possible green alternative to transition-metal-catalyzed cross-coupling reaction would be direct C-H arylation polymerisation, which eliminates the using of toxic organic tin compound.⁴⁶⁻⁴⁷

The Stille coupling is a palladium-catalyzed cross-coupling reaction between an organostannane and an organic halide or pseudo-halide while Suzuki reaction couples an organoboronic acid or ester

with an organic halide or pseudo-halide catalyzed by palladium. Compared to Stille reaction, Suzuki reaction shows lower cost and less toxicity due to the absence of organostannane. However, the reaction condition for Suzuki reaction requires the using of aqueous base solution, which is not applicable for the monomers with functional groups that are water and/or base sensitive. Furthermore, the stannyl groups attached to the benzene ring of the monomer shows insufficient reactivity with aryl halides under Stille reaction conditions. Hence, the Suzuki reaction was used for the synthesis of polymers from monomers with the boronic groups substituted on the benzene ring. In the case of thiophene-containing polymers, Stille reaction is used for polymerisation from monomers with stannyl groups on the thiophene ring.

3.4. Preparation of water dispersible nanoparticles for OPVs

In 2002, Landfester et al. reported aqueous dispersions of conjugated polymer nanoparticles prepared with surfactant using a miniemulsion method,⁴⁸ presenting the possibility to process semiconducting polymer nanospheres from water. Based on this miniemulsion method, water-dispersed NPs were successfully prepared from PBDTTPD:PC₇₁BM and subsequently applied to form active layer in OPVs, which achieved PCE of 3.8%.⁴⁹ Furthermore, another surfactant-free method so-called precipitation method was reported by Yamamoto et al.,⁵⁰⁻⁵¹ who prepared poly(3-hexylthiophene) (P3HT) colloidal alcoholic dispersions. Following work have been carried out on using P3HT NPs prepared through precipitation method in the organic field effect transistors (OFETs),⁵² predicting the potential of these NPs for the fabrication and optimisation of OPVs. The first working OPVs with active layer formed from precipitated P3HT:PCBM nanoparticles was reported in 2011 by Darwis et al.⁵³ Although at that time only 0.018% of PCE was achieved, the optimisation of the deposition and annealing of NP layers leads to over 4% of PCE.⁵⁴

3.4.1. Miniemulsion method

A typical procedure of miniemulsion method used to prepare NPs is depicted in **Figure 3.8** and can be simply described as below:

- 1) Emulsification of macroemulsion formed by blending organic phase containing active materials with aqueous phase containing surfactant through high shearing force, i.e. ultrasonication, to generate miniemulsion;
- 2) Continuous heating of the mixture to remove the miniemulsion dispersed phase solvent;
- 3) Dialysis of the water dispersion to remove excess surfactant.

To support the formation of nano-droplet in the miniemulsion and stabilize the nanoparticles in the prepared dispersion, surfactant is noticeably important, which effectively prevents the aggregation and/or coalescence of NPs in water prior to the deposition. The most commonly used surfactant to make semiconducting material NPs in water is sodium dodecyl sulphate (SDS), though other surfactant may also be applied. However, it is reported that the sulphate groups and sodium ions

remaining in the NP films may act as charge traps, resulting in the decrease of charge mobility.⁵⁵ In **Chapter 6** presented in this thesis, efforts have been put to study the using of alternatives to SDS in the preparation of NPs.

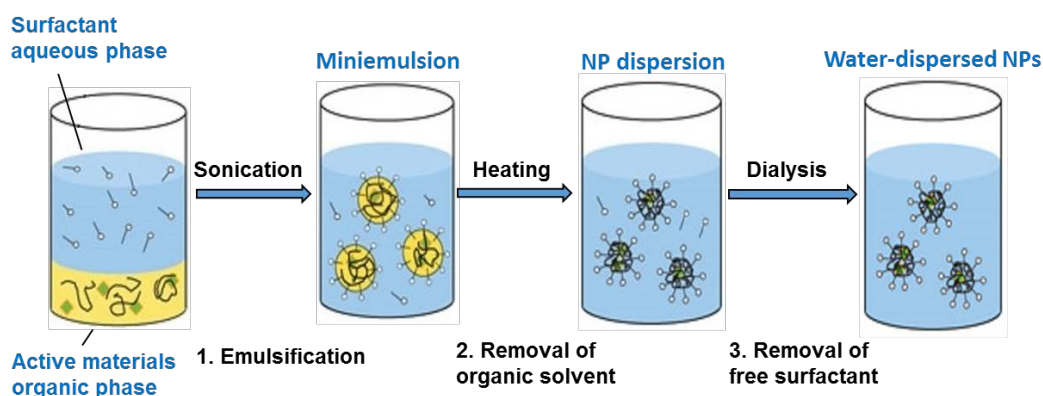


Figure 3.8 Schematic overview of NP preparation using miniemulsion method.

The miniemulsion dispersed phase solvent used in this method should meet the requirements: a) immiscibility with water; b) acceptable solubility of photoactive material; c) relatively high vapour pressure under the boiling point of water. Hence, as a superb low boiling solvent for conjugated polymer, chloroform has been widely used in the preparation of NPs in miniemulsion method.⁵⁶

The removal of organic solvent described in this thesis was achieved by thermally heating the miniemulsion in ambient condition. Though other methods, such as rotary evaporation, may also be used. When organic solvents with high boiling point (>100 °C) was applied as the miniemulsion dispersed phase solvent, temperature applied to convert miniemulsion into aqueous dispersion was chosen based on the vapour pressure (P) calculation from Antoine equations.⁵⁷ $\log P = A - \frac{B}{t+C}$, where the P term is in pound per square inch (psi), t term is the temperature in degree Celsius and A, B and C are component-specific constants. The Antoine equation constants for the solvents used in the work is listed in **Table 3.1** below.

Table 3.1 Antoine equation constants and boiling point at 1 atm for different organic solvents.⁵⁷

Solvent	A	B	C	Boiling point (°C)
<i>o</i> -Xylene	6.9989	1474.68	213.69	144
Anisole	7.0526	1489.99	203.57	153.8

One crucial point to achieve stable aqueous dispersion is to avoid or reduce the material aggregation during the removal of organic solvent. Although the miniemulsion dispersed phase solvents used

may have higher boiling point compared to water, their intrinsic high vapour pressure in the temperature range between 60°C and 90 °C (**Figure 3.9**) facilitate the evaporation of organic solvents at the temperature below the boiling point of water (100 °C). Hence using mild heating together with introduction of extra water into the mixture can effectively convert miniemulsion to dispersion without aggregation of NPs.

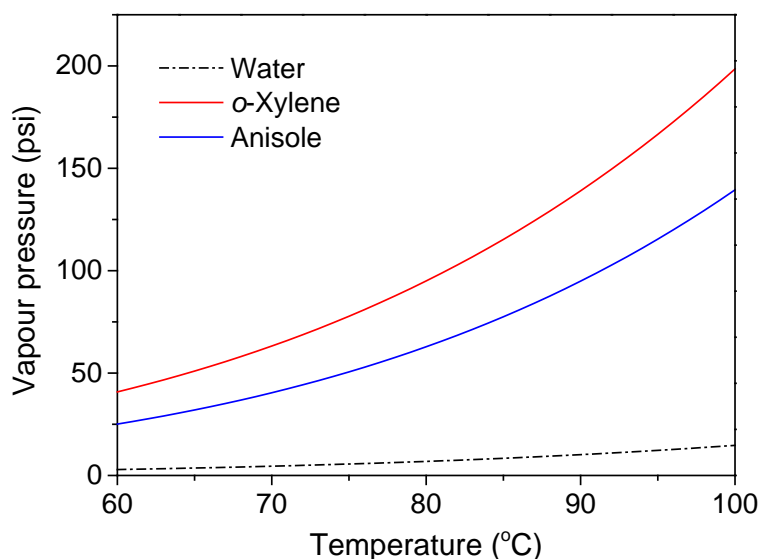


Figure 3.9 Vapour pressure of organic solvents and water as a function of temperature.

To minimize the unwanted effect introduced by ionic surfactant, the excess of free surfactant is removed from the formed dispersion by dialysis, which can be done by adding NP dispersion in a dialysis tube placing in large quantities of pure water⁵⁸⁻⁵⁹ or more efficiently performed by centrifugal dialysis.⁶⁰⁻⁶¹ The extra centrifugal dialysis steps used also concentrate the final NP ink to the desirable concentration for active layer deposition.

The NPs prepared through miniemulsion method have the advantage of decent stability in water. Combining with other water/alcohol processable interfacial materials and vacuum deposition of metal electrode, the utilisation of water-dispersed NPs to form active layer eliminate the usage of harmful organic solvents, especially halogenated solvents in the fabrication of OPVs. However, the miniemulsion processed NPs also have significant disadvantages, such as, the morphology within a single nanoparticle observed to have core-shell structure^{56, 58, 60} and the preparation procedure requires additional surfactant. The core-shell structure of NPs, which normally composes of fullerene-rich core and polymer-rich shell (**Figure 3.10**), will affect the charge transport when given NPs are applied as active layer.⁶² Hence, appropriate annealing is required to coalesce the NPs in the solid state applied as active layer in OPV to modify the morphology, which directly attributes to enhanced exciton dissociation and charge transport.^{60, 63}

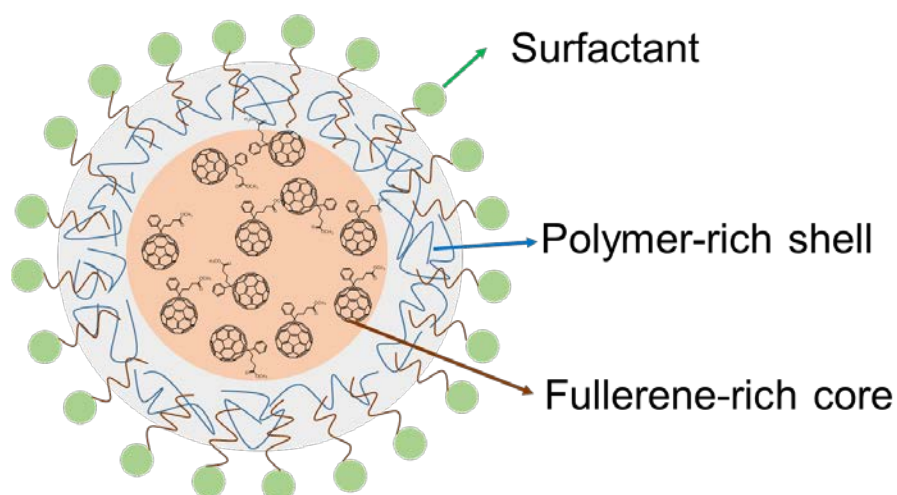


Figure 3.10 Schematic showing the core-shell structure of NPs prepared using miniemulsion method.

3.4.2. Precipitation method

Due to the insulating property of surfactant used in the miniemulsion method and core-shell structure of the prepared NPs described above, precipitation method was developed to eliminate the negative effect of ionic surfactant as well as to increase the intermixing between donor and acceptor materials on the nanoscale.⁶⁴ A typical precipitation method is depicted in **Figure 3.11**: the active components are first dissolved in a solvent followed by injection of the solution into another solvent that exhibits poor solubility of hydrophobic conjugated materials. But the two solvents used need to be miscible. The injection step is commonly performed rapidly into a vigorously stirred solvent in order to effectively achieve precipitated nanoparticles, which is a straightforward single-step process.⁶³

The solvent applied to disperse particles, so called non-solvent, can be water or alcohol, such as ethanol and methanol. In the case of making aqueous dispersed NPs, a photoactive material blend is initially dissolved in an organic solvent which is miscible with water, such as THF. Whereas using alcohol as non-solvent expands the varieties of applicable solvents to dissolved conjugated materials. Therefore, alcohol dispersed NPs can be prepared from active materials that are not soluble in THF.

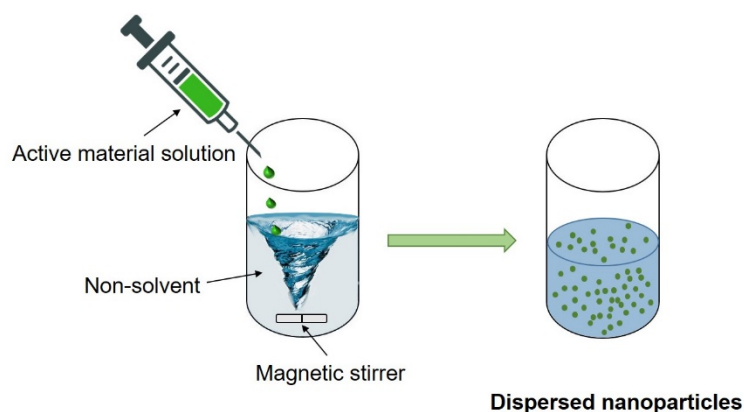


Figure 3.11 Schematic overview of NP preparation using precipitation method.

So far, this method only worked well in the preparation of P3HT NPs, based on which the highest PCE of 4% have been obtained in an inverted device structure.⁵⁴ Compared to P3HT:PCBM NPs prepared from miniemulsion method, precipitated P3HT:PCBM NPs were reported to exhibit more uniformly blended morphology, leading to improved device performance.⁶² Nevertheless, one of the greatest challenges in the application of NPs prepared from precipitation method is to find the knowhow about stabilizing NPs in the dispersion. Another difficulty comes from the fabrication of active layer from precipitated NPs due to their low concentration compared to NP dispersion made from miniemulsion method. Hence, multiple deposition or using other depositing methods are essential to reach decent thickness of the active layer. Recently, Prunet et al. reported aqueous PCDTBT:PC₇₁BM NPs made by precipitation method and subsequently used in OPVs, showing power conversion efficiency of only 0.33% in the best cell.⁶³ In their work, it is claimed that aggregation starts to take place as soon as the final solid concentration in water reaching 0.4 mg/mL, which might explain the reason for the unsatisfactory photovoltaic performance of these NPs.

Despite the intrinsic instability of NPs in the absence of surfactant, the precipitation method was shown to be an efficient tool to tune the morphology of the active layer in OPVs.^{62, 64} Furthermore, since the precipitation method do not require high energy-consuming ultrasonication process, it is more suitable to upscale the preparation of NPs, especially in the case of serving as active layer in large-scale printed OPVs.

The methods developed to disperse photoactive materials in water or alcohol expands the varieties of possible donor/acceptor candidatures to fulfil the green deposition of active layer in polymer solar cells.

3.4.3. Stabilisation of nanoparticles

Two methods used to prepare conjugated NPs have been intensively investigated in the field of application in organic electronics. However, a fundamental understanding of the factors influencing the stability of NPs is required in order to achieve stable NP ink for the fabrication of active layer.

The aggregation of particles, which is often observed when precipitating a polymer organic solution to an anti-solvent/non-solvent, can be explained by the van der Waals interaction between the particles.⁶⁵ Therefore, necessary repulsive force is required to separate particles in the dispersed medium.

In the case of ionic surfactant, such as SDS, being used to stabilise polymer NPs, negative charge of the sulfonate ion is closely bound to the particle, and sodium counterions line up parallel to the negative charge, forming a double layer of charges (**Figure 3.12a**). The electrostatic attraction between the two opposite and separated charges cause an electrical field to be established across the interface, and an electrical double layer (EDL) is formed around the particle surface. The EDL consists an inner layer called the Stern layer, where ions are strongly bound to the particle surface, and an outer layer called diffuse layer, where ions are less associated. The repulsive effect of EDL is responsible for the stability of particles. As illustrated in **Figure 3.12a**, the potential energy decreases linearly from the thermodynamic surface potential to the Stern potential, then decays exponentially to the zeta potential, which is defined as the potential difference between the diffuse layer and the dispersion medium. The zeta potential is an important parameter to characterise the stability of a formed NP dispersion. For the negatively charge particle surface, the lower negative potential indicates more stable colloid or NP dispersion.⁶⁶

To characterise or predict the stability of a colloidal system, DLVO theory⁶⁷ was established 70 years ago, which combines the van der Waals attraction with the EDL repulsive force to result a total interaction potential as shown in **Figure 3.12b**. The maximum of the curve in the total interaction potential represents the aggregation barrier that two particles have to overcome to form aggregate. Any disturbance to the EDL repulsive force will lead to the decrease or increase of the aggregation barrier, thus, resulting in different stability of the NP suspension.

There are different factors that can influence the repulsion introduced by EDL, such as the ion strength of the suspension, value of the surface potential and the particle size. For example, high ion concentration in the disperse medium can lead to smaller EDL, hence, resulting in reduced repulsive force. In contrast, the van der Waals attraction is relatively independent of the ion strength, but is highly dependent on the size and surface area of a NP.

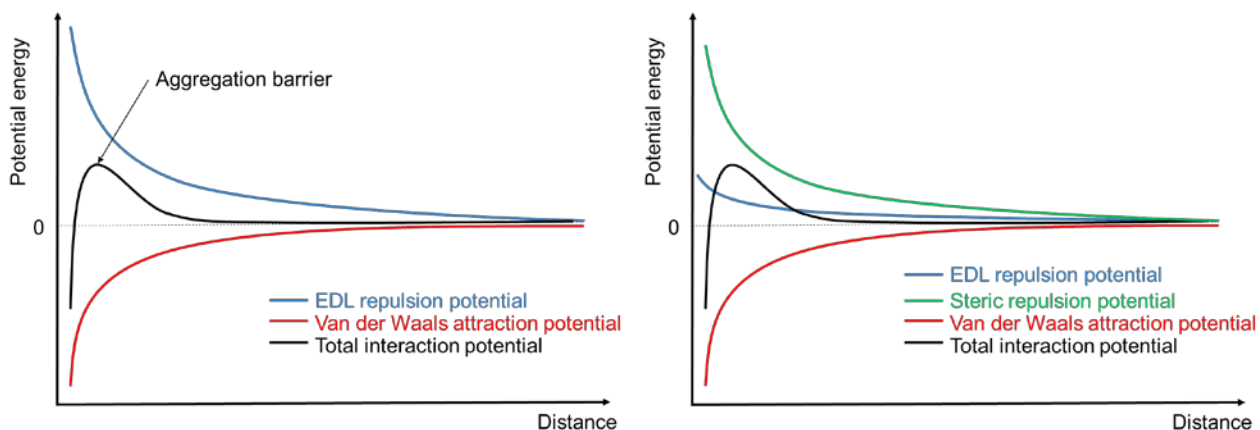
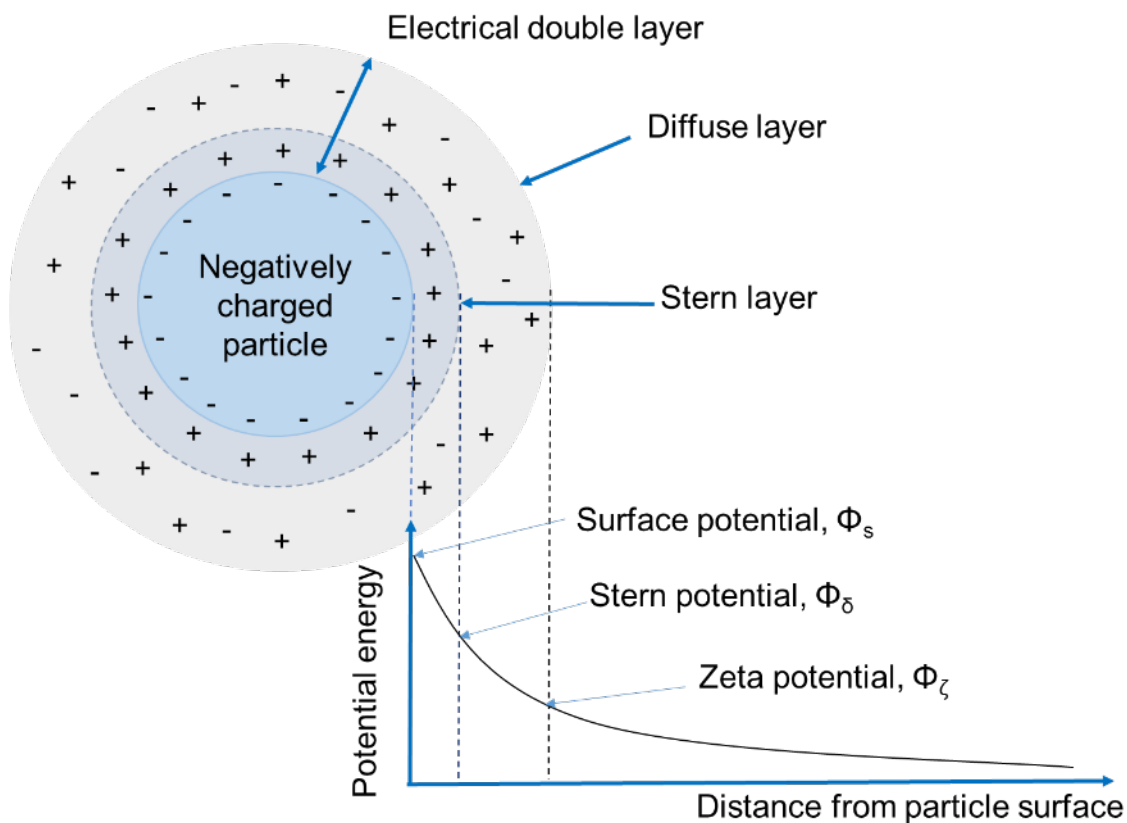


Figure 3.12 (a) Schematic of the electrical double layer around a NP and the potential energy corresponds to the different position of a NP in a suspension. Illustration of the potential energy between two particles based on DLVO theory (b) and DLVO theory with an extended steric repulsion (c).

If the electrostatic repulsion is sufficiently high, high aggregation barrier can be achieved, thus, aggregation of particles can be effectively suppressed.⁶⁸

In the case of non-ionic surfactant being introduced to the preparation of NPs, these non-ionic species serves as a protective layer to increase steric repulsion (e.g. hydration force) between particles.⁶⁵ Hence, the interaction potential in the DLVO theory can be extended by the addition of a term describing the force due to the steric stabilisation (**Figure 3.12c**). In this case, the repulsive

force introduced by EDL could be too weak to overcome the van der Waals attraction. However, if the steric repulsion established between the conjugated polymer/molecule particles can overcome the van der Waals attraction between particles, stable NP ink can be obtained with high aggregation barrier between particles.

In order to obtain stable NP suspension prepared by the precipitation method without an additional surfactant, the EDL repulsive force and steric stabilisation force in the polymer colloidal system have to overcome the van der Waals attractive force. Otherwise, surfactant is required to enhance the repulsion between particles, and the repulsive strength introduced by the additional surfactant needs to be carefully studied. Furthermore, conjugated polymers with charged side groups or hydrophilic side chains (i.e. oligoethylene glycol) are potential candidates to increase the repulsive force between particles in a colloidal system, and the possibility of NP formation using functionalized polymers will be investigated.

3.5. Characterisation techniques

3.5.1. UV-Vis Spectroscopy

The light absorption is one of the key properties for conjugated polymers and active material blend, which can effectively influence the photovoltaic performance of the given solar devices. To characterise the optical property of synthesised material, UV-vis spectroscopy is an important and straightforward analytical tool to detect the absorption spectrum and optical bandgap (E_g^{opt}). E_g^{opt} is the energy threshold for photons to be absorbed by conjugated materials and can be inferred from the absorption onset (λ_{onset}) at low-energy region of the solid state UV-vis spectrum (shown in **Figure 3.13**). Hence, E_g^{opt} can be calculated by the formula $E_g^{opt} = hc/\lambda_{onset}$, in which h is the Planck constant, c is the speed of light in vacuum. The photoactive material used for superior performance of OPVs should not only have a preferable optical band gap between 1-2 eV,⁶⁹⁻⁷¹ but also show broad range of absorption in the solar radiation spectrum,⁷² which is favourable for maximizing the utilisation of solar energy.

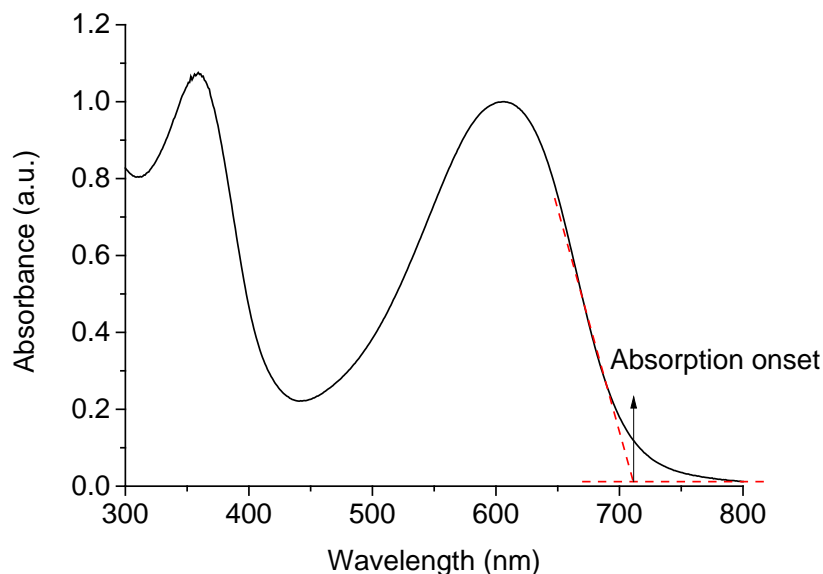


Figure 3.13 A typical UV-vis spectrum of a conjugated polymer film, the red-dashed lines illustrate the determination of absorption onset from the intersection of line with greatest slope.

3.5.2. Photoluminescence (PL) spectroscopy

Photoluminescence (PL) spectroscopy is a non-destructive method for the investigation of the electronic structure of semiconducting materials^{14, 73} and can be applied to probe the efficiency of exciton dissociation in BHJ active layer.⁷⁴

In a typical PL measurement, a conjugated polymer is excited upon the illumination providing photons with energy larger than its bandgap energy, leading the movement of electrons from the ground state to the permissible excited states (formation of exciton). The excited electrons then undergo the non-radiative relaxation to the lower excited state, prior to the return to their ground state (in the absence of electron acceptor), releasing the excess energy through photon emission. The release of excess energy may also be a non-radiative decay, which would not result in the emission of light. Due to the delocalization of electrons presented in the conjugated backbone of a donor polymer, typical PL spectrum of a conjugated polymers shows significant emission peak at the photon energy region below the bandgap.⁷⁵

By virtue of the electron-affinity of acceptor molecules, the excited electrons from a donor polymer upon illumination may transfer to the LUMO of the acceptor, leading to the exciton dissociation. Hence PL quenching of the blend film can be observed in the emission spectrum. To achieve superior performance of organic photovoltaics, improving short-circuit current is one important issue, which strongly depends on the efficient exciton dissociation. PL quenching can directly provide information about the dissociation of excitons.⁷⁴

3.5.3. Cyclic voltammetry

As described earlier, HOMO and LUMO energy level of a given donor polymer are key parameters in determining the performance of resulting photovoltaic devices. The HOMO and LUMO of a conjugated polymer represent the energy required for the initial injection of holes and electrons, respectively, hence can be deduced from the estimation of redox potentials. One of the widely used methods to investigate the electrochemical behaviors of conjugated polymers is cyclic voltammetry (CV),⁷⁶ which is performed by cycling the potential of a working electrode against a reference electrode.

Through CV measurements electrochemical redox waves can be obtained, from which we can estimate the onset of oxidation and reduction potentials of a given polymer. The CV measurements presented in this thesis were calibrated using an internal reference of ferrocene/ferrocenium (Fc/Fc⁺). The energy level of HOMO (E_{HOMO}) and LUMO (E_{LUMO}) of the polymers were estimated from the peak onset potentials by setting the oxidative potential of Fc/Fc⁺ vs. the normal hydrogen electrode (NHE) to 0.630 V, and the NHE vs. the vacuum level to 4.5 V.^{70, 77} Hence, the respective energy levels can be calculated based on formulas: $E_{HOMO} = -(E_{ox}^{onset} + 5.13) eV$, $E_{LUMO} = -(E_{red}^{onset} + 5.13) eV$, where E_{ox}^{onset} is the onset oxidation potential and E_{red}^{onset} the onset redox potential of polymers against reference electrode.^{70, 75, 77} The determination of onset potentials from a cyclic voltammogram is shown in **Figure 3.14**. The electrochemical bandgaps of donor polymers can be acquired for the estimation of energy alignment with acceptor materials.

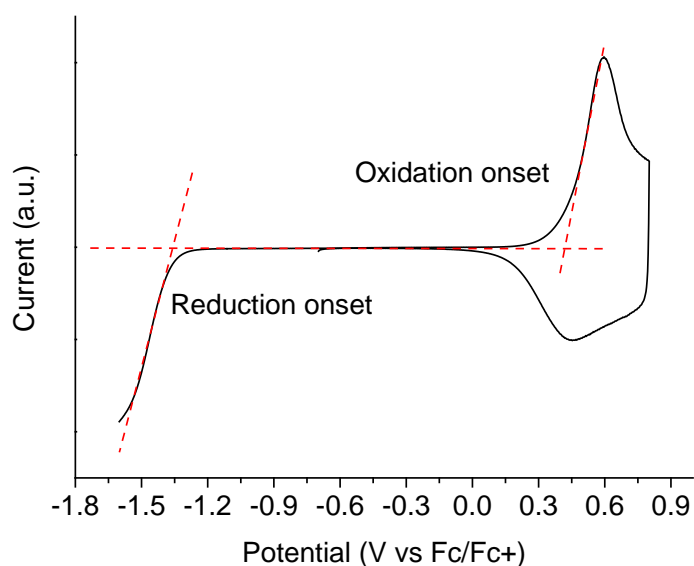


Figure 3.14 A typical cyclic voltammogram of a conjugated polymer, the red-dashed lines illustrate the determination of onset potentials.

3.5.4. Thermal gravimetric analysis (TGA)

To achieve long-lasting organic photovoltaic devices, polymers applied as photoactive materials should ideally exhibit superior thermal stability. The evaluation of thermal stability of a given material

is normally carried out through thermal gravimetric analysis (TGA), which studies the mass of a sample over time as a function of temperature.

As mentioned earlier in the design of water soluble conjugated polymer, solid films of tertiary amine or pyridine side-chain substituted polymers can be processed from aqueous solution after the protonation of side chains with the presence of volatile acid. To deprotonate the polymers in the solid state, thermal annealing of the solid film on substrates is a straight-forward way. TGA is effectively used to estimate the deprotonation temperature and time require for water soluble conjugated polymers.

3.5.5. Differential scanning calorimetry (DSC)

DSC is a thermoanalytical technique applied to measure the heat flow difference between a sample and a reference as a function of temperature and characteristic temperatures of a reaction or transition.⁷⁸ This technique has been widely used to investigate the phase transitions of a given material under the heat flow, for example melting (endothermic process) and crystallization (exothermic process). The work presented in the thesis was using conventional DSC to probe the phase behavior of PCBM with polymers to study the miscibility between acceptor molecules and side-chain modified TQ1 derivatives.

3.5.6. Dynamic mechanical thermal analysis (DMTA)

In order to gain better control of the processing parameters and to achieve the optimal morphology of the active layers, the glass transition temperature (T_g) of conjugated polymers needs to be carefully studied.⁷⁹⁻⁸⁰ Although DSC has been widely applied to estimate the T_g of materials⁸¹, using DSC to determine the T_g of conjugated polymers faces a lot of difficulties due to that only the amorphous fraction of polymers shows a glass transition. Furthermore, the β transition, which is often associated with the side chain movements and can be related to the stiffness of a polymer,⁸² is too faint to be detected in DSC.⁸³ Hence, DMTA has been used in strain-controlled mode to probe the thermal transition of conjugated polymers presented in this thesis.

In a typical DMTA measurement, a complex dynamic modulus (E^*), a storage modulus (E') and a loss modulus (E'') are calculated from the material response to an oscillating force.⁸³ The ratio between E' and E'' is the $\tan \delta$, the peak temperature of which is commonly used to define T_g of a measured sample.⁸⁴ Although DMTA is a powerful and direct technique to probe the thermal transitions of polymers, its application for conjugated polymers has been limited. The biggest problem originates from the sample preparation, which requires free-standing film of reasonable thickness. Due to the frangibility of the most conjugated polymers, it is unpractical to prepare a thick free-standing film for DMTA measurement. Hence, we have developed a woven glass fibre based technique to prepare the DMTA samples, which is shown in **Figure 3.15**. The sample preparation is performed by drop casting a polymer solution on to a pre-cut glass fibre (**Figure 3.15c**), which should

have the strands on 45 ° bias to avoid any continuous fibre being connected between two clamps and contributing to the DMTA signal. The prepared sample supported by the glass fibre mesh (Figure 3.15d) should be uniformly covered by the polymer, which is required to be less than 5 mg. This technique has successfully solved the problem of sample preparation, and the thermal transitions of conjugated polymers can be detected with high sensitivity.⁸⁵

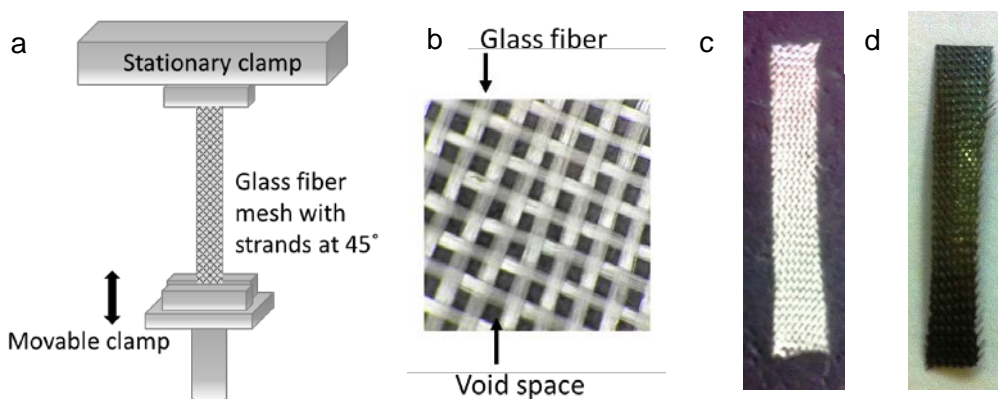


Figure 3.15 (a) Schematic depicting a woven glass fibre supported sample mounted between the clamps for DMTA measurement. (b) Optical image of woven glass fibre. Pictures of (c) uncoated glass fibre and (d) glass fibre coated with a conjugated polymer.⁸⁵

3.5.7. Scanning electron microscopy (SEM)

One useful tool to characterise nanoparticles forming active layer is SEM,⁸⁶ which produces images of NP samples by scanning the surface with focused beam of electrons. Due to the semiconductive property of the active materials used in NP OPVs, the NP specimens may collect charge when exposing under the electron beam with high accelerating voltage, resulting in image artefacts. Furthermore, the energy accumulated on the NP surface after long-time scanning could fuse the NPs and create holes on the film. To avoid the image artefacts and/or the destruction of the topography of NP samples, low accelerating voltage (1-2 kV) is utilised in imaging. The most important information obtained from topographic SEM images of NP active layer is the degree of phase separation upon annealing, shape of particles and size distribution. The size distribution of NPs in the solid state is calculated by applying a circular Hough transform algorithm⁶⁰ to the SEM image.

In addition to SEM, energy-dispersive X-ray spectroscopy (EDS)⁸⁷ is used with the electron beam of SEM to analyse the elemental composition in the NP films. As described earlier in 3.4, the preparation of NPs using miniemulsion method requires the presence of surfactant to form miniemulsion as well as to stabilize active material NPs in water. Through EDS analysis sodium concentration can be deduced, which is originated from the surfactant SDS. We could directly study the effectiveness of different method applied to the removal of SDS.

3.6. References

1. Zhao, W.; Li, S.; Yao, H.; Zhang, S.; Zhang, Y.; Yang, B.; Hou, J., Molecular Optimization Enables over 13% Efficiency in Organic Solar Cells. *Journal of the American Chemical Society* **2017**, *139* (21), 7148-7151.
2. Zhao, W.; Qian, D.; Zhang, S.; Li, S.; Inganäs, O.; Gao, F.; Hou, J., Fullerene-Free Polymer Solar Cells with over 11% Efficiency and Excellent Thermal Stability. *Advanced Materials* **2016**, *28* (23), 4734-9.
3. Ebenhoch, B.; Thomson, S. A. J.; Genevičius, K.; Juška, G.; Samuel, I. D. W., Charge carrier mobility of the organic photovoltaic materials PTB7 and PC71BM and its influence on device performance. *Organic Electronics* **2015**, *22*, 62-68.
4. Zhang, S.; Qin, Y.; Zhu, J.; Hou, J., Over 14% Efficiency in Polymer Solar Cells Enabled by a Chlorinated Polymer Donor. *Advanced Materials* **2018**, *30* (20), e1800868.
5. Mihailetchi, V. D.; van Duren, J. K. J.; Blom, P. W. M.; Hummelen, J. C.; Janssen, R. A. J.; Kroon, J. M.; Rispens, M. T.; Verhees, W. J. H.; Wienk, M. M., Electron Transport in a Methanofullerene. *Advanced Functional Materials* **2003**, *13* (1), 43-46.
6. Singh, T. B.; Marjanovic, N.; Stadler, P.; Auinger, M.; Matt, G. J.; Gunes, S.; Sariciftci, N. S.; Schwodiauer, R.; Bauer, S., Fabrication and characterization of solution-processed methanofullerene-based organic field-effect transistors. *Journal of Applied Physics* **2005**, *97* (8), 083714-5.
7. Cheng, Y.-J.; Yang, S.-H.; Hsu, C.-S., Synthesis of conjugated polymers for organic solar cell applications. *Chemical Reviews* **2009**, *109* (11), 5868-5923.
8. Mikroyannidis, J. A.; Kabanakis, A. N.; Sharma, S. S.; Sharma, G. D., A Simple and Effective Modification of PCBM for Use as an Electron Acceptor in Efficient Bulk Heterojunction Solar Cells. *Advanced Functional Materials* **2011**, *21* (4), 746-755.
9. Mikroyannidis, J. A.; Tsagkournos, D. V.; Sharma, S. S.; Sharma, G. D., Synthesis of a Broadly Absorbing Modified PCBM and Application As Electron Acceptor with Poly(3-Hexylthiophene) As Electron Donor in Efficient Bulk Heterojunction Solar Cells. *The Journal of Physical Chemistry C* **2011**, *115* (15), 7806-7816.
10. Varotto, A.; Treat, N. D.; Jo, J.; Shuttle, C. G.; Batara, N. A.; Brunetti, F. G.; Seo, J. H.; Chabinyk, M. L.; Hawker, C. J.; Heeger, A. J.; Wudl, F., 1,4-Fullerene Derivatives: Tuning the Properties of the Electron Transporting Layer in Bulk-Heterojunction Solar Cells. *Angewandte Chemie International Edition* **2011**, *50* (22), 5166-5169.
11. Zhang, M.; Wu, F.; Cao, Z.; Shen, T.; Chen, H.; Li, X.; Tan, S., Improved photovoltaic properties of terpolymers containing diketopyrrolopyrrole and an isoindigo side chain. *Polymer Chemistry* **2014**, *5* (13), 4054-4060.
12. Chochos, C. L.; Choulis, S. A., How the structural deviations on the backbone of conjugated polymers influence their optoelectronic properties and photovoltaic performance. *Progress in Polymer Science* **2011**, *36* (10), 1326-1414.
13. Winder, C.; Sariciftci, N. S., Low bandgap polymers for photon harvesting in bulk heterojunction solar cells. *Journal of Materials Chemistry* **2004**, *14* (7), 1077-1086.
14. Schwarz, C.; Bäessler, H.; Bauer, I.; Koenen, J. M.; Preis, E.; Scherf, U.; Köhler, A., Does Conjugation Help Exciton Dissociation? A Study on Poly(p-phenylene)s in Planar Heterojunctions with C60 or TNF. *Advanced Materials* **2012**, *24* (7), 922-925.
15. Dang, D.; Chen, J.; Zhou, P.; Duan, L.; Bao, X.; Yang, R.; Chen, J.; Zhu, W., Tuning the fused aromatic rings to enhance photovoltaic performance in wide band-gap polymer solar cells. *Polymer* **2016**, *104*, 130-137.
16. Dang, D.; Zhou, P.; Zhong, J.; Fan, J.; Wang, Z.; Wang, Y.; Pei, Y.; Bao, X.; Yang, R.; Hu, W.; Zhu, W., Novel wide band-gap polymer utilizing fused hetero-aromatic unit for efficient polymer solar cells and field-effect transistors. *Polymer* **2014**, *55* (26), 6708-6716.
17. Gedefaw, D.; Prosa, M.; Bolognesi, M.; Seri, M.; Andersson, M. R., Recent Development of Quinoxaline Based Polymers/Small Molecules for Organic Photovoltaics. *Advanced Energy Materials* **2017**, 1700575.
18. Ko, S.; Hoke, E. T.; Pandey, L.; Hong, S.; Mondal, R.; Risko, C.; Yi, Y.; Noriega, R.; McGehee, M. D.; Brédas, J.-L., Controlled conjugated backbone twisting for an increased open-circuit voltage while having a high short-circuit current in poly(hexylthiophene) derivatives. *Journal of the American Chemical Society* **2012**, *134* (11), 5222-5232.

19. Liang, Y.; Wu, Y.; Feng, D.; Tsai, S.-T.; Son, H.-J.; Li, G.; Yu, L., Development of new semiconducting polymers for high performance solar cells. *Journal of the American Chemical Society* **2008**, *131* (1), 56-57.
20. Liang, Y.; Feng, D.; Wu, Y.; Tsai, S.-T.; Li, G.; Ray, C.; Yu, L., Highly Efficient Solar Cell Polymers Developed via Fine-Tuning of Structural and Electronic Properties. *Journal of the American Chemical Society* **2009**, *131* (22), 7792-7799.
21. Singh, R.; Pagona, G.; Gregoriou, V. G.; Tagmatarchis, N.; Toliopoulos, D.; Han, Y.; Fei, Z.; Katsouras, A.; Avgeropoulos, A.; Anthopoulos, T. D.; Heeney, M.; Keivanidis, P. E.; Chochos, C. L., The impact of thienothiophene isomeric structures on the optoelectronic properties and photovoltaic performance in quinoxaline based donor–acceptor copolymers. *Polymer Chemistry* **2015**, *6* (16), 3098-3109.
22. Havinga, E.; Ten Hoeve, W.; Wynberg, H., A new class of small band gap organic polymer conductors. *Polymer Bulletin* **1992**, *29* (1-2), 119-126.
23. Zhou, H.; Yang, L.; Xiao, S.; Liu, S.; You, W., Donor–Acceptor Polymers Incorporating Alkylated Dithienylbenzothiadiazole for Bulk Heterojunction Solar Cells: Pronounced Effect of Positioning Alkyl Chains. *Macromolecules* **2009**, *43* (2), 811-820.
24. Roncali, J., Molecular Engineering of the Band Gap of π -Conjugated Systems: Facing Technological Applications. *Macromolecular Rapid Communications* **2007**, *28* (17), 1761-1775.
25. Wang, E.; Hou, L.; Wang, Z.; Hellström, S.; Zhang, F.; Inganäs, O.; Andersson, M. R., An Easily Synthesized Blue Polymer for High - Performance Polymer Solar Cells. *Advanced Materials* **2010**, *22* (46), 5240-5244.
26. Tseng, W.-H.; Chen, H.-C.; Chien, Y.-C.; Liu, C.-C.; Peng, Y.-K.; Wu, Y.-S.; Chang, J.-H.; Liu, S.-H.; Chou, S.-W.; Liu, C.-L.; Chen, Y.-H.; Wu, C.-I.; Chou, P.-T., Comprehensive study of medium-bandgap conjugated polymer merging a fluorinated quinoxaline with branched side chains for highly efficient and air-stable polymer solar cells. *Journal of Materials Chemistry A* **2014**, *2* (47), 20203-20212.
27. Hansson, R.; Ericsson, L. K. E.; Holmes, N. P.; Rysz, J.; Opitz, A.; Campoy-Quiles, M.; Wang, E.; Barr, M. G.; Kilcoyne, A. L. D.; Zhou, X.; Dastoor, P.; Moons, E., Vertical and lateral morphology effects on solar cell performance for a thiophene–quinoxaline copolymer:PC70BM blend. *Journal of Materials Chemistry A* **2015**, *3* (13), 6970-6979.
28. Dang, D.; Chen, W.; Himmelberger, S.; Tao, Q.; Lundin, A.; Yang, R.; Zhu, W.; Salleo, A.; Müller, C.; Wang, E., Enhanced Photovoltaic Performance of Indacenodithiophene-Quinoxaline Copolymers by Side-Chain Modulation. *Advanced Energy Materials* **2014**, *4* (15), 1400680.
29. Dang, D.; Chen, W.; Yang, R.; Zhu, W.; Mammo, W.; Wang, E., Fluorine substitution enhanced photovoltaic performance of a D-A(1)-D-A(2) copolymer. *Chemical Communications* **2013**, *49* (81), 9335-7.
30. Chen, H.-C.; Chen, Y.-H.; Liu, C.-C.; Chien, Y.-C.; Chou, S.-W.; Chou, P.-T., Prominent Short-Circuit Currents of Fluorinated Quinoxaline-Based Copolymer Solar Cells with a Power Conversion Efficiency of 8.0%. *Chemistry of Materials* **2012**, *24* (24), 4766-4772.
31. Zhao, Z.; Zhang, Y.; Wang, Y.; Qin, X.; Wu, J.; Hou, J., Fluorinated and non-fluorinated conjugated polymers showing different photovoltaic properties in polymer solar cells with PFNBr interlayers. *Organic Electronics* **2016**, *28*, 178-183.
32. Yang, Y.; Zhang, Z. G.; Bin, H.; Chen, S.; Gao, L.; Xue, L.; Yang, C.; Li, Y., Side-Chain Isomerization on an n-type Organic Semiconductor ITIC Acceptor Makes 11.77% High Efficiency Polymer Solar Cells. *Journal of the American Chemical Society* **2016**, *138* (45), 15011-15018.
33. He, Z.; Zhong, C.; Su, S.; Xu, M.; Wu, H.; Cao, Y., Enhanced power-conversion efficiency in polymer solar cells using an inverted device structure. *Nature Photonics* **2012**, *6* (9), 591-595.
34. Liu, Y.; Zhao, J.; Li, Z.; Mu, C.; Ma, W.; Hu, H.; Jiang, K.; Lin, H.; Ade, H.; Yan, H., Aggregation and morphology control enables multiple cases of high-efficiency polymer solar cells. *Nature Communications* **2014**, *5*, 5293.
35. Li, Z.; Xu, X.; Zhang, W.; Meng, X.; Ma, W.; Yartsev, A.; Inganäs, O.; Andersson, M. R.; Janssen, R. A.; Wang, E., High Performance All-Polymer Solar Cells by Synergistic Effects of Fine-Tuned Crystallinity and Solvent Annealing. *Journal of the American Chemical Society* **2016**, *138* (34), 10935-44.
36. Søndergaard, R.; Helgesen, M.; Jørgensen, M.; Krebs, F. C., Fabrication of Polymer Solar Cells Using Aqueous Processing for All Layers Including the Metal Back Electrode. *Advanced Energy Materials* **2011**, *1* (1), 68-71.

37. Nguyen, T. L.; Lee, C.; Kim, H.; Kim, Y.; Lee, W.; Oh, J. H.; Kim, B. J.; Woo, H. Y., Ethanol-Processable, Highly Crystalline Conjugated Polymers for Eco-Friendly Fabrication of Organic Transistors and Solar Cells. *Macromolecules* **2017**, *50* (11), 4415-4424.
38. Katritzky, A. R.; Ramsden, C. A.; Joule, J. A.; Zhdankin, V. V., *Handbook of heterocyclic chemistry*. Elsevier: 2010.
39. Wu, Z.; Sun, C.; Dong, S.; Jiang, X. F.; Wu, S.; Wu, H.; Yip, H. L.; Huang, F.; Cao, Y., n-Type Water/Alcohol-Soluble Naphthalene Diimide-Based Conjugated Polymers for High-Performance Polymer Solar Cells. *Journal of the American Chemical Society* **2016**, *138* (6), 2004-13.
40. Sabouraud, G.; Sadki, S.; Brodie, N., The mechanisms of pyrrole electropolymerization. *Chemical Society Reviews* **2000**, *29* (5), 283-293.
41. Roncali, J., Synthetic principles for bandgap control in linear π -conjugated systems. *Chemical reviews* **1997**, *97* (1), 173-206.
42. Toshima, N.; Hara, S., Direct synthesis of conducting polymers from simple monomers. *Progress in Polymer Science* **1995**, *20* (1), 155-183.
43. Xia, Y.; Qiu, D.; Wang, J., Transition-Metal-Catalyzed Cross-Couplings through Carbene Migratory Insertion. *Chemical Reviews* **2017**.
44. Stille, J. K., The Palladium-Catalyzed Cross-Coupling Reactions of Organotin Reagents with Organic Electrophiles [New Synthetic Methods (58)]. *Angewandte Chemie International Edition in English* **1986**, *25* (6), 508-524.
45. Miyaura, N.; Suzuki, A., Palladium-Catalyzed Cross-Coupling Reactions of Organoboron Compounds. *Chemical Reviews* **1995**, *95* (7), 2457-2483.
46. Dudnik, A. S.; Aldrich, T. J.; Eastham, N. D.; Chang, R. P.; Facchetti, A.; Marks, T. J., Tin-Free Direct C-H Arylation Polymerization for High Photovoltaic Efficiency Conjugated Copolymers. *Journal of the American Chemical Society* **2016**, *138* (48), 15699-15709.
47. Pappenfus, T. M.; Almyahi, F.; Cooling, N. A.; Culver, E. W.; Rasmussen, S. C.; Dastoor, P. C., Exploration of the Direct Arylation Polymerization Method for the Practical Application of Conjugated Materials: Synthetic Scale-Up, Solar Cell Performance, and Cost Analyses. *Macromolecular Chemistry and Physics* **2018**, 1800272.
48. Landfester, K.; Montenegro, R.; Scherf, U.; GüNTNER, R.; Asawapirom, U.; Patil, S.; Neher, D.; Kietzke, T., Semiconducting polymer nanospheres in aqueous dispersion prepared by a miniemulsion process. *Advanced Materials* **2002**, *14* (9), 651-655.
49. D'Olieslaeger, L.; Pirotte, G.; Cardinaletti, I.; D'Haen, J.; Manca, J.; Vanderzande, D.; Maes, W.; Ethirajan, A., Eco-friendly fabrication of PBDTTPD:PC71BM solar cells reaching a PCE of 3.8% using water-based nanoparticle dispersions. *Organic Electronics* **2017**, *42*, 42-46.
50. Yamamoto, T.; Komarudin, D.; Kubota, K.; Sasaki, S., Stacking of Poly (3-alkylthiophene) s and Poly (4-alkylthiazole) s in a Colloidal Solution and in the Solid. *Chemistry letters* **1998**, *27* (3), 235-236.
51. Yamamoto, T.; Komarudin, D.; Arai, M.; Lee, B.-L.; Suganuma, H.; Asakawa, N.; Inoue, Y.; Kubota, K.; Sasaki, S.; Fukuda, T.; Matsuda, H., Extensive Studies on π -Stacking of Poly(3-alkylthiophene-2,5-diyl)s and Poly(4-alkylthiazole-2,5-diyl)s by Optical Spectroscopy, NMR Analysis, Light Scattering Analysis, and X-ray Crystallography. *Journal of the American Chemical Society* **1998**, *120* (9), 2047-2058.
52. Millstone, J. E.; Kavulak, D. F.; Woo, C. H.; Holcombe, T. W.; Westling, E. J.; Briseno, A. L.; Toney, M. F.; Frechet, J. M., Synthesis, properties, and electronic applications of size-controlled poly(3-hexylthiophene) nanoparticles. *Langmuir* **2010**, *26* (16), 13056-61.
53. Darwis, D.; Elkington, D.; Sesa, E.; Cooling, N.; Bryant, G.; Zhou, X.; Belcher, W.; Dastoor, P.; Iskandar, F.; Abdullah, M. In *Surfactant Free P3HT / PCBM Nanoparticles for Organic Photovoltaics (OPV)*, AIP Conference Proceedings, 2011; pp 120-123.
54. Gärtner, S.; Christmann, M.; Sankaran, S.; Röhm, H.; Prinz, E.-M.; Penth, F.; Pütz, A.; Türel, A. E.; Penth, B.; Baumstümmeler, B.; Colsmann, A., Eco-Friendly Fabrication of 4% Efficient Organic Solar Cells from Surfactant-Free P3HT:ICBA Nanoparticle Dispersions. *Advanced Materials* **2014**, *26* (38), 6653-6657.
55. Vaughan, B.; Stapleton, A.; Sesa, E.; Holmes, N. P.; Zhou, X.; Dastoor, P. C.; Belcher, W. J., Engineering vertical morphology with nanoparticulate organic photovoltaic devices. *Organic Electronics* **2016**, *32*, 250-257.
56. Holmes, N. P.; Burke, K. B.; Sista, P.; Barr, M.; Magurudeniya, H. D.; Stefan, M. C.; Kilcoyne, A. L. D.; Zhou, X.; Dastoor, P. C.; Belcher, W. J., Nano-domain behaviour in P3HT:PCBM

- nanoparticles, relating material properties to morphological changes. *Solar Energy Materials and Solar Cells* **2013**, *117*, 437-445.
57. Dean, J. A., *lange's handbook of chemistry (15th Ed.)*. McGRAW-HILL, INC.: New York, 1999.
58. Colberts, F. J. M.; Wienk, M. M.; Janssen, R. A. J., Aqueous Nanoparticle Polymer Solar Cells: Effects of Surfactant Concentration and Processing on Device Performance. *ACS Applied Materials & Interfaces* **2017**, *9* (15), 13380-13389.
59. Pedersen, E. B. L.; Pedersen, M. C.; Simonsen, S. B.; Brandt, R. G.; Böttiger, A. P. L.; Andersen, T. R.; Jiang, W.; Xie, Z. Y.; Krebs, F. C.; Arleth, L.; Andreasen, J. W., Structure and crystallinity of water dispersible photoactive nanoparticles for organic solar cells. *Journal of Materials Chemistry A* **2015**, *3* (33), 17022-17031.
60. Holmes, N. P.; Marks, M.; Kumar, P.; Kroon, R.; Barr, M. G.; Nicolaidis, N.; Feron, K.; Pivrikas, A.; Fahy, A.; Mendaza, A. D. D. Z.; Kilcoyne, A.; Müller, C.; Zhou, X.; Andersson, M. R.; Dastoor, P. C.; Belcher, W. J., Nano-pathways: Bridging the divide between water-processable nanoparticulate and bulk heterojunction organic photovoltaics. *Nano Energy* **2016**, *19*, 495-510.
61. Parrenin, L.; Laurans, G.; Pavlopoulou, E.; Fleury, G.; Pecastaings, G.; Brochon, C.; Vignau, L.; Hadziioannou, G.; Cloutet, E., Photoactive Donor-Acceptor Composite Nanoparticles Dispersed in Water. *Langmuir* **2017**, *33* (6), 1507-1515.
62. Darwis, D.; Holmes, N.; Elkington, D.; David Kilcoyne, A. L.; Bryant, G.; Zhou, X.; Dastoor, P.; Belcher, W., Surfactant-free nanoparticulate organic photovoltaics. *Solar Energy Materials and Solar Cells* **2014**, *121*, 99-107.
63. Prunet, G.; Parrenin, L.; Pavlopoulou, E.; Pecastaings, G.; Brochon, C.; Hadziioannou, G.; Cloutet, E., Aqueous PCDTBT:PC71 BM Photovoltaic Inks Made by Nanoprecipitation. *Macromol Rapid Commun* **2017**.
64. Schwarz, K. N.; Farley, S. B.; Smith, T. A.; Ghiggino, K. P., Charge generation and morphology in P3HT:PCBM nanoparticles prepared by mini-emulsion and reprecipitation methods. *Nanoscale* **2015**, *7* (47), 19899-904.
65. Moore, T. L.; Rodriguez-Lorenzo, L.; Hirsch, V.; Balog, S.; Urban, D.; Jud, C.; Rothen-Rutishauser, B.; Lattuada, M.; Petri-Fink, A., Nanoparticle colloidal stability in cell culture media and impact on cellular interactions. *Chemical Society Reviews* **2015**, *44* (17), 6287-305.
66. Yu, Z.; Yang, F.; Dai, S.; Qiao, R., Structure and Dynamics of Polymeric Canopies in Nanoscale Ionic Materials: An Electrical Double Layer Perspective. *Sci Rep* **2018**, *8* (1), 5191.
67. Verwey, E.; Overbeek, J. T. G., *Theory of the stability of Lyophobic colloids*. Elsevier: Amsterdam, 1948.
68. Polte, J., Fundamental growth principles of colloidal metal nanoparticles – a new perspective. *CrystEngComm* **2015**, *17* (36), 6809-6830.
69. Kroon, R.; Lenes, M.; Hummelen, J. C.; Blom, P. W.; De Boer, B., Small bandgap polymers for organic solar cells (polymer material development in the last 5 years). *Polymer Reviews* **2008**, *48* (3), 531-582.
70. Gedefaw, D.; Sharma, A.; Pan, X.; Bjuggren, J. M.; Kroon, R.; Gregoriou, V. G.; Chochos, C. L.; Andersson, M. R., Optimization of the power conversion efficiency in high bandgap pyridopyridinedithiophene-based conjugated polymers for organic photovoltaics by the random terpolymer approach. *European Polymer Journal* **2017**, *91*, 92-99.
71. Dong, X.; Deng, Y.; Tian, H.; Xie, Z.; Geng, Y.; Wang, F., Isoindigo-based low bandgap conjugated polymer for o-xylene processed efficient polymer solar cells with thick active layers. *Journal of Materials Chemistry A* **2015**, *3* (39), 19928-19935.
72. Lin, Y.; Wang, J.; Zhang, Z. G.; Bai, H.; Li, Y.; Zhu, D.; Zhan, X., An electron acceptor challenging fullerenes for efficient polymer solar cells. *Advanced Materials* **2015**, *27* (7), 1170-4.
73. Mirzov, O.; Scheblykin, I. G., Photoluminescence spectra of a conjugated polymer: from films and solutions to single molecules. *Physical Chemistry Chemical Physics* **2006**, *8* (47), 5569-76.
74. Li, G.; Yao, Y.; Yang, H.; Shrotriya, V.; Yang, G.; Yang, Y., "Solvent Annealing" Effect in Polymer Solar Cells Based on Poly(3-hexylthiophene) and Methanofullerenes. *Advanced Functional Materials* **2007**, *17* (10), 1636-1644.
75. Kroon, R.; Diaz de Zerio Mendaza, A.; Himmelberger, S.; Bergqvist, J.; Bäcke, O.; Faria, G. C.; Gao, F.; Obaid, A.; Zhuang, W.; Gedefaw, D.; Olsson, E.; Inganäs, O.; Salleo, A.; Müller, C.; Andersson, M. R., A New Tetracyclic Lactam Building Block for Thick, Broad-Bandgap Photovoltaics. *Journal of the American Chemical Society* **2014**, *136* (33), 11578-11581.

76. Wang, E.; Wang, M.; Wang, L.; Duan, C.; Zhang, J.; Cai, W.; He, C.; Wu, H.; Cao, Y., Donor Polymers Containing Benzothiadiazole and Four Thiophene Rings in Their Repeating Units with Improved Photovoltaic Performance. *Macromolecules* **2009**, *42* (13), 4410-4415.
77. Hellström, S.; Zhang, F.; Inganäs, O.; Andersson, M. R., Structure-property relationships of small bandgap conjugated polymers for solar cells. *Dalton Transactions* **2009**, (45), 10032-10039.
78. Höhne, G.; Hemminger, W. F.; Flammersheim, H.-J., *Differential scanning calorimetry*. Springer Science & Business Media: 2013.
79. Diaz de Zerio Mendaza, A.; Melianas, A.; Nugroho, F. A. A.; Bäcke, O.; Olsson, E.; Langhammer, C.; Inganäs, O.; Müller, C., A fullerene alloy based photovoltaic blend with a glass transition temperature above 200 °C. *Journal of Materials Chemistry A* **2017**, *5* (8), 4156-4162.
80. Nugroho, F. A.; Diaz de Zerio Mendaza, A.; Lindqvist, C.; Antosiewicz, T. J.; Muller, C.; Langhammer, C., Plasmonic Nanospectroscopy for Thermal Analysis of Organic Semiconductor Thin Films. *Analytical Chemistry* **2017**, *89* (4), 2575-2582.
81. Müller, C., On the Glass Transition of Polymer Semiconductors and Its Impact on Polymer Solar Cell Stability. *Chemistry of Materials* **2015**, *27* (8), 2740-2754.
82. Kline, D. E.; Sauer, J. A.; Woodward, A. E., Effect of branching on dynamic mechanical properties of polyethylene. *Journal of Polymer Science* **1956**, *22* (102), 455-462.
83. Menard, K. P., *Dynamic mechanical analysis: a practical introduction*. CRC press: 2008.
84. Hopkinson, P. E.; Staniec, P. A.; Pearson, A. J.; Dunbar, A. D. F.; Wang, T.; Ryan, A. J.; Jones, R. A. L.; Lidzey, D. G.; Donald, A. M., A Phase Diagram of the P3HT:PCBM Organic Photovoltaic System: Implications for Device Processing and Performance. *Macromolecules* **2011**, *44* (8), 2908-2917.
85. Sharma, A.; Pan, X.; Campbell, J. A.; Andersson, M. R.; Lewis, D. A., Unravelling the Thermomechanical Properties of Bulk Heterojunction Blends in Polymer Solar Cells. *Macromolecules* **2017**, *50* (8), 3347-3354.
86. Reichelt, R., Scanning electron microscopy. In *Science of microscopy*, Springer: 2007; pp 133-272.
87. Shindo, D.; Oikawa, T., Energy Dispersive X-ray Spectroscopy. In *Analytical Electron Microscopy for Materials Science*, Springer: 2002; pp 81-102.

4. Chapter Four - Water/Ethanol Processable P-type Conjugated Polymers with Functional Side Groups for Organic Electronics

This chapter is a reformatted version of a manuscript to be submitted in an international peer reviewed journal

Author contribution:

Xun Pan: Performed all the synthesis and characterisation of polymers, part of the device fabrication & testing, data analysis and interpretation, prepared the first draft of manuscript.

Dr. Anirudh Sharma: Performed part of the device fabrication & testing, contributed to the revision of manuscript.

Dr. Renee Kroon: Intellectual contribution in conceptualizing the design of amino polymers, contributed to the revision of manuscript.

Dr. Desta Gedefaw & Dr. Sait Elmas: Performed electrochemistry experiments, contributed to the revision of manuscript.

Yanting Yin: Performed UPS measurements, contributed to the revision of manuscript.

Prof. Gunther Andersson: Contributed to the UPS data interpretation.

Prof. Mats R. Andersson: Intellectual contribution in conceptualizing experiments & revision of manuscript.

4.1. Abstract

To fulfil the goal of environmentally friendly fabrication of organic photovoltaics (OPVs), two series of p-type conjugated polymers were designed and synthesised based on poly[2,3-bis-(3-octyloxyphenyl)quinoxaline-5,8-diyl-alt-thiophene-2,5-diyl] (TQ1) polymeric backbone utilising polar pendant groups, i.e. tertiary amine and pyridine, to achieve switchable solubility in water/ethanol. Protonation of the functionalized polymers using volatile acid achieves aqueous processibility for deposition, and after mild thermal annealing uncharged films that are insoluble in water are formed. The molar ratio between the functional polar side groups and the octyl groups in the target polymers have been carefully tuned to achieve water and ethanol solubility as well as functional devices based on the new polymers. The new polymers exhibit nearly identical UV/vis-absorption properties in the solid states compared to the reported TQ1 without functional groups. The photovoltaic performance of the amino/pyridine-functionalized polymers was evaluated using organic solvent by incorporating PC₆₁BM due to the unavailability of water/alcohol soluble acceptor. Both amino and pyridine functionalities on the polymers were found to significantly reduce the MoO₃ work function in an energetically unfavourable way for functional devices, as seen from UPS studies. To reduce the unwanted interaction between functional polar groups with the MoO₃ interlayer, the devices were systematically engineered by inserting a buffer layer consisting N,N'-bis(3-methylphenyl)-N,N'-bis(phenyl)-benzidine (TPD) between the active layer and the MoO₃ hole transport layer. The TPD buffer layer enhanced the device performance of ethanol soluble amino polymer TQ1-50A and pyridine polymer TQ1-50P4, resulting in a maximum power conversion efficiency (PCE) of 0.82% and 1.33%, respectively. Our work demonstrated the possibility of substituent modification for high performing conjugated polymers using tertiary amine and pyridine groups to achieve functional donor materials for green solvent processable OPVs.

4.2. Introduction

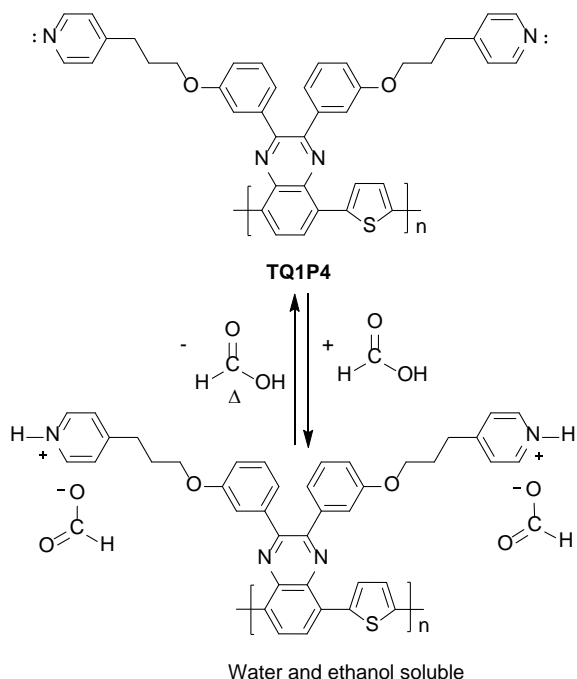
Organic photovoltaic (OPV)¹⁻³ is an attractive renewable energy technology with the potential of low-cost and high-throughput printing.⁴⁻⁵ The power conversion efficiencies (PCE) of OPVs have already been reported to exceed 14%,⁶ making them more viable for commercial production than ever. However, the fabrication of OPV devices generally involves harmful, halogenated solvents such as chloroform, chlorobenzene or ortho-dichlorobenzene (*o*-DCB). Using these type of solvents are undesirable for large-scale printing of OPV due to the large quantities of solar ink required,⁷⁻⁸ and diverges from the environmentally friendly aim of OPV.⁹⁻¹⁰ Recent research activities have studied more environmentally benign solvents such as anisole,¹¹ *o*-xylene¹²⁻¹³ and 2-methyl-tetrahydrofuran (Me-THF)¹⁴ for the OPV manufacturing, achieving comparable device performance to the OPVs fabricated using halogenated solvents. However, these non-halogenated solvents still pose a health-risk to the ecosystem and are cost-ineffective due to their high price and the necessary solvent recovery system.

Using water or ethanol as basis for solar inks is an ideal solution to fulfil the aim of green and low-cost processing of OPVs. One solution is offered through water dispersed nanoparticles (NPs) based on conjugated materials to realise the fabrication of OPVs from the most ideal eco-friendly solvent, water. The use of NP inks additionally circumvents the tedious development of water-soluble semiconducting donor and acceptor pairs with high PCE.¹⁵⁻¹⁷ The fabrication process of NP-inks is however not without issues, as the NP preparation via miniemulsion method is a time-consuming process and requires both insulating surfactants and chlorinated precursor solvents¹⁸ while NPs made by precipitation method¹⁹ suffer from high instability of the final solar ink.²⁰

Alternatively, water/alcohol soluble conjugated polymers (WSCPs) have been investigated as active layer materials for water/alcohol-based solar inks. Through the side-chain engineering,^{10, 21-25} i.e., replacing the hydrophobic aliphatic substituent with hydrophilic polar side groups, for example, ionic moieties (e.g. sulfonate groups,²⁶ quaternary ammonium salt²³) and non-ionic functional groups (e.g. tertiary amine,²⁷⁻³¹ oligoethylene glycol^{9, 32}). However, the ionic moieties have been reported to act as charge carrier traps/recombination site,³³ and the WSCPs designed based on this approach have only been successfully applied as interface layer materials for OPVs.^{22, 24, 34} OPVs based on active layer fabricated from WSCP elaborated with tertiary amine functionalities showed no photovoltaic response.²⁷ So far, the highest photovoltaic performance was reported by Nguyen et al,³² achieving 0.75% PCE with an oligoethylene glycol-functionalized WSCP.

In this work, we have modified the polymer, poly[2,3-bis-(3-octyloxyphenyl)quinoxaline-5,8-diyl-alt-thiophene-2,5-diyl] (TQ1),³⁵⁻³⁶ by complete or partial replacement of the aliphatic solubilizing side-chains with side groups having tertiary amine and pyridine groups. In this way, a series of new polymers were obtained that allowed us to study the effect of functional group loading on the solubility in green solvents and their photovoltaic performances. For polymers containing tertiary

amine/pyridine-functionalized side-chains of 50% and higher, we find that using small amounts of formic acid (FA) (3%) switches the property of our conjugated polymer being water/ethanol soluble due to the protonation of lone-pair nitrogens in the functional groups. Furthermore, the reversed deprotonation process could be achieved by mildly heating the acidified water/ethanol processed polymer in the solid state, thus, uncharged neutral polymer was regenerated. This highly reversible process is depicted in **Scheme 4.1**, showing the protonation and deprotonation process of pyridine-functionalized polymer TQ1P4. Hence, the utilisation of tertiary amine and pyridine functionalities provide switchable, water/ethanol processable p-type conjugated polymers.



Scheme 4.1 Protonation of pyridine-functionalized polymer TQ1P4 using formic acid and the deprotonation process to remove formic acid under heating.

The evaluation of the photovoltaic performance revealed that using less basic polar functionality (pyridine) and decreasing the functional group loading to 50% or lower resulted in improved photovoltaic performance, up to 1.6% of PCE. The improved device performance was partly resulted from the lower miscibility between polymer and fullerene in the photoactive layer, with replacing tertiary amine with pyridine or lowering the loading of amino groups in donor polymer. Our results show that pyridine pendant groups can give green solvent processibility and decent photovoltaic performance, which will be beneficial for environmentally friendly fabrication of OPVs in future.

4.3. Experimental

All reactions were performed under nitrogen protection unless otherwise stated. Chemicals were commercially available from Sigma-Aldrich and used without further purification. 5,8-Dibromo-2,3-bis(3-(octyloxy)phenyl)quinoxaline and 2,5-bis(trimethylstannyl)thiophene were purchased from

Solarmer Energy, Inc., and the latter was purified by recrystallisation from methanol. All solvents were used as obtained from supplier except toluene, which was dried and distilled prior to the polymerisation reactions. The structures of the small molecular compounds synthesised were confirmed by $^1\text{H-NMR}$ spectra measured on Bruker 300 MHz NMR spectrometer. The $^1\text{H-NMR}$ spectra of all polymers were measured on Bruker 600 MHz NMR spectrometer. The recorded $^1\text{H-NMR}$ were referred to tetramethylsilane (TMS) as internal standard.

4.3.1. Material characterisation

Gel-permeation chromatography (GPC) measurements were performed at 35 °C on an Agilent PL-GPC 220 equipped with a differential refractive index detector. Dimethylformamide (DMF) was used as eluent at a flow rate of 1.0 mL/min, and the solvent DMF as well as sample solutions were filtered through a filter with the pore size of 0.45 μm (Nylon, Millex-HN 13 mm Syringes Filters, Millipore, US). The number average molecular weights (M_n) and polydispersity index (PDI) were calculated using a calibration curve based on polyethylene glycol (PEG) standards.

The ultraviolet-visible (UV-vis) study was performed on a Perkin Elmer UV-vis-NIR Lambda950 spectrophotometer.

Thermal gravimetric analysis (TGA) measurements were performed on TA instruments Discovery TGA series TGA1-0288, with the temperature range of 25 - 400°C under nitrogen gas flow, and the heating ramp of 10 °C/min. The acid treated polymer samples were prepared by dissolving polymer in ethanol with 3% formic acid prior to drop casting on freshly cleaned glass substrate, followed by drying in air and then collected with a scalpel. Prior to the TGA measurements, the collected solid samples were further dried overnight in a vacuum oven at room temperature. The isothermal treatment of FA protonated samples was conducted in the TGA at 120 °C for TQ1A and 110 °C in the case of TQ1P4 under a nitrogen gas flow of 25 mL/min.

Differential scanning calorimetry (DSC) measurements were performed on Discovery DSC from TA instrument, with temperature range -20-300°C, heating/cooling ramp 10°C/min under nitrogen gas flow. The sample to be measured was prepared by drop casting a polymer:PC₆₁BM solution (chloroform blended with *o*-DCB) on a freshly cleaned glass slide followed by solvent evaporation before the solid mixture being removed collected using a scalpel. The sample was dried in a vacuum oven overnight prior to the DSC measurement.

Cyclic voltammetry (CV) measurements were performed using a 0.1 M solution of tetrabutylammonium hexafluorophosphate (Bu_4NPF_6) in anhydrous acetonitrile as the supporting electrolyte and a Ag/Ag⁺ quasi reference electrode. The ferrocene/ferrocenium (Fc/Fc⁺) reference was used to calibrate the measurements. The highest occupied molecular orbital energy levels (E_{HOMO}) and the lowest unoccupied molecular orbital energy levels (E_{LUMO}) were estimated from the

onset potentials by setting the oxidative potential of Fc/Fc⁺ vs. the normal hydrogen electrode (NHE) to 0.630 V, and the NHE vs. the vacuum level to 4.5 V.³⁷⁻³⁸

4.3.2. Device fabrication

Inverted solar cells with the structure ITO/ZnO/BHJ/MoO₃/Ag or ITO/ZnO/BHJ/N,N'-bis(3-methylphenyl)-N,N'-bis(phenyl)-benzidine (TPD)/MoO₃/Ag were fabricated using fixed weight ratio of 1:2.5 donor-polymer:PC₆₁BM in the active layer. Patterned ITO-coated glass substrates (10 Ω/sq, purchased from Xin Yan Technology Ltd) were cleaned using the procedure published elsewhere.³⁶ ITO-coated glass substrates were cleaned by soaking in a 5% detergent solution (pyroneg from Johnson Diversey) at 90 °C for 20 minutes and then rinsing in deionized (DI) water, before sonicating in DI water, acetone and isopropanol for 10 min each. Substrates were then cleaned in UV-ozone for 20 minute immediately before spin coating the ZnO layer. ZnO sol-gel³⁹ on the cleaned ITO substrate was thermally annealed at 280 °C for 10 minute in air to yield a 25 - 30 nm thick film. The BHJ layers were spin-coated in the glove box to give approximate 80 nm thickness. In the case of TPD being introduced in the device, a TPD buffer layer (3 nm) was thermally evaporated on top of the BHJ layer (using a Covap system supplied by Angstrom Engineering) before depositing 12 nm of MoO₃ hole transport layer. Finally, the Ag electrode (80 nm) was deposited by thermal evaporation through a shadow mask, which defined the active area to be 0.1 cm².

4.3.3. Device characterisation

Photovoltaic properties of solar cells were measured in air by an Oriel solar simulator fitted with a 150 W xenon lamp (Newport), filtered to give an irradiation of 100 mW/cm² at an atmospheric mass (AM) of 1.5 and calibrated using a silicon reference cell with NIST traceable certification. The photocurrent–voltage (*I*-*V*) characteristics of the devices were measured through a Keithley 2400 source meter unit.

Atomic force microscopy (AFM) (supplied by Bruker, Billerica, MA) was performed in tapping mode using silicon tips. The films were spin-coated from the same solutions used for active layer forming in device fabrication on freshly cleaning ITO-glass.

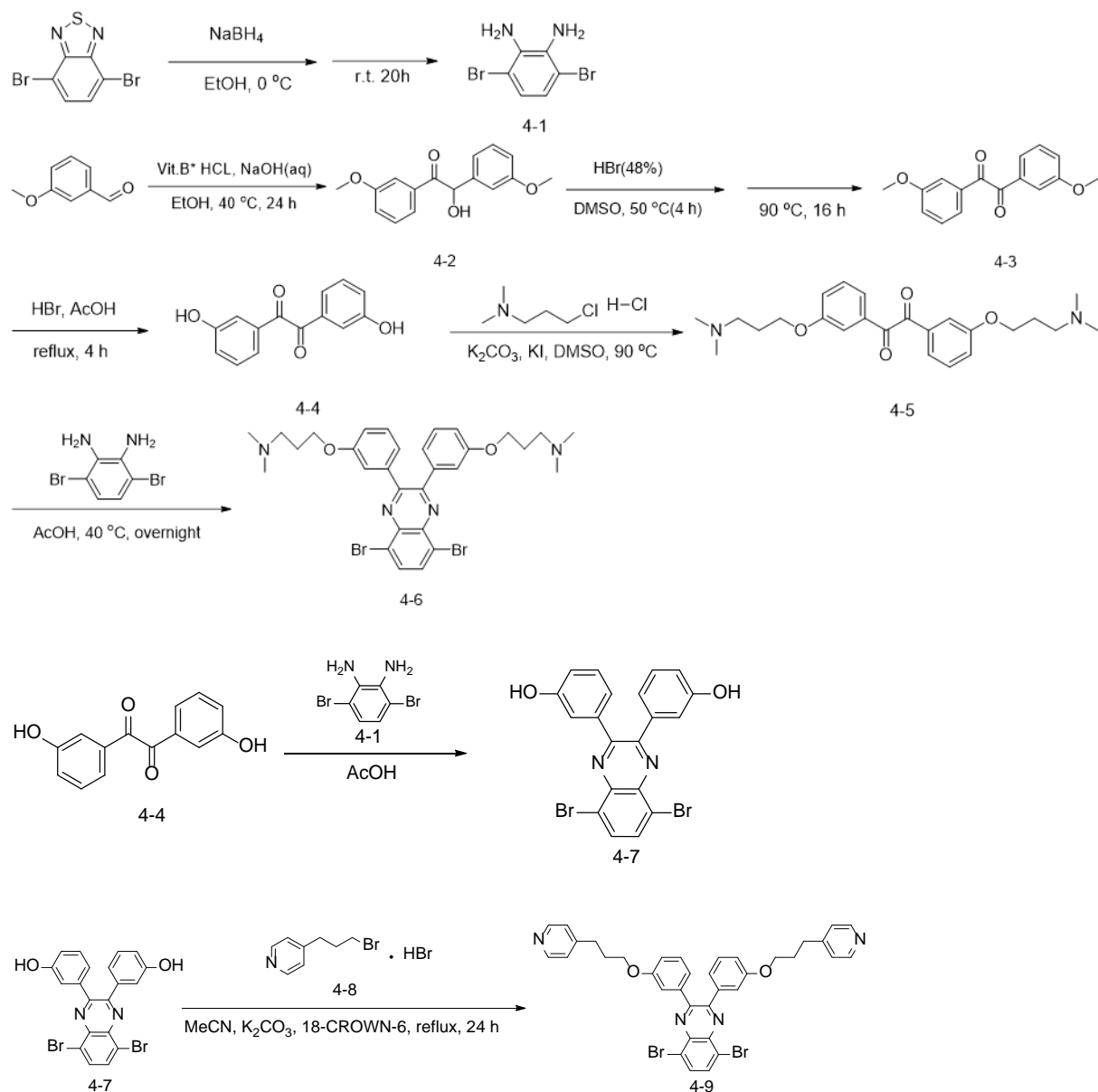
4.3.4. Electron spectroscopy

Ultraviolet photoelectron spectroscopy (UPS) measurements were performed under an ultra-high vacuum (UHV) apparatus build by SPECS (Berlin, Germany) using a low intensity UV light source (HeI) with an excitation energy of 21.21 eV, to measure the work functions as described elsewhere.³⁶ The UPS samples were prepared by thermally evaporating MoO₃ (12 nm) on freshly cleaned glass substrates in a vacuum deposition chamber followed by spin-coating polymer solution (1 mg/mL *o*-DCB) at 500 rpm for 60 s and 3000 rpm for 30 s in a glove box under nitrogen. The prepared samples were transferred from the glove box to the load lock for UPS measurements using a nitrogen filled zip-lock bag.

4.4. Results and discussion

4.4.1. Material synthesis

Due to the flexibility of quinoxaline moieties for substituent modification,⁴⁰ the design of green solvent soluble polymers was carried out on substituting the quinoxaline unit with polar side-chains containing hydrophilic pendant end groups.



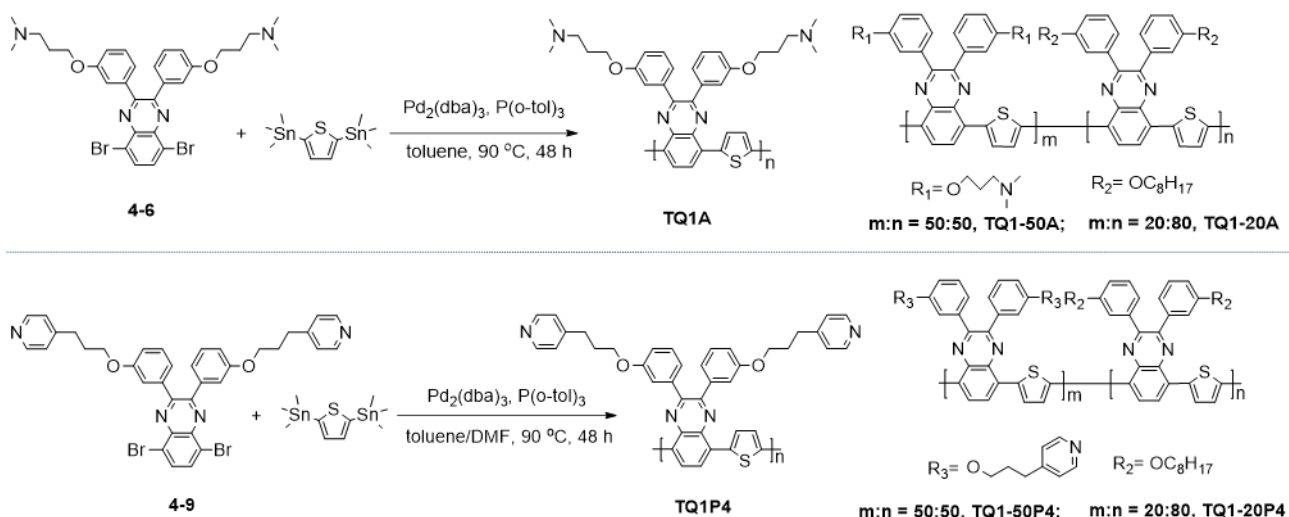
Scheme 4.2 Synthetic route for quinoxaline monomers with amino side groups and pyridine side groups.

The synthesis procedures to obtain amine and pyridine functionalised quinoxaline monomers are shown in **Scheme 4.2**. Through reduction of 4,7-dibromobenzo[*c*][1,2,5]thiadiazole with NaBH_4 , diamine compound **4-1** was prepared in a quite mild condition, which was used in further condensation to afford monomer for TQ1A. Compound **4-2** was prepared through benzoin condensation in the presence of thiamine hydrochloride and was used for the next oxidation step to

synthesis compound **4-3** without further purification. Oxidation was performed in DMSO as the solvent and HBr as the oxidizing agent instead of using ammonium nitrate and copper (II) acetate⁴¹, simplifying the purification of the crude product using one step recrystallisation. Purified compound **4-3** was reacted with HBr in acetic acid under reflux to generate compound **4-4**, which showed a good yield of 94.67%. The Williamson etherification between compound **4-4** and 3-dimethylamino-1-propylchloride hydrochloride led to compound **4-5** as yellow oil after purification via column chromatography. Although different parameters such as temperature, solvent and the purity of starting materials had been taken into consideration to improve the reaction yield, the Williamson reaction performed under different conditions yielded only about 14% conversion. Better yield was achieved in the synthesis of TQ1A monomer **4-6**. The monomer was prepared through condensation of compound **4-5** and **4-1** followed by purification via column chromatography and recrystallisation, and the pale yellow monomer **4-6** was obtained in 87.4% yield.

To prepare quinoxaline monomer with pyridine side groups, firstly 3,3'-(5,8-dibromoquinoxaline-2,3-diyl)diphenol (compound **4-7**) was synthesised by condensation reaction from compound **4-1** and **4-4** in acetic acid under mild condition. Compound **4-8** was synthesized from commercially available 4-pyridinepropanol by reacting with HBr under reflux overnight. It is worth noting that 4-(3-bromopropyl)pyridine was intrinsically unstable and protonation of the compound with HBr was necessary to be able to isolate the compound. The TQ1P4 monomer **4-9** was synthesized through Williamson etherification between compound **4-7** and compound **4-8** in refluxed acetonitrile (MeCN). The detailed synthesis procedures can be found in **Appendix A**.

The molecular structures of the quinoxaline monomers attached with tertiary amine side groups and pyridine side groups were confirmed by ¹H NMR spectroscopy (**Appendix B, Figure B1**).



Scheme 4.3 Synthetic route for polymers with amino side groups and pyridine side groups.

The structure and synthesis procedures of polymers are shown in **Scheme 4.3**. Polymer TQ1A was synthesized via Stille coupling by copolymerising monomer **4-6** and 2,5-

bis(trimethylstannyl)thiophene using freshly distilled toluene as the reaction solvent. Significant amount of precipitate was observed over the course of the reaction when using pure toluene to synthesis TQ1P4. The influence of different solvents used during the polymerisation on the properties of TQ1P4 has been studied, details can be found in **Chapter 5**. Hence, a polar solvent blend of dry toluene/DMF (4:1 volume ratio) was used to increase the solubility of pyridine polymer during the polymerisation reaction. The copolymers TQ1-50A, TQ1-20A, TQ1-50P4 and TQ1-20P4 were polymerised using three monomers with different molar ratio to obtain the products with different loading of functional groups attached to the polymer backbone. The ratio between the functional polar groups and octyl groups in the polymers was confirmed by their accordant ¹H NMR spectra (**Appendix B, Figure B2 and Table B1**). The detailed synthesis procedures of polymerisation can be found in **Appendix A**.

The number average molecular weights (M_n) of TQ1P4 and TQ1-50P4 were measured to be 9.6 kg/mol and 8.6 kg/mol with the PDI of 2.7 and 4.3, respectively. The low M_n and high value of PDI could be a result from the limited solubility of oligomer/polymers in the toluene/DMF reaction solvent, which impeded the chain growth during the coupling reaction. The molecular weights of amino polymers and TQ1-20P4 could not be measured properly due to their limited solubility in DMF and tetrahydrofuran (THF). In addition, 1,2,4-trichlorobenzene (1,2,4-TCB) has also been tried as the eluent for GPC measurements of amine-functionalized polymers, but no response was observed, which was probably caused by the adhesion of the amino groups to the columns and the metal tubing.

4.4.2. Optical properties and switchable solubility in green solvents

We first probed the solubility of the synthesised polymers in ethanol and water acidified with formic acid (FA), to have an indication how their solubility depends on the concentration of functional groups.

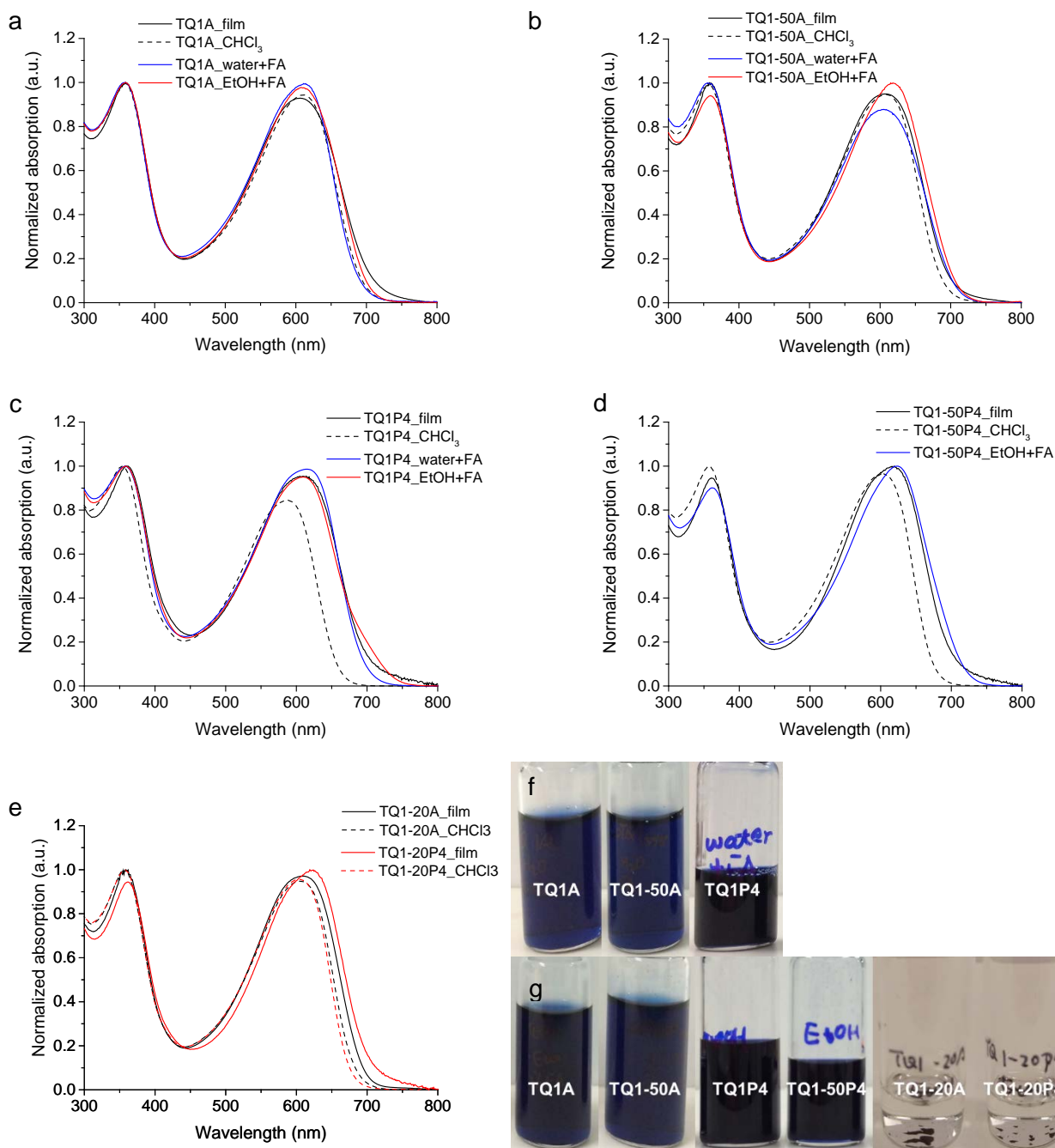


Figure 4.1 Normalized UV-vis absorption spectra of (a) TQ1A, (b) TQ1-50A, (c) TQ1P4, (d) TQ1-50P4, (e) TQ1-20A and TQ1-20P4 in different solvents and in the solid state. Photographs of (f) polymer in water + 3% FA solution, (g) polymer in EtOH + 3% FA solution.

The amine-functionalized polymer TQ1A and TQ1-50A showed good solubility in water and ethanol with a small amount of FA (3% v/v), due to the protonation of tertiary amine forming conjugated polyelectrolyte TQ1A-FA and TQ1-50A-FA, respectively. Similarly, attributing to the localization of the lone-pair electrons on the nitrogen atoms in sp^2 orbital, pyridine can also be easily protonated by FA to generate a pyridinium salt TQ1P4-FA. Hence, TQ1P4 was found to be soluble in acidic water/ethanol in concentration that is typical for solar cell ink, and TQ1-50P4, containing 50% pyridine in the quinoxaline unit, can be dissolved in ethanol (EtOH) with FA. The UV-vis spectra of

these two new series of polymers in chloroform and green solvents were compared with the solid states, and the polymer solutions in water and ethanol are shown in **Figure 4.1**. The ethanol and water solution of TQ1A-FA revealed an enhanced absorption (**Figure 4.1a**), which could have resulted from the ion introduced electrostatic perturbation.²² However, the TQ1-50A-FA (**Figure 4.1b**) water solution exhibits reduced absorption in the low-energy band while opposite behaviour being observed in the ethanol solution, which could be explained by the influence of solvent on the charge transfer state or different degrees of torsion/planarity in polymer backbone using different solvents.⁴¹

The UV-vis absorption of the pyridine polymers in the solid states are virtually identical to the amino analogues. The absorption bands of TQ1P4 film (**Figure 4.1c**) were enhanced and red-shifted in the long wavelength region compared to the chloroform solution, which presumably due to the higher intermolecular interaction and/or better packing in the solid condition. Red-shifted absorption spectra were also found in the water and ethanol solutions of protonated polymer compared to the neutral polymer in chlorinated solvent, indicating multichain aggregation⁴² or solvatochromic effects resulted from the polar solvent.^{22, 43} Similar absorption behaviour was also found in the UV-vis spectra of TQ1-50P4 (**Figure 4.1d**).

We found that TQ1-20A and TQ1-20P4 could not be dissolved in EtOH + 3% FA (**Figure 4.1g**) due to the low content of the tertiary amine or pyridine substituent in the conjugated polymer structure. The large number of octyl groups inhibits the switching of polymer solubility assisted by acid. The UV-vis spectra of TQ1-20A and TQ1-20P4 in chloroform solutions and in the solid state (**Figure 4.1e**) present similar absorption properties compared to TQ1A and TQ1P4, respectively.

Since ionic side groups presented in photoactive layers are known to be unfavourable for efficient charge transfer,³²⁻³³ it is important to study the possibility of regenerating neutral polymers after acidified water/ethanol processing.

The TGA measurements were performed on TQ1A-FA and TQ1P4-FA with neat polymer samples as references, respectively (**Figure 4.2**), revealing FA release under heating, as significant weight losses from about 100 °C to 150 °C were observed in protonated samples. However, the weight loss of TQ1A-FA was calculated to be higher than the weight of formic acid required to completely protonate TQ1A, which could be a result from trapped free acid and/or water in the TQ1A-FA sample. Upon 120 °C isotherm were performed on TQ1A-FA, the sample did not exhibit any obvious weight loss before degradation, which is above 300 °C (**Figure 4.2a**). Due to the weaker basicity of pyridine compared to tertiary amine, it was suspected that pre-drying TQ1P4-FA under vacuum have already released part of the binding acid, thus the weight loss of TQ1P4-FA is comparably less than the amino counterpart (**Figure 4.2b**). The TGA results reveal a mild thermal treatment (120 °C for TQ1A and 110 °C for TQ1P4) on the solid state of the protonated polymers could effectively release FA and regenerate neutral polymers. Furthermore, we found that the deprotonation procedure under

isothermal process was completed in about 10 min for bulk material as shown in **Figure 4.2c&d**. Hence, it is possible to process functional polymers from green solvents in the presence of volatile acid and achieve neutral polymer films in the fabrication of OPVs under mild condition. This switchable solubility observed in tertiary amine/pyridine-functionalized polymers could also be beneficial for various electronic applications.⁴⁴⁻⁴⁵

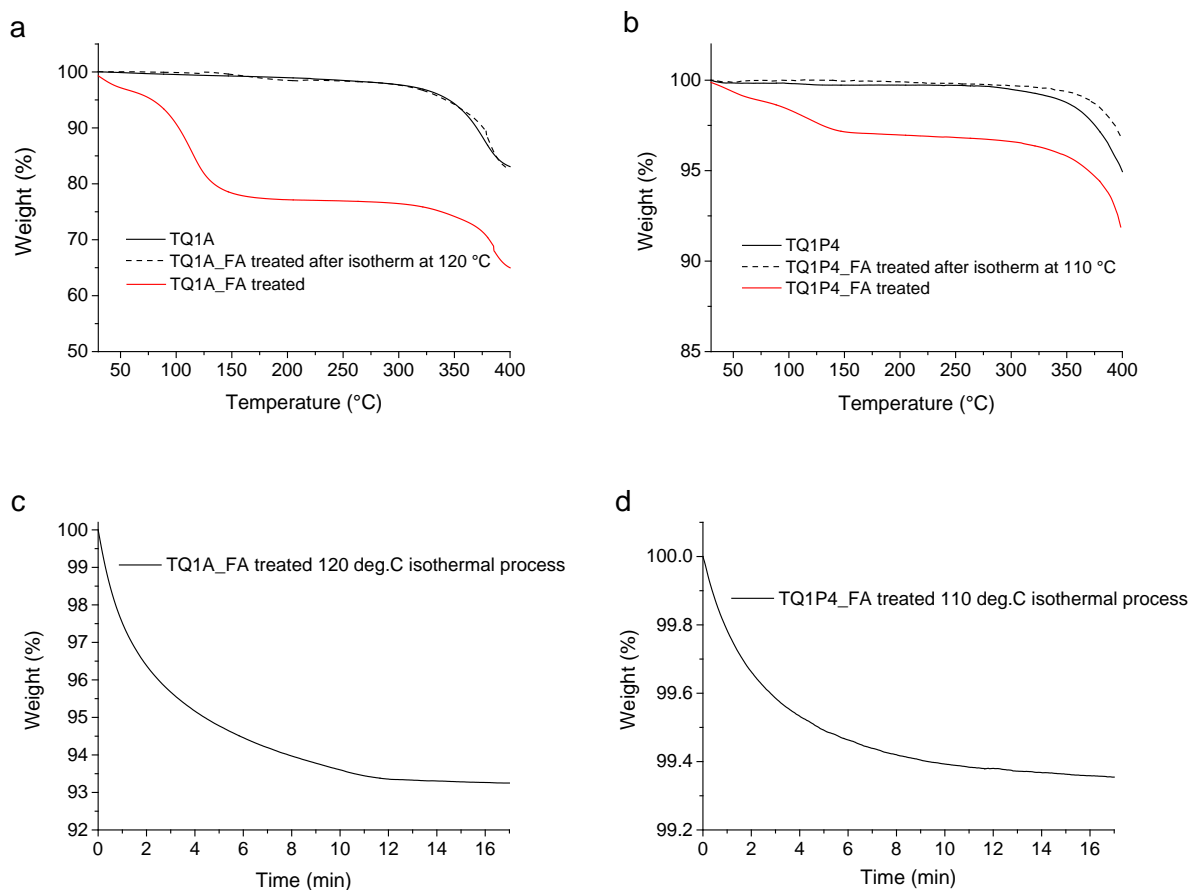


Figure 4.2 TGA plots of (a) TQ1A-FA thermally annealed at 120°C for 10 min, with neat TQ1A and TQ1A-FA as references and (b) TQ1P4-FA thermally annealed at 110°C for 10 min, with neat TQ1P4 and TQ1P4-FA as references. (c) TQ1A-FA and (d) TQ1P4-FA weight change as a function time in the 120 °C and 110 °C isothermal process, respectively.

4.4.3. Electrochemical properties

The electrochemical properties of new polymers presented in this chapter were investigated by cyclic voltammetry (CV), and cyclic voltammograms are shown in **Figure 4.3**. Compared to the reported TQ1,³⁵ the tertiary amine or pyridine functionalized polymers in the solid states all exhibit near-identical optical bandgaps and energy levels (**Table 4.1**), indicating that the modification of substituents attached to the quinoxaline backbone have negligible influence on the conjugation of the resulting polymers.

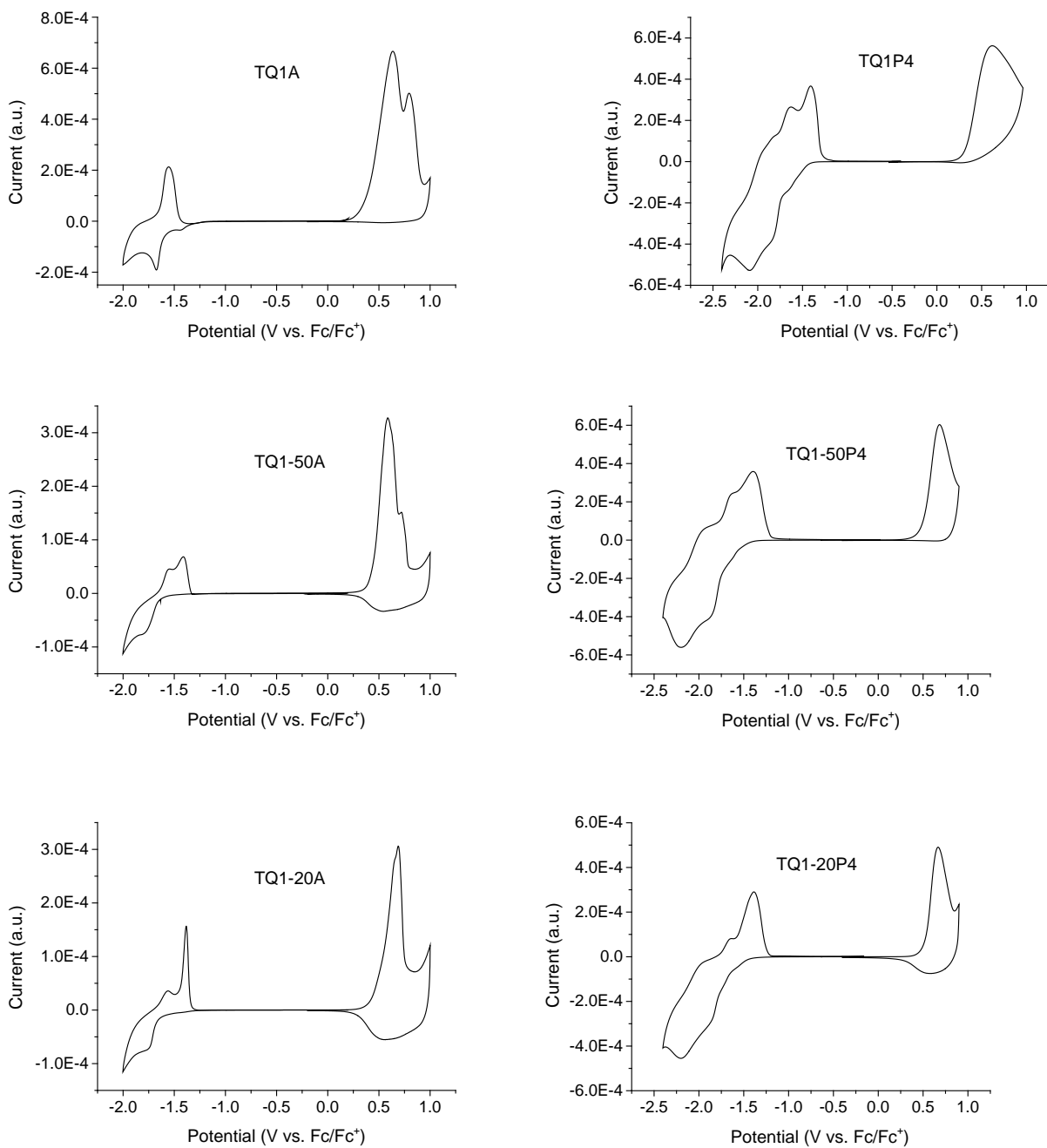


Figure 4.3 Cyclic voltammograms of the polymers. 0.1 M solution of Bu₄NPF₆ in anhydrous acetonitrile as the supporting electrolyte and a Ag/Ag⁺ quasi reference electrode. Calibrated using the ferrocene/ferrocenium (Fc/Fc⁺) reference. Scan rate of 100 mV/s.

Table 4.1 UV-vis absorption, electrochemical properties and energy levels of polymers.

Polymers	λ_{\max} (nm)	λ_{onset} (nm)	E_g^{opt} (eV)	$E_{\text{ox}}^{\text{onset}}$ (V)	$E_{\text{red}}^{\text{onset}}$ (V)	E_{HOMO} (eV)	E_{LUMO} (eV)	E_g^{CV} (eV)
TQ1A	361 606	730	1.70	0.34	-1.29	-5.47	-3.84	1.63
TQ1-50A	358 609	719	1.73	0.40	-1.61	-5.53	-3.52	2.01
TQ1-20A	358 610	709	1.75	0.43	-1.60	-5.56	-3.53	2.03
TQ1P4	361 610	720	1.73	0.32	-1.41	-5.45	-3.72	1.73
TQ1-50P4	361 618	723	1.72	0.44	-1.48	-5.57	-3.65	1.92
TQ1-20P4	361 624	725	1.72	0.47	-1.46	-5.60	-3.67	1.93

$$E_g^{\text{CV}} = (E_{\text{LUMO}} - E_{\text{HOMO}})$$

It has been previously reported that amino groups are potential hole traps in the BHJ devices containing amine-functionalized active materials, due to that the highest occupied molecular orbital (HOMO) level of p-type polymer lies below the ionization state of amine.³⁰ Hence, electrochemistry was also performed on triethylamine to compare its oxidation process with amine-functionalized TQ1A. Furthermore, since we are the first to report pyridine substituted polymer as electron-donor in the BHJ system, the oxidation process of pyridine was carefully studied to compare with that of TQ1P4. The CV oxidation curves of amino compounds are presented in **Figure 4.4a**, showing an onset oxidation potential of TQ1A conjugated backbone to be 0.34 V vs. Fc/Fc⁺, which is similar to the onset oxidation potential of triethylamine (~0.32 V). Thus, the HOMO of TQ1A lies very close or slightly below the ionization state of amine side groups. This result raised our concern about the viability and effectiveness of utilising amine-functionalized p-type polymers in OPVs. Nevertheless, the onset oxidation potential of pyridine was measured to be ~1.0 V, which is far above the value of TQ1P4 backbone (0.32 V) (**Figure 4.4b**), revealing the low-lying ionization state of pyridine groups compared to the pyridine-functionalized polymer. Hence, theoretically the introduced side-chain with pyridine pendant group should not affect hole transfer in the pyridine-functionalized polymer.³⁰

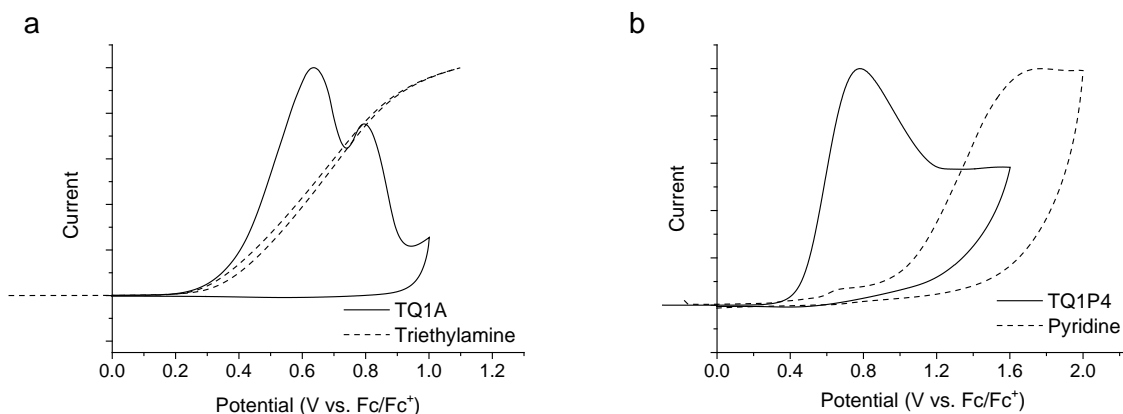


Figure 4.4 Cyclic voltammetry (CV) oxidation curves of (a) TQ1A in the solid state and triethylamine in solution, (b) TQ1P4 in the solid state and pyridine in solution.

4.4.4. Interfacial engineering

Materials with amino and pyridine functionalities have been previously reported as interface layers to reduce the electrode work function,^{22, 27, 36} the origin of which is related to the presence of nitrogens with free electron pair in these material. Since tertiary amines and pyridine groups are well known for reducing the work function of the underlying metal oxide electrodes,^{30, 46-47} studying these donor polymers in devices with an inverted structure (ITO/ZnO/BHJ/MoO₃/Ag) would be ideal as the work function of the underlying cathode layer would be further altered in an energetically favourable direction. However, it is equally important to also understand the interaction of the amine/pyridine groups of the donor polymer with the top anode interface, due to its potential to influence the energetics at the BHJ-MoO₃ interface.

First, water contact angle measurements were carried out on neat TQ1A, PC₆₁BM and blend TQ1A:PC₆₁BM films. The water contact angle value of neat TQ1A (60°) and TQ1A:PC₆₁BM blend (60°) films were found to be similar (detailed information can be found in **Chapter 5**), indicating a high content of amino polymer on the top surface of the BHJ layer (towards the air interface) post spin-coating. Presence of amino groups towards the air interface makes the potential interaction between amines and MoO₃ layer highly likely in an actual device.

Therefore, to gain more insight into the work function modification of MoO₃ as a result of its interaction with the tertiary amine or pyridine groups in working devices, UPS measurements were performed on evaporated MoO₃ with a thin layer of spin-coated functional polymer. The work function of freshly evaporated pristine MoO₃ sample was found to be 5.4 eV (**Figure 4.5a**). Since the polymer films were deposited from *o*-DCB solution, work function of MoO₃ washed with *o*-DCB was also measured to study any changes in the MoO₃ work function due to surface treatment with *o*-DCB. The work function of *o*-DCB treated MoO₃ was found to slightly reduce to 5.3 eV and was used as a reference for MoO₃ in this study. The difference in the absolute work function value of MoO₃

measured in this study (5.4/5.3 eV) as compared to 6.7 eV reported in literature⁴⁸⁻⁴⁹ can be attributed to slight air exposure during the sample transfer and mounting.

Modification of the MoO₃ surface with a thin layer of TQ1-50A and TQ1-20A was found to markedly reduce the work function of MoO₃ by around 1.0 eV, as seen by the shift in the secondary electron cut off from 5.3 eV to 4.3 eV (**Figure 4.5b**). Furthermore, the work function of MoO₃ was significantly shifted from 5.3 eV to 3.0 eV upon coating an extreme thin layer of TQ1A. While these results shows the strong ability of amino polymers to alter the surface properties of transition metal oxides, it also opens up the possibility of selectively tuning their electronic functionalities, i.e. being switched from being an anode layer to a cathode layer. Our UPS findings showed significant change in the MoO₃ work function post modification with amino polymer and its possible utilisation as a bi-functional interlayer was validated by the photovoltaic response measured from solar cells incorporating these interlayers (ITO/MoO₃/TQ1A/BHJ/MoO₃/Ag) (**Table 4.2**). It should be noted that the lower performance presented in **Table 4.2** compared to the reported values³⁶ resulted from the unoptimised BHJ layer morphology possibly due to the *o*-DCB redissolving the TQ1A interlayer and introducing defects in the active layer.

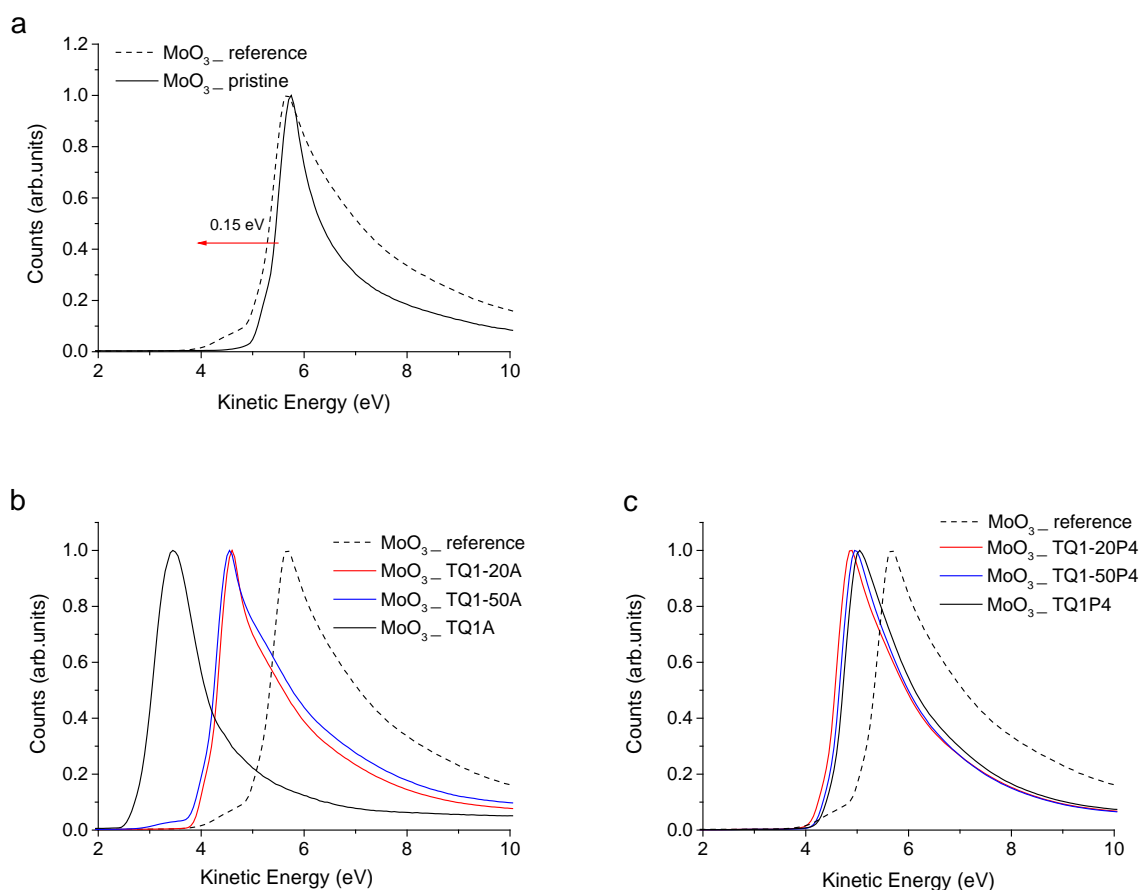


Figure 4.5 UPS spectra of (a) pristine MoO₃ and *o*-DCB washed MoO₃ reference sample, (b) thin layer of amino polymer coated MoO₃ samples and (c) thin layer of pyridine polymer coated MoO₃ with *o*-DCB washed MoO₃ reference. The red arrow in (a) indicates 0.15 eV of work function change after washing.

TQ1P4 and its analogues were also found to significantly reduce the work function of MoO₃ as seen from a shift of ~ 0.7 eV in the secondary electron cut-off of the spectra (**Figure 4.5c**). However, the relatively smaller shift in the case of TQ1P4 as compared to TQ1A indicates that the interaction between pyridine and MoO₃ is weaker as compared to tertiary amine.

Table 4.2 Photovoltaic performance parameters of *o*-DCB processed TQ1:PC₇₁BM (1:2.5) BHJ OPVs using the inverted device structure of ITO/MoO₃/TQ1A/BHJ/MoO₃/Ag, with mean values ± standard deviation from eight devices in parentheses.

BHJ	J _{sc} (mA/cm ²)	FF (%)	V _{oc} (V)	PCE (%)
TQ1:PC ₇₁ BM	4.69 (4.48 ± 0.19)	48 (49 ± 3)	0.59 (0.55 ± 0.03)	1.31 (1.19 ± 0.06)

4.4.5. Photovoltaic performance

To evaluate the photovoltaic properties of tertiary amine/pyridine-functionalized polymers in solar cell devices, a typical fullerene derivative PC₆₁BM was used as an acceptor due to the lack of a readily available water or ethanol soluble acceptor material in this study. Thus, we used *o*-DCB and anisole to process solar inks containing PC₆₁BM for BHJ OPVs. Anisole, which has also been used in some recent studies,^{11, 50} was selected as a relatively greener solvent of choice compared to its halogenated counterparts. In addition, anisole was utilised to process the TQ1P4 and TQ1-50P4 containing active layer due to the limited solubility of these two pyridine polymers in *o*-DCB, revealed from large polymer aggregations in *o*-DCB processed films (**Figure 4.6**).

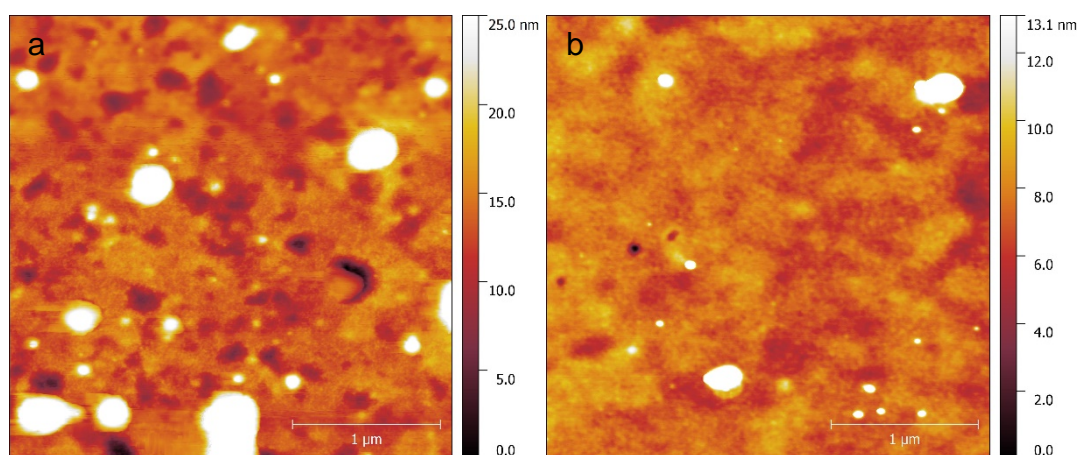


Figure 4.6 3 × 3 μm AFM images of (a) neat TQ1P4, (b) TQ1P4:PC₆₁BM blend films processed from *o*-DCB solutions.

Devices based on TQ1A:PC₆₁BM BHJ layer and an inverted structure (ITO/ZnO/BHJ/MoO₃/Ag) showed very limited PCE of 0.07%, with J_{sc} of 0.93 mA/cm² and V_{oc} of 0.18 V (**Table 4.3**). The significant voltage loss could be a result from the unwanted interaction between tertiary amine

groups and MoO₃, or the complex formed between tertiary amine and PC₆₁BM, which could lead to severe charge recombination.⁵¹ To improve the device performance, the BHJ and the anode interface was carefully engineered by inserting an additional thin layer of TPD⁵²⁻⁵³ between the BHJ and the MoO₃. A thin layer of TPD was utilised to not only reduce the unwanted interaction between polar pendant groups and MoO₃ as seen from UPS studies, but it has previously been shown to enhance the blocking of electrons at the anode interface.^{52, 54} Upon applying a thin layer of TPD (3 nm), the V_{OC} was marginally improved to 0.34 V, leading to an efficiency of 0.13%. Although the devices based on TQ1A showed photovoltaic response, the PCE is much lower compared to that of TQ1:PC₆₁BM devices,⁴¹ which could be due to the charge traps formed by the amino groups, indicated from the electrochemistry results.³⁰

To further understand the OPV devices containing amine-functionalized donor polymer, polymers substituted with 50% and 20% amine groups were studied subsequently. For the optimised device structure with an additional TPD passivation layer, replacing TQ1A with TQ1-50A and TQ1-20A resulted in enhanced PCEs of 0.82% and 1.06%, respectively. While the J_{SC} was increased from 0.93 mA/cm² (TQ1A) to 4.17 mA/cm² (TQ1-50A) and 3.95 mA/cm² (TQ1-20A), the V_{OC} also saw an improvement from 0.34 V (TQ1A) to 0.46 V (TQ1-50A) and 0.58 V (TQ1-20A). These results show a strong dependence of the J_{SC} and V_{OC} on the tertiary amine content in donor polymers, in particular for devices without TPD. It is worth noting that with the decrease of amine content in the BHJ layer, the difference in the average photovoltaic performance with and without TPD becomes less significant (**Figure 4.7, Table 4.3**) and is in agreement with the UPS results showing the interaction between the amine-functionalized polymer and MoO₃ became weaker with less tertiary amine loading.

Devices with BHJ composed of TQ1P4:PC₆₁BM having the same inverted structure ITO/ZnO/BHJ/MoO₃/Ag were found to have a maximum J_{SC} of 1.53 mA/cm², FF of 36% and V_{OC} of 0.47 V, resulting in a the PCE of 0.24%, which is notably higher compared to their TQ1A counterparts. The PCE was further improved to 0.57%, with an enhancement of FF to 43%, V_{OC} to 0.6 V and J_{SC} to 2.19 mA/cm², when an additional TPD layer was used. For optimised devices with BHJ composed of TQ1-50P4:PC₆₁BM and TQ1-20P4:PC₆₁BM, the PCEs were found to increase to 1.33% (J_{SC} = 4.23 mA/cm², FF of 54 %) and 1.75% (J_{SC} = 5.67 mA/cm², V_{OC} of 0.65 V) respectively (**Figure 4.7, Table 4.3**). As seen in the case of the pyridine-functionalized polymers, the J_{SC} is increasing significantly with the decrease of pyridine content in the polymer structure (**Figure 4.7d**), while V_{OC} was found to be less dependent on the pyridine content (**Figure 4.7e**).

While polymers substituted with 50% and 100% of tertiary amine and pyridine side groups show excellent solubility in ethanol, the PCE of the pyridine based polymer (TQ1-50P4) was found to be 62% higher as compared to that of TQ1-50A. Thus utilising materials such as TQ1-50P4 for polymer

solar cells may be a good compromise between the green solvent solubility and decent photo-conversion efficiencies.

Table 4.3 Photovoltaic performance of the best BHJ OPVs based on TQ1A, TQ1-50A, TQ1-20A, TQ1P4, TQ1-50P4 and TQ1-20P4 with PC₆₁BM (fixed Donor:Acceptor 1:2.5 weight ratio) blends with device structure of ^aITO/ZnO/BHJ/TPD/MoO₃/Ag and ^bITO/ZnO/BHJ/MoO₃/Ag.

Polymer	Device structure	BHJ solvent	J_{sc} (mA/cm ²)	FF (%)	V_{oc} (V)	PCE (%)
TQ1A	a	o-DCB	0.94	43	0.34	0.13
	b		0.93	39	0.18	0.07
TQ1-50A	a	o-DCB	4.17	43	0.46	0.82
	b		3.37	43	0.41	0.59
TQ1-20A	a	o-DCB	3.95	46	0.58	1.06
	b		3.94	46	0.54	0.97
TQ1P4	a	Anisole	2.19	43	0.60	0.57
	b		1.53	36	0.47	0.26
TQ1-50P4	a	Anisole	4.23	54	0.59	1.33
	b		5.07	43	0.51	1.11
TQ1-20P4	a	o-DCB	5.67	47	0.65	1.75
	b		5.79	47	0.62	1.69

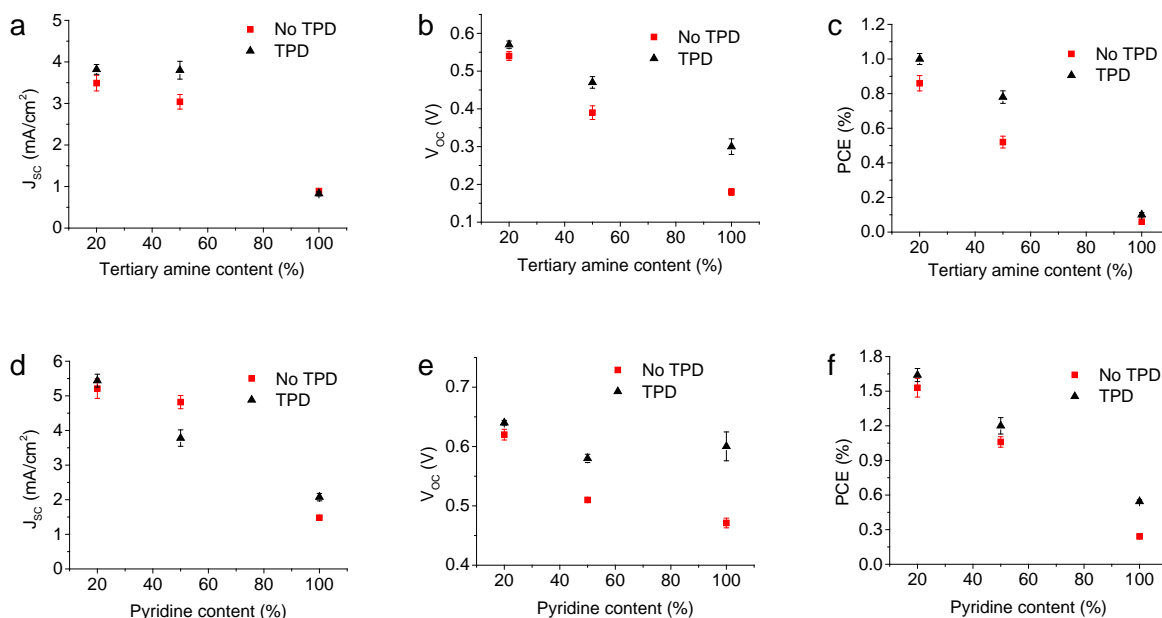


Figure 4.7 Device characteristics as a function of tertiary amine (a-c) and pyridine content in the quinoxaline unit of polymers (d-f).

4.4.6. Active layer morphology

To understand the reason of the low photovoltaic performance found in devices based on tertiary amine/pyridine-functionalized polymers, TQ1 with comparably low molecular weight (LMW) ($M_n = 10.8$ kg/mol, PDI = 2.0) was synthesised and evaluated in BHJ devices incorporating PC₆₁BM with the same device geometry (**Table 4.4**). The maximum PCE of OPV based on LMW-TQ1:PC₆₁BM was found to be 2.55% ($J_{SC} = 5.77$ mA/cm², $V_{OC} = 0.85$ V and FF = 52%), which is comparably lower than the high molecular weight counterpart.⁴¹ Hence, the low PCEs observed in amine/pyridine polymer based devices could be partly explained by the low molecular weight of our polymers.

Table 4.4 Photovoltaic performance of BHJ OPVs based on low molecular TQ1 (LMW-TQ1) with PC₆₁BM (D:A 1:2.5 weight ratio) blends with device structure of ^aITO/ZnO/BHJ/TPD/MoO_x/Ag and ^bITO/ZnO/BHJ/MoO_x/Ag. The mean values ± standard deviation from eight devices are shown in parentheses.

Polymer	Device structure	BHJ solvent	J_{SC} (mA/cm ²)	FF (%)	V_{OC} (V)	PCE (%)
LMW-TQ1	a	o-DCB	5.25	44	0.88	2.04
			(4.98 ± 0.21)	(45 ± 1)	(0.88 ± 0.01)	(1.97 ± 0.07)
	b		5.77	52	0.85	2.55
			(5.66 ± 0.17)	(51 ± 1)	(0.84 ± 0.02)	(2.43 ± 0.07)

To further understand the lower photovoltaic performance of these functional polymers compared to their unfunctionalized counterpart TQ1, atomic force microscopy (AFM) was performed to investigate the surface topography of blend films with different donor polymers.

The AFM image of TQ1A:PC₆₁BM blend film (**Figure 4.8a**) reveals an extremely smooth surface with the root-mean-square roughness (R_q) value of only 0.5 nm, indicating highly miscible morphology. The lack of phase separation between donor-rich phase and acceptor-rich phase could be resulted from the strong interaction between tertiary amine and the fullerene,⁵¹ which could lead to high degree of charge recombination. In the case of lower content of tertiary amine, an increase in R_q was observed as well as more phase separated feature being indicated (**Figure 4.8b,c**).

To further probe the extent of miscibility between amine-functionalized polymer with PC₆₁BM, differential scanning calorimetry (DSC) was performed on amino polymer:PC₆₁BM blends with different donor:acceptor (D:A) weight ratios and a TQ1:PC₆₁BM blend as the reference(**Figure 4.9**). As amorphous polymers, TQ1, TQ1A and its derivatives do not exhibit melting behaviour before decomposing. The thermogram of TQ1:PC₆₁BM (1:1) blend shows two endothermic peaks, which is attributed to the melting of PC₆₁BM in the blend.⁵⁵ Interestingly, no melting behaviour of fullerene could be observed in the case of TQ1-20A:PC₆₁BM at 1:4 ratio. The results indicate strong interaction

between amino polymers with PC₆₁BM or new complex forming⁵¹, and highly intermixed morphology of these blends even with small content of amine side groups in the polymer. In the case of TQ1-50A:PC₆₁BM blend with varied donor:acceptor ratio, only one melting peak with a small area can be observed upon the ratio decreased to 1:6. Furthermore, TQ1A:PC₆₁BM blend do not exhibit the melting behaviour of PC₆₁BM until the mass concentration of fullerene was increased to 88.9% (1:8 ratio). This interesting results suggested that TQ1A was intimately mixed with PC₆₁BM at the ratio used (1:2.5) to process active layer in OPVs, and possibly formed homogenous phase or new complex⁵⁵, hence there was no pure PC₆₁BM phase that could melt under the DSC measurement condition. A clear trend can be observed that the miscibility between amino polymer and PC₆₁BM decreased with the lower content of tertiary amine in the polymers, agreeing with more phase separation indicated from **Figure 4.8b** and **Figure 4.8c** compared to **Figure 4.8a**. Therefore, the improved performance of amino polymer based OPVs observed with lower content of tertiary amine substituents could be explained by the enhanced phase separation between donor and acceptor.

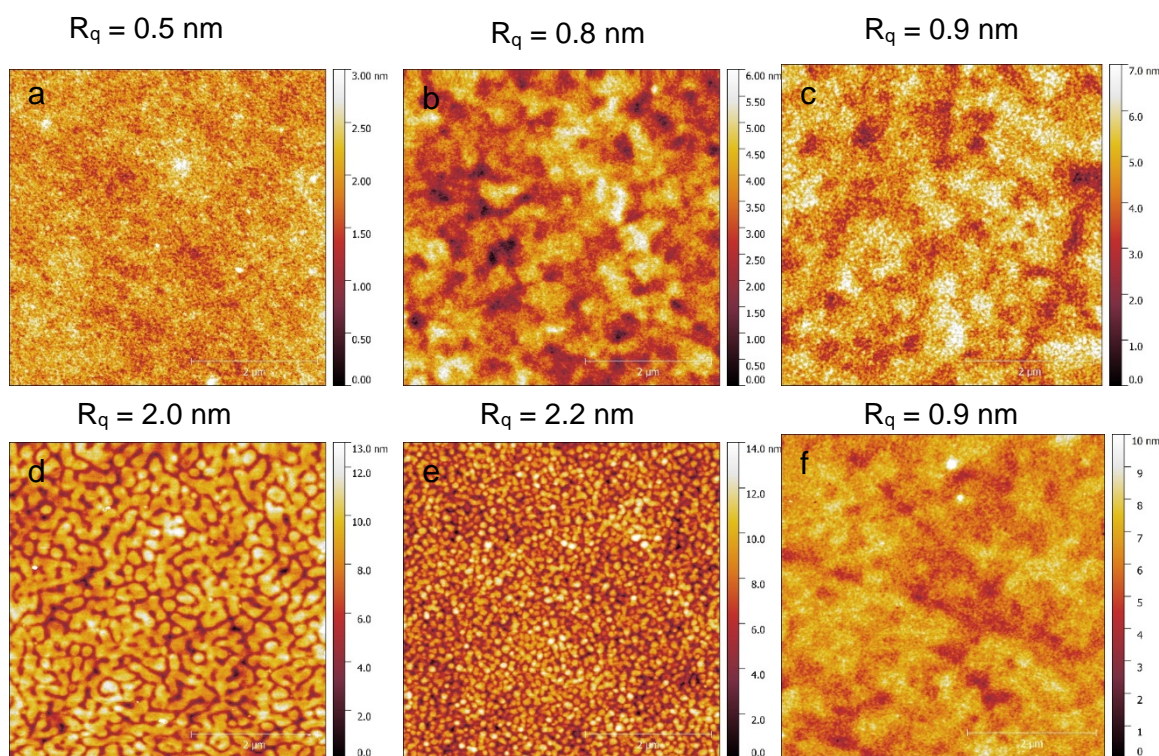


Figure 4.8 $5 \times 5 \mu\text{m}$ AFM images of (a) TQ1A:PC₆₁BM, (b) TQ1-50A:PC₆₁BM, (c) TQ1-20A:PC₆₁BM, (d) TQ1P4:PC₆₁BM, (e) TQ1-50P4:PC₆₁BM and (f) TQ1-20P4:PC₆₁BM films processed the same solution as device fabrication.

The blend film containing TQ1P4 (**Figure 4.8d**) or TQ1-50P4 (**Figure 4.8e**) shows more phase separated morphology compared to TQ1A:PC₆₁BM film, which could explain the improved photovoltaic performance upon the alteration of donor material from tertiary amine functionalized polymer to TQ1P4 and its analogues in the devices. The TQ1-20P4:PC₆₁BM film exhibits smoother surface compared to other films containing pyridine polymers, resulting from different processing

solvent. However, the R_q of it is comparable with TQ1-20A:PC₆₁BM film, indicating similar degree of phase separation. Further evidence of the phase separation between TQ1-20P4 and PC₆₁BM was revealed from the DSC result, which clearly shows melting behaviour of PC₆₁BM in the blend with D:A ratio of 1:2.5 (**Figure 4.9**). Photoluminescence quenching studies have also been performed to study the miscibility between the amine/pyridine functionalized polymer and PC₆₁BM. However, completed quenching results were found for all systems with the D:A ratio of 1:2.5. Therefore, the high degree of miscibility between polar group functionalized polymer and fullerene derivative has to be overcome to achieve sufficient phase separation for OPV operation.

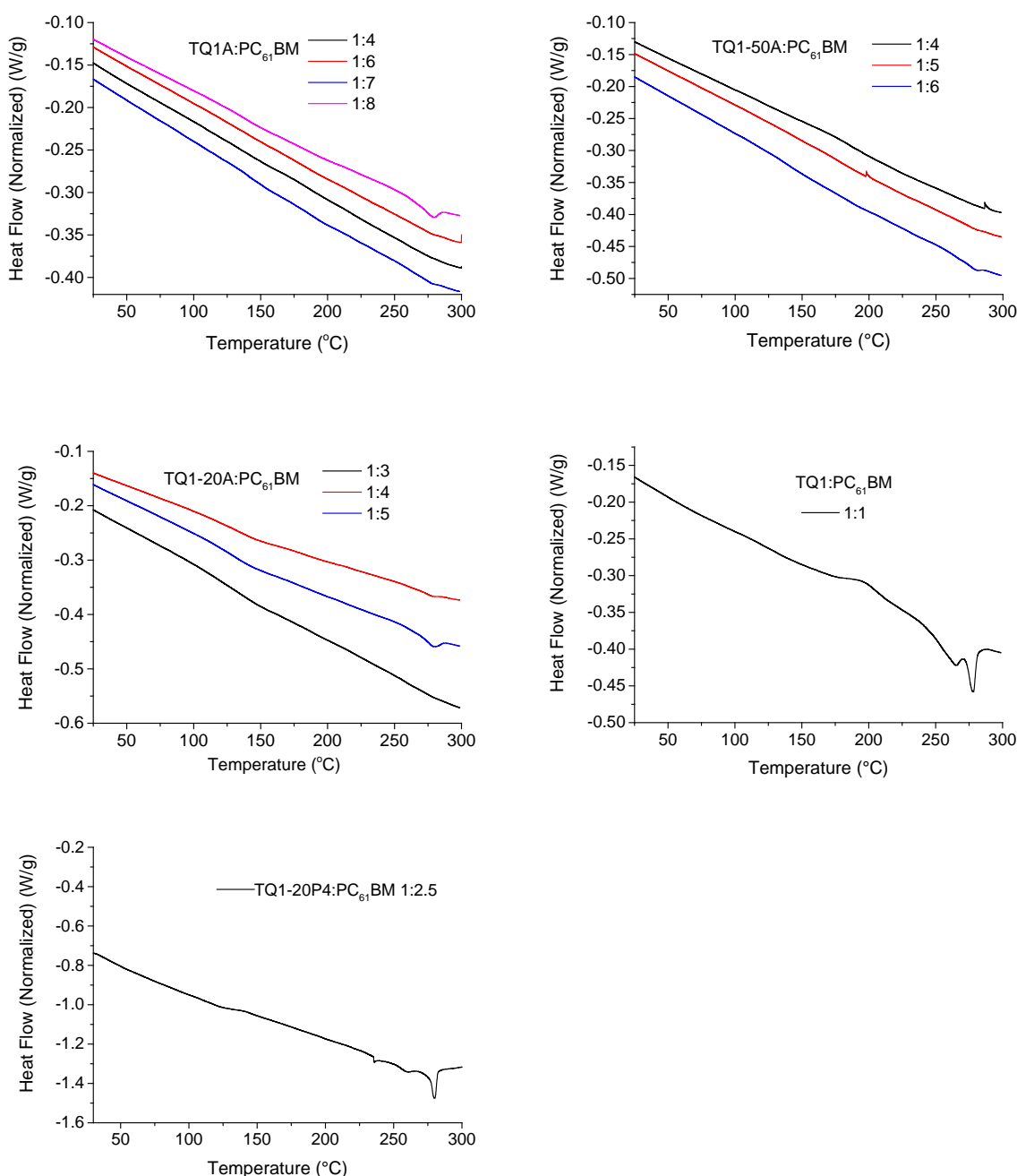


Figure 4.9 DSC thermograms of amino polymer:PC₆₁BM blends in varied weight ratios and TQ1:PC₆₁BM (1:1) blend as the reference. DSC thermogram of TQ1-20P4:PC₆₁BM in 1:2.5 weight ratio.

4.5. Conclusions

Two series of p-type conjugated polymers were successfully synthesised incorporating tertiary amine and pyridine pendant groups. TQ1A, TQ1-50A, TQ1P4 and TQ1-50P4 showed outstanding switchable solubility in water/ethanol, indicating the potential of processing photoactive materials in an environmentally friendly way. The electrochemical properties of tertiary amine/pyridine-functionalized polymers indicate the possibility of hole trapping in the case of amino polymers, and OPV devices based on TQ1A:PC₆₁BM were found to have a PCE of 0.07%. TQ1A was also found to remarkably reduce the work function of anode interlayer MoO₃, partly explaining the unsatisfactory performance of the inverted OPVs. On carefully passivating the BHJ-MoO₃ interfaces with an additional TPD layer, the PCE was found to increase to 0.13% for TQ1A based OPV and 0.82% for TQ1-50A. The low performance of TQ1A based solar cells was also a result from the high miscibility of fullerene in the donor polymer. Hence, using non-fullerene acceptors is a potential method to overcome the high miscibility between amine functionalized donor polymer and acceptor, and will be investigated in the future.

Solar cells fabricated from TQ1P4:PC₆₁BM achieved a maximum PCE of 0.57%, which was further increased to 1.33% for TQ1-50P4. In this case, the phase separation is too large compared to optimal surface morphology, which could potentially be optimised in future to improve the photovoltaic performance. Moreover, further investigation is required to understand the device behaviour, such as studying the interface dipole in the donor:acceptor interfaces and the charge mobility in these amine/pyridine polymer based OPVs. OPVs based on lower content of functionalized group substituted polymers TQ1-20A and TQ1-20P4 offered highest efficiencies of 1.06% and 1.71%, respectively, but their insolubility in ethanol or water impedes the continuous study for green solvent processed OPVs. It can be concluded that the ratio between polar substituents and hydrophobic alkyl groups need to be well balanced to achieve water/alcohol soluble p-type conjugated polymers as well as decent photovoltaic performance.

4.6. References

1. Nelson, J., Organic photovoltaic films. *Current Opinion in Solid State and Materials Science* **2002**, 6 (1), 87-95.
2. Bai, H.; Shi, Q.; Zhan, X., Polymer Solar Cells. In *Organic Optoelectronics*, Wiley-VCH Verlag GmbH & Co. KGaA: 2013; pp 407-435.
3. Xiao, Z.; Jia, X.; Ding, L., Ternary organic solar cells offer 14% power conversion efficiency. *Science Bulletin* **2017**.
4. Angmo, D.; Larsen - Olsen, T. T.; Jørgensen, M.; Søndergaard, R. R.; Krebs, F. C., Roll - to - Roll Inkjet Printing and Photonic Sintering of Electrodes for ITO Free Polymer Solar Cell Modules and Facile Product Integration. *Advanced Energy Materials* **2013**, 3 (2), 172-175.
5. Søndergaard, R.; Hösel, M.; Angmo, D.; Larsen-Olsen, T. T.; Krebs, F. C., Roll-to-roll fabrication of polymer solar cells. *Materials Today* **2012**, 15 (1-2), 36-49.
6. Li, H.; Xiao, Z.; Ding, L.; Wang, J., Thermostable single-junction organic solar cells with a power conversion efficiency of 14.62%. *Science Bulletin* **2018**, 63 (6), 340-342.
7. Krebs, F. C.; Gevorgyan, S. A.; Alstrup, J., A roll-to-roll process to flexible polymer solar cells: model studies, manufacture and operational stability studies. *Journal of Materials Chemistry* **2009**, 19 (30), 5442.
8. Krebs, F. C.; Tromholt, T.; Jorgensen, M., Upscaling of polymer solar cell fabrication using full roll-to-roll processing. *Nanoscale* **2010**, 2 (6), 873-86.
9. Søndergaard, R.; Helgesen, M.; Jørgensen, M.; Krebs, F. C., Fabrication of Polymer Solar Cells Using Aqueous Processing for All Layers Including the Metal Back Electrode. *Advanced Energy Materials* **2011**, 1 (1), 68-71.
10. Park, K.-Y.; Lee, J.-S.; Namkung, H.-S.; Koo, M.-S.; Cho, S.-J.; Yoon, B.-W.; Kim, Y.-M.; Lee, Y.-S.; Song, S.-H.; Park, D.-K.; Kim, C.-G., Enhanced Performance in Bulk Heterojunction Polymer Solar Cell Using Water Soluble Conjugated Polymer. *Journal of Nanoscience and Nanotechnology* **2015**, 15 (2), 1683-1686.
11. Venkatesan, S.; Chen, Q.; Ngo, E. C.; Adhikari, N.; Nelson, K.; Dubey, A.; Sun, J.; Bommisetty, V.; Zhang, C.; Galipeau, D.; Qiao, Q., Polymer Solar Cells Processed Using Anisole as a Relatively Nontoxic Solvent. *Energy Technology* **2014**, 2 (3), 269-274.
12. Yu, Y.-Y.; Tsai, T.-W.; Yang, C.-C.; Chen, C.-P., Highly Efficient Non-Fullerene Organic Photovoltaics Processed from o-Xylene without Using Additives. *The Journal of Physical Chemistry C* **2017**, 121 (40), 21969-21974.
13. Xu, X.; Yu, T.; Bi, Z.; Ma, W.; Li, Y.; Peng, Q., Realizing Over 13% Efficiency in Green-Solvent-Processed Nonfullerene Organic Solar Cells Enabled by 1,3,4-Thiadiazole-Based Wide-Bandgap Copolymers. *Advanced Materials* **2017**.
14. Fan, B.; Ying, L.; Wang, Z.; He, B.; Jiang, X.-F.; Huang, F.; Cao, Y., Optimisation of processing solvent and molecular weight for the production of green-solvent-processed all-polymer solar cells with a power conversion efficiency over 9%. *Energy & Environmental Science* **2017**, 10 (5), 1243-1251.
15. D'Olieslaeger, L.; Pirotte, G.; Cardinaletti, I.; D'Haen, J.; Manca, J.; Vanderzande, D.; Maes, W.; Ethirajan, A., Eco-friendly fabrication of PBDTTPD:PC71BM solar cells reaching a PCE of 3.8% using water-based nanoparticle dispersions. *Organic Electronics* **2017**, 42, 42-46.
16. Gärtner, S.; Christmann, M.; Sankaran, S.; Röhm, H.; Prinz, E.-M.; Penth, F.; Pütz, A.; Türel, A. E.; Penth, B.; Baumstümmeler, B.; Colsmann, A., Eco-Friendly Fabrication of 4% Efficient Organic Solar Cells from Surfactant-Free P3HT:ICBA Nanoparticle Dispersions. *Advanced Materials* **2014**, 26 (38), 6653-6657.
17. Holmes, N. P.; Marks, M.; Kumar, P.; Kroon, R.; Barr, M. G.; Nicolaidis, N.; Feron, K.; Pivrikas, A.; Fahy, A.; Mendaza, A. D. D. Z.; Kilcoyne, A.; Müller, C.; Zhou, X.; Andersson, M. R.; Dastoor, P. C.; Belcher, W. J., Nano-pathways: Bridging the divide between water-processable nanoparticulate and bulk heterojunction organic photovoltaics. *Nano Energy* **2016**, 19, 495-510.
18. Colberts, F. J. M.; Wienk, M. M.; Janssen, R. A. J., Aqueous Nanoparticle Polymer Solar Cells: Effects of Surfactant Concentration and Processing on Device Performance. *ACS Applied Materials & Interfaces* **2017**, 9 (15), 13380-13389.
19. Schwarz, K. N.; Farley, S. B.; Smith, T. A.; Ghiggino, K. P., Charge generation and morphology in P3HT:PCBM nanoparticles prepared by mini-emulsion and reprecipitation methods. *Nanoscale* **2015**, 7 (47), 19899-904.

20. Prunet, G.; Parrenin, L.; Pavlopoulou, E.; Pecastaings, G.; Brochon, C.; Hadziioannou, G.; Cloutet, E., Aqueous PCDTBT:PC71 BM Photovoltaic Inks Made by Nanoprecipitation. *Macromol Rapid Commun* **2017**.
21. Mei, J.; Bao, Z., Side Chain Engineering in Solution-Processable Conjugated Polymers. *Chemistry of Materials* **2013**, *26* (1), 604-615.
22. Wu, Z.; Sun, C.; Dong, S.; Jiang, X. F.; Wu, S.; Wu, H.; Yip, H. L.; Huang, F.; Cao, Y., n-Type Water/Alcohol-Soluble Naphthalene Diimide-Based Conjugated Polymers for High-Performance Polymer Solar Cells. *Journal of the American Chemical Society* **2016**, *138* (6), 2004-13.
23. Hu, Z.; Zhang, K.; Huang, F.; Cao, Y., Water/alcohol soluble conjugated polymers for the interface engineering of highly efficient polymer light-emitting diodes and polymer solar cells. *Chemical Communications* **2015**, *51* (26), 5572-85.
24. Huang, F.; Wu, H.; Cao, Y., Water/alcohol soluble conjugated polymers as highly efficient electron transporting/injection layer in optoelectronic devices. *Chemical Society Reviews* **2010**, *39* (7), 2500-21.
25. He, Z.; Wu, H.; Cao, Y., Recent Advances in Polymer Solar Cells: Realization of High Device Performance by Incorporating Water/Alcohol-Soluble Conjugated Polymers as Electrode Buffer Layer. *Advanced Materials* **2014**, *26* (7), 1006-1024.
26. Mwaurea, J. K.; Pinto, M. R.; Witker, D.; Ananthakrishnan, N.; Schanze, K. S.; Reynolds, J. R., Photovoltaic cells based on sequentially adsorbed multilayers of conjugated poly (p-phenylene ethynylene) s and a water-soluble fullerene derivative. *Langmuir* **2005**, *21* (22), 10119-10126.
27. Duan, C.; Cai, W.; Hsu, B. B. Y.; Zhong, C.; Zhang, K.; Liu, C.; Hu, Z.; Huang, F.; Bazan, G. C.; Heeger, A. J.; Cao, Y., Toward green solvent processable photovoltaic materials for polymer solar cells: the role of highly polar pendant groups in charge carrier transport and photovoltaic behavior. *Energy & Environmental Science* **2013**, *6* (10), 3022-3034.
28. Lv, M.; Lei, M.; Zhu, J.; Hirai, T.; Chen, X., [6,6]-phenyl-C(6)(1)-butyric acid 2-((2-(dimethylamino)ethyl)(methyl)amino)-ethyl ester as an acceptor and cathode interfacial material in polymer solar cells. *ACS Applied Materials & Interfaces* **2014**, *6* (8), 5844-51.
29. Li, S.; Lei, M.; Lv, M.; Watkins, S. E.; Tan, Z. a.; Zhu, J.; Hou, J.; Chen, X.; Li, Y., [6,6]-Phenyl-C61-Butyric Acid Dimethylamino Ester as a Cathode Buffer Layer for High-Performance Polymer Solar Cells. *Advanced Energy Materials* **2013**, *3* (12), 1569-1574.
30. Cai, W.; Zhong, C.; Duan, C.; Hu, Z.; Dong, S.; Cao, D.; Lei, M.; Huang, F.; Cao, Y., The influence of amino group on PCDTBT-based and P3HT-based polymer solar cells: Hole trapping processes. *Applied Physics Letters* **2015**, *106* (23), 233302.
31. Ma, D.; Lv, M.; Lei, M.; Zhu, J.; Wang, H.; Chen, X., Self-Organization of Amine-Based Cathode Interfacial Materials in Inverted Polymer Solar Cells. *ACS Nano* **2014**, *8* (2), 1601-1608.
32. Nguyen, T. L.; Lee, C.; Kim, H.; Kim, Y.; Lee, W.; Oh, J. H.; Kim, B. J.; Woo, H. Y., Ethanol-Processable, Highly Crystalline Conjugated Polymers for Eco-Friendly Fabrication of Organic Transistors and Solar Cells. *Macromolecules* **2017**, *50* (11), 4415-4424.
33. Yang, J.; Garcia, A.; Nguyen, T.-Q., Organic solar cells from water-soluble poly(thiophene)/fullerene heterojunction. *Applied Physics Letters* **2007**, *90* (10), 103514.
34. Xu, B.; Zheng, Z.; Zhao, K.; Hou, J., A Bifunctional Interlayer Material for Modifying Both the Anode and Cathode in Highly Efficient Polymer Solar Cells. *Advanced Materials* **2016**, *28* (3), 434-9.
35. Wang, E.; Hou, L.; Wang, Z.; Hellstrom, S.; Zhang, F.; Inganas, O.; Andersson, M. R., An easily synthesized blue polymer for high-performance polymer solar cells. *Advanced Materials* **2010**, *22* (46), 5240-4.
36. Sharma, A.; Kroon, R.; Lewis, D. A.; Andersson, G. G.; Andersson, M. R., Poly(4-vinylpyridine): A New Interface Layer for Organic Solar Cells. *ACS Applied Materials & Interfaces* **2017**, *9* (12), 10929-10936.
37. Hellström, S.; Zhang, F.; Inganäs, O.; Andersson, M. R., Structure-property relationships of small bandgap conjugated polymers for solar cells. *Dalton Transactions* **2009**, (45), 10032-10039.
38. Gedefaw, D.; Sharma, A.; Pan, X.; Bjuggren, J. M.; Kroon, R.; Gregoriou, V. G.; Chochos, C. L.; Andersson, M. R., Optimization of the power conversion efficiency in high bandgap pyridopyridinedithiophene-based conjugated polymers for organic photovoltaics by the random terpolymer approach. *European Polymer Journal* **2017**, *91*, 92-99.

39. Sun, Y.; Seo, J. H.; Takacs, C. J.; Seifert, J.; Heeger, A. J., Inverted polymer solar cells integrated with a low-temperature-annealed sol-gel-derived ZnO Film as an electron transport layer. *Advanced Materials* **2011**, *23* (14), 1679-83.
40. Gedefaw, D.; Prosa, M.; Bolognesi, M.; Seri, M.; Andersson, M. R., Recent Development of Quinoxaline Based Polymers/Small Molecules for Organic Photovoltaics. *Advanced Energy Materials* **2017**, 1700575.
41. Kroon, R.; Gehlhaar, R.; Steckler, T. T.; Henriksson, P.; Müller, C.; Bergqvist, J.; Hadipour, A.; Heremans, P.; Andersson, M. R., New quinoxaline and pyridopyrazine-based polymers for solution-processable photovoltaics. *Solar Energy Materials & Solar Cells* **2012**, *105*, 280-286.
42. Dang, D.; Chen, J.; Zhou, P.; Duan, L.; Bao, X.; Yang, R.; Chen, J.; Zhu, W., Tuning the fused aromatic rings to enhance photovoltaic performance in wide band-gap polymer solar cells. *Polymer* **2016**, *104*, 130-137.
43. Woo, H. Y.; Liu, B.; Kohler, B.; Korystov, D.; Mikhailovsky, A.; Bazan, G. C., Solvent Effects on the Two-Photon Absorption of Distyrylbenzene Chromophores. *Journal of the American Chemical Society* **2005**, *127* (42), 14721-14729.
44. Hellström, S.; Henriksson, P.; Kroon, R.; Wang, E.; Andersson, M. R., Blue-to-transmissive electrochromic switching of solution processable donor-acceptor polymers. *Organic Electronics* **2011**, *12* (8), 1406-1413.
45. Xing, X.; Zeng, Q.; Vagin, M.; Fahlman, M.; Zhang, F., Fast Switching Polymeric Electrochromics with Facile Processed Water Dispersed Nanoparticles. *Nano Energy* **2018**.
46. van Reenen, S.; Kouijzer, S.; Janssen, R. A. J.; Wienk, M. M.; Kemerink, M., Origin of Work Function Modification by Ionic and Amine-Based Interface Layers. *Advanced Materials Interfaces* **2014**, *1* (8), 1400189.
47. George, Z.; Xia, Y.; Sharma, A.; Lindqvist, C.; Andersson, G.; Inganäs, O.; Moons, E.; Müller, C.; Andersson, M. R., Two-in-one: cathode modification and improved solar cell blend stability through addition of modified fullerenes. *Journal of Materials Chemistry A* **2016**, *4* (7), 2663-2669.
48. Meyer, J.; Hamwi, S.; Kroger, M.; Kowalsky, W.; Riedl, T.; Kahn, A., Transition metal oxides for organic electronics: energetics, device physics and applications. *Advanced Materials* **2012**, *24* (40), 5408-27.
49. Kröger, M.; Hamwi, S.; Meyer, J.; Riedl, T.; Kowalsky, W.; Kahn, A., Role of the deep-lying electronic states of MoO₃ in the enhancement of hole-injection in organic thin films. *Applied Physics Letters* **2009**, *95* (12), 123301.
50. Zhang, S.; Ye, L.; Zhang, H.; Hou, J., Green-solvent-processable organic solar cells. *Materials Today* **2016**, *19* (9), 533-543.
51. Ghosh, H. N.; Pal, H.; Sapre, A. V.; Mittal, J. P., Charge recombination reactions in photoexcited fullerene C₆₀-amine complexes studied by picosecond pump probe spectroscopy. *Journal of the American Chemical Society* **1993**, *115* (25), 11722-11727.
52. Lu, K.; Yuan, J.; Peng, J.; Huang, X.; Cui, L.; Jiang, Z.; Wang, H.-Q.; Ma, W., New solution-processable small molecules as hole-transporting layer in efficient polymer solar cells. *Journal of Materials Chemistry A* **2013**, *1* (45), 14253.
53. Ishii, H.; Sugiyama, K.; Ito, E.; Seki, K., Energy level alignment and interfacial electronic structures at organic/metal and organic/organic interfaces. *Advanced materials* **1999**, *11* (8), 605-625.
54. Subbiah, J.; Kim, D. Y.; Hartel, M.; So, F., MoO₃/poly(9,9-dioctylfluorene-co-N-[4-(3-methylpropyl)]-diphenylamine) double-interlayer effect on polymer solar cells. *Applied Physics Letters* **2010**, *96* (6), 063303.
55. Bernardo, G.; Deb, N.; King, S. M.; Bucknall, D. G., Phase behavior of blends of PCBM with amorphous polymers with different aromaticity. *Journal of Polymer Science Part B: Polymer Physics* **2016**, *54* (10), 994-1001.

5. Chapter Five - Green Solvent Soluble Conjugated Polymers Based on Side Chain Modification with Tertiary Amine, Pyridine and Oligoethylene Glycol

5.1. Introduction

Recently, water-soluble conjugated polymers (WSCPs) based on side chain modification with tertiary amine or quaternary amine groups have been reported,¹⁻² which were successfully applied as green solvent processed electron transport layer (ETL)³ for efficient polymer solar cells. Meanwhile, conjugated polymers equipped with pyridine groups have been recently reported to be used as an alcohol processable cathode interface layer⁴ and donor polymer to form nanoparticles⁵ for OPVs. PCBM derivative modified with pyridine pendant groups has also been investigated, which improved the thermal stability of ternary blend BHJ layer in devices.⁶ Compared to tertiary amine side groups, pyridine exhibits slightly lower basicity and is an alternative candidature of substituents to design new water/alcohol soluble conjugated polymers based on side chain engineering.⁷⁻⁸ Furthermore, another possible candidate of side groups is oligoethylene glycol (OEG), conjugated polymer based on which was processed from ethanol to form active layer that achieved 0.75% of PCE.⁹ Until so far, most of the photoactive BHJ layers were still fabricated using harmful organic solvent,¹⁰ and the investigation of WSCPs serving as photoactive materials requires urgent development to fulfil the goal of green fabrication of OPVs.⁹

In this chapter, more polymers that can be applied in green fabrication of OPVs are presented. A new polymer TQ1-5A was synthesised by reducing the content of amino side chains in the polymeric repeating unit to investigate the influence of amino content on the polymer properties, as compared to amino polymers presented in **Chapter 4**. The quinoxaline structure used in polymer TQ1¹¹ has also been modified by replacing the aliphatic solubilizing side chains with different tertiary amine side chain or alkyl chain that contains different pyridine pendant groups. Furthermore, OEG group was introduced as the solubilizing groups on quinoxaline unit, and a new polymer TQ-OEG was successfully synthesised by Stille coupling polymerisation. The optical and electrochemical properties as well as water/ethanol-solubility of new polymers were carefully studied and correlated to the properties of different functional groups. Interestingly, the OEG modified polymer presents low stiffness at room temperature, which could be potentially applied in flexible electronic device.

More photovoltaic characterisation of OPVs based on amino polymer containing active layer has been presented in this chapter, showing inferior performance compared to the unfunctionalized counterpart on varied device structure.⁴ To further understand the influence of amino groups to the morphology of BHJ layer, which could be the reason of unsatisfactory performance, differential

scanning calorimetry (DSC) and atomic force microscopy (AFM) measurements were employed to study the donor-acceptor phase property. Furthermore, Fourier transform photocurrent spectroscopy (FTPS) measurement was performed to study the charge-transfer (CT) state energy in amino polymer based devices.

The photovoltaic properties of pyridine or OEG modified polymers were evaluated using PC₆₁BM as the charge acceptor in aromatic solvent processed BHJ OPVs. The morphology of active layers has been investigated using AFM.

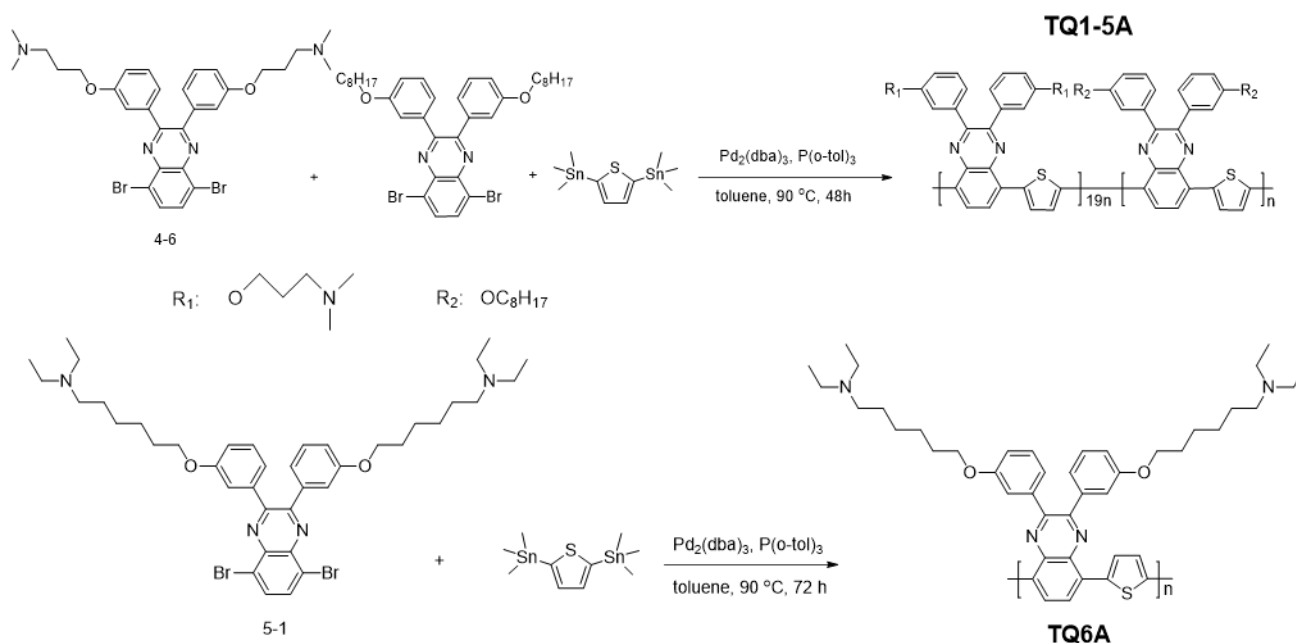
In order to expand the application of tertiary amine functionalized polymers, electrochromic devices were fabricated that showed electro-switching property between intensive blue colour in the neutral state and transmissive yellow in the oxidized state. A methanol processed amino polymer device displayed fastest response times at the high switching speed, showing the potential of using green solvent in the preparation of electrochromic devices.

Based on manipulating the donor-accepter (D-A) approach, wide bandgap conjugated polymers were synthesised using tertiary amine functionalized quinoxaline moiety and fluorene units, which are potential ethanol processable interface materials. The quaternization of tertiary amine modified polymer offered a new ammonium-functionalized derivative, which was evaluated as a cathode interlayer in OPVs.

The amine, pyridine or OEG functionalized polymers presented water/alcohol processibility, which could realise the green fabrication of interfacial layer and photoactive layer for OPVs without using harmful solvent upon incorporating with appropriate water/alcohol soluble acceptor materials in future.

5.2. Materials synthesis

5.2.1. Amino polymers

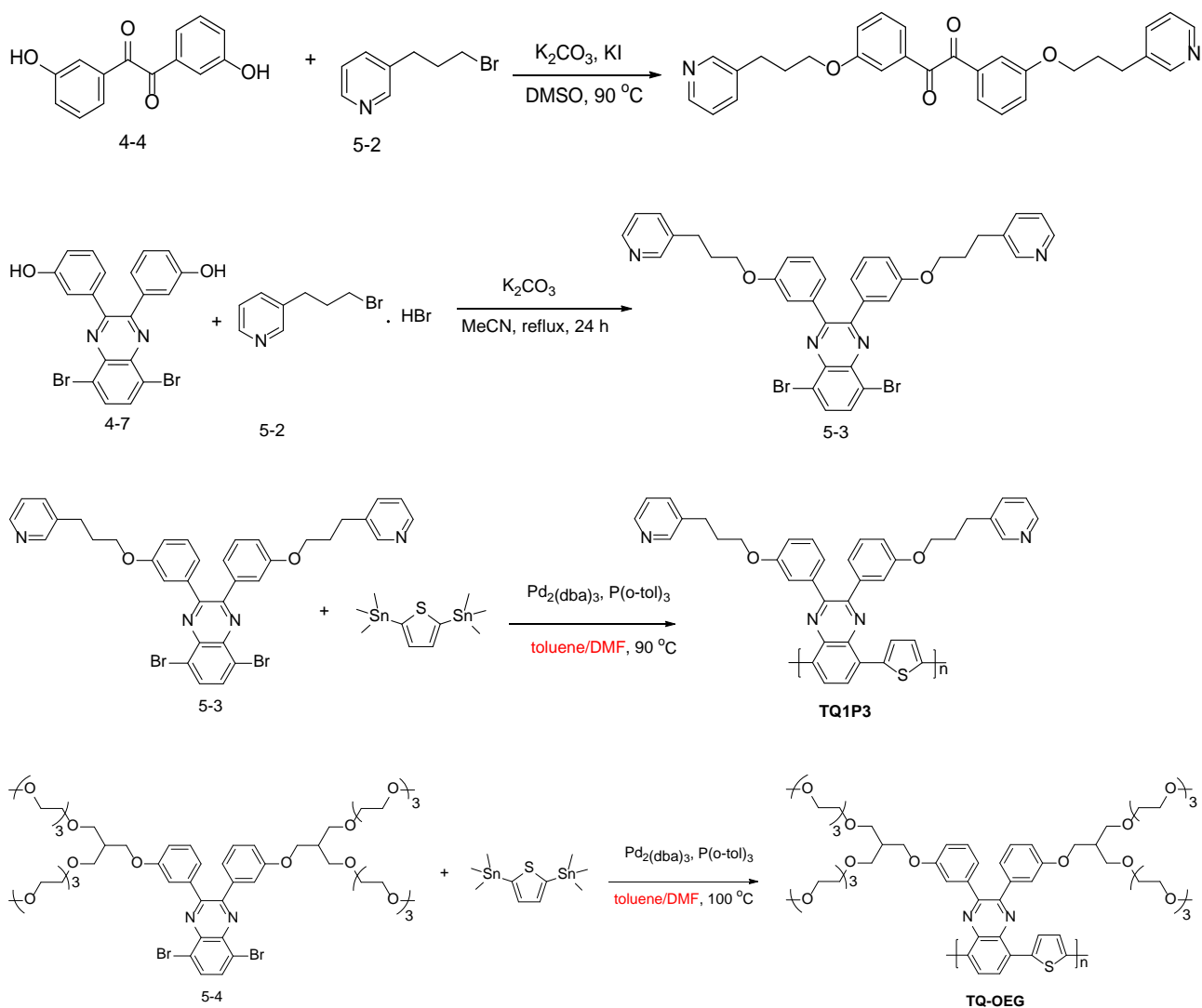


Scheme 5.1 Synthesis route of polymer TQ1-5A and TQ6A.

The synthesis procedure of polymer TQ1-5A and TQ6A is shown in **Scheme 5.1**. Polymer TQ1-5A was synthesised by Stille coupling copolymerisation from monomer **4-6**, 5,8-dibromo-2,3-bis(3-(octyloxy)phenyl)quinoxaline and 2,5-bis(trimethylstannyl)thiophene following the similar procedure described in **Chapter 4**. Polymer TQ6A was polymerised via Stille coupling from monomer 5,8-dibromo-2,3-bis(3-(diethylamino)hexyloxy)phenyl)quinoxaline (**5-1**) and 2,5-bis(trimethylstannyl)thiophene. During the purification step, polymer TQ6A was found to have limited solubility in CHCl_3 , but most of it can be dissolved well in methanol. It was assumed that polymer could be protonated post polymerisation and an additional washing with KOH aqueous solution was performed to the methanol solution of TQ6A. However, this washing step did not completely change the solubility of TQ6A in chloroform and concentrated TQ6A solution precipitated into hexane resulted in extremely fine particles, which was impossible to filter for the collection of the polymer solid. After purification, the methanol soluble fraction of the polymer was collected by evaporating solvent. Dark blue/black polymer was obtained after drying in a vacuum oven at r.t. overnight. The detailed synthesis procedure can be found in Appendix A.

5.2.2. Pyridine and OEG polymers





Scheme 5.2 Synthesis route of polymer TQ1P3 and TQ-OEG.

The synthesis procedure of targeting polymer TQ1P3 and TQ-OEG is shown in **Scheme 5.2**. Compound **5-2** was synthesised from 3-pyridinepropanol by reacting with HBr under reflux overnight. Similarly to 4-(3-bromopropyl)pyridine presented in **Chapter 4**, 3-(3-bromopropyl)pyridine was also intrinsically unstable and protonation of the compound with HBr was necessary to be able to isolate the compounds for the next alkylation step. It is worth to note here that the trial of the Williamson etherification between compound **4-4** and **5-2** could not afford the target compound. Hence, the Williamson etherification between compound **4-7** and **5-2** was performed, offering TQ1P3 monomer compound **5-3**. The monomer **5-3** was copolymerised with 2,5-bis(trimethylstannyl)thiophene via Stille coupling copolymerisation, to afford polymer TQ1P3. Polymer TQ-OEG was synthesised by Stille coupling from quinoxaline monomer **5-4** with OEG side groups and 2,5-bis(trimethylstannyl)thiophene. The detailed synthesis procedure can be found in **Appendix A**.

5.2.3. Influence of solvent polarity on molecular weight of pyridine functionalized polymer.

To achieve high performing p-type conjugated polymer, molecular weight of it is very important, which has direct influence on the polymer bandgap and charge transfer property.¹² It has been discussed in **Chapter 4**, that using pure toluene as the polymerisation solvent for TQ1P4 led to significant amount of aggregates. Hence, different solvents were utilised in the Stille Coupling polymerisation to study their influence on molecular weight of pyridine functionalized polymer.

The polymerisation solvent used to synthesis TQ1P4 was initially chosen as toluene, which is most commonly used reaction solvent in Stille Coupling.¹³ However, the first batch polymerisation yielded large amounts of precipitated solids in the reaction mixture. The undissolved solid was proven to be polymer TQ1P4, which has bad solubility in commonly used solvent with low polarity, i.e. toluene. After the solubility test performed with different solvent, it was found that TQ1P4 has relatively good solubility in anisole and DMF, which exhibit higher polarity compared to toluene. However, the synthesis of TQ1P4 with anisole as solvent still resulted in material precipitating, which hindered continuous growth of the polymer chain in the solvent environment. It has been reported that using a blend solvent containing DMF could accelerate the Stille polymerisation.¹⁴ Therefore a solvent mixture with toluene:DMF 1:1 volume ratio was utilised to increase the polarity of reaction environment for the synthesis of polymer TQ1P4 and TQ1P3. The three batches of TQ1P4 synthesised using different solvents were characterised through size exclusion chromatography (SEC), showing that higher molecular weight was achieved using toluene:DMF (1:1) mixture (**Table 5.1**).

Table 5.1 Molecular weight of TQ1P4 synthesised in different solvent.

TQ1P4	M_n (kg/mol)	M_w (kg/mol)	PDI
Batch 1: Toluene	6.23	16.34	2.62
Batch 2: Anisole	8.26	17.74	2.15
Batch 3: Toluene:DMF 1:1	9.61	26.27	2.73

UV-vis and cyclic voltammetry (CV) was performed to compare the energy level difference of the three batches of TQ1P4. The UV-vis spectra of the polymers are presented in **Figure 5.1** and **Figure 5.2** shows the cyclic voltammograms of the batch 1 and batch 3 TQ1P4. The batch 2 and 3 show a slightly red-shifted absorption spectra and higher intensity of the peaks in the long wavelength region compared to the batch 1, indicating longer conjugated length was achieved in the batch 2 and 3. The bandgap estimated by CV shows that batch 3 has lower bandgap compared to batch 1. The UV-vis

and CV results agree with the molecular weight results (**Table 5.1**), suggesting that using the solvent mixture of toluene:DMF could offer higher molecular weight of conjugated polymers containing polar side groups.

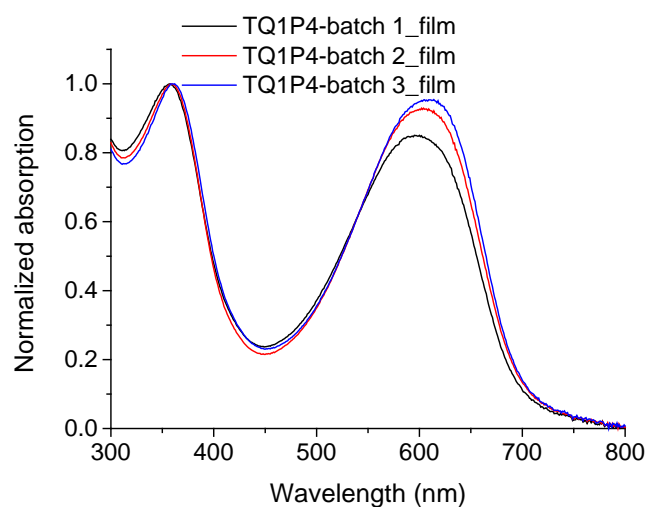


Figure 5.1 Normalized UV-vis absorption spectra of TQ1P4 synthesised with different solvent.

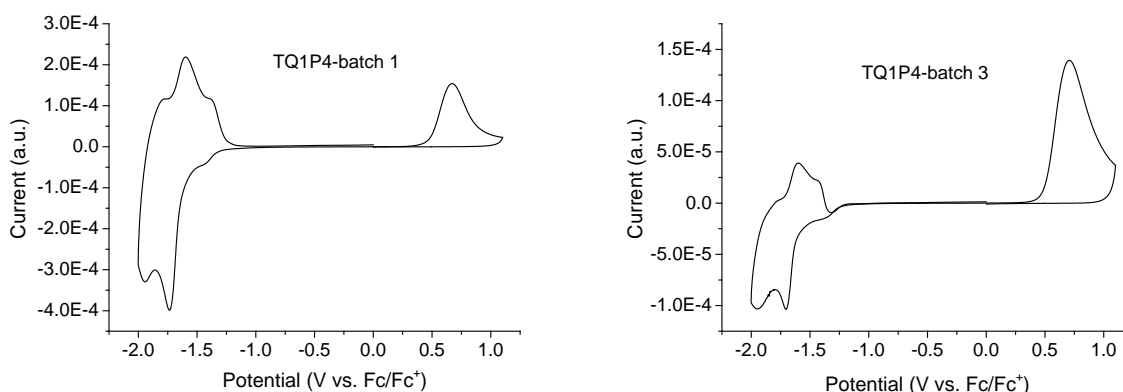


Figure 5.2 Cyclic voltammograms of the two batches of TQ1P4.

Based on the formula $E_{HOMO} = -(E_{ox}^{onset} + 5.13) eV$, $E_{LUMO} = -(E_{red}^{onset} + 5.13) eV$, HOMO and LUMO level energy of the two batches TQ1P4 were estimated and presented in **Table 5.2**.

Table 5.2 Electrochemical properties of the polymers. E_g^{CV} was calculated by $E_{LUMO} - E_{HOMO}$.

Polymers	E_{ox}^{onset} (V)	E_{red}^{onset} (V)	E_{HOMO} (eV)	E_{LUMO} (eV)	E_g^{CV} (eV)
TQ1P4-batch 1	0.47	-1.28	-5.60	-3.85	1.75
TQ1P4-batch 3	0.49	-1.22	-5.62	-3.91	1.71

5.3. Material characterisation

5.3.1. Optical and electrochemical properties

The UV-vis spectra of TQ1-5A, TQ6A, TQ1P3 and TQ-OEG films are shown in **Figure 5.3**, with TQ1 film as the reference. Compared to unfunctionalized polymer TQ1, near-identical UV-vis absorption properties were suggested in the case of TQ1-5A, indicating that the modification of side groups with 5% tertiary amine did not affect the conjugation of the polymer backbone. The long wavelength peak is attributed to the localized intramolecular charge transfer between thiophene moieties and quinoxaline units in the polymer backbone, while the short wavelength peak owing to the delocalized π - π^* transitions.¹⁵ Compared to TQ1 and TQ1-5A, TQ1P3 film showed decreased relative absorption intensity in low-energy region than that in high-energy area, indicating that compared to octyl side groups, the pyridine side groups slightly weakened the electron-withdrawing property of quinoxaline units.¹⁶ The TQ6A film was found to show intense absorption in the high energy region, which could be a result from the low molecular weight oligomers that cannot be removed during the purification post polymerisation. In the case of TQ-OEG, bathochromic shift of the absorption spectrum is found compared to TQ1, and slight vibronic peaks is observed at high wavelength region as well as a feature near the absorption onset, indicating some degree of aggregation and ordering of TQ-OEG in the solid state.

The photophysical characteristics of these functional polymers are listed in **Table 5.3**. The optical bandgap (E_g^{opt}) of the polymers is determined by its absorption spectrum in the solid state. The E_g^{opt} is calculated by the formula $E_g^{opt} = hc/\lambda_{onset}$, in which h is the Planck constant, c is the speed of light in vacuum and λ_{onset} is the wavelength of the onset absorption at low-energy region in the solid state.

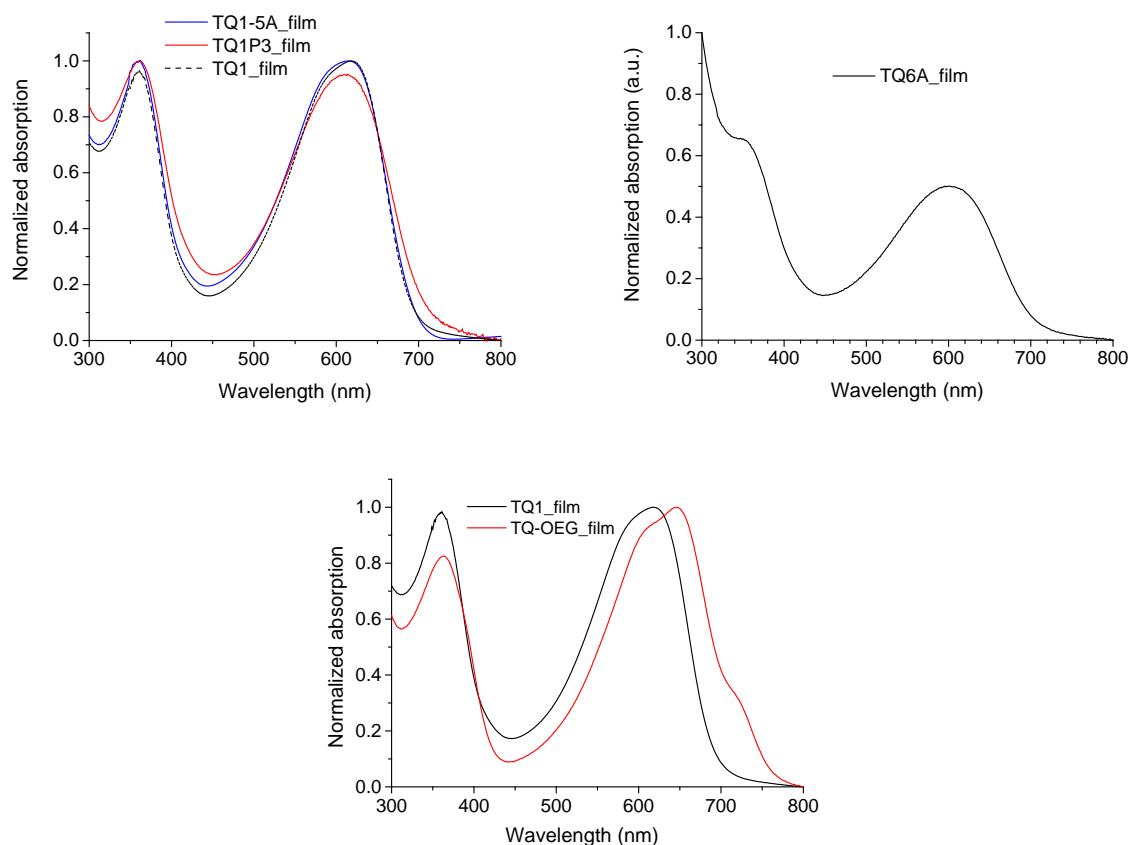


Figure 5.3 Normalized UV-vis absorption of polymers as thin films.

It can be concluded from the UV-vis data that introducing pyridine or OEG side groups to thiophene-quinoxaline based polymer did not result in the blue-shifted absorption onset, i.e. increase of the optical bandgap.

Table 5.3 Optical characteristics of polymers.

Polymers	λ_{max} (nm)	λ_{onset} (nm)	E_g^{opt} (eV)
TQ1-5A	362 614	717	1.73
TQ1P3	361 615	725	1.72
TQ6A	602	715	1.73
TQ-OEG	364 646	769	1.68
TQ1	361 618	711	1.75

HOMO and LUMO energy levels of TQ1-5A and TQ6A were estimated from the oxidation and reduction onset potential of polymers, respectively, from the cyclic voltammetry (CV) measurements, and are shown in **Table 5.4**.

Table 5.4 Electrochemical properties of TQ1-5A and TQ6A. E_g^{CV} was calculated by $E_{LUMO} - E_{HOMO}$.

Polymers	E_{ox}^{onset} (V)	E_{red}^{onset} (V)	E_{HOMO} (eV)	E_{LUMO} (eV)	E_g^{CV} (eV)
TQ1-5A	0.42	-1.30	-5.55	-3.83	1.72
TQ6A	0.48	-1.16	-5.58	-3.97	1.73

5.3.2. Solubility in green solvents

Due to the low content of functionalized tertiary amine groups in polymer TQ1-5A, this polymer did not show any solubility in acidified water/ethanol as compared to TQ1A (**Chapter 4**). It is interesting to find that polymer TQ6A can be dissolved in methanol and benzyl alcohol in the neutral state. TQ1P3 can be protonated by formic acid to offer conjugated polyelectrolytes and TQ1P3-FA, which is soluble in water, methanol (MeOH) and ethanol (EtOH), while the large OEG side groups endows the polymer TQ-OEG being soluble in methanol and ethanol without introducing any acid. **Figure 5.4** presents the UV-vis absorption spectra of TQ6A, TQ1P3 and TQ-OEG in different solvents and in the solid states. Compared to the TQ6A solution, the long wavelength absorption bands were enhanced and red-shifted in the solid state (spin-coated from 10 mg/mL methanol solution), which is attributed to the higher intermolecular interaction in the solid film. The absorption bands of TQ1P3 film were enhanced and red-shifted in the long wavelength region compared to the chloroform and *o*-DCB solution, which was a result from the higher intermolecular interaction in the solid state. Red-shifted absorption spectra was also found in the alcohol/water solution of TQ1P3-FA compared to TQ1P3 in chlorinated solvent, indicating multichain aggregation or solvatochromic effects caused by polar solvent.¹ The light absorption properties of TQ1P3 in different conditions is similar to that of TQ1P4 (presented in **Chapter 4**), indicating no influence on the conjugation using different substituent positions on pyridine rings. The room temperature TQ-OEG ethanol solution exhibits similar feature near the long-wavelength absorption onset as the film, while this feature is absent in methanol solution, indicating some aggregation formed in the case of using ethanol as the solvent. Hence, varied temperature (25 °C to 75 °C) UV-vis study was performed on TQ-OEG ethanol solution and the corresponding UV-vis spectra are shown in **Figure 5.4d**. Blue shifted absorption spectrum can be clearly observed when the temperature was increased, revealing the suppression of aggregation upon heating.

The green solvent solubility found from these polymers makes them very promising for the application in environment-friendly fabrication of OPVs.

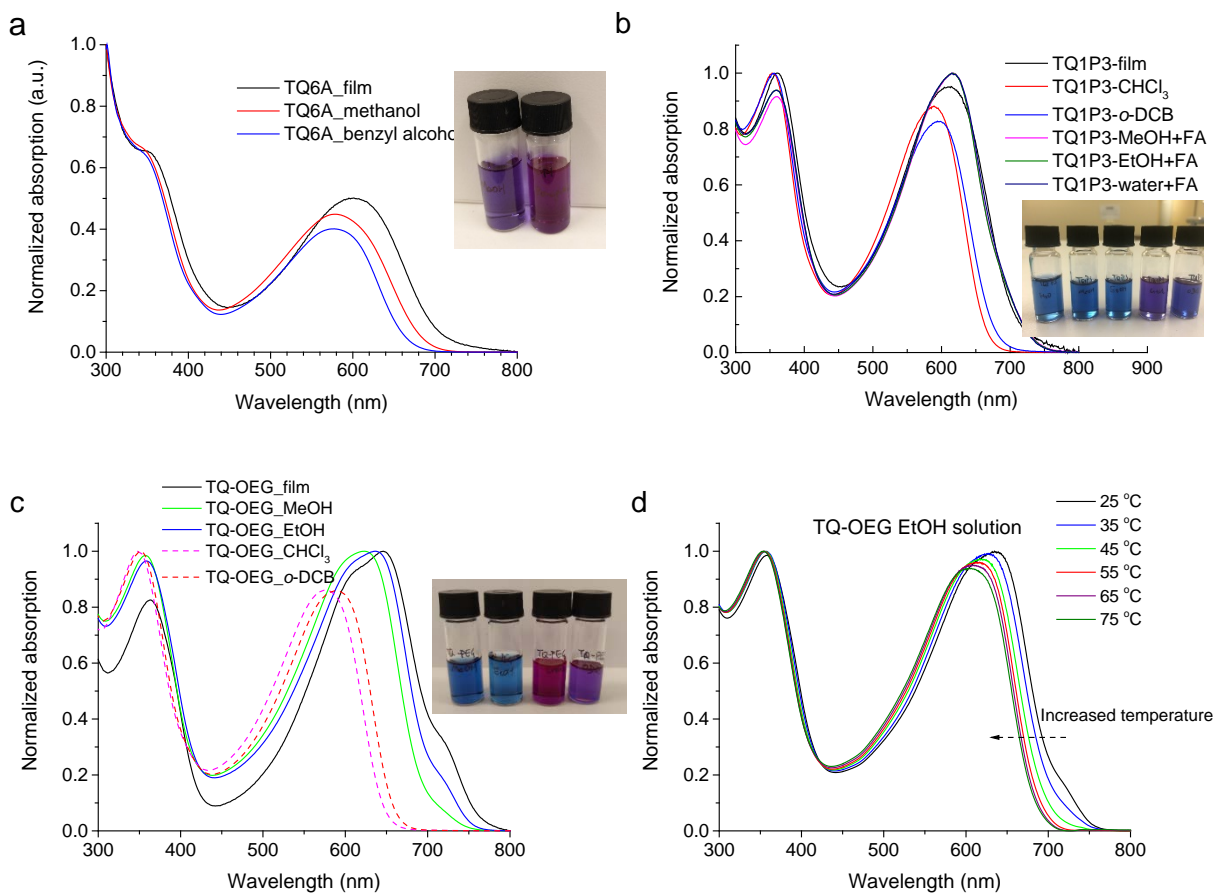


Figure 5.4 (a) Normalized UV-vis absorption spectra of (a) TQ6A, (b) TQ1P3 and (c) TQ-OEG in different condition. (d) Normalized UV-vis absorption profiles of TQ-OEG EtOH solution at varied temperatures. The photo images next to the UV-vis spectra present polymer solutions.

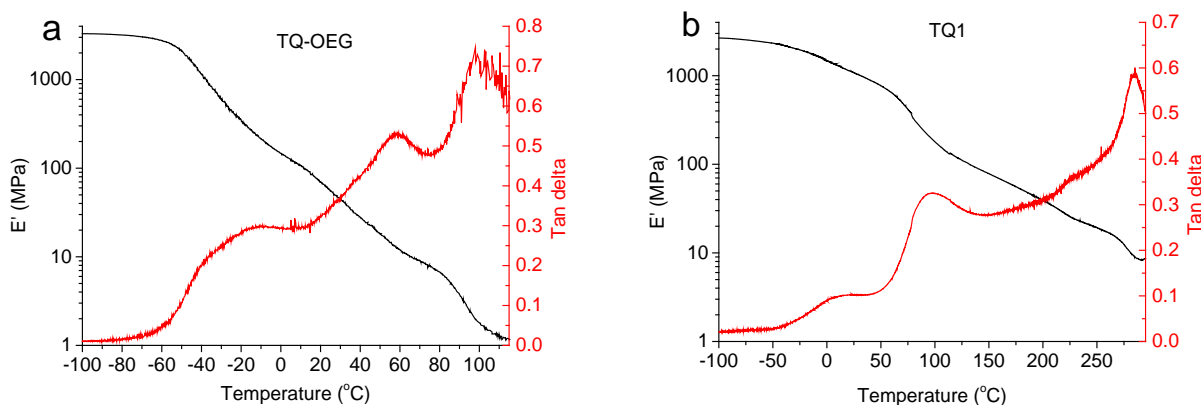
5.3.3. Thermal stability and property

Thermal stability of active materials is crucial to achieve thermally stable OPVs, which could reach temperature of 85 °C in working condition.¹⁷ Hence, the thermal stability of tertiary amine, pyridine and OEG functionalized polymers was evaluated using TGA under nitrogen gas flow. The temperatures which polymers underwent 1% weight loss and 5% weight loss are listed in **Table 5.5** (including polymers presented in **Chapter 4**). It can be observed TQ-OEG exhibit 1% weight loss at 137 °C and started major degradation at 340 °C. The weight loss at low temperature could be explained by the thermocleavable property of the OEG side groups.¹⁸ Considering 5% weight loss temperature to be the start of the main degradation, all polymers exhibit ideal thermal stability to meet the requirement for OPV operating condition (85°C)¹⁹.

Table 5.5 Thermal stability of amine, pyridine and OEG containing polymers.

TGA	TQ1A	TQ1-50A	TQ1-20A	TQ1-5A	TQ1P4	TQ1P3	TQ-OEG
1% weight loss (°C)	133	279	338	347	340	381	137
3% weight loss (°C)	359	346	409	417	401	417	340

To further investigate the thermal property of TQ-OEG, dynamic mechanical thermal analysis (DMTA) was performed using the sample preparation technique described elsewhere.²⁰ The DMTA temperature scan of TQ-OEG coated on the glass fibre mesh is shown in **Figure 5.5a**, and the DMTA scan of TQ1 is shown in **Figure 5.5b** as a comparison. A broad tan δ peak was observed at -25 °C accompanied by a remarkable storage modulus (E') over one order of magnitude in TQ-OEG sample, which could be attributed to the β transition of TQ-OEG. Since TQ-OEG is equipped with very large OEG groups, the relaxation of OEG groups could affect the stiffness of polymer to a great extent. A prominent tan δ peak was found at 60 °C, which is primarily attributed to the glass transition (T_g) of polymer. Due to the continuous decrease of the sample stiffness, the TQ-OEG coated glass fibre mesh fell apart at 104 °C during the measurement. It was suspected that TQ-OEG was in the viscous flow state beyond 104 °C; however, the differential scanning calorimetry (DSC) analysis of TQ-OEG did not show any thermal transition signal. Differently, the DMTA measurement of TQ1 could probe the thermomechanical properties of it until ~300 °C, further proves the low stiffness of TQ-OEG in nature. There are two tan δ peaks can be observed from the DMTA scan the TQ1 below 200 °C, which are attributed to the beta transition (10 °C) and glass transition (95 °C) of TQ1.²⁰ The DMTA result reveals that the OEG functionalized polymer has low stiffness at room temperature, indicating the potential to apply TQ-OEG in flexible electronic device.

**Figure 5.5 DMTA temperature scans of (a) TQ-OEG and (b) TQ1.**

5.4. Photovoltaic performance of amino polymers

In order to evaluate the photovoltaic performance of TQ1A processed from green solvent, a water/alcohol soluble fullerene derivative, namely PCBDAN²¹ was introduced and the structure is shown in **Figure 5.6**. Amine-functionalized PCBDAN has been reported to form a self-assembled cathode interface layer²² and also been applied as an electron-acceptor with P3HT donor, which achieved PCE of 3.1%²³. However, the reported OPVs still consisted of active layers fabricated from halogenated solvents, which is divergent to the purpose of structure modification with water/alcohol solubilizing amine groups.

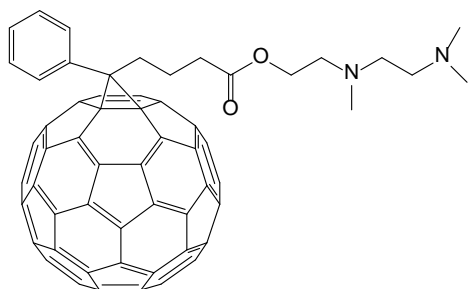


Figure 5.6 Chemical structure of PCBDAN.

Inverted devices with the structure of ITO/ZnO/BHJ/MoO_x/Ag were fabricated using ethanol with acetic acid (3%) to process the TQ1A:PCBDAN active layer. Disappointingly, the solar cells fabricated with ethanol processed BHJ layer did not show any photovoltaic response. One of the possible reasons could be the ester bond in the molecular structure of PCBDAN being hydrolysed in acidic condition. The BHJ film showed high degree of visible aggregations, indicating the deteriorated morphology of the active layer. To circumvent the problem of inferior morphology in active layer, OPVs were subsequently fabricated with TQ1A:PCBDAN active layer processed from *o*-DCB solution. The *o*-DCB processed device only showed 0.02% of PCE, which is far below the efficiency of TQ1:PC₆₁BM based devices.

To exclude the interference introduced by PCBDAN and to study the influence of amino groups attached to donor polymer on OPVs, PC₆₁BM or PC₇₁BM was subsequently used as the acceptor to fabricate BHJ devices with TQ1A using chlorinated solvents. Meanwhile, ternary-blend active layer consisting TQ1:TQ1A:PCBM (4:1:12.5 weight ratio) was evaluated to investigate if amine groups can form charge-trap sites.²⁴ To avoid any unwanted interaction between amine groups and interface layers, different buffer layer materials were introduced, including TPD,²⁵ PEI,²⁶⁻²⁷ PEIE²⁷⁻²⁸ and C₆₀ in both the inverted geometry and conventional structure.

Photovoltaic characteristics of amino polymer based OPVs are listed in **Table 5.6** and different device structures (described below **Table 5.6**) were employed to optimise the device configuration, aiming to improve the performance.

Table 5.6 Photovoltaic performance of TQ1A:PCBM (1:2.5) BHJ solar cells and TQ1:TQ1A:PCBM (4:1:12.5) BHJ solar cells.

Active layer	J_{SC} (mA/cm ²)	FF (%)	V_{OC} (V)	PCE (%)
TQ1A:PC ₆₁ BM ^a	0.91	39	0.19	0.07
TQ1A:PC ₆₁ BM ^b	2.20	45	0.36	0.30
TQ1A:PC ₆₁ BM ^c	1.56	45	0.33	0.23
TQ1A:PC ₆₁ BM ^d	1.40	45	0.30	0.19
TQ1A:PC ₆₁ BM ^e	1.53	41	0.39	0.25
TQ1A:PC ₆₁ BM ^f	1.47	43	0.34	0.22
TQ1A:PC ₇₁ BM ^d	1.65	41	0.40	0.27
TQ1A:PC ₇₁ BM ^g	1.78	40	0.50	0.35
TQ1A:PC ₇₁ BM ^h	1.83	42	0.49	0.38
TQ1:TQ1A:PC ₇₁ BM ^a	4.71	54	0.70	1.79
TQ1:TQ1A:PC ₇₁ BM ^b	4.02	57	0.78	1.76
TQ1:TQ1A:PC ₇₁ BM ^c	4.68	52	0.73	1.78
TQ1:TQ1A:PC ₇₁ BM ^d	4.64	54	0.78	1.95

α -DCB as BHJ processing solvent; Device architecture: ^aITO/ZnO/BHJ/MoO_x/Ag,

^bITO/ZnO/BHJ/TPD/MoO_x/Ag, ^cITO/ZnO/PEI/BHJ/TPD/MoO_x/Ag,

^dITO/ZnO/PEIE/BHJ/TPD/MoO_x/Ag, ^eITO/MoO_x/BHJ/LiF/Al, ^fITO/MoO_x/TPD/BHJ/LiF/Al,

^gITO/MoO_x/BHJ/C₆₀/LiF/Al, ^hITO/MoO_x/TPD/BHJ/LiF/Al.

Though lots of efforts have been put in the device engineering, maximum PCE value of 0.38% was achieved from OPV based on TQ1A:PC₇₁BM active layer and 0.30% in the case of TQ1A:PC₆₁BM. The devices with TQ1A as the sole donor all showed very poor J_{SC} and V_{OC} . However, the devices containing ternary blend with 20% of TQ1A achieved approximate 2% of PCE, accompanying with V_{OC} of 0.78 V, which is comparable to TQ1:PCBM devices.¹⁶ Therefore, the low PCE of TQ1:TQ1A:PCBM based OPVs was mainly driven by the low J_{SC} , which could be a result from the undesirable morphology of active layer.²⁹

Further device engineering was carried out by utilising Poly(9-vinylcarbazole) (PVK), which has been reported as a hole-transporting and electron-blocking material.³⁰ The introduction of PVK is to avoid the direct interaction between amine groups and MoO_x, which could otherwise reduce the work function of the anode interface.^{28, 31} To have a direct comparison of OPVs based on TQ1 and TQ1A, conventional solar cells with TQ1:PC₆₁BM and TQ1A:PC₆₁BM active layer were fabricated respectively, with the same geometry using a thin layer of PVK in between the BHJ layer and underlying MoO_x. Compared to TQ1 based device, OPV with TQ1A as the donor material still presented very low PCE of only 0.32% (**Table 5.7**).

Table 5.7 Device characteristics of TQ1A:PC₆₁BM (1:2.5) BHJ layer solar cells and TQ1:PC₆₁BM (1:2.5) BHJ solar cells.

Active layer	J_{SC} (mA/cm ²)	FF (%)	V_{OC} (V)	PCE (%)
TQ1A:PC ₆₁ BM	1.98	39	0.40	0.32
TQ1:PC ₆₁ BM	2.60	54	0.82	1.17

o-DCB as BHJ processing solvent; Device architecture ITO/MoO_x/PVK/BHJ/LiF/Al

Furthermore, ternary blends consisting TQ1:TQ1A:PC₆₁BM with different loading of TQ1A were processed as active layers respectively in the inverted OPVs to evaluate their photovoltaic performance as a function of TQ1A content. The representative *J-V* curves are shown in **Figure 5.7**. It can be observed that both J_{SC} and V_{OC} showed the trend of decrease with the increase of TQ1A content in the ternary blend. However, with 10% of TQ1A content in the active layer, effective photovoltaic response with the PCE of 1.23% was achieved, which is inconsistent with the results reported from p-type conjugated polymers modified by amino groups.²⁴

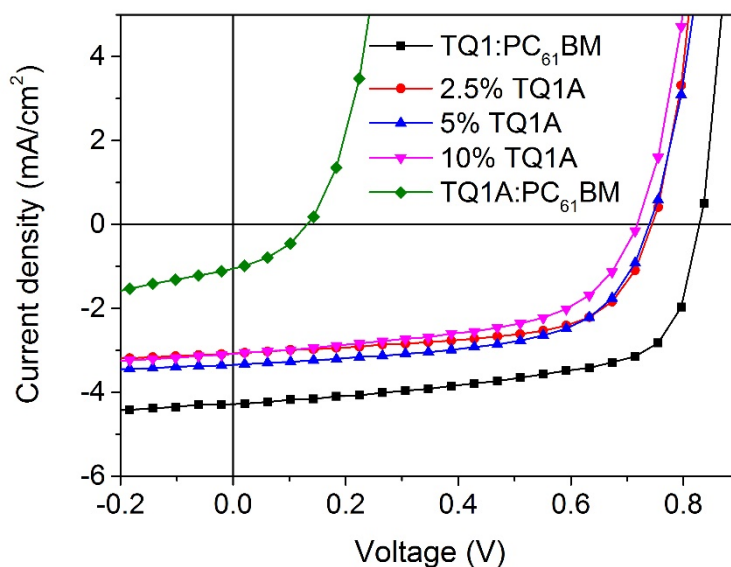


Figure 5.7 *J-V* curves of TQ1:PC₆₁BM device (black line), TQ1A:PC₆₁BM device (green line) and TQ1:TQ1A:PC₆₁BM devices with different load of TQ1A in the active layers.

To investigate the reason of insufficient photovoltaic performance in TQ1A containing organic solar cells, different characterisation was performed.

5.4.1. Miscibility of the polymers and PC₆₁BM

Amine containing materials have been reported to increase the intermixing between TQ1 and PCBM,⁶ and DSC results presented in **Chapter 4** showed TQ1A was intimately mixed with PCBM. To investigate the miscibility between PCBM with TQ1-5A, which is only equipped with 5% amino

side chains, DSC measurements were performed on TQ1-5A:PCBM blend as well as TQ1:PCBM as the reference. The DSC thermograms are shown in **Figure 5.8**.

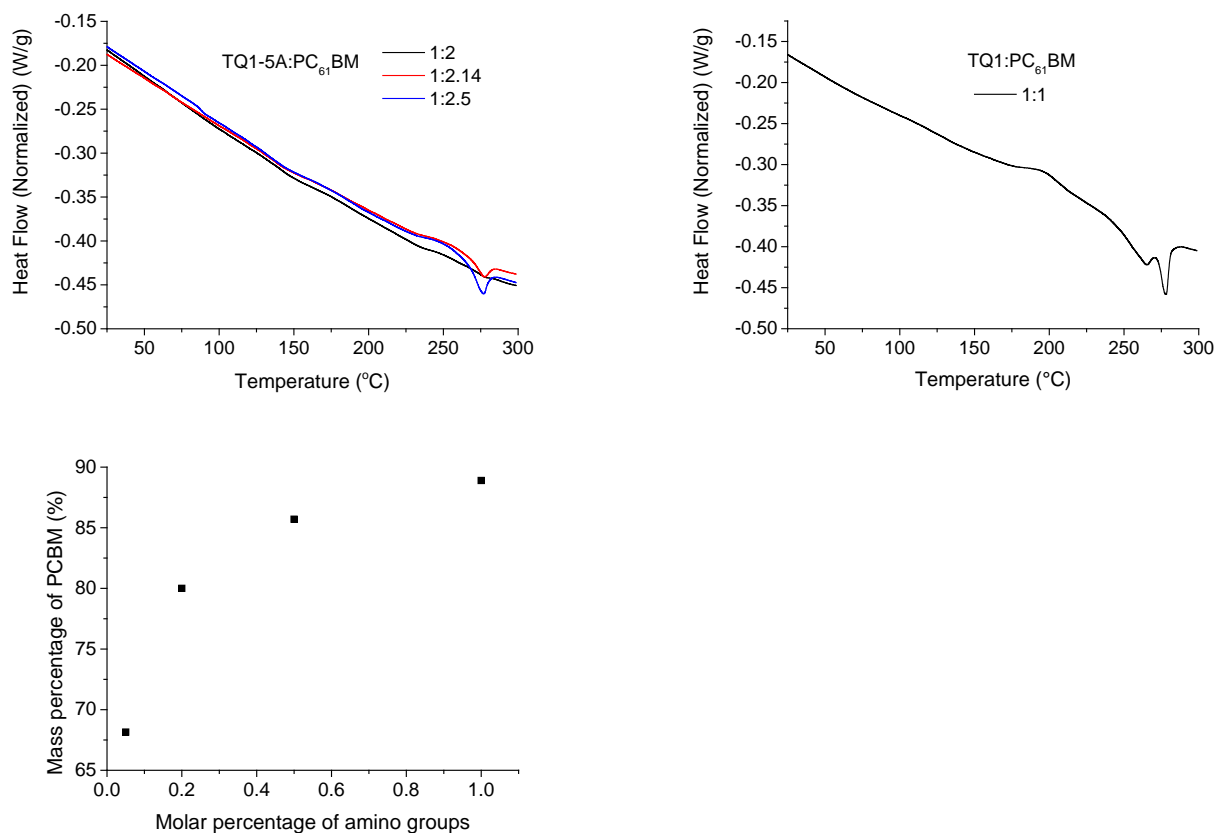


Figure 5.8 DSC thermograms of TQ1-5A:PC₆₁BM blends in varied weight ratios and TQ1:PC₆₁BM (1:1) blend as the reference. A plot showing the critical mass percentage of PC₆₁BM in the blend above which the melting peak of PC₆₁BM could be observed as a function of molar percentage of amino groups in the polymer structure (The DSC data of other amino polymers can be found in Chapter 4).

Interestingly, no melting behaviour of fullerene could be observed in the case of TQ1-5A:PC₆₁BM at 1:2 weight ratio, indicating that even a small number of amino side groups in the polymer can introduce strong interaction between the polymer and PC₆₁BM. The miscibility between amine-functionalized polymer and PC₆₁BM was found to increase with the increased amount of tertiary amine in the polymer structure. The high extent of miscibility between TQ1A and PCBM (presented in **Chapter 4**) could partially explain the low photovoltaic performance presented in the TQ1A based OPVs, as the phase separation between donor and acceptor is essential for charge separation.³²

5.4.2. Morphology

The DSC results showed the highly intermixed behaviour between amine-functionalized polymer and PCBM. To further understand the surface property of amine containing photoactive layer, atomic force microscopy (AFM) measurement was performed on binary blend systems containing amine-functionalized materials processed from different solvents as well as unfunctionalized TQ1:PC₆₁BM

films as the references. The AFM topographical images of the measured films are shown in **Figure 5.9**.

Modifying the BHJ processing solvent and using co-solvent/additive have been known to be an effective way to modify the active layer morphology.³³⁻³⁵ Since chloroform and *o*-DCB are among the most commonly used solvents for conjugated materials due to their good solubility in these solvents, the films for AFM study were spin-coated from chloroform and *o*-DCB solutions, respectively. In the case of chloroform being used as the processing solvent, large domain features or phase separation were suggested from both TQ1:PC₆₁BM and TQ1A:PC₆₁BM surface topographical images. In contrast, finer interpenetrating or more intermixed morphology was obtained from *o*-DCB processed TQ1A:PC₆₁BM film compared to the TQ1 counterpart, indicating insufficient phase separation for efficient exciton dissociation,³⁶ and the results are in accordance with the DSC results. Moreover, when PC₆₁BM was replaced with PCBDAN in the blend, aggregation (**bright spots on AFM images**) appeared on the sample surface either processed from chloroform or *o*-DCB, which could be resulted from the inferior solubility of PCBDAN in chlorinated solvent compared to PC₆₁BM. The results from the AFM study indicated that chloroform results in large phase separation in TQ1A:PC₆₁BM film morphology while too fine intermixing in the case of processing from *o*-DCB.

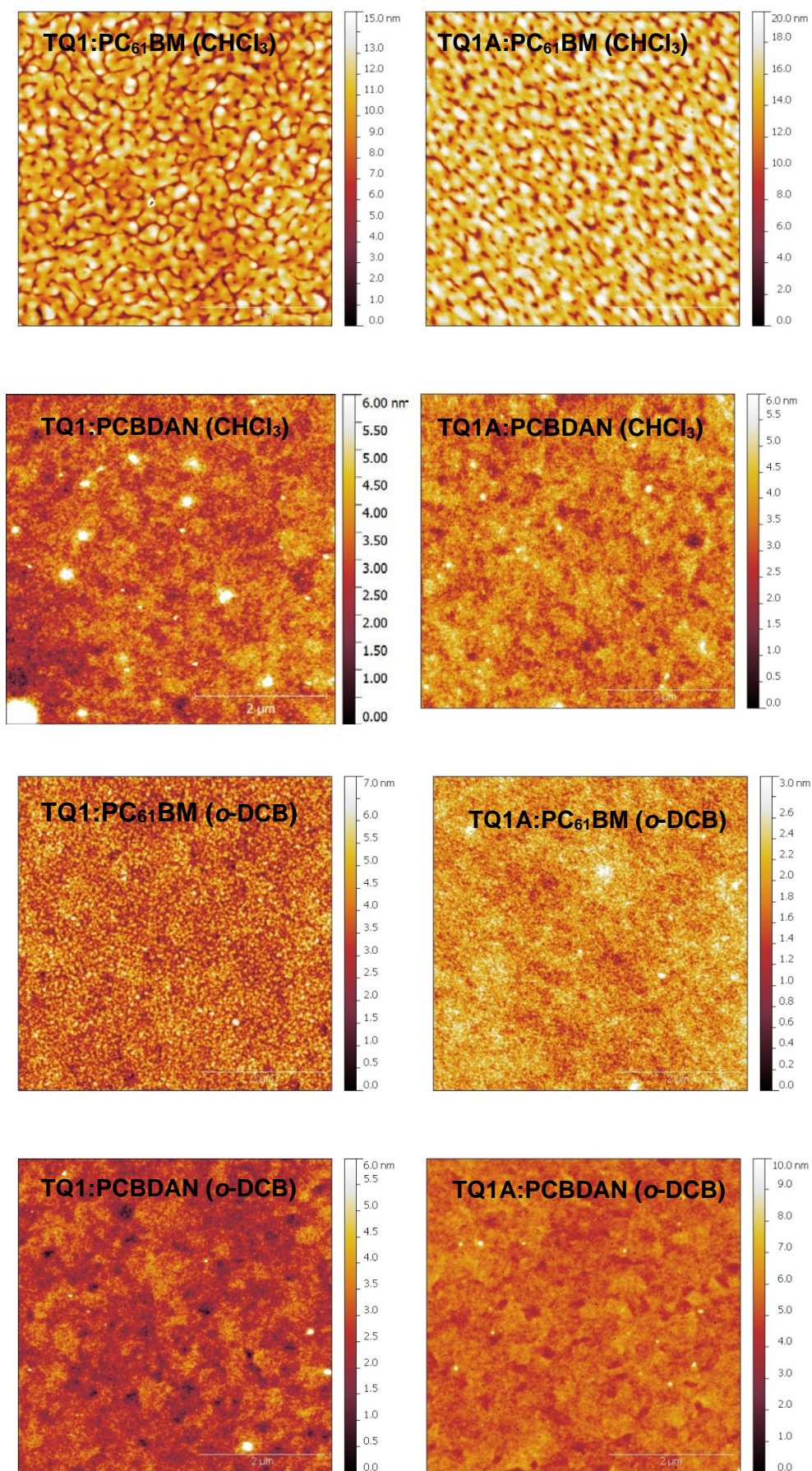


Figure 5.9 AFM topographical images (5x5 μm) of different polymer:acceptor (1:2.5 weight ratio) blend spin coated from chloroform and o-DCB.

Finely intermixed morphology with nanoscale phase separation is known to be essential for high performing OPVs,²⁹ therefore, solvent vapour (SV) annealing³⁷ was introduced to amino polymer containing films that were deposited using *o*-DCB to study if nanoscale phase separation could be achieved.

The SV annealing experiment was performed by putting the polymer:fullerene films separately in a closed chamber with saturated chloroform vapour. During SV annealing, all films were kept in a closed desiccator for 2 hours, then dried in a vacuum oven at r.t. overnight before AFM measurement. AFM topographical images of SV annealed films are shown in **Figure 5.10**. The TQ1:PC₆₁BM film (**Figure 5.10a**) showed the formation of large aggregation (bright spot at top-left corner) after SV annealing. Compared to the TQ1:PC₆₁BM film, gross phase separation was revealed from the topographical images of amine-functionalized polymer based films. Large gaps between disconnected materials were suggested from **Figure 5.10b&c**, forming deteriorated film morphology. The SV annealed TQ1A:PC₆₁BM film (**Figure 5.10d**) presented massive material agglomeration and pinhole formation on the surface. This SV annealing experiment turned out to be unsuccessful, as macroscale phase separation was observed instead of nanoscale.

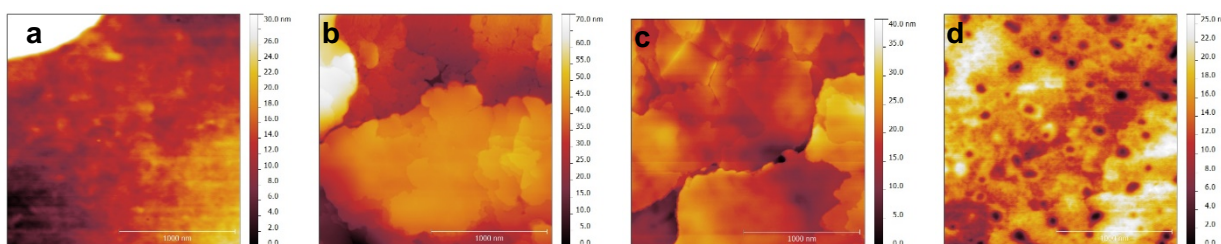


Figure 5.10 2x2 μm AFM topographical images from solvent vapour annealed films of (a) TQ1:PC₆₁BM, (b) TQ1-20A:PC₆₁BM, (c) TQ1-50A:PC₆₁BM and (d) TQ1A:PC₆₁BM, respectively.

5.4.3. Surface energy

It is presented in the device characteristics that using a thin layer of TPD in the inverted device structure could slightly improve the J_{SC} and V_{OC} , which was assumed to be the suppression of unwanted interaction between tertiary amine and MoO_x. Since the tertiary amine side groups in TQ1A significantly improved the hydrophilicity of the conjugated polymer compared to TQ1, which only substituted with hydrophobic alkyl side groups. Contact angle measurements were carried out to understand the distribution of amino materials on the top surface of the blend film, which is in direct contact with a hole transport layer in an inverted OPVs.

From the result of contact angle measurement (**Table 5.8**), it can be found that the contact angle of the blend film TQ1A:PC₆₁BM is nearly identical compared to the value of neat TQ1A film, revealing high content of TQ1A on the top surface post spin-coating. Hence, in a conventional device structure, TQ1A has high possibility to interact with a cathode, which would induce an electron extraction barrier and further reduce the built-in electric field. In the inverted devices based on TQ1A:PCBM,

tertiary amine groups could interact with the MoO_x layer and reduce the work function of anode interface (presented in **Chapter 4**).

Table 5.8 Contact angle (water) results of neat and blend films on ITO coated glass.

Pure film	Contact angle (°)	Blend film	Contact angle (°)
TQ1	83	TQ1:PC ₆₁ BM	83
TQ1A	60	TQ1A:PC ₆₁ BM	60
PC ₆₁ BM	78	TQ1:PCBDAN	82
PCBDAN	69	TQ1A:PCBDAN	66

The results from contact angle measurements of blend films are accordant with the device results that using a TPD as a passivation layer, slightly improved photovoltaic performance was achieved. In the case of TQ1:PC₆₁BM film, no clear conclusion could be draw due to the relatively similar surface energy between TQ1 and PC₆₁BM, while TQ1A:PCBDAN films shows higher hydrophilicity compared to films without amine-functionalized groups. Furthermore, TQ1:PCBDAN film shows high content of TQ1 on the top surface, indicating high content of PCBDAN underneath, which is agreeing with the reported self-organization behaviour of PCBDAN.²²

Because of the property of amino side chains, the molecular weights of tertiary amine functionalized polymers could not be detected by size exclusion chromatography (SEC) (explanation can be found in **Chapter 4**). Hence, the influence on the photovoltaic performance introduced by different molecular weight cannot be studied.

5.4.4. Energy losses

Excessively intermixed morphology revealed from experimental results described above could possibly lead to more charge recombination, explaining low short-circuit current in TQ1A:PCBM based OPVs compared to TQ1:PCBM counterpart. But the origin of low V_{OC} in the amino material containing OPVs cannot be simply imputed to the undesirable active layer morphology. Since charge-transfer (CT) state energy determines the value of V_{OC} ³⁸⁻³⁹, highly sensitive EQE measurements by Fourier transform photocurrent spectroscopy (FTPS)⁴⁰ was performed to estimate the energy of CT state (E_{CT}) according to Marcus theory, as shown in [eq 1](#).⁴¹

$$EQE(E) = \frac{f}{E\sqrt{4\pi\lambda kT}} \exp\left[\frac{-(E_{CT} + \lambda - E)^2}{4\lambda kT}\right] \quad (1)$$

where f is the oscillator strength, proportional to the D/A (CT state) interface area and the D/A interaction strength; λ is a reorganisation energy associated with CT absorption process; k is the Boltzmann constant and T is absolute temperature.

Through fitting the EQE-FTPS curve (**Figure 5.11**) in the sub-bandgap region, E_{CT} , λ and f of different binary blend system were extracted and listed in **Table 5.9**.

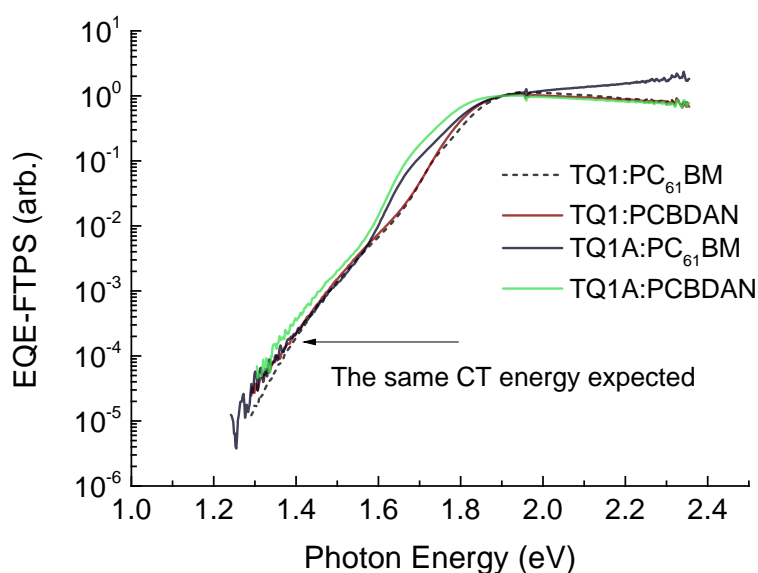


Figure 5.11 EQE-FTPS for inverted solar cells with different active layer. The amino containing device used TPD in between the active layer and MoO_x.

Table 5.9 Parameters extracted by fitting the sub-bandgap EQE-FTPS curves with Marcus theory.

Parameters	TQ1:PC ₆₁ BM	TQ1:PCBDAN	TQ1A:PC ₆₁ BM	TQ1A:PCBDAN
E_{CT} (eV)	1.472	1.465	1.439	1.425
λ (eV)	0.392	0.491	0.334	0.382
f (eV)	0.020	0.055	0.006	0.012

Since E_{CT} of TQ1A:PC₆₁BM based device extracted through the fitting is similar to that of TQ1:PC₆₁BM reference device, the voltage loss must be associated with charge recombination. Furthermore, the work function of the electrodes are easily modified by amine-functionalized polymer,²⁸ the weak built-in field and strong diffusion losses are most likely to be the reason for the low V_{OC} . The other reasons of the weak photovoltaic effect observed in amino active material based OPVs are still not clear and under investigation.

5.5. Photovoltaic performance of TQ1P3 and TQ-OEG

To evaluate the photovoltaic performance of donor polymer modified with pyridine/OEG side chains, TQ1P3 and TQ-OEG were tested with PC₆₁BM as an acceptor, from which the blend was processed using organic solvent anisole and *o*-DCB, respectively. To reduce any unwanted interaction between pyridine groups and MoO₃ interface, N,N'-bis(3-methylphenyl)-N,N'-bis(phenyl)-benzidine (TPD)²⁵ was utilised as a hole transport and buffer layer between BHJ and MoO₃ interlayer. An inverted device structure of ITO/ZnO/BHJ/TPD/MoO₃/Ag or ITO/ZnO/BHJ/MoO₃/Ag was used in the device fabrication for the evaluation of the functionalized polymers.

It was observed that the introduction of the TPD buffer layer in the TQ1P3 based OPVs only slightly improved the device performance, and the effect of TPD was comparably lower than in the TQ1P4 based devices (presented in **Chapter 4**). The similar PCEs achieved in the TQ1P3 devices with and without introducing TPD could be explained by the reduced interaction between nitrogen groups and MoO₃ in the case of the meta-substituent pyridine compared to the para-substituent one. Since the meta-position substituent could result in the delocalization of the lone-pair electrons on the nitrogen as well as create more steric hindrance.

The devices based on TQ-OEG:PC₆₁BM BHJ layer achieved higher PCE (0.51%) compared to the TQ1P3 based devices (PCE of 0.41%) using the same geometry, showing the potential of side chain engineering with OEG side groups on different polymer backbone.

Table 5.10 Photovoltaic performance of BHJ OPVs based on Donor polymer:PC₆₁BM (1:2.5 weight ratio) blends with device structure of ^aITO/ZnO/BHJ/TPD/MoO₃/Ag and ^bITO/ZnO/BHJ/MoO₃/Ag.

BHJ	Device structure	J_{sc} (mA/cm ²)	FF (%)	V_{oc} (V)	PCE (%)
TQ1P3:PC ₆₁ BM	a	2.17 (2.12 ± 0.07)	49 (48 ± 2)	0.46 (0.46 ± 0.00)	0.49 (0.47 ± 0.01)
	b	2.05 (1.98 ± 0.04)	48 (48 ± 1)	0.42 (0.42 ± 0.00)	0.41 (0.40 ± 0.01)
TQ-OEG:PC ₆₁ BM	b	1.87 (1.54 ± 0.15)	46 (45 ± 1)	0.59 (0.60 ± 0.01)	0.51 (0.42 ± 0.04)

To study the active layer morphology containing functional donor polymers, atomic force microscopy (AFM) was performed on films spin-coated from the same solutions used for device fabrication. **Figure 5.8a** shows the AFM topographical image of TQ1P3:PC₆₁BM, revealing smooth surface with a root-mean-squared roughness (R_q) of 1.71 nm. Whereas, the TQ-OEG:PC₆₁BM film exhibits large phase separation (**Figure 5.8b**), and highly rough surface with R_q of one magnitude higher than that

of the TQ1P3 counterpart. The gross phase separation observed in film containing TQ-OEG could be a result from the low miscibility between TQ-OEG and PCBM induced by different surface energy, since OEG side groups endows highly hydrophilic property of TQ-OEG as opposing to the hydrophobic PCBM.

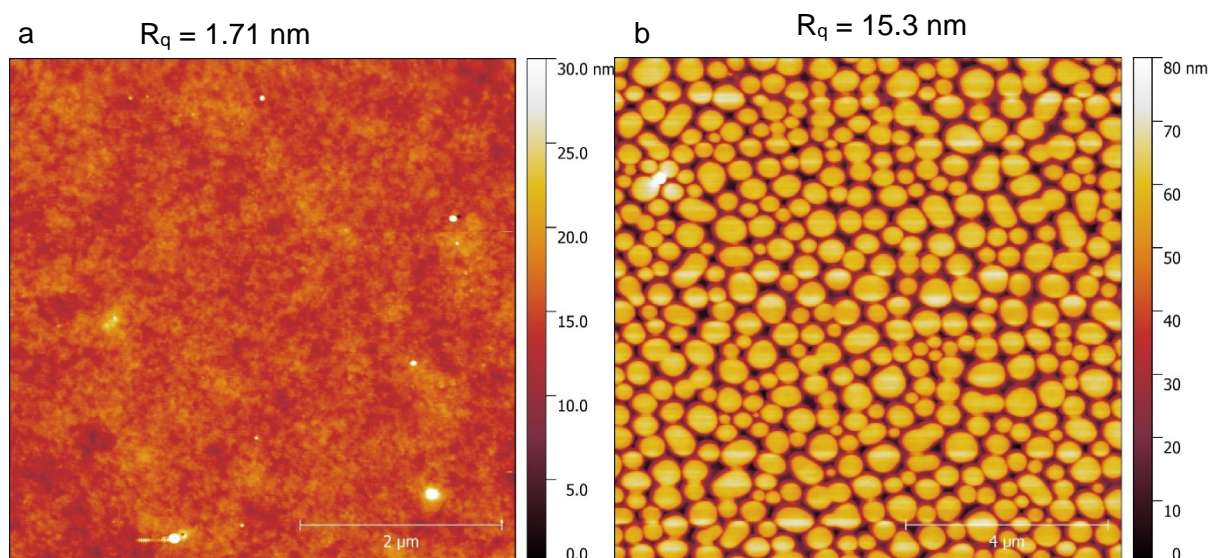


Figure 5.12 5×5 μm AFM images of (a) TQ1P3:PC₆₁BM film processed from anisole and (b) TQ-OEG:PC₆₁BM film processed from *o*-DCB.

5.6. Electrochromic Properties of amino polymers

Conjugated polymers are candidates for electrochromic switching applications, such as camouflage and smart windows.⁴²⁻⁴³ It has been reported that TQ1 film shows excellent electrochromic switching performance from dark blue in the reduced state to transmissive yellow upon oxidation.⁴² As described above, TQ1A and its derivatives exhibit low oxidation potentials and solution processibility, which are essential requirements for electrochromic application.⁴⁴ To investigate the optical switching properties of TQ1A and its derivatives, electrochemical and spectroelectrochemical measurements have been performed. Chloroform and a green solvent, methanol with formic acid were used respectively to spray coat TQ1A and TQ1-50A films while TQ1-20A and TQ1-5A were processed from chloroform only. In the case of methanol with a small amount of formic acid being used for processing, the formed films were annealed at 130 °C to deprotonate amine and regenerate neutral polymers.

5.6.1. Spectroelectrochemistry

Spectroelectrochemistry of amino polymers (**Figure 5.13**) shows that all polymers switched from a neutral state to a transmissive oxidized state. Upon +1 V vs. Ag/Ag⁺ applied potential, the colour of all polymer films were switched from intensive blue to faint yellow. With the increase of the applied

potential, the oxidized polymers showed the depletion of the original absorption peaks in the low energy region, which is associated with the new polarons forming in the near infra-red (NIR) region. The new charge carriers prompt the formation of quinoidal geometry in the polymer backbone and lowers the bandgap of polymer. Hence the absorption in the visible light region was suppressed in the oxidized state.

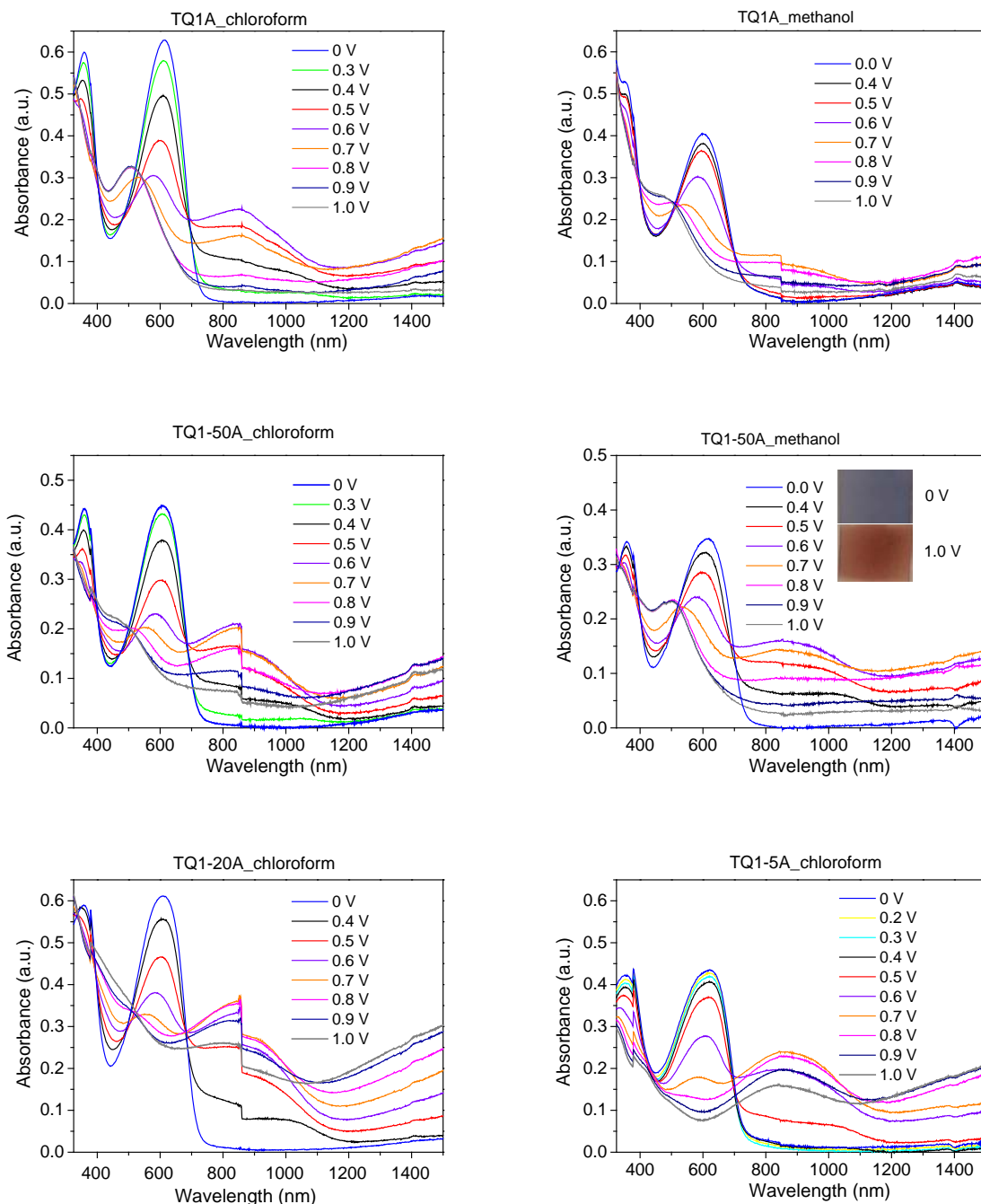


Figure 5.13 Spectroelectrochemical measurements on amino polymers, using 0.1 M NBu_4PF_6 in anhydrous acetonitrile as supporting electrolyte. Films were switched between 0 and +1.0 V.

New absorption peak at 505 nm was observed in TQ1A sample upon oxidation, the origin of which is unclear. It is interesting to find that the peak around 505 nm became less pronounced with the

decrease of the content of amine side groups in the polymer structures. Hence, the new absorption peak could be associated to the oxidation of tertiary amine containing quinoxaline repeating unit.

The optical contrasts (ΔT) of all polymers were evaluated from the transmittance change at the low energy absorption maxima (623 nm) and are listed in **Table 5.11**. The lowest optical contrast of only 28% for TQ1-5A among all the chloroform processed films was observed, which might be resulted from the difference in film thickness compared to other polymer films. Reduction of the optical contrast was observed in TQ1A sample when altering the processing solvent from chloroform to methanol. The reduced ΔT in the methanol processed samples were possibly attributed to the poor adhesion of polymer film to the substrate or undesirable film quality after thermal annealing.

Table 5.11 Optical contrast of amino polymers at the low energy absorption maxima.

Processing solvent	TQ1A ΔT (%)	TQ1-50A ΔT (%)	TQ1-20A ΔT (%)	TQ1-5A ΔT (%)
CHCl ₃	40	37	34	28
Methanol	20	34		

5.6.2. Kinetic study

The response times of amino polymers were studied by measuring the difference in the transmittance at 623 nm under an applied potential as a function of time. The kinetic measurements are shown in **Figure 5.14** with the pulse duration of the applied potential decreasing from 10 s to 0.5 s successively to analyse the switching speed.

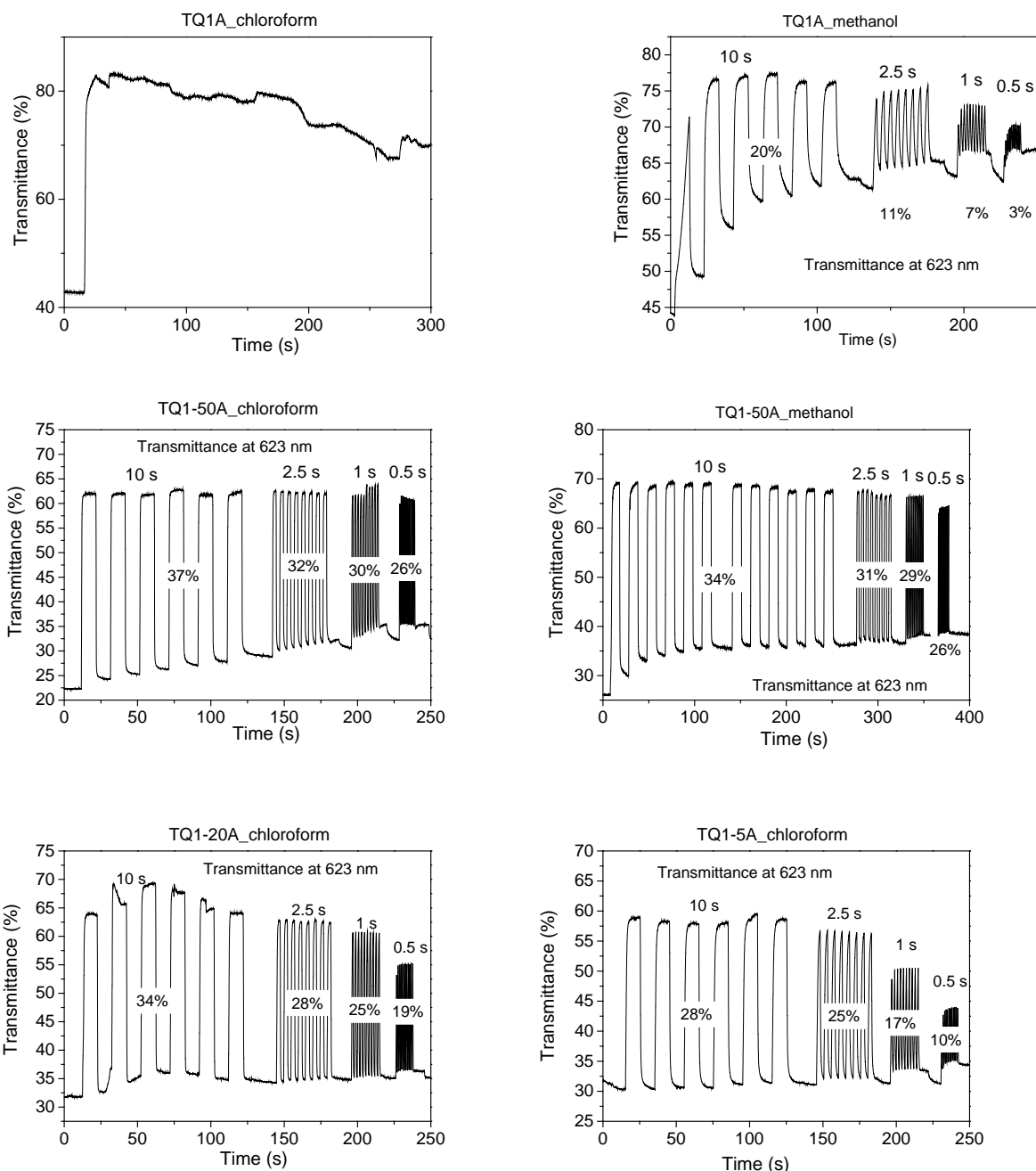


Figure 5.14 Kinetic measurements on amino polymer films. Films were switched between 0 and +1.0 V.

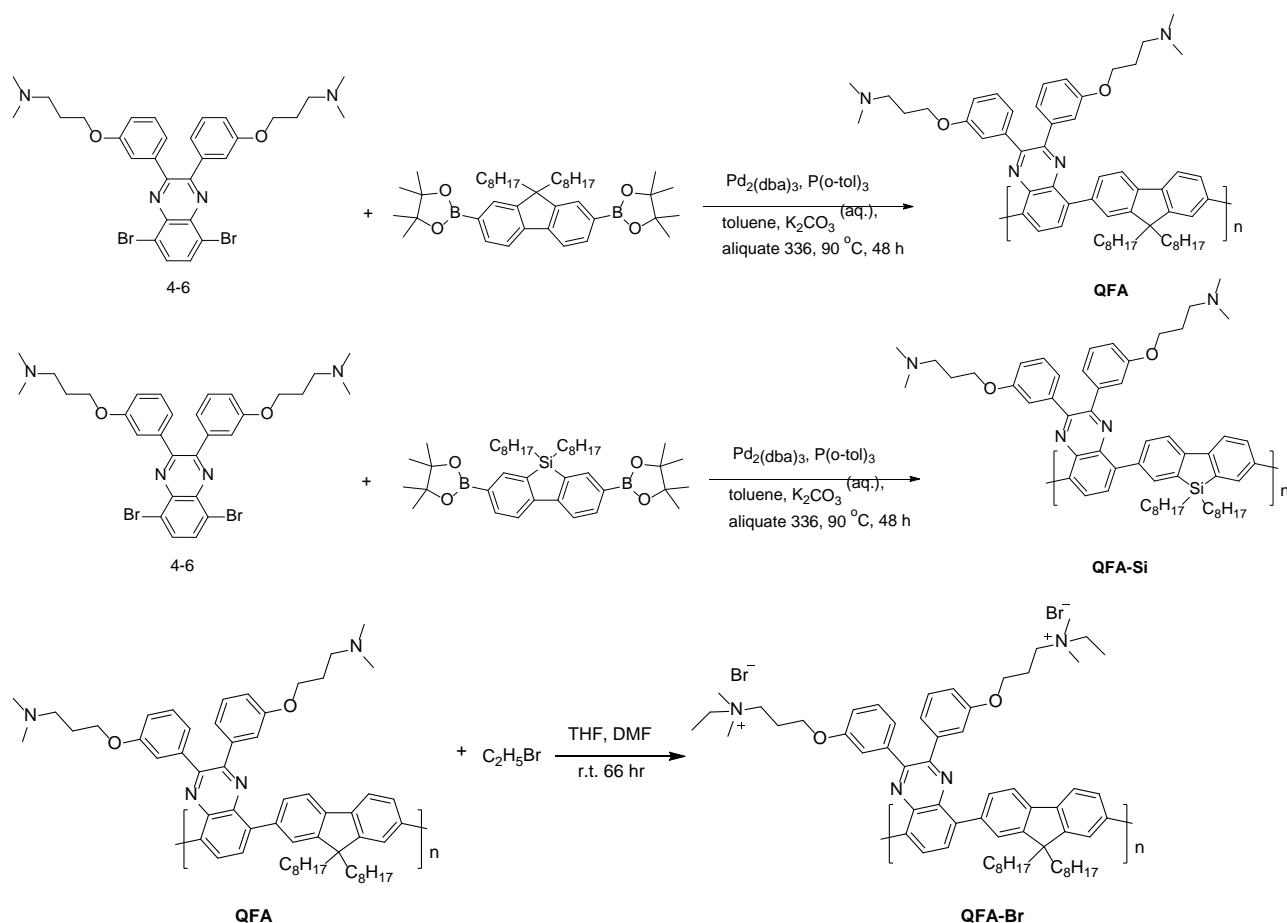
It is disappointing to find that after the first oxidation was performed to chloroform processed TQ1A film, no returning in transmittance was observed, which is possibly a result from the positive charge trap generating from amino groups.²⁴ The methanol processed TQ1A film shows the fast response times with 15% of the transmittance modulation maintained at 0.5 s switching duration. The reason for the improvement in the switching reversibility is still unclear. Comparing the TQ1-50A films processed from different solvents, similarly fast response times were presented with 70% for chloroform and 76% for methanol of the maintained transmittance modulation at 0.5 s of the switching time. This result opens the possibility of utilising green solvent in the preparation process

of electrochromic devices. TQ1-20A and TQ1-5A displayed insufficient response compared to TQ1-50A at faster switching speed, which could be resulted from the more packed film morphology impeding the ion transport during oxidation.⁴⁵

5.7. Interface materials with amino side groups.

It has been reported that conjugated polymers with amino side groups are interesting candidates for cathode interface layer due to their ability to modify the work function of electrode and superb processibility using green solvents, i.e. ethanol (EtOH) and water.^{1, 8, 27} New polymers were synthesised coupling the amine modified quinoxaline and fluorene, and optical, electrochemical as well as photovoltaic properties were studied.

5.7.1. Suzuki coupling polymerisation



Scheme 5.3 Suzuki coupling copolymerisation to synthesis polymer QFA and QFA-Si. Quaternization of QFA to synthesis QFA-Br.

TQ1A monomer **4-6** was reacted with fluorene monomers via Suzuki cross-coupling polymerisation to afford light green polymer QFA (43.9%) and QFA-Si, respectively, shown in **Scheme 5.3**. The polymerisation to synthesise QFA-Si only obtained less than 10% yield. The structure design of the polymer QFA and QFA-Si is aiming at green solvent processable cathode interface material. The tertiary amine side groups make these two polymers being soluble in ethanol in the presence of a

small amount of volatile acid, similarly to TQ1A. Quaternization of polymer QFA were performed by reacting QFA with excess of bromoethane in THF/DMF solvent blend at room temperature to afford QFA-Br, which showed remarkable solubility in ethanol but is insoluble in halogenated solvent. Hence, the solubility of QFA-Br realised the orthogonal solvent processibility in organic solar device fabrication.^{1, 4} The detailed synthesis procedure can be found in **Appendix A**.

5.7.2. Optical and electrochemical properties

The UV-vis spectra and photoluminescence (PL) spectra of QFA and QFA-Si in the solid state are shown in **Figure 5.15a and b**.

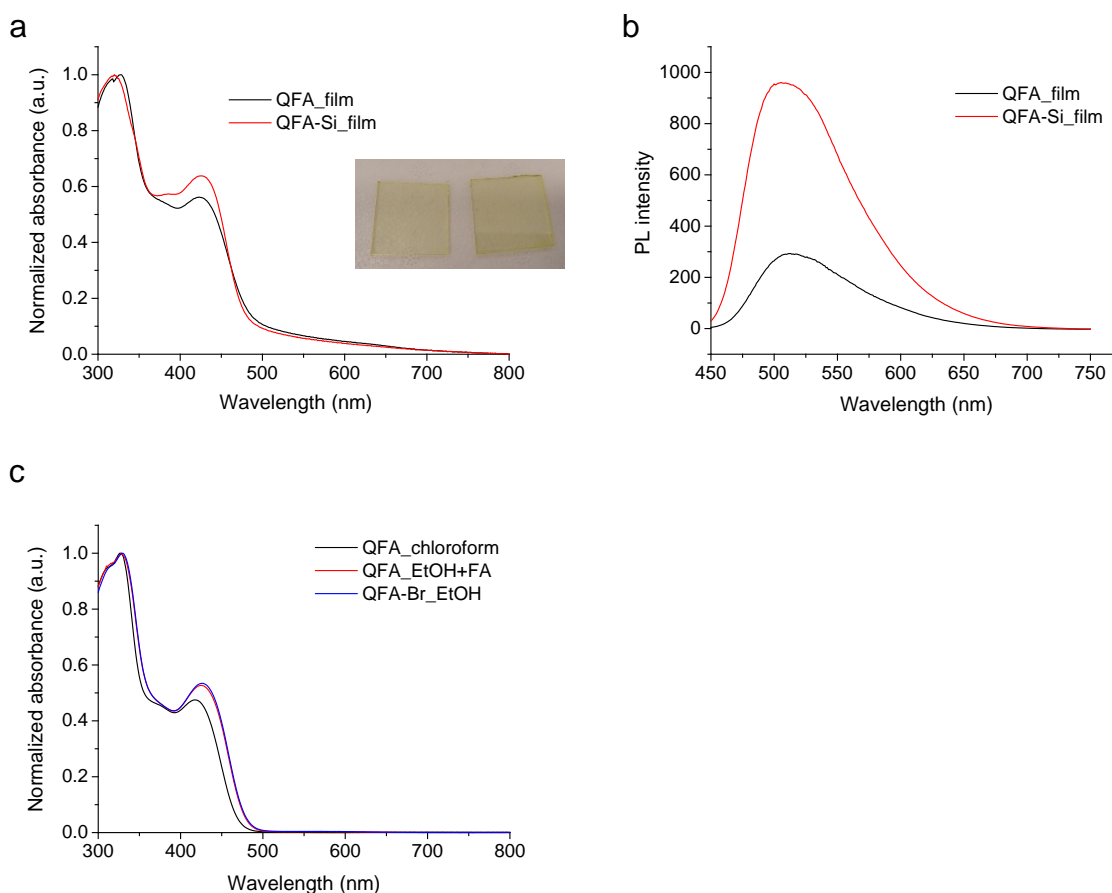


Figure 5.15 Normalized UV-vis absorbance spectra and (b) PL spectra of polymer films from QFA and QFA-Si, respectively. (c) Normalized UV-vis absorbance spectra of QFA in different solvent and QFA-Br ethanol solution.

Both QFA and QFA-Si have absorption peak at high-energy region, which is attributed to the delocalized π - π^* transitions in polymer chains. With silicon atom replacing carbon in the fluorene unit in the polymer backbone, PL intensity of QFA-Si at the peak of emission spectra is much higher compared to the intensity of QFA, which was possibly resulted from the difference of molecular weight and crystallinity in these polymers. The bathochromic shift of QFA in acidified ethanol solution (**Figure 5.15c**) compared to the chloroform one was possibly attributed to the multi-chain aggregation of polymers in ethanol, similar spectrum was also found in QFA-Br ethanol solution.

The oxidation and reduction potentials of QFA and QFA-Si were measured by CV, giving the value $E_{ox}^{onset} = 0.74$ V, $E_{red}^{onset} = -1.58$ V vs Fc/Fc⁺ for QFA and $E_{ox}^{onset} = 1.01$ V, $E_{red}^{onset} = -1.45$ V vs Fc/Fc⁺ for QFA-Si. Based on the formula $E_{HOMO} = -(E_{ox}^{onset} + 5.13)$ eV, $E_{LUMO} = -(E_{red}^{onset} + 5.13)$ eV, HOMO and LUMO level energy of polymer QFA and QFA-Si are listed in **Table 5.12** below. The large bandgap and deep lying HOMO levels of these two polymers indicates the potential of utilising QFA or QFA-Si as a cathode interlayer in OPVs. However, the superb solubility of QFA in commonly used halogenated solvent resulted in the solvent erosion problem during the fabrication of inverted solar cells, in which QFA was applied as an electron transport layer in between ITO and BHJ layer. Hence, QFA-Br with quaternary amine side groups was used as an alternative of QFA in the device fabrication process.

Table 5.12 Optical and electrochemical properties of QFA and QFA-Si.

Polymers	λ_{max}^f (nm)	λ_{onset} (nm)	E_g^{opt} (eV)	E_g^{cv} (eV)	E_{HOMO} (eV)	E_{LUMO} (eV)
QFA	328 424	491	2.53	2.32	-5.87	-3.55
QFA-Si	320 427	489	2.54	2.46	-6.14	-3.68

Furthermore, due to the difficulty of CV measurement resulted from the ammonium-functionalized QFA-Br being soluble in the used electrolyte, Ultraviolet photoelectron spectroscopy (UPS) and inverse photoelectron spectroscopy (IPES) measurements were performed on QFA-Br film to probe the HOMO and LUMO energy level of the quaternary amine polymer. The UPS and IPES spectra are shown in **Figure 5.16**, where IP is the ionization potential and EA is the electron affinity. Hence, HOMO and LUMO energy levels as well as the bandgap calculated by $E_{LUMO} - E_{HOMO}$ are estimated and listed in **Table 5.13**. It is worth to note that the UPS and IPES probes the electronic energy state of the material surface, while CV measures the bulk property. Therefore, the energy level of QFA measured by CV is not comparable to that of QFA-Br, which is analysed by photoelectron spectroscopy.

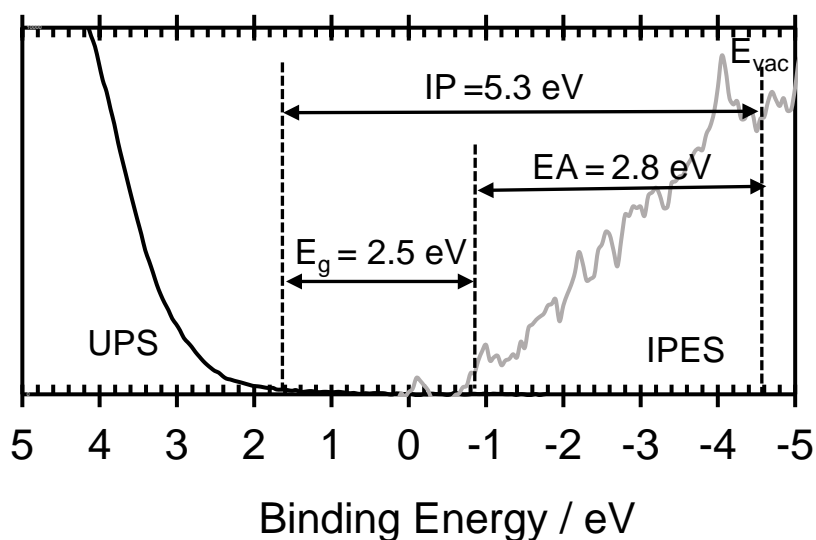


Figure 5.16 UPS and IPES spectra of QFA-Br.

Table 5.13 Electronic properties of QFA-Br measured by UPS and IPES.

Polymers	E_g (eV)	E_{HOMO} (eV)	E_{LUMO} (eV)
QFA-Br	2.5	-5.3	-2.8

UPS measurement was also performed on thin layer of QFA-Br coated ITO-glass to investigate the work function modification of ITO surface. **Figure 5.17** shows the vacuum level shift in the secondary electron cutoff in the UPS spectra of QFA-Br coated ITO, revealing the work function modification of ITO by QFA-Br. Compared to pure ITO-glass, which has the work function of 4.6 eV, QFA-Br significantly reduced the work function to 3.5 eV. The work function modification is attributed to the presence of nitrogen and Br^- in the quaternary amine pendent groups inducing dipole formation at the interface of amine-based material and ITO²⁸, which is also reported by other researchers.^{1,4}

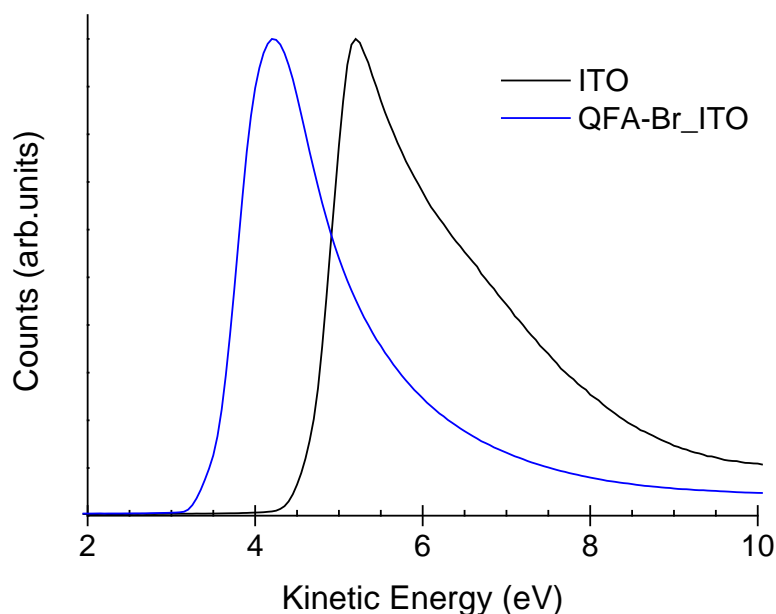


Figure 5.17 UPS spectra of ITO and thin layer of QFA-Br coated ITO.

5.7.3. Device performance

QFA-Br was successfully applied as an electron transport layer in the inverted OPVs with PTB7-Th:PC₇₁BM⁴⁶ as the active layer, which achieved decent photovoltaic performance. The device characteristics are shown in **Table 5.14**. The QFA-Br layer was processed from ethanol, while active layer was spin-coated from *o*-DCB with 3% 1,8-diiodooctane.

Table 5.14 Device performance of PTB7-th:PC₇₁BM devices with QFA-Br as electron transport layer and buffer layer.

ETL	J_{sc} (mA/cm ²)	FF (%)	V_{oc} (V)	PCE (%)
QFA-Br	17.13	48	0.79	6.52
ZnO:QFA-Br	16.76	53	0.79	7.08

device structure: ITO/ETL/PTB7-th:PC₇₁BM/MoO_x/Ag.

5.8. Experimental

5.8.1. Materials

All reactions were performed under nitrogen protection unless otherwise stated. Chemicals were commercially available from Sigma-Aldrich and used without further purification. 5,8-Dibromo-2,3-bis(3-(octyloxy)phenyl)quinoxaline and 2,5-bis(trimethylstannyl)thiophene were purchased from Solarmer Energy, Inc., and the latter was purified by recrystallisation from methanol. All solvents were used as obtained from supplier except toluene, which was dried and distilled prior to the

polymerisation reactions. The structures of the small molecular compounds synthesised were confirmed by ¹H-NMR spectra measured on Bruker 300 MHz NMR spectrometer. Detailed synthesis procedures can be found in **Appendix A**.

The OEG modified quinoxaline (**5-4**) and 5,8-dibromo-2,3-bis(3-(diethylamino)hexyloxy)phenyl)quinoxaline (**5-1**) were synthesised in our lab by a previous group member Desta.

5.8.2. Material characterisation

Gel-permeation chromatography (GPC) measurements were performed at 35 °C on an Agilent PL-GPC 220 equipped with a differential refractive index detector. Dimethylformamide (DMF) was used as eluent at a flow rate of 1.0 mL/min, and the solvent DMF as well as sample solutions were filtered through a filter with the pore size of 0.45 µm (Nylon, Millex-HN 13 mm Syringes Filters, Millipore, US). The number average molecular weights (M_n) and polydispersity index (PDI) were calculated using a calibration curve based on polyethylene glycol (PEG) standards.

Cyclic voltammetry (CV) measurements were performed using a 0.1 M solution of tetrabutylammonium hexafluorophosphate (Bu₄NPF₆) in anhydrous acetonitrile as the supporting electrolyte and a Ag/Ag⁺ quasi reference electrode. The ferrocene/ferrocenium (Fc/Fc⁺) reference was used to calibrate the measurements. The highest occupied molecular orbital energy levels (E_{HOMO}) and the lowest unoccupied molecular orbital energy levels (E_{LUMO}) were estimated from the onset potentials by setting the oxidative potential of Fc/Fc⁺ vs. the normal hydrogen electrode (NHE) to 0.630 V, and the NHE vs. the vacuum level to 4.5 V.⁴⁷⁻⁴⁸

The room temperature ultraviolet-visible (UV-vis) study was performed on a Perkin Elmer UV-vis-NIR Lambda950 spectrophotometer.

Varied temperature UV-vis study was performed on a Cary 60 UV-vis spectrophotometer (Agilent Technologies) with a heating block attached to the cuvette holder.

The photoluminescence (PL) measurements were performed on a Varian Cary Eclipse fluorescence spectrophotometer at the excitation wavelength of 550 nm for polymer TQ6A and 450 nm for polymer QFA and QFA-Si.

Thermal gravimetric analysis (TGA) measurements were performed on TA instruments Discovery TGA series TGA1-0288, with the temperature range of 25 - 400°C under nitrogen gas flow, and the heating ramp of 10 °C/min.

Water contact angle measurements were performed using a PAT-1 tensiometer supplied by Sinterface Technologies (Berlin, Germany). The contact angle values are average values measured on 4 different spots on the same film.

Dynamic mechanical thermal analysis (DMTA) samples were prepared by repeatedly drop-casting the TQ-OEG or TQ1 chloroform solution onto a 20-30 mm long, approximately 5 mm wide piece of glass fibre mesh, as described elsewhere²⁰, followed by drying under ambient condition until a uniformly fully covered film on the glass mesh was obtained. The samples were stored in a vacuum oven overnight to remove the solvent before performing DMTA measurements. DMTA measurements were carried out on a TA Q800 DMA in strain-controlled mode at a frequency of 1 Hz and an amplitude of 5 μm . The samples were measured under a continuous flow of nitrogen gas with a heating rate of 3 $^{\circ}\text{C}$ per minute. The first run was performed from room temperature up to 80 $^{\circ}\text{C}$ for further drying the sample, followed by a second run from -110 $^{\circ}\text{C}$ to 300 $^{\circ}\text{C}$. The data from the second run was utilised to study thermomechanical properties of polymer TQ-OEG in this study.

Differential scanning calorimetry (DSC) measurements were performed on Discovery DSC from TA instrument, with temperature range -20-300 $^{\circ}\text{C}$, heating/cooling ramp 10 $^{\circ}\text{C}/\text{min}$ under nitrogen gas flow. The sample to be measured was prepared by drop casting a TQ1-5A:PC₆₁BM or TQ1: PC₆₁BM solution (chloroform blended with *o*-DCB) on a freshly cleaned glass slide followed by solvent evaporation before the solid mixture being removed collected using a scalpel. The sample was dried in a vacuum oven overnight prior to the DSC measurement.

Atomic force microscopy (AFM) (supplied by Bruker, Billerica, MA) was performed in tapping mode using silicon tips. The films were spin-coated from the polymer:PCBM or polymer:PCBDAN blend solution on freshly cleaning ITO-glass. SV annealing was conducted by keeping the polymer:PCBM blend films in a closed desiccator for 2 hours. The annealed samples were then dried in a vacuum oven at r.t. overnight before AFM measurement.

Ultraviolet photoelectron spectroscopy (UPS) measurements were performed under an ultra-high vacuum (UHV) apparatus build by SPECS (Berlin, Germany) using a low intensity UV light source (HeI) with an excitation energy of 21.21 eV, to measure the work functions as described elsewhere.⁴ The UPS samples were prepared by spin-coating polymer solution on to a silicon substrate to form polymer films.

5.8.3. Device fabrication

ITO-coated glass substrates were cleaned by soaking in a 5% detergent solution (pyroneg from Johnson Diversey) at 90 $^{\circ}\text{C}$ for 20 minutes and then rinsing in deionized (DI) water, before sonicating in DI water, acetone and isopropanol for 10 min each. Substrates were then cleaned in UV-ozone for 20 minute prior to the deposition of different interlayers.

Inverted device with the structure of (a) ITO/ZnO/BHJ/MoO_x/Ag, (b) ITO/ZnO/BHJ/TPD/MoO_x/Ag, (c) ITO/ZnO/PEI/BHJ/TPD/MoO_x/Ag and (d) ITO/ZnO/PEIE/BHJ/TPD/MoO_x/Ag for TQ1A containing BHJ OPVs, the ZnO layer was prepared by spin-coating the ZnO sol-gel⁴⁹ on the cleaned ITO substrate, followed by thermal annealing at 280 $^{\circ}\text{C}$ for 10 minute in air to yield a 25 - 30 nm thick

film. The BHJ layers were deposited in a glove-box by spin-coating TQ1A:PC₆₁BM/PC₇₁BM (1:2.5 weight ratio), or TQ1:TQ1A:PC₇₁BM (4:1:12.5) *o*-DCB solution (25 mg/mL) on ZnO coated ITO-glass. MoO₃ (12 nm) was thermally evaporated (using a Covap system supplied by Angstrom Engineering) on top of the active layer to serve as a hole transporting layer. In the case of TPD being introduced in the device, a TPD buffer layer (3 nm) was thermally evaporated on top of the BHJ layer at 2×10⁻⁶ torr before the deposition of MoO₃. In the case of PEI and PEIE being used in the device fabrication, PEI or PEIE layer was deposited by spin-coating PEI (0.4 mg/mL) or PEIE (0.4 mg/mL) 2-methoxyethanol solution respectively at 5000 rpm for 1 min, prior to the evaporation of MoO₃. Finally the Ag electrode (80 nm) was deposited by thermally evaporating through a shadow mask, which defined the active area to be 0.1 cm².

Device with the structure of (a) ITO/ZnO/BHJ/MoO_x/Ag, (b) ITO/ZnO/BHJ/TPD/MoO_x/Ag for TQP3 or TQ-OEG based OPVs were fabricated follow procedures described above. The BHJ layers were deposited in a glove-box by spin-coating TQ1P3:PC₆₁BM (1:2.5) anisole solution (35 mg/mL), or TQ-OEG:PC₆₁BM (1:2.5) *o*-DCB solution (29.4 mg/mL) on to ZnO interface layer coated ITO-glass.

Conventional device with the structure of (e) ITO/MoO_x/BHJ/LiF/Al, (f) ITO/MoO_x/TPD/BHJ/LiF/Al, (g) ITO/MoO_x/BHJ/C₆₀/LiF/Al, (h) ITO/MoO_x/TPD/BHJ/LiF/Al and ITO/MoO_x/PVK/BHJ/LiF/Al for TQ1A containing BHJ OPVs were fabricated by first thermally evaporating MoO₃ (12 nm) on pre-cleaned ITO substrates. In the case of TPD being used, a TPD buffer layer (3 nm) was thermally evaporated on top of the MoO_x prior to the deposition of the active layer. In the case of PVK being applied as an anode buffer layer, a thin layer of PVK was spin-coated from 0.9 mg/mL PVK solution using a blend solvents of THF:acetone (7:4 volume ratio) at 5000 rpm for 1 min. Then the active layers were spin-coated from TQ1A:PC₆₁BM/PC₇₁BM (1:2.5) or TQ1: PC₆₁BM (1:2.5) *o*-DCB solution (25 mg/mL) on top of MoO_x, or TPD, or PVK layer. LiF (~1nm) layer was thermally evaporated on top of the BHJ layer followed by thermally evaporating Al (80 nm) electrode through a shadow mask, which defined the active area to be 0.1 cm². In the case of C₆₀ was used, 10 nm of C₆₀ layer was thermally evaporated on top of active layer before the deposition of LiF.

Inverted device with the structure of ITO/ETL/PTB7-th:PC₇₁BM/MoO_x/Ag was fabricated follow the described procedure above in the case of the deposition of ZnO and MoO_x layer and the Ag electrode. The QFA-Br layer was spin-coated from QFA ethanol solution (1 mg/mL) at 3000 rpm for 1 min on the ITO or ZnO coated ITO. The active layer was spin coated from 25 mg/mL PTB7-th:PC₇₁BM (1:1.5 weight ratio) chlorobenzene solution (containing 3% 1,8-diiodooctane) at 2000 rpm for 1 min.

5.8.4. Device characterisation

Photovoltaic properties of solar cells were measured in air by an Oriel solar simulator fitted with a 150 W xenon lamp (Newport), filtered to give an irradiation of 100 mW/cm² at an atmospheric mass (AM) of 1.5 and calibrated using a silicon reference cell with NIST traceable certification. The

photocurrent–voltage (I-V) characteristics of the devices were measured through a Keithley 2400 source meter unit.

5.9. Conclusions

A series of polymers were synthesised with tertiary amine and quaternary amine functional side groups, which endows the green solvent solubility for most of the new polymers. Side chain engineering has been proven to be an efficient tool to modify the polymer structure, and water/ethanol soluble polymer TQ1P3 was successfully synthesised using pyridine polar side chain. By introducing OEG side groups, TQ-OEG was synthesised that showed remarkably solubility in ethanol. The TGA measurements performed on amine, pyridine or OEG functionalized polymers revealed their decent thermal stability, which is crucial for the long term stability of OPVs. The morphology of amino polymer:PCBM blend films was investigated, and insufficient phase separation was found in TQ1A:PCBM film, which is part of the reasons for the low PCE of TQ1A based OPVs. The other reasons of unsatisfactory photovoltaic performance in TQ1A containing OPVs could be strong charge recombination and is still under investigation. The opto-electronic properties of the new amino polymers were systematically studied, showing the potential of fabricating electrochromic devices using green solvent. The ethanol soluble polymer QFA-Br presented promising results when applied as a cathode interface layer in the inverted solar cells, resulting from the remarkable reduction of the ITO work function. In future, by incorporating with water/ethanol soluble acceptor materials, we can realise the environment-friendly fabrication of OPVs using truly green solvent.

Author contribution:

Xun Pan: Performed all the synthesis presented in this chapter and most characterisation of polymers, part of the device fabrication & testing, data analysis and interpretation.

Dr. Anirudh Sharma: Performed UPS characterisation and part of the device fabrication & testing.

Dr. Renee Kroon: Synthesised PCBDAN.

Dr. Desta Gedefaw: synthesised two quinoxaline monomers for TQ6A and TQ-OEG.

Dr. Armantas Melianas and Dr. Zheng Tang: Performed FTPS measurement.

Kim Bini: Performed electrochemical and Spectroelectrochemical measurements.

5.10. References

1. Wu, Z.; Sun, C.; Dong, S.; Jiang, X. F.; Wu, S.; Wu, H.; Yip, H. L.; Huang, F.; Cao, Y., n-Type Water/Alcohol-Soluble Naphthalene Diimide-Based Conjugated Polymers for High-Performance Polymer Solar Cells. *Journal of the American Chemical Society* **2016**, *138* (6), 2004-13.
2. Park, K.-Y.; Lee, J.-S.; Namkung, H.-S.; Koo, M.-S.; Cho, S.-J.; Yoon, B.-W.; Kim, Y.-M.; Lee, Y.-S.; Song, S.-H.; Park, D.-K.; Kim, C.-G., Enhanced Performance in Bulk Heterojunction Polymer Solar Cell Using Water Soluble Conjugated Polymer. *Journal of Nanoscience and Nanotechnology* **2015**, *15* (2), 1683-1686.
3. Zhao, K.; Ye, L.; Zhao, W.; Zhang, S.; Yao, H.; Xu, B.; Sun, M.; Hou, J., Enhanced efficiency of polymer photovoltaic cells via the incorporation of a water-soluble naphthalene diimide derivative as a cathode interlayer. *Journal of Materials Chemistry C* **2015**, *3* (37), 9565-9571.
4. Sharma, A.; Kroon, R.; Lewis, D. A.; Andersson, G. G.; Andersson, M. R., Poly(4-vinylpyridine): A New Interface Layer for Organic Solar Cells. *ACS Applied Materials & Interfaces* **2017**, *9* (12), 10929-10936.
5. Zappia, S.; Scavia, G.; Ferretti, A. M.; Giovanella, U.; Vohra, V.; Destri, S., Water-Processable Amphiphilic Low Band Gap Block Copolymer: Fullerene Blend Nanoparticles as Alternative Sustainable Approach for Organic Solar Cells. *Advanced Sustainable Systems* **2018**, 1700155.
6. George, Z.; Xia, Y.; Sharma, A.; Lindqvist, C.; Andersson, G.; Inganäs, O.; Moons, E.; Müller, C.; Andersson, M. R., Two-in-one: cathode modification and improved solar cell blend stability through addition of modified fullerenes. *Journal of Materials Chemistry A* **2016**, *4* (7), 2663-2669.
7. Mei, J.; Bao, Z., Side Chain Engineering in Solution-Processable Conjugated Polymers. *Chemistry of Materials* **2013**, *26* (1), 604-615.
8. Hu, Z.; Zhang, K.; Huang, F.; Cao, Y., Water/alcohol soluble conjugated polymers for the interface engineering of highly efficient polymer light-emitting diodes and polymer solar cells. *Chemical Communications* **2015**, *51* (26), 5572-85.
9. Nguyen, T. L.; Lee, C.; Kim, H.; Kim, Y.; Lee, W.; Oh, J. H.; Kim, B. J.; Woo, H. Y., Ethanol-Processable, Highly Crystalline Conjugated Polymers for Eco-Friendly Fabrication of Organic Transistors and Solar Cells. *Macromolecules* **2017**, *50* (11), 4415-4424.
10. He, Z.; Wu, H.; Cao, Y., Recent Advances in Polymer Solar Cells: Realization of High Device Performance by Incorporating Water/Alcohol-Soluble Conjugated Polymers as Electrode Buffer Layer. *Advanced Materials* **2014**, *26* (7), 1006-1024.
11. Wang, E.; Hou, L.; Wang, Z.; Hellstrom, S.; Zhang, F.; Inganäs, O.; Andersson, M. R., An easily synthesized blue polymer for high-performance polymer solar cells. *Advanced Materials* **2010**, *22* (46), 5240-4.
12. Dang, D.; Chen, W.; Himmelberger, S.; Tao, Q.; Lundin, A.; Yang, R.; Zhu, W.; Salleo, A.; Müller, C.; Wang, E., Enhanced Photovoltaic Performance of Indacenodithiophene-Quinoxaline Copolymers by Side-Chain Modulation. *Advanced Energy Materials* **2014**, *4* (15), 1400680.
13. Espinet, P.; Echavarren, A. M., The mechanisms of the Stille reaction. *Angewandte Chemie International Edition in English* **2004**, *43* (36), 4704-34.
14. Espinet, P.; Echavarren, A. M., The mechanisms of the Stille reaction. *Angewandte Chemie International Edition* **2004**, *43* (36), 4704-4734.
15. Skotheim, T. A.; Reynolds, J., *Conjugated polymers: theory, synthesis, properties, and characterization*. CRC press: 2006.
16. Kroon, R.; Gehlhaar, R.; Steckler, T. T.; Henriksson, P.; Müller, C.; Bergqvist, J.; Hadipour, A.; Heremans, P.; Andersson, M. R., New quinoxaline and pyridopyrazine-based polymers for solution-processable photovoltaics. *Solar Energy Materials & Solar Cells* **2012**, *105*, 280-286.
17. Tessarolo, M.; Guerrero, A.; Gedefaw, D.; Bolognesi, M.; Prosa, M.; Xu, X.; Mansour, M.; Wang, E.; Seri, M.; Andersson, M. R.; Muccini, M.; Garcia-Belmonte, G., Predicting thermal stability of organic solar cells through an easy and fast capacitance measurement. *Solar Energy Materials and Solar Cells* **2015**, *141*, 240-247.
18. Bini, K.; Xu, X.; Andersson, M. R.; Wang, E., Synthesis and Characterization of Isoindigo-Based Polymers with Thermocleavable Side Chains. *Macromolecular Chemistry and Physics* **2018**, 1700538.

19. Diaz de Zerio Mendaza, A.; Melianas, A.; Nugroho, F. A. A.; Bäcke, O.; Olsson, E.; Langhammer, C.; Inganäs, O.; Müller, C., A fullerene alloy based photovoltaic blend with a glass transition temperature above 200 °C. *Journal of Materials Chemistry A* **2017**, *5* (8), 4156-4162.
20. Sharma, A.; Pan, X.; Campbell, J. A.; Andersson, M. R.; Lewis, D. A., Unravelling the Thermomechanical Properties of Bulk Heterojunction Blends in Polymer Solar Cells. *Macromolecules* **2017**, *50* (8), 3347-3354.
21. Li, S.; Lei, M.; Lv, M.; Watkins, S. E.; Tan, Z. a.; Zhu, J.; Hou, J.; Chen, X.; Li, Y., [6,6]-Phenyl-C61-Butyric Acid Dimethylamino Ester as a Cathode Buffer Layer for High-Performance Polymer Solar Cells. *Advanced Energy Materials* **2013**, *3* (12), 1569-1574.
22. Ma, D.; Lv, M.; Lei, M.; Zhu, J.; Wang, H.; Chen, X., Self-Organization of Amine-Based Cathode Interfacial Materials in Inverted Polymer Solar Cells. *ACS Nano* **2014**, *8* (2), 1601-1608.
23. Lv, M.; Lei, M.; Zhu, J.; Hirai, T.; Chen, X., [6,6]-phenyl-C(6)(1)-butyric acid 2-((2-(dimethylamino)ethyl)(methyl)amino)-ethyl ester as an acceptor and cathode interfacial material in polymer solar cells. *ACS Applied Materials & Interfaces* **2014**, *6* (8), 5844-51.
24. Duan, C.; Cai, W.; Hsu, B. B. Y.; Zhong, C.; Zhang, K.; Liu, C.; Hu, Z.; Huang, F.; Bazan, G. C.; Heeger, A. J.; Cao, Y., Toward green solvent processable photovoltaic materials for polymer solar cells: the role of highly polar pendant groups in charge carrier transport and photovoltaic behavior. *Energy & Environmental Science* **2013**, *6* (10), 3022-3034.
25. Lu, K.; Yuan, J.; Peng, J.; Huang, X.; Cui, L.; Jiang, Z.; Wang, H.-Q.; Ma, W., New solution-processable small molecules as hole-transporting layer in efficient polymer solar cells. *Journal of Materials Chemistry A* **2013**, *1* (45), 14253.
26. Kang, H.; Hong, S.; Lee, J.; Lee, K., Electrostatically self-assembled nonconjugated polyelectrolytes as an ideal interfacial layer for inverted polymer solar cells. *Advanced Materials* **2012**, *24* (22), 3005-9, 2938.
27. Xiao, B.; Wu, H.; Cao, Y., Solution-processed cathode interfacial layer materials for high-efficiency polymer solar cells. *Materials Today* **2015**, *18* (7), 385-394.
28. van Reenen, S.; Kouijzer, S.; Janssen, R. A. J.; Wienk, M. M.; Kemerink, M., Origin of Work Function Modification by Ionic and Amine-Based Interface Layers. *Advanced Materials Interfaces* **2014**, *1* (8), 1400189.
29. Zhao, F.; Wang, C.; Zhan, X., Morphology Control in Organic Solar Cells. *Advanced Energy Materials* **2018**, 1703147.
30. Cheng, Y.-J.; Yang, S.-H.; Hsu, C.-S., Synthesis of conjugated polymers for organic solar cell applications. *Chemical Reviews* **2009**, *109* (11), 5868-5923.
31. Meyer, J.; Hamwi, S.; Kroger, M.; Kowalsky, W.; Riedl, T.; Kahn, A., Transition metal oxides for organic electronics: energetics, device physics and applications. *Advanced Materials* **2012**, *24* (40), 5408-27.
32. Treat, N. D.; Chabynyc, M. L., Phase separation in bulk heterojunctions of semiconducting polymers and fullerenes for photovoltaics. *Annual Review of Physical Chemistry* **2014**, *65*, 59-81.
33. Fan, B.; Ying, L.; Wang, Z.; He, B.; Jiang, X.-F.; Huang, F.; Cao, Y., Optimisation of processing solvent and molecular weight for the production of green-solvent-processed all-polymer solar cells with a power conversion efficiency over 9%. *Energy & Environmental Science* **2017**, *10* (5), 1243-1251.
34. Liu, D.; Wang, Z.; Zhang, S.; Zheng, Z.; Yang, B.; Ma, W.; Hou, J., Rational selection of solvents and fine tuning of morphologies toward highly efficient polymer solar cells fabricated using green solvents. *RSC Advances* **2015**, *5* (85), 69567-69572.
35. Derue, L.; Lecourtier, C.; Gorisse, T.; Hirsch, L.; Dautel, O.; Wantz, G., A solvent additive to enhance the efficiency and the thermal stability of polymer:fullerene solar cells. *RSC Advances* **2015**, *5* (5), 3840-3843.
36. Hodgkiss, J. M.; Albert-Seifried, S.; Rao, A.; Barker, A. J.; Campbell, A. R.; Marsh, R. A.; Friend, R. H., Exciton-Charge Annihilation in Organic Semiconductor Films. *Advanced Functional Materials* **2012**, *22* (8), 1567-1577.
37. Li, Z.; Xu, X.; Zhang, W.; Meng, X.; Ma, W.; Yartsev, A.; Inganäs, O.; Andersson, M. R.; Janssen, R. A.; Wang, E., High Performance All-Polymer Solar Cells by Synergistic Effects of Fine-Tuned Crystallinity and Solvent Annealing. *Journal of the American Chemical Society* **2016**, *138* (34), 10935-44.

38. Guan, Z.; Li, H.-W.; Cheng, Y.; Yang, Q.; Lo, M.-F.; Ng, T.-W.; Tsang, S.-W.; Lee, C.-S., Charge-Transfer State Energy and Its Relationship with Open-Circuit Voltage in an Organic Photovoltaic Device. *The Journal of Physical Chemistry C* **2016**, *120* (26), 14059-14068.
39. Deibel, C.; Strobel, T.; Dyakonov, V., Role of the charge transfer state in organic donor-acceptor solar cells. *Advanced Materials* **2010**, *22* (37), 4097-4111.
40. Vanecek, M.; Poruba, A., Fourier-transform photocurrent spectroscopy of microcrystalline silicon for solar cells. *Applied Physics Letters* **2002**, *80* (5), 719-721.
41. Vandewal, K.; Tvingstedt, K.; Gadisa, A.; Inganäs, O.; Manca, J. V., Relating the open-circuit voltage to interface molecular properties of donor:acceptor bulk heterojunction solar cells. *Physical Review B* **2010**, *81* (12).
42. Hellström, S.; Henriksson, P.; Kroon, R.; Wang, E.; Andersson, M. R., Blue-to-transmissive electrochromic switching of solution processable donor-acceptor polymers. *Organic Electronics* **2011**, *12* (8), 1406-1413.
43. Verswyvel, M.; Koeckelberghs, G., Chirality in conjugated polymers: when two components meet. *Polymer Chemistry* **2012**, *3* (12), 3203.
44. de Leeuw, D. M.; Simenon, M. M. J.; Brown, A. R.; Einerhand, R. E. F., Stability of n-type doped conducting polymers and consequences for polymeric microelectronic devices. *Synthetic Metals* **1997**, *87* (1), 53-59.
45. Xing, X.; Zeng, Q.; Vagin, M.; Fahlman, M.; Zhang, F., Fast Switching Polymeric Electrochromics with Facile Processed Water Dispersed Nanoparticles. *Nano Energy* **2018**.
46. Chen, J. D.; Cui, C.; Li, Y. Q.; Zhou, L.; Ou, Q. D.; Li, C.; Li, Y.; Tang, J. X., Single-junction polymer solar cells exceeding 10% power conversion efficiency. *Advanced Materials* **2015**, *27* (6), 1035-41.
47. Hellström, S.; Zhang, F.; Inganäs, O.; Andersson, M. R., Structure-property relationships of small bandgap conjugated polymers for solar cells. *Dalton Transactions* **2009**, (45), 10032-10039.
48. Gedefaw, D.; Sharma, A.; Pan, X.; Bjuggren, J. M.; Kroon, R.; Gregoriou, V. G.; Chocho, C. L.; Andersson, M. R., Optimization of the power conversion efficiency in high bandgap pyridopyridinedithiophene-based conjugated polymers for organic photovoltaics by the random terpolymer approach. *European Polymer Journal* **2017**, *91*, 92-99.
49. Sun, Y.; Seo, J. H.; Takacs, C. J.; Seifert, J.; Heeger, A. J., Inverted polymer solar cells integrated with a low-temperature-annealed sol-gel-derived ZnO Film as an electron transport layer. *Advanced Materials* **2011**, *23* (14), 1679-83.

6. Chapter Six - Water Processable Conjugated Nanoparticles for OPVs

6.1. Introduction

OPVs with active layers deposited from water or alcohol dispersed nanoparticles (NPs) have been reported recently, which overcome the solubility bottleneck of conjugated polymers and fullerene derivatives in water or ethanol for green fabrication.¹⁻⁴ To form NPs from donor-acceptor material blends, generally two methods have been employed, which are miniemulsion method⁵ and precipitation method.⁶ The NPs prepared using miniemulsion method show excellent reproducibility and stability, which are supreme for up-scaling the fabrication of OPVs without using harmful organic solvent for active layer deposition. Furthermore, NPs made from photoactive materials expand the candidates of materials that can be deposited as active layer from green solvents.

In this chapter, the parameters in the procedure of making NPs have been studied to understand their influences on the particle size and NP-OPV devices. Different miniemulsion dispersed phase solvents and solvent additive have been utilised in the preparation of nanoparticles to study the photovoltaic performance of OPVs based on NP forming active layers.

To achieve efficiently working solar cells with NP as active layer, the coalescence of NPs in the solid state to form homogenous film is essential. Different methods were investigated to compare their effectiveness in coalescing particles and the quality of treated films.

To eliminate the unwanted effect of sodium dodecyl sulphate (SDS) on OPVs, which is caused by the mobile ionic species, water/alcohol-soluble functionalized conjugated polymers and fullerene derivatives are used to successfully prepare aqueous NP dispersion through miniemulsion method in the absence of SDS. Besides functionalized conjugated materials, alternative ionic surfactants as well as non-ionic surfactants to avoid the influence of ions were studied to understand their feasibility to help the formation of miniemulsion and to stabilize NPs from active materials. Moreover, efforts have been put in to remove SDS in the final NP dispersion or reduce the SDS concentration post preparation of NPs stabilized with SDS.

The precipitation method was studied on different conjugated systems to obtain water/alcohol dispersed particles. Parameters in the preparation procedure were adjusted aiming to achieve stable NP inks with high solid loading for OPVs. An inclusion of extra stabilizing agent has been presented, and NPs formed have been characterised, showing the potential to optimise the preparation procedure of NP via precipitation method.

6.2. Parameters in the preparation procedure and their influence in the particle size and photovoltaic performance

The ultimate goal to prepare NPs from photoactive material blend is to apply NPs in an active layer, which can be considered as a nano-BHJ layer in a solar device. Compared to traditional BHJ films directly processed from organic solvent, of which the morphology is influenced by processing solvent⁷ and post-treatment,⁸ the morphology of NP forming film is not only dependent on the post-treatment of cast film⁹⁻¹⁰ but also affected by the size and nanomorphology of the NPs.¹¹ Suppression of the size of NPs would theoretically result in less pin holes in the films and smaller donor and acceptor domains, which is beneficial for efficient exciton diffusion to the donor-acceptor interface. Hence, the parameters in the NP preparation procedure needs to be studied to find out the knowhow to achieve ideal NP size.

The utilisation of miniemulsion method to prepare NPs is not a straightforward technique and involves several steps, among which the formation of miniemulsion is the key procedure. The parameters in the formation of miniemulsion that can be varied includes: concentration of surfactant, miniemulsion dispersed phase solvent, concentration of active materials in organic phase, ratio of organic solvent to water and power used to form miniemulsion. However, due to the limited time the influence of the ratio between organic solvent and water was not studied.

6.2.1. The influence of initial SDS concentration on particle size

One important property of surfactants is their critical micelle concentration (CMC), above which micelles start forming and the concentration of free surfactant in an aqueous solution remains constant.¹² SDS has been widely studied and commonly used in the preparation of NPs for OPVs, the CMC value of which at 25 °C is approximate 8.0 mM.¹³ Hence, in order to achieve stable aqueous NPs through miniemulsion method, the concentration of SDS in the miniemulsion is required to be above 8.0 mM. Colberts et al. reported that the when the initial concentration of SDS was increased from 10.2 mM to 41.2 mM, the size of NPs prepared from a donor polymer and PCBM blend showed the reduction accordingly.¹⁴

When controlling the other experimental parameters to be exactly the same, we found that the size of TQ1:PC₇₁BM NPs was measured to be 153 ± 52 nm when initial concentration of SDS used in the miniemulsion was 1.0 mM, which decreased to 37 ± 7 nm when the concentration of SDS was increased to 34.1 mM. The SEM images of TQ1:PC₇₁BM NPs prepared with these two different concentrations of SDS were shown in **Figure 6.1**. Since the size of NPs is crucial for high performing OPVs based on NP active layer, the result showing in **Figure 6.1b** presents small NPs ideal for solar cell fabrication. What's more, to gain better understanding of other parameters in the NPs preparation, the initial concentration of SDS in the miniemulsion is controlled to be 34.1 mM for all NP studies discussed in this chapter.

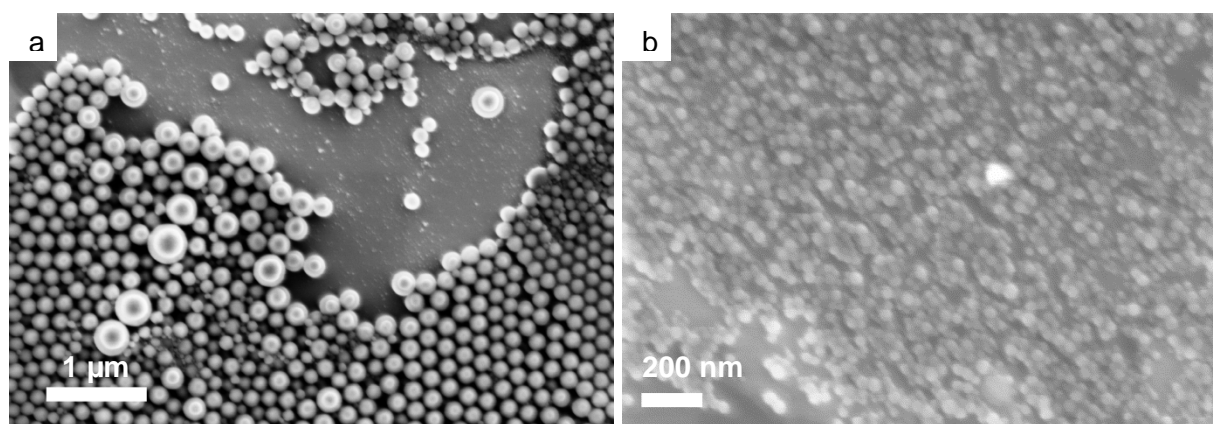


Figure 6.1 SEM images of TQ1:PC71BM NPs prepared with SDS concentration of 1.0 mM (a) and 34.1 mM (b), respectively.

6.2.2. The influence of shearing force on particle size

As described in Chapter 3, the formation of a miniemulsion is highly dependent on the shearing force introduced to the aqueous-organic mixture, which is generated by ultra-sonication in the work presented in this Chapter. The size of oil droplet in the miniemulsion directly determines the size of the formed NPs after the removal of organic solvent. Considering the size of NPs influences the morphology of NP forming active layer, the power/amplitude of ultra-sonication and the duration that a mixture exposed to ultra-sonication should be carefully controlled to achieve small size as well as narrow size distribution. Furthermore, the ultra-sonication process is conducted in ambient atmosphere, excessively high amplitude or long duration could possibly degrade the photoactive materials. In order to find ideal working condition of probe sonicator, TQ1:PCBM (1:2.5) NPs were prepared under varied amplitude and duration. **Figure 6.2** shows the SEM images of TQ1:PCBM NPs, indicating higher amplitude resulted in smaller size while longer duration offered uniform size.

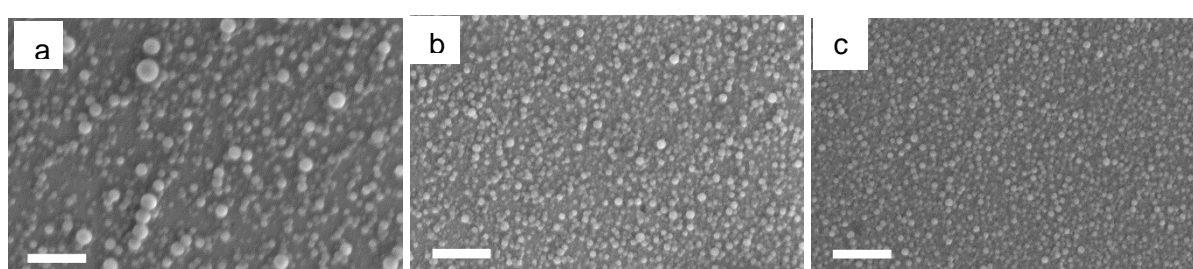


Figure 6.2 SEM images of TQ1:PCBM NPs underwent 20% amplitude and 2 min (a), 30% amplitude and 2 min (b) and 30% amplitude and 3 min sonication, respectively. Scale bars are 400 nm.

6.2.3. The influence of solvent additive on the morphology and photovoltaic performance of NPs

1-Chloronaphthalene (CN) has been used as a solvent additive to process BHJ layer, and has been reported to ideally tune the morphology of BHJ active layer as the donor and acceptor materials have different solubility in it.¹⁵⁻¹⁷ As an easily synthesised polymer, TQ1 has been widely studied as a

donor material in BHJ OPVs,¹⁸⁻¹⁹ which used CN as the solvent additive to improve the morphology of active layer,¹⁵ and also been reported in water-dispersed NP solar cells.²⁰ However, due to the observed core-shell structure of particles,²⁰ further annealing is required to convert the nanoparticulate film into finely smoothed film. The aim of this study with additive, i.e. CN, was to understand whether CN could optimise the internal morphology within the single nanoparticle, ideally increase the intermixing between TQ1 and PC₇₁BM, which could be beneficial for the enhancement of device performance with NP active layer.

TQ1:PC₇₁BM nanoparticles were prepared using the weight ratio of 1:2.5 through miniemulsion method. The weight ratio was chosen based on the best performing BHJ devices from TQ1:PC₇₁BM blend without solvent processing additive pre-studied in our group. TQ1:PC₇₁BM blends without additive were initially dissolved in chloroform to prepare NPs as control experiment, while 2% CN was mixed with chloroform to dissolve material blends for additive study. As shown in SEM images (**Figure 6.3**), with 2% CN in miniemulsion dispersed phase solvent, the NPs obtained were distinctly spherical with no aggregation of materials or increase in particle size. The scanning transmission X-ray microscopy (STXM) measurements (**Figure 6.4**) indicate that the NPs prepared from chloroform are identical core-shell structure, with a polymer-rich shell and PCBM-rich core, which is in good agreement with the literature.²⁰ However, additional 2% CN introduced in the miniemulsion dispersed phase solvent mixture also resulted in core-shell structure measured by STXM.

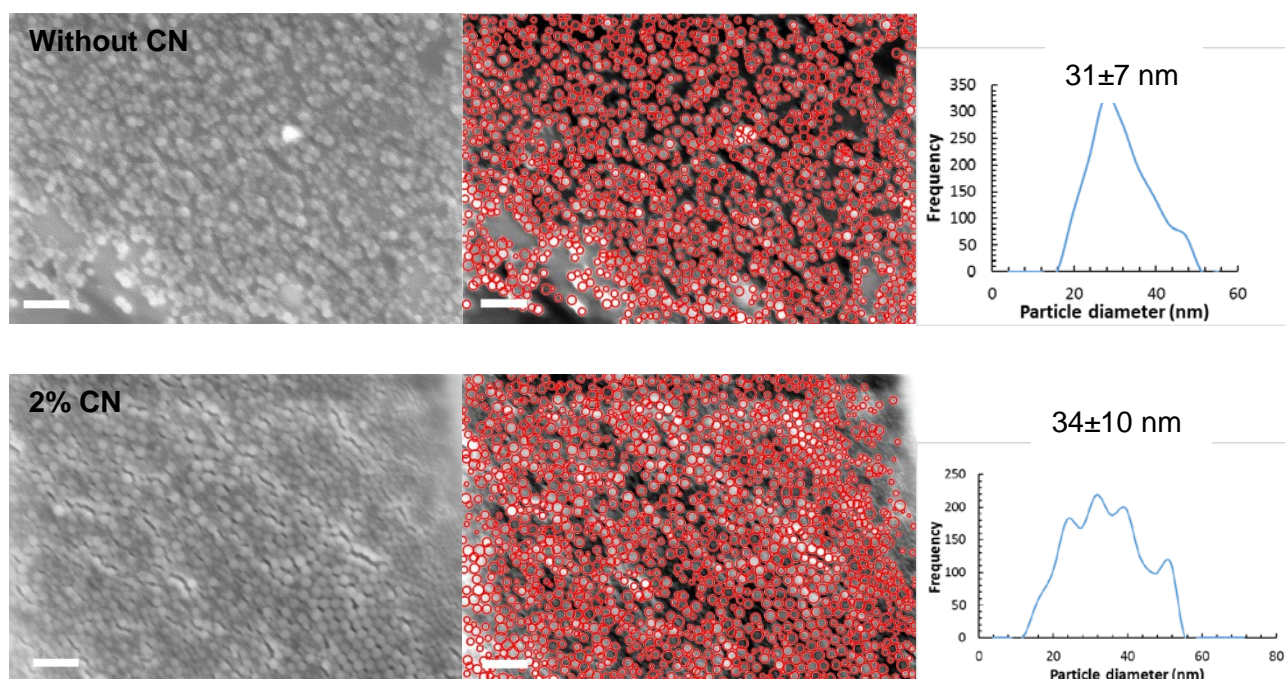


Figure 6.3 TQ1:PC₇₁BM NPs SEM images, circle identification output using a circular Hough transform algorithm and size distribution of NPs. Scale bars are 200 nm. Top images are NPs without CN, bottom images are NPs with CN.

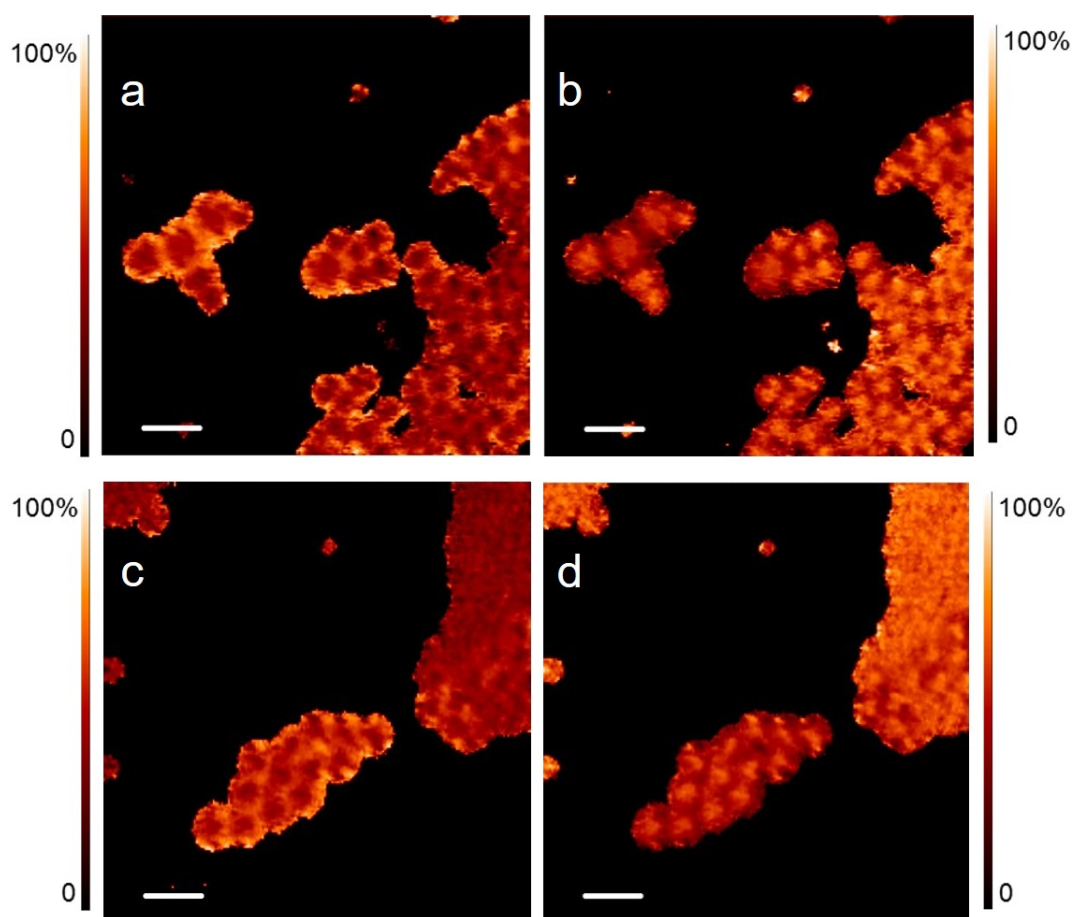


Figure 6.4 STXM fractional composition maps showing the concentration of (a, c) TQ1 and (b, d) PC₇₁BM of TQ1:PC₇₁BM nanoparticles without using CN (a & b) and using CN in the preparation (c & d). All scale bars are 0.5 μm. The colour contrast is scaled such that light colours correspond to higher component concentrations. Minima and maxima for the colour scale bar in (a) and (b) are black = 0 and white = 100%.

In order to study the influence of solvent additive on the morphology of NP film after thermal annealing to coalesce NPs, atomic force microscopy (AFM) measurements were performed. Upon annealing at 140 °C for 4 min, the NP film cast from the ink without solvent additive were observed to be mildly smoothed (**Figure 6.5a**), whereas the counterpart with 2% CN in the procedure showed higher degree of phase separation and pin-holes forming(**Figure 6.5b**). Due to its intrinsic high boiling point (259 °C), CN could not be effectively removed from the active material mixture under the solvent evaporating condition used for chloroform. Hence, the large phase separation detected in the NP forming film may result from the escape of residual CN from the cast film during thermal annealing.

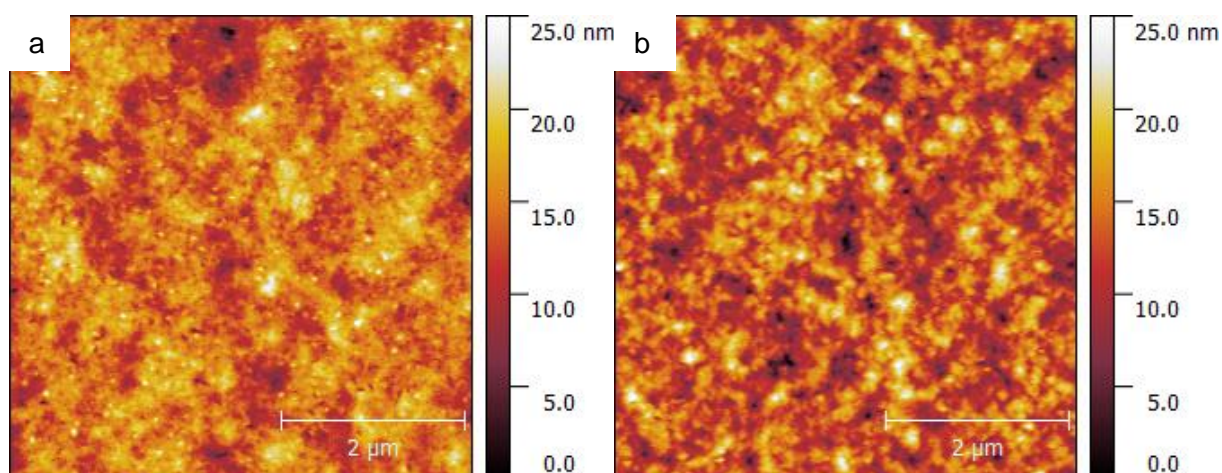


Figure 6.5 AFM topographical images (5×5 μm) of 140 °C annealed TQ1-PC₇₁BM NPs (a) without CN and (b) with 2% CN.

To study the influence of solvent additive on NP based device performance, OPVs were fabricated using TQ1:PC₇₁BM NPs with the conventional structure of ITO/PEDOT:PSS/NPs/Ca/Al. The device characteristics of additive-free NP OPVs are listed in **Table 6.1** and **Table 6.2** shows the device performance of CN containing NPs. Without using solvent additive in the synthesis of NPs, the NP device gave best performance when the NP film was thermally annealed at 140 °C, with maximum PCE of 1.49% ($J_{SC} = 4.76 \text{ mA/cm}^2$, $V_{OC} = 0.68 \text{ V}$ and $FF = 46\%$). The NPs synthesised with 2% CN blended with chloroform resulted in poorer photovoltaic performance, giving highest value of PCE = 0.37% ($J_{SC} = 4.94 \text{ mA/cm}^2$, $V_{OC} = 0.25 \text{ V}$ and $FF = 31\%$) upon thermal annealing of NP film at 130 °C. The major difference of device characteristics between two batches of NP devices is open-circuit voltage, only 0.25 V was reached in CN introduced NP devices. The insufficient V_{OC} might be caused by the residual CN in water dispersion diffused into PEDOT:PSS layer under the NPs. But we don't have a clear evidence to explain the loss of V_{OC} . The unsatisfactory photovoltaic performance of TQ1:PC₇₁BM NPs with CN as the solvent additive could also be resulted from the large phase separation upon annealing observed in AFM images (**Figure 6.5b**). However, using other solvent additives might be more beneficial for the NP film morphology and device performance.

Table 6.1 Photovoltaic performance of OPVs based on active layer of TQ1:PC₇₁BM NPs prepared from CHCl₃ without additive, best device for varied NP film annealing temperature with average \pm standard deviation in parentheses.

Annealing condition	J_{sc} (mA/cm ²)	FF (%)	V_{oc} (V)	PCE (%)
110 °C 4 min	3.15 (2.83 \pm 0.28)	36 (35 \pm 1)	0.56 (0.52 \pm 0.05)	0.64 (0.51 \pm 0.08)
120 °C 4 min	4.61 (4.59 \pm 0.15)	36 (35 \pm 1)	0.48 (0.44 \pm 0.02)	0.79 (0.71 \pm 0.04)
130 °C 4 min	4.36 (4.74 \pm 0.30)	37 (36 \pm 1)	0.52 (0.47 \pm 0.04)	0.84 (0.80 \pm 0.04)
140 °C 4 min	4.76 (4.77 \pm 0.10)	46 (40 \pm 3)	0.68 (0.60 \pm 0.04)	1.49 (1.16 \pm 0.18)
150 °C 4 min	4.40 (4.16 \pm 0.33)	39 (37 \pm 1)	0.62 (0.58 \pm 0.04)	1.06 (0.90 \pm 0.11)

Table 6.2 Photovoltaic performance of OPVs based on active layer of TQ1:PC₇₁BM NPs prepared from CHCl₃ with 2% CN, best device for varied NP film annealing temperature with average \pm standard deviation in parentheses.

Annealing condition	J_{sc} (mA/cm ²)	FF (%)	V_{oc} (V)	PCE (%)
110 °C 4 min	2.55 (2.33 \pm 0.45)	30 (28 \pm 1)	0.29 (0.23 \pm 0.06)	0.22 (0.15 \pm 0.03)
120 °C 4 min	3.1 (3.35 \pm 0.70)	29 (28 \pm 1)	0.21 (0.18 \pm 0.03)	0.19 (0.16 \pm 0.02)
130 °C 4 min	4.94 (3.81 \pm 0.78)	31 (30 \pm 1)	0.25 (0.27 \pm 0.05)	0.37 (0.30 \pm 0.04)
140 °C 4 min	3.45 (3.32 \pm 0.22)	30 (29 \pm 1)	0.24 (0.19 \pm 0.04)	0.25 (0.18 \pm 0.05)
150 °C 4 min	1.92 (1.45 \pm 0.54)	26 (25 \pm 2)	0.45 (0.37 \pm 0.09)	0.22 (0.14 \pm 0.06)

Figure 6.6 shows the trend of average values in device characteristics with varied annealing temperature. The trend in the performance of solar devices based on NPs synthesised with CN is not accordant with the control devices, which might be resulted from different degree of phase separation formed upon annealing when CN was utilised.

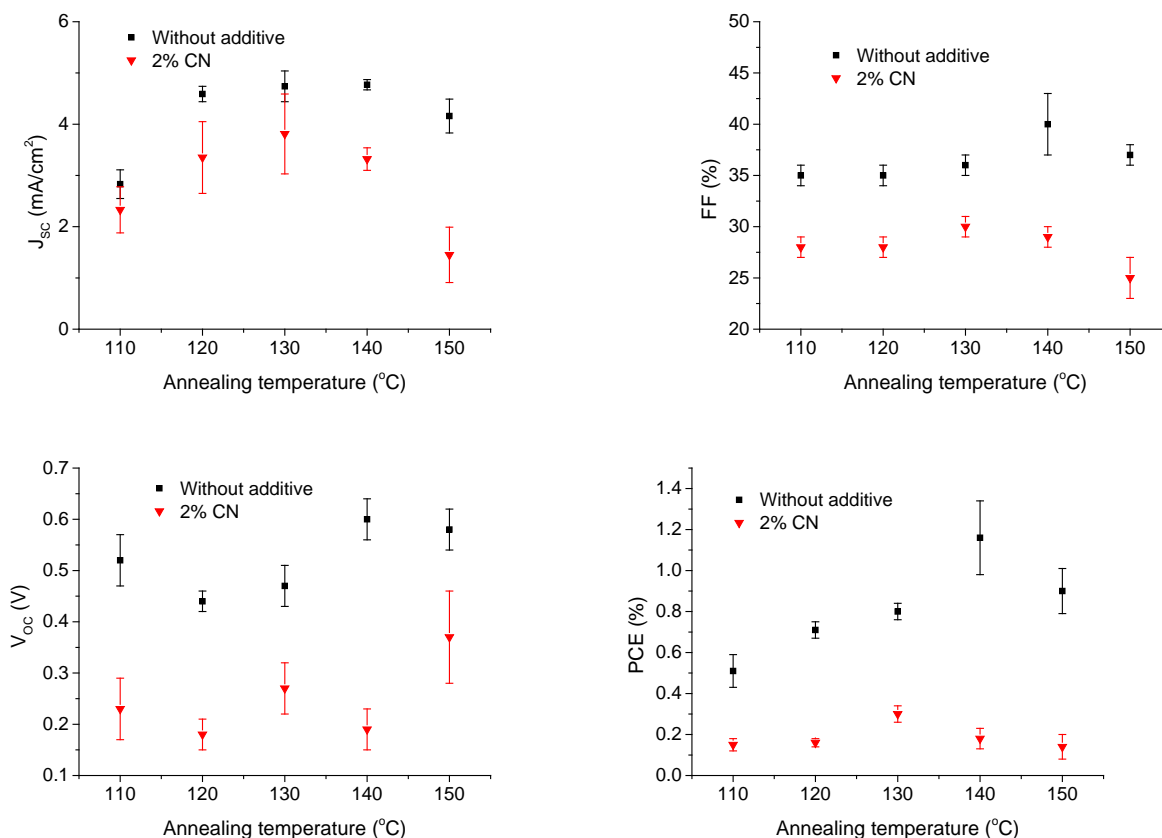


Figure 6.6 Average device characteristics with standard deviations presented by error bars at varied thermal annealing temperature.

6.2.4. The influence of final concentration of surfactant in water dispersed NPs prepared from green solvent

The final concentration of surfactant, SDS, remaining in the NP ink prior to the active layer deposition plays different roles, such as stabilizing the NPs to avoid large agglomerates, and facilitating the film wetting during processing.¹⁴ Hence, studying the final loading of SDS in the NP ink could be beneficial to control the quality of NP active layer and to understand its influence on the NP based OPVs.

Chloroform is the most commonly used miniemulsion dispersed phase solvent in the preparation of water dispersed NPs from conjugated materials due to its low boiling point and good dissolubility for wide range of photoactive materials.²⁰⁻²¹ Other organic solvents can also be used to prepare NPs, such as *o*-DCB, chlorobenzene and *o*-xylene. Considering the upscaling of NPs, the hazard of solvents used need to be taken into account. By comparing the hazard rating of some organic solvents used in miniemulsion method in **Table 6.3**, it can be noticeably found that anisole exhibits minimum hazard rating in both toxicity and chronic effect. Furthermore, anisole is biodegradable²² and enjoys ideal dissolubility of commonly used conjugated donor polymers and fullerene derivatives, i.e., PCBM.

Table 6.3 ChemWatch hazard ratings of different solvent used as miniemulsion dispersed phase solvent.

Solvent	ChemWatch hazard rating	
	Toxicity	Chronic
Chloroform	2	3
Chlorobenzene	2	0
<i>o</i> -DCB	2	2
<i>o</i> -Xylene	2	0
Anisole	0	0

0 = Minimum, 1 = Low, 2 = Moderate, 3 = High, 4 = Extreme

To eliminate the usage of harmful halogenated solvent in the preparation procedure, anisole was applied as the miniemulsion dispersed phase solvent to produce TQ1:PC₇₁BM NPs. The density of anisole is 0.995 g/cm³, which is very close to the density of water. Hence, during the preparation of macroemulsion prior to the ultrasonication, organic phase showed outstanding intermixing with aqueous phase compared to other miniemulsion dispersed phase solvents used, such as chloroform and *o*-xylene. The excellent dispersity observed in anisole-water system directly contributes to the suppression of material loss during ultrasonication. The subsequential evaporation of organic solvent in order to convert miniemulsion into dispersion is conducted by heating in ambient condition. Although anisole exhibits a boiling point of 153.8 °C, its high vapour pressure enables the removal of anisole from water without resulting in severe water loss. The removal of anisole in this NP preparation procedure required higher temperature and longer time compared to the removal of chloroform. Hence, during the heating process additional water was added to the system to compensate the water loss. The TQ1:PC₇₁BM NPs prepared from anisole were measured to have mean diameters of 26.6 ± 9.3 nm in the solid state. The particle size was measured through a circular Hough transform algorithm to SEM images of NP film. The circle identification overlaid SEM image as well as the original SEM image used for calculation are show in **Figure 6.7**.

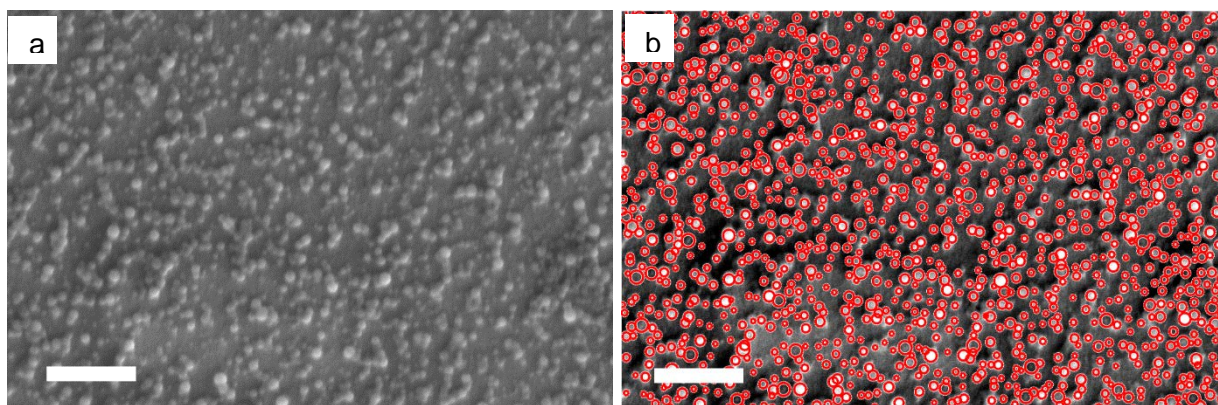


Figure 6.7 (a) SEM image of TQ1:PC₇₁BM NPs prepared using anisole showing size distribution, (b) circle identification output using a circular Hough transform algorithm. Scale bars are 400 nm.

As described earlier, initial concentration of surfactant in the miniemulsion determines the size of NPs, which should not change after the removal of free surfactant.¹⁴ Even though the surfactant, i.e. SDS is crucial to stabilize NPs from photoactive materials in water, SDS is undesired in the complete NP solar cells due to its insulating property. The concentration of surfactant in the final ink directly influences the film quality of NP forming active layer, relating to the photovoltaic performance. The removal of free surfactant was carried out by repetitive centrifugal dialysis with adding water in between. Theoretically, more steps of dialysis results in lower concentration of SDS. It has been observed that the NP forming film shows unwanted aggregation at high concentration of SDS (less steps of dialysis), whereas film dewetting at low concentration (more steps dialysis). The water-dispersed TQ1:PC₇₁BM NPs prepared using anisole as miniemulsion dispersed phase solvent were dialyzed with different repetitive steps, resulting in different concentration of SDS in the final inks. The photovoltaic performance of the solar cells based on TQ1:PC₇₁BM NPs was characterised and best performing device characteristics are shown in **Table 6.4**. With 5 dialysis steps performed on NP dispersion, the best performing OPV base on NPs forming active layer was achieved with PCE of 1.42%. Compared to 5 steps dialyzed NPs, only 0.89% efficiency was obtained in OPV based on 3 steps dialyzed NPs and similar PCE of 0.84% from the 7 steps counterparts. The inferior performance of solar devices based on 3 steps dialyzed NPs was resulted from the solid state aggregations formed during spin-coating as well as the high concentration of insulating SDS remained in the photoactive layer. Moreover, the 7 steps dialyzed NP dispersion led to film dewetting on ZnO coated substrates, affording heterogeneous forming of active layer, which is reflected from the low J_{SC} .

Figure 6.8 compares the average device characteristics of NP-active layer forming OPVs as a function of different steps of dialysis accomplished to NP dispersion. It can be noticeably observed that 5 steps dialysis leads to highest average J_{SC} and PCE, though more steps of dialysis to NPs contributes to the increase of FF and slight decrease of V_{OC} . Hence, it can be concluded that the

final concentration of SDS in water-dispersed NPs needs to be carefully controlled before the deposition of NP active layer in order to achieve high efficiency.

Table 6.4 Photovoltaic performance of OPVs based on active layer of TQ1:PC₇₁BM NPs (prepared using anisole as miniemulsion dispersed phase solvent) under different steps of dialysis.

Dialysis steps	J_{sc} (mA/cm ²)	FF (%)	V_{oc} (V)	PCE (%)
3	7.18	17	0.71	0.89
5	7.17	28	0.72	1.42
7	4.35	30	0.64	0.84

Device architecture: ITO/ZnO/NPs/MoO₃/Ag. NP layer thermally annealed at 140 °C for 4 min. Complete devices post-annealed at 140 °C for 4 min.²⁰

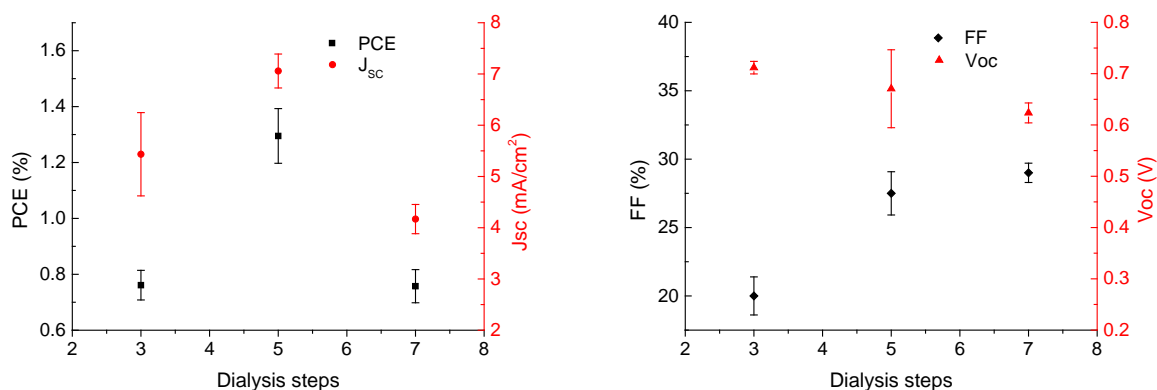


Figure 6.8 Average device characteristics with standard deviations presented by error bars for TQ1:PC₇₁BM NP (anisole batch) OPV.

6.2.5. The influence of molecular weight of donor polymer on particle size

Holmes et al. reported that the molecular weight of semicrystalline polymer, P3HT, exhibits an influence on the size of P3HT:PCBM NPs.²³ To study the influence of molecular weight of amorphous donor polymer to the NP size, two batches of TQ1 were synthesised and blended with PC₇₁BM to prepare NPs through miniemulsion method. The molecular weight data of high molecular weight (HMW) TQ1 and low molecular weight (LMW) TQ1 are shown in **Table 6.5**.

Table 6.5 Molecular weight characterisation data for two batches of TQ1.

Polymer	M_n (g/mol)	M_w (g/mol)	PDI
HMW-TQ1	53,100	131,900	2.5
LMW-TQ1	10,800	21,800	2.0

The SEM images of TQ1:PC₇₁BM NPs prepared using HMW-TQ1 and LMW-TQ1, respectively, were depicted in **Figure 6.9**. By comparing the size distribution in **Figure 6.9c**, it can be observed that NPs prepared from LMW-TQ1 show less population of particles with diameter beyond 40 nm. The HMW-TQ1:PC₇₁BM (1:3 weight ratio) NPs were measured to have mean diameter of 31.7 ± 14.7 nm, while LMW-TQ1:PC₇₁BM (1:3 weight ratio) NPs show smaller size of 26.4 ± 13.0 nm. It should be noted that the experimental parameters were kept constant for these two batches of NP preparation. Hence it can be concluded that high molecular weight of amorphous polymer results in slightly larger size of NPs. The sizes of NPs have been calculated from several different SEM images and HMW-TQ1 containing NPs all clearly showed slightly bigger size.

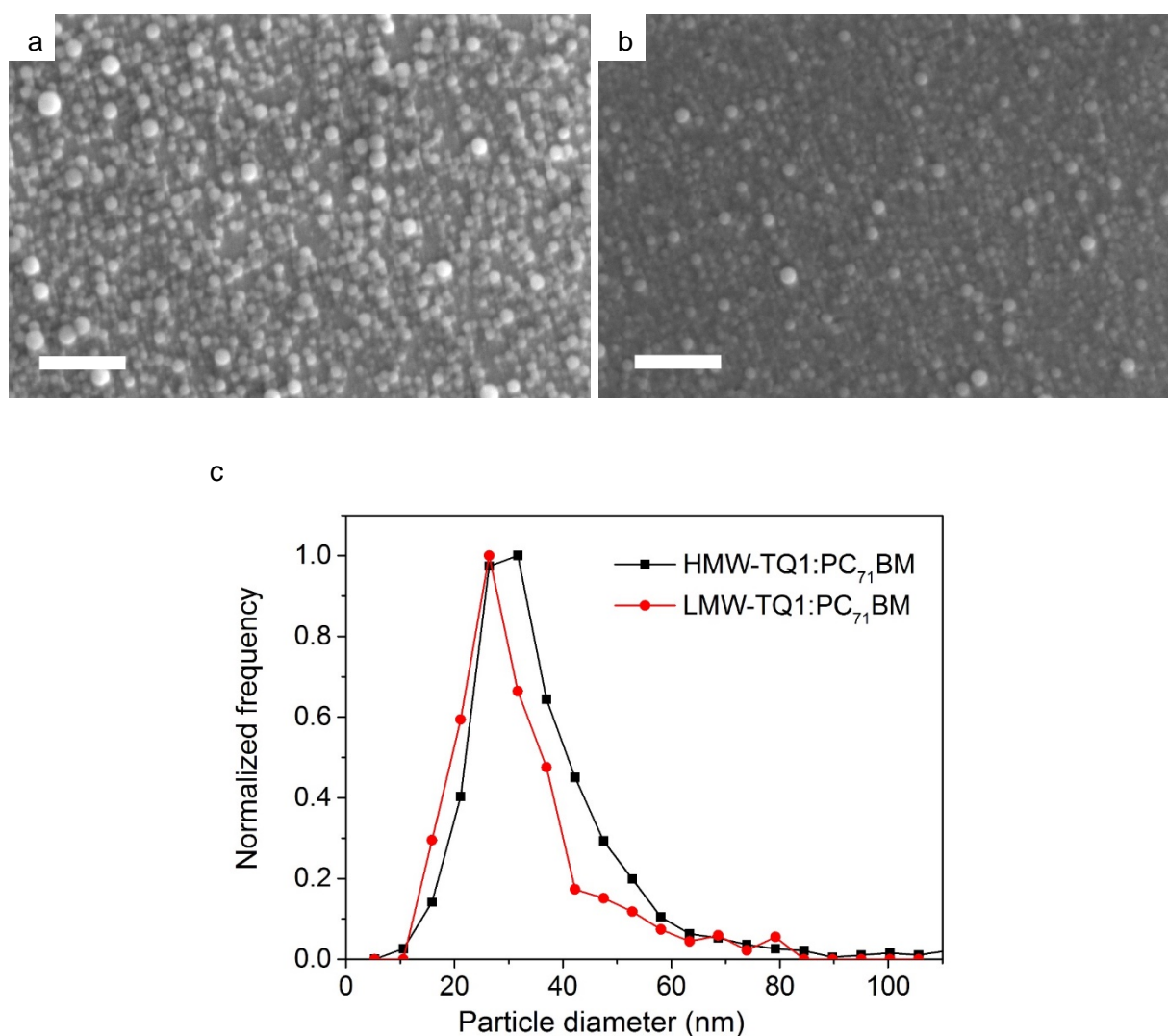


Figure 6.9 SEM images of HMW-TQ1:PC₇₁BM NPs (a) and LMW-TQ1:PC₇₁BM (b). Scale bars are 400 nm. (c) Size distribution of NPs calculated by a circular Hough transform algorithm to the SEM images.

6.3. Methods to coalesce NPs in the solid state

The polymer:PCBM NPs prepared via miniemulsion method were measured to be core-shell structure, which show the donor polymer-rich shell and PCBM-rich core. The core-shell structure reported create hindrance for efficient charge generation due to the larger-scale phase separation in the NP forming film compared to the solution processed BHJ layer.²⁴ Moreover, the discrete structure of NP forming film could introduce pinholes in the active layer, which is responsible for the shorting in complete devices. Hence, methods used to coalesce NPs in the solid state were developed and studied.

6.3.1. Thermal annealing

Thermal annealing is one of the most commonly applied treatments to both BHJ layer possessed directly from organic solution²⁵⁻²⁶ and NP forming layer.^{6, 10} The utilisation of thermal energy to coalesce NPs is largely affected by the thermal transition temperature of the polymer. To find out the optimal thermal annealing temperature applied to coalesce NPs in the solid state, glass transition temperature (T_g) of donor polymer and thermal transition of fullerene required to be taken into account. When a given polymer is heated so that it pass through its glass transition temperature, it changes from glassy to the rubbery state.²⁷ In the case of polymer-fullerene NPs, only when the polymer is in the rubbery state, can the polymer-rich shell be softened to form a continuous polymer matrix (**Figure 6.10**).^{20, 23} Hence, PCBM in the core are able to diffuse in the polymer matrix and form connection, which is crucial for electron to transfer to the electron transport layer for charge collection in the electrode. However, if the annealing temperature went beyond the thermal transition temperature of fullerene-rich phase in the NP film, large crystals will form and result in large phase separation, which deteriorate the morphology of NP active layer.

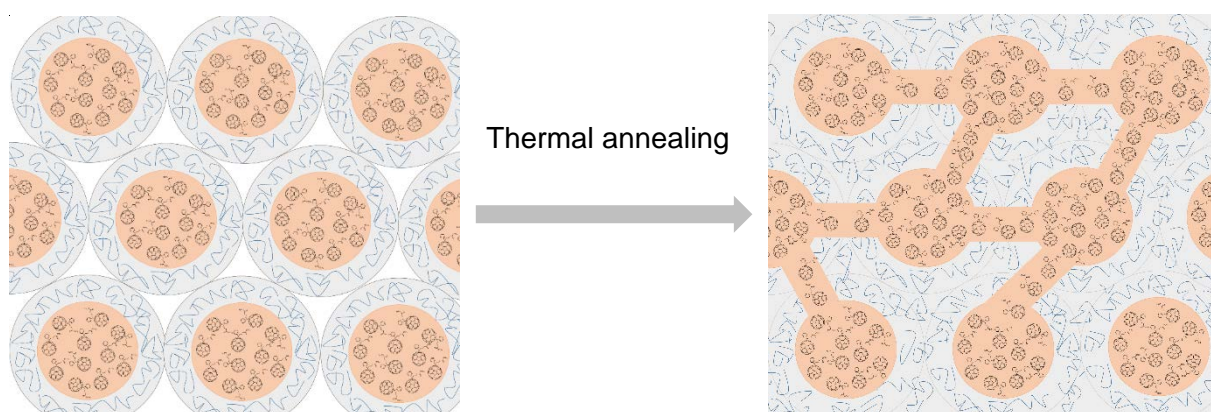


Figure 6.10 Schematic of donor polymer:PCBM NPs behaviour upon thermal annealing.

For amorphous polymers with the same backbone and identical side groups, a polymer with less repeating units should exhibit T_g at lower temperature compared to its high molecular weight

counterpart.²⁷⁻²⁸ The influence of molecular weight on T_g is simplistically described by Flory-Fox equation $T_g = T_{g,\infty} - K/M_n$, where $T_{g,\infty}$ is the maximum glass transition temperature at a theoretical infinite molecular and K is an empirical parameter related to the free volume of a given polymer.²⁸ Hence, the T_g of polymer-rich shell and thermal transition temperature of fullerene-rich core should both shift to lower temperature with the decrease of M_n of the polymer.

Two batches of TQ1:PC₇₁BM NPs prepared using HMW-TQ1 and LMW-TQ1, respectively, to study their morphological change upon thermal annealing. As described in 7.2.5, the NP as spun films show clearly discrete NPs. After thermally annealed at 140 °C for 4 min, the HMW-TQ1:PC₇₁BM NP film (**Figure 6.11a**) shows a mildly smoothed feature, presenting discrete particles haven't been sintered on the top surface. While the LMW-TQ1:PC₇₁BM NP film (**Figure 6.11b**) treated the same way reveals a much finer morphology with well-established connections. When 160 °C thermal annealing was applied, HMW-TQ1:PC₇₁BM NP film (**Figure 6.11c**) indicates the aggregation of materials, which is observed to be more severe in LMW-TQ1:PC₇₁BM NP film (**Figure 6.11d**). The large agglomeration detected in LMW sample reveals the fullerene-rich core passing through its thermal transition, resulting in the crystallization of PC₇₁BM, which will be explained below.

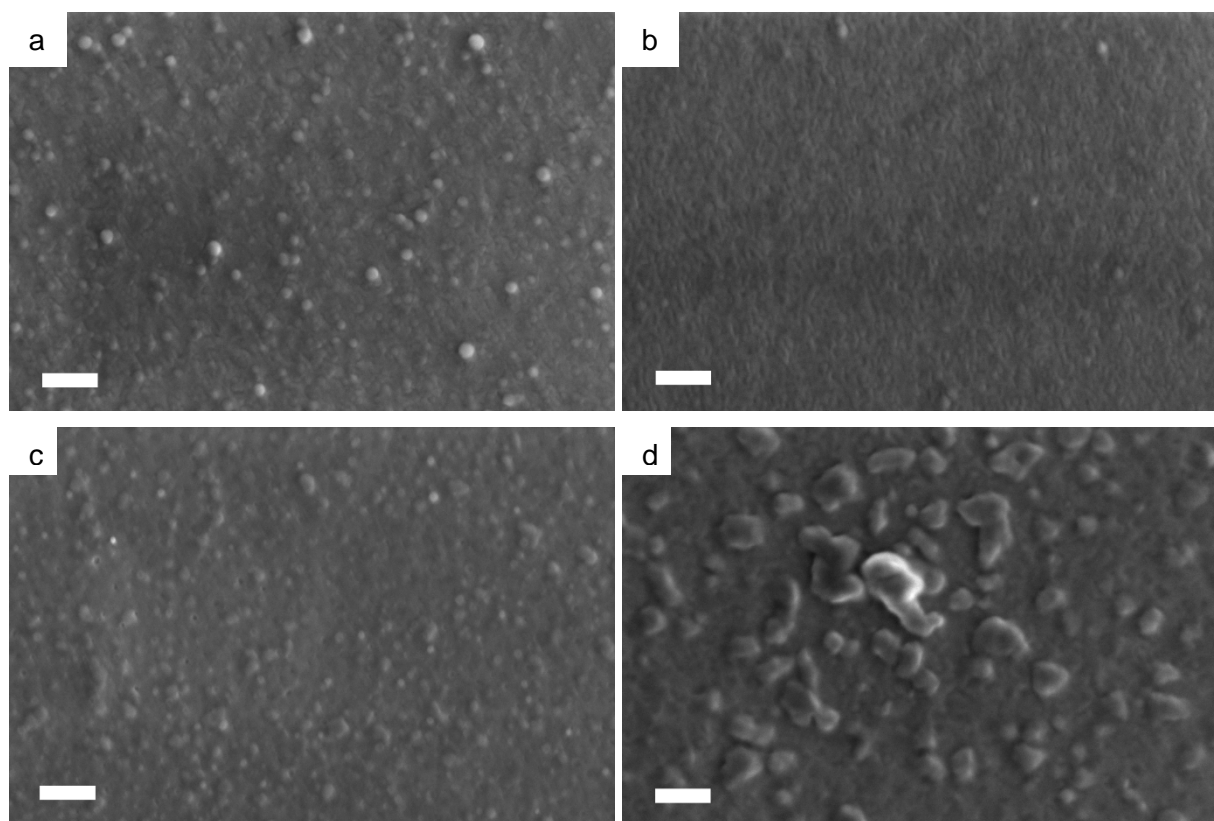


Figure 6.11 SEM images of 140 °C thermally annealed (a) HMW-TQ1:PC₇₁BM NP film and (b) LMW-TQ1:PC₇₁BM NP film; 160 °C thermally annealed (c) HMW-TQ1:PC₇₁BM NP film and (d) LMW-TQ1:PC₇₁BM NP film. Scale bars are 400 nm.

To further probe the morphological changes and thermomechanical behaviour of these NPs, dynamic mechanical thermal analysis (DMTA) measurements²⁹ were performed on thin films cast from HMW-TQ1:PC₇₁BM NPs and LMW-TQ1:PC₇₁BM NPs, respectively. The $\tan \delta$ in the DMTA temperature scan of NP film was shown in **Figure 6.12**. For both samples, two distinct thermal transition temperatures are revealed from the $\tan \delta$ peaks, which is in accordance with the core-shell structure measured. The $\tan \delta$ peak at approximate 134 °C presented in HMW sample is attributed to the glass transition of TQ1-rich shell and peak located at 160 °C is primarily attributed to the thermal transition of fullerene-rich core. It can be clearly observed the T_g of TQ1-rich shell in LMW sample is only 111 °C, while the thermal transition temperature of fullerene-rich core were measured to be 152 °C. The thermomechanical behaviour of these two batches of NPs further explains the difference of film morphology upon annealing at 140 °C for 4 min (**Figure 6.11a and b**). It should be noted that the thermal annealing of NP film was performed by heating the thin film on silicon substrate with temperature controlled on the hotplate, whereas the temperature of DMTA scan shows the real temperature of the atmosphere surrounding NP film. Hence the actual temperature of film undergoes thermal annealing should be lower than 140 °C in the microscopy study. At 140 °C annealing, the TQ1-rich shell in LMW NPs was already in its rubbery state and the coalescence of particles was completed in a short time frame. However, the shell in HMW sample was experiencing glass transition around 140 °C, resulting in incomplete sintering after only 4 min annealing at 140 °C. The thermal transition of fullerene-rich core at 152 °C for LMW sample illustrates the severe aggregation of LMW NP film upon 160 °C annealing. The DMTA result is supportive well with our observation through SEM.

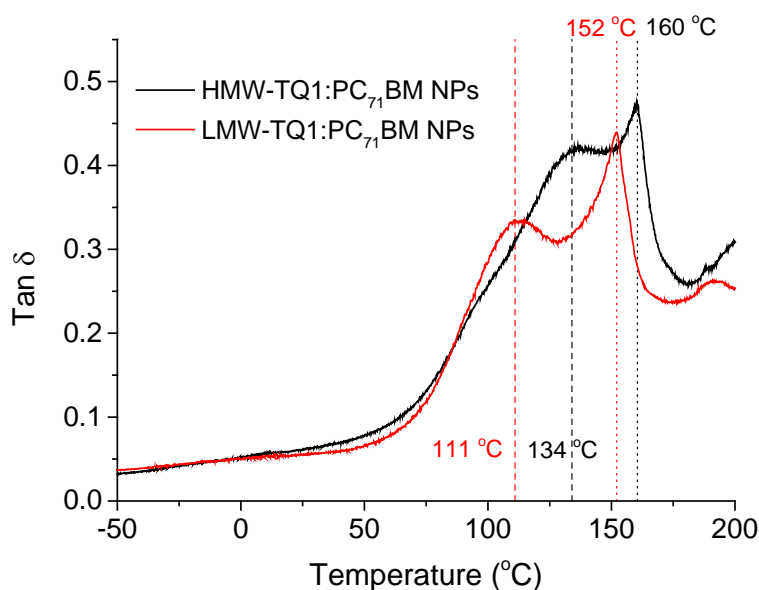


Figure 6.12 DMTA temperature scan of HMW-TQ1:PC₇₁BM NPs (black solid line) and LMW-TQ1:PC₇₁BM NPs (red solid line) with the indication of thermal transition temperature in dash lines.

It can be concluded that thermal annealing is an effective method to coalesce NPs on condition that the temperature applied is prudently chosen based on the thermomechanical property of NPs.

6.3.2. Solvent vapour annealing

Solvent vapour (SV) annealing is another technique used to tune the morphology of BHJ films.³⁰⁻³¹ The purpose of SV annealing is to achieve highly ordered film with interpenetrating morphology,³² which is beneficial for light harvesting and efficient exciton dissociation in donor-acceptor interfaces. However, to the best of our knowledge this technique has not been reported to be applied to NP forming active layer in polymer solar cells. It will be described in the **Chapter 7** that in the case of the PTNT:PC₇₁BM NP film, thermal annealing at 160 °C resulted in the coalescence of NPs and lead to the best performing NP-OPVs. Considering this high temperature used in thermal annealing is not applicable to large-scale printed devices with polyethylene terephthalate (PET) substrate, SV annealing was investigated to find out the possibility to coalesce NPs in the solid state without heating. Upon solvent vapour annealing with chloroform, which has high vapour pressure, for 1 hour, the NP films spin coated from aqueous PTNT:C₆₀:C₇₀ (2:1:1) NPs and PTNT:PC₆₁BM (1:1) NPs did not indicate the complete coalescence of NPs shown in **Figure 6.13**. Furthermore, large particle aggregations were observed in both samples, which could be resulted from the solidification of partly softened materials upon SV annealing.

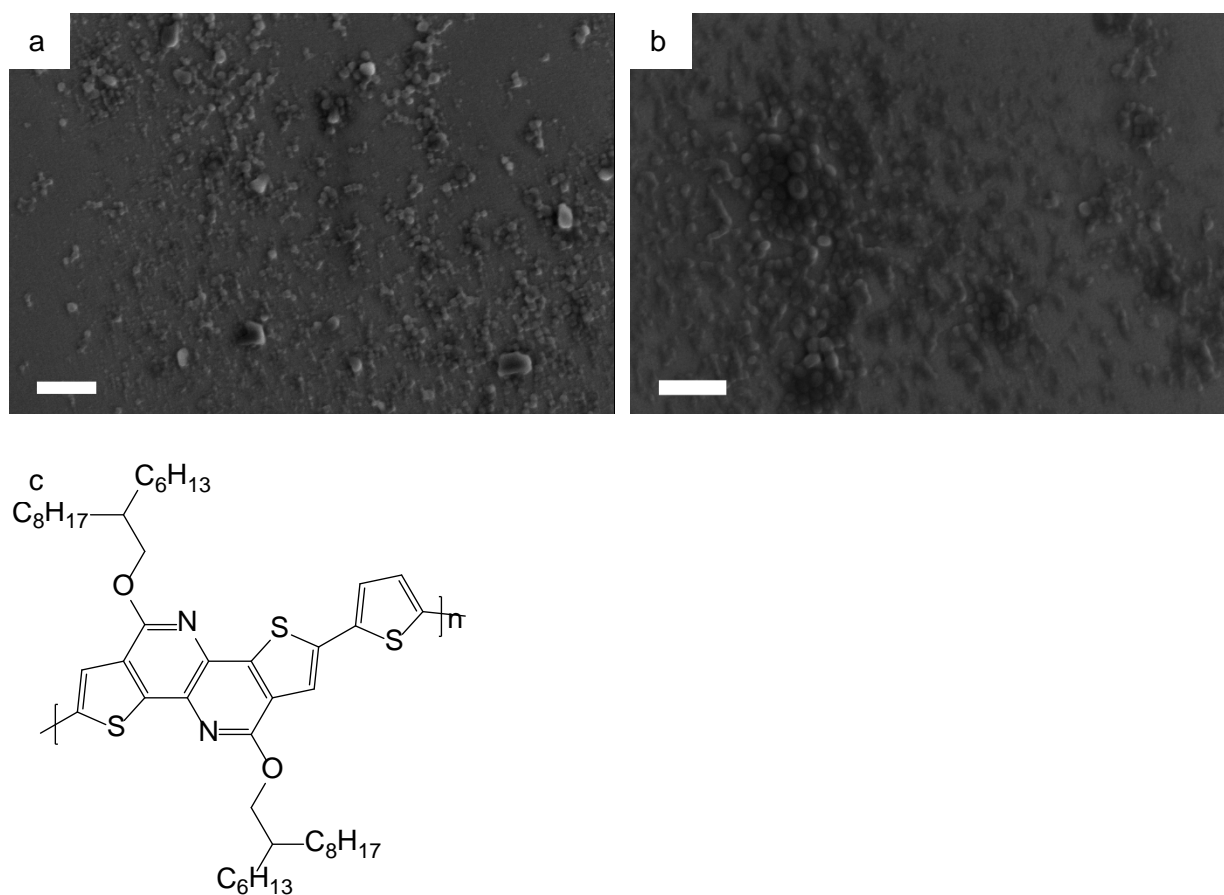


Figure 6.13 SEM images of (a) PTNT-C₆₀-C₇₀ NPs and (b) PTNT-PC₆₁BM NPs upon chloroform vapour annealing for 1 hour. Scale bars are 500 nm. (c) Chemical structure of PTNT.

Considering SV annealing could result in different effectiveness on NPs prepared with different polymers, annealing with chloroform vapour was also applied to TQ1:PC₇₁BM (1:2.5) NPs. After exposing the NP film in saturated chloroform vapour for 10 min, incomplete coalescence of NPs and agglomeration of materials were observed (**Figure 6.14a**). When the duration of SV annealing was prolonged for 30 min, large amount of discrete NPs were still remaining on the surface (**Figure 6.14b**).

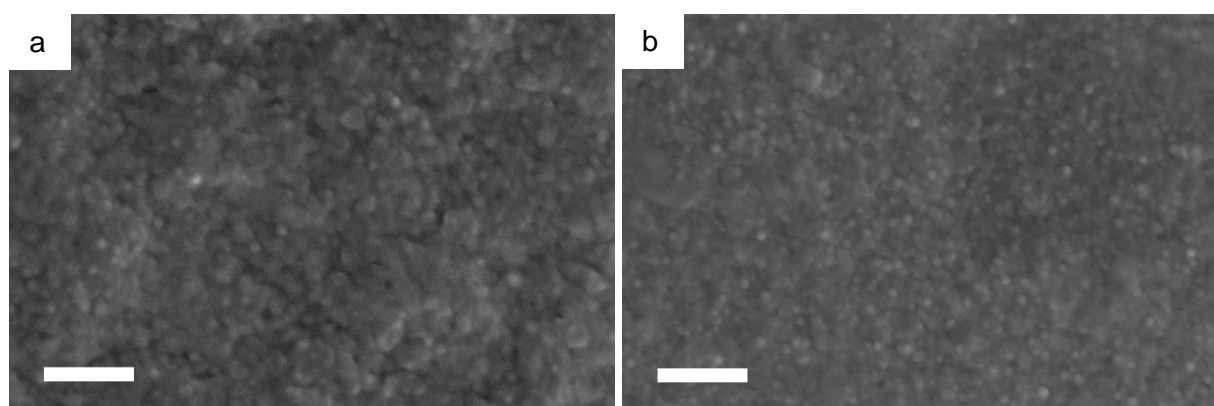


Figure 6.14 SEM images of TQ1:PC₆₁BM NPs upon chloroform vapour annealing for (a) 10 min and (b) 30 min. Scale bars are 400 nm.

Based on this unsatisfactory result, SV annealing was not conducted on other NP films used as active layers in OPV study. However, other solvents might be more beneficial to the coalescence of NPs and will be studied in the future.

6.3.3. Solvent blend washing

It has been reported that washing the NP film with a solvent blend of ethanol (EtOH) and water could effectively remove the surfactants¹⁴ though did not result in the coalescence of NPs. Considering 1-chloronaphthalene (CN) has a high boiling point which endows it to be an excellent solvent additive to process BHJ active layer, a solvent mixture of CN and EtOH was prepared to investigate whether NPs can be coalesced by blend solvent washing.

TQ1:PC₆₁BM (1:2.5) NPs were prepared through miniemulsion method as described before. The NP as spun film was subsequently washed by dipping in pure EtOH followed by spin coating to remove any residual solvent. The SEM images of the as spun film and the washed film are shown in **Figure 6.15a, b**, indicating that washing the NP film with EtOH did not result in aggregation of NPs or film delaminating from substrate.

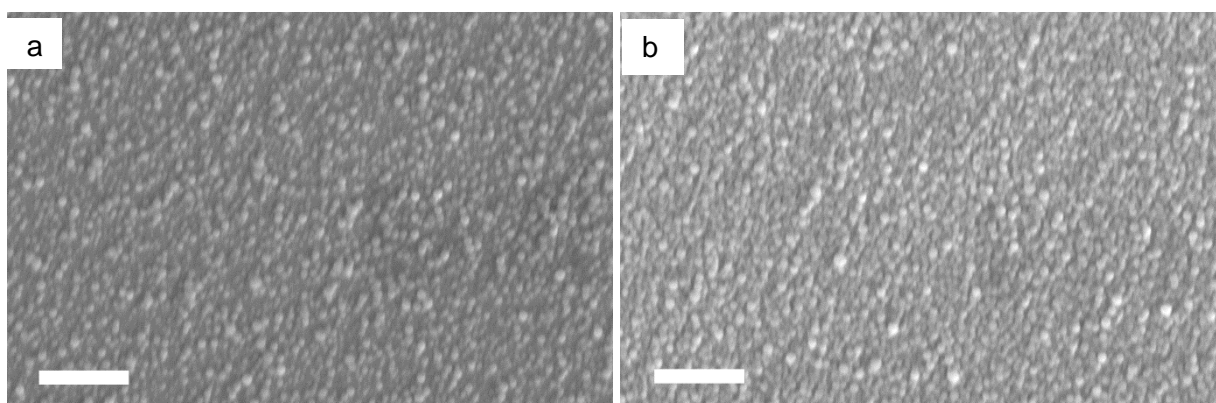


Figure 6.15 SEM images of TQ1:PC₆₁BM (1:2.5) NPs (a) as spun and (b) washed with EtOH. Scale bars are 400 nm.

Solvent mixture containing 2%, 5% and 10% of CN in EtOH were prepared separately. The washing step was performed by dropping solvent mixture on NP film for 10 s, followed by spin-coating to remove remaining solvent. After solvent washing, EtOH was removed under spinning while trace amount of CN should still remain on the film to soften the polymer-rich shell. **Figure 6.16a** shows the SEM image of TQ1:PC₆₁BM NP films washed by 2% of CN, indicating partially coalesced NPs. Considering the low volume of washing solvent applied, 2% of CN could possibly be inadequate to connect most of the NPs in the solid state, thus, higher content of CN was applied in the subsequent study. After washing with a 5% of CN in ethanol solution, coalesced NPs were observed (**Figure 6.16b**), however, solid flakes instead of continuous film formed on silicon substrate. The formation of discontinuous flakes was assumed to be attributed to the remaining CN droplet on the substrate, which was not visibly observed. Pushing this washing step to an extreme condition by using 10% of

CN resulted in the appearance of holes in macro-scale (**Figure 6.16c**). The photo of washed NP film with solvent droplets is shown in **Figure 6.16d**, revealing that the discrete CN droplets were responsible for the deteriorated morphology.

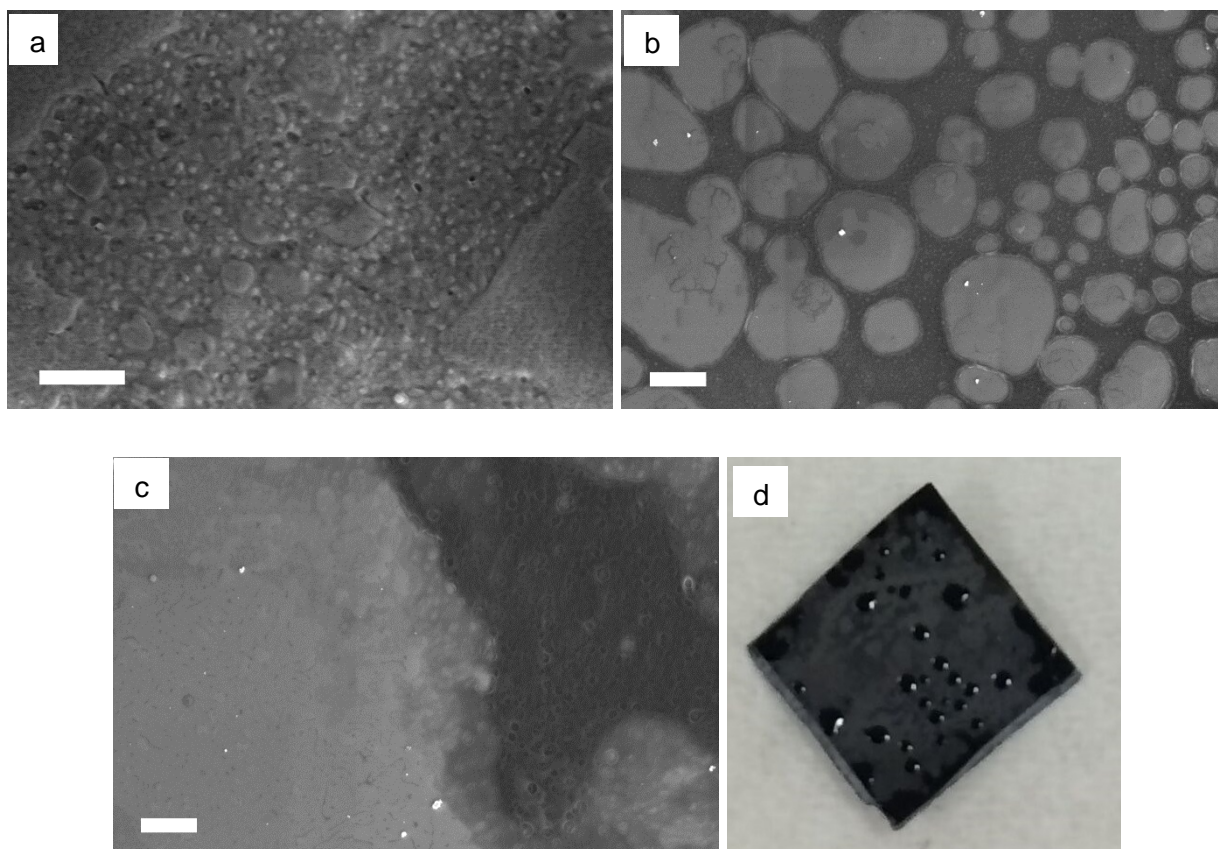


Figure 6.16 (a) SEM images of TQ1:PC₆₁BM (1:2.5) NPs washed with EtOH+2% CN, (b) washed with EtOH+5% CN and (c) washed with EtOH+10% CN. (d) Photo of NP film on silicon substrate after washing with EtOH+10% CN followed by spin-coating. Scale bars are 1 μ m.

Due to the difficulty of controlling film morphology, solvent blend washing was not used in the fabrication of NP OPVs presented in this thesis. However, other solvent blend systems might be beneficial to the morphology of NP films and will be investigated in the future.

6.4. Synthesis of nanoparticles without additional surfactant

Most procedures describe the preparation of nanoparticles requiring the use of SDS as the surfactant to achieve stable emulsion and avoiding aggregation of materials in aqueous dispersion. However, as a non-volatile compound, SDS cannot be simply removed by thermal annealing or other

treatment, and remains in the active layer of OPVs after fabricating, which could influence device performance.¹⁴

The work presented in this part was aiming at processing water-dispersed nanoparticles without an addition of surfactant. The preparation of NPs in this work was based on the utilisation of tertiary amine/pyridine functionalized polymer TQ1A, TQ1-50A, TQ1-20A, TQ1P4 as well as sodium sulfonate substituted fullerene derivative (PSCS) (**Figure 6.17**). Upon protonation of the dimethylamine side groups on polymer TQ1A, TQ1-50A and TQ1-20A, or the pyridine end groups attached to TQ1P4 with formic acid, the polymeric salts obtained from these polymers exhibit the property of micelle formation similarly to a surfactant, facilitating the formation of a miniemulsion and stabilizing the nanoparticles of amine or pyridine containing polymer, TQ1 and PC₆₁BM blends. The sodium sulfonate substitution on PSCC also endows the modified fullerene to be able to form micelle in aqueous condition.

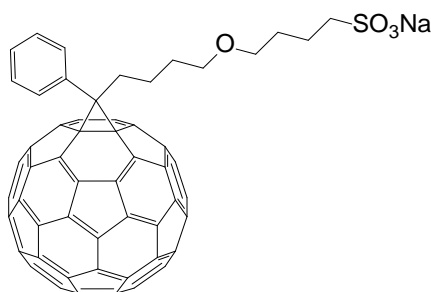


Figure 6.17 Chemical structure of PSCC.

6.4.1. SDS effect study

To study the effect of SDS in polymer solar cells, BHJ (TQ1:PC₆₁BM) devices were fabricated with a thin layer of SDS subsequently spin coated (from 1% weight SDS aqueous solution) on top of the electron transport layer, ZnO, followed by thermal annealing at 120 °C prior to the deposition of active layer. Thermal annealing of SDS layer was performed in order to remove moisture, which would also impact the performance of OPVs. Due to this consideration, control experiments (water-control) were performed with only water spin-coated during fabrication of devices instead of SDS.

As shown in **Table 6.6**, the presence of SDS resulted in slight deterioration in the performance of devices, with the decrease in V_{OC} by 0.1 V observed, compared to the water-control devices. The treatment of water in the device fabrication lead to the decrease in both J_{SC} and FF, resulting in lower value of PCEs compared to the reference BHJ device. The reduction of J_{SC} in the water-control device could be attributed to the surface energy alteration of ZnO introduced by water, affecting the morphology of active layer in an unwanted aspect. It can be preliminarily concluded that the presence of SDS in OPV resulted in inferior photovoltaic performance.

Table 6.6 Device characteristics of TQ1: PC₆₁BM BHJ OPVs with the presence of SDS, the control OPVs with only coated water and reference OPVs without any treatment.

Device description	J_{sc} (mA/cm ²)	FF (%)	V_{oc} (V)	PCE (%)
1% SDS	6.91	59	0.74	3.02
Water-control	6.61	57	0.85	3.18
Reference	8.07	68	0.86	4.74

6.4.2. Preparation of NPs using polymers with functionalized side groups

To eliminate the usage of additional SDS in the preparation procedure of NPs through the miniemulsion method, novel materials with functionalized side groups were carefully utilised and studied. The general preparation procedure of NPs without an addition of surfactant is described as below. Firstly material blends were dissolved in chloroform and 2% formic acid aqueous solution was prepared. Then formic acid aqueous solution was gently transferring into organic phase under stirring followed by ultra-sonication to offer the miniemulsion. Finally chloroform was removed under heating and water-dispersed nanoparticles were obtained.

Figure 6.18 shows the SEM images of NPs prepared from different polymer:PCBM blends with the inserting pictures of NP inks. It is convincible that TQ1 derivatives with functionalized side groups (TQ-FSG), which were protonated by volatile acid, could effectively stabilize TQ1:TQ-FSG:PCBM blend NP system. Using 10wt% loading of TQ1A in the blends, TQ1:TQ1A:PC₆₁BM (4:1:5) NPs were achieved with the size of 20-200 nm detected under SEM (**Figure 6.18a**). Larger particles were observed (**Figure 6.18b**) using TQ1-50A to form TQ1:TQ1-50A:PC₆₁BM (4:1:5) NPs, indicating lower concentration of amino groups in the material blend resulting in wider size distribution of forming particles. Moreover, spherical NPs were successfully obtained from TQ1:TQ1P4:PC₆₁BM (4:1:5) material combination (**Figure 6.18c**). The evidence of successfully made NPs without SDS have a great potential in the application of photoactive layer in OPVs. After the deposition of NP layer, volatile acid can be removed from the thin film under mild thermal annealing, which is also crucial to coalesce NPs. However, post preparation of NP dispersion, partial aggregation of the materials precipitated out from the water and resulted in low solid concentration in the stable water-dispersed NPs after filtration. Furthermore, large amount of aggregations and pinholes were observed on the films spin coated from these NP dispersion, which were mainly resulted from the film dewetting. Therefore, these SDS-free NP systems are still under optimisation before being utilised to form active layer in OPVs.

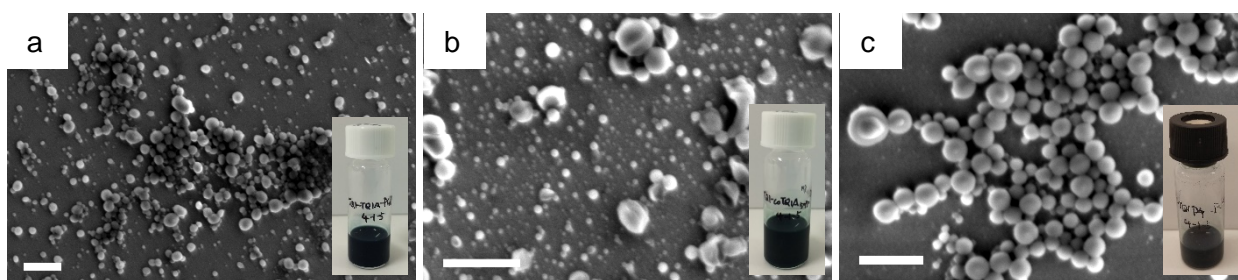


Figure 6.18 SEM images of NPs prepared from (a) TQ1:TQ1A:PC₆₁BM (b) TQ1:TQ1-50A:PC₆₁BM and (c) TQ1:TQ1P4:PC₆₁BM in (4:1:5 weight ratio). Scale bars are 500 nm.

Besides the preparation of NPs from TQ1:TQ-FSG:PCBM ternary blend, NPs were also synthesised using pure amine functionalized polymers blended with PCBM. The SEM image of film spin coated from TQ1-50A:PC₆₁BM (1:2.5) NPs (**Figure 6.19a**) indicates the nanostructure obtained post NP preparation being not spherical. The crystal-like nano structures are possibly resulted from the aggregation of materials or the shrink of NPs during drying. In the case of 20% amine containing polymer used to form TQ1-20A:PC₆₁BM (1:2.5) NPs, gross amount of aggregations in the water were observed (**Figure 6.19b insert**) after the preparation of the NP dispersion. The higher degree of agglomeration in the NP ink based on TQ1-20A compared to the ones containing TQ1-50A were attributed to the decrease of amino concentration in the dispersion, which significantly affected the stability of NPs.

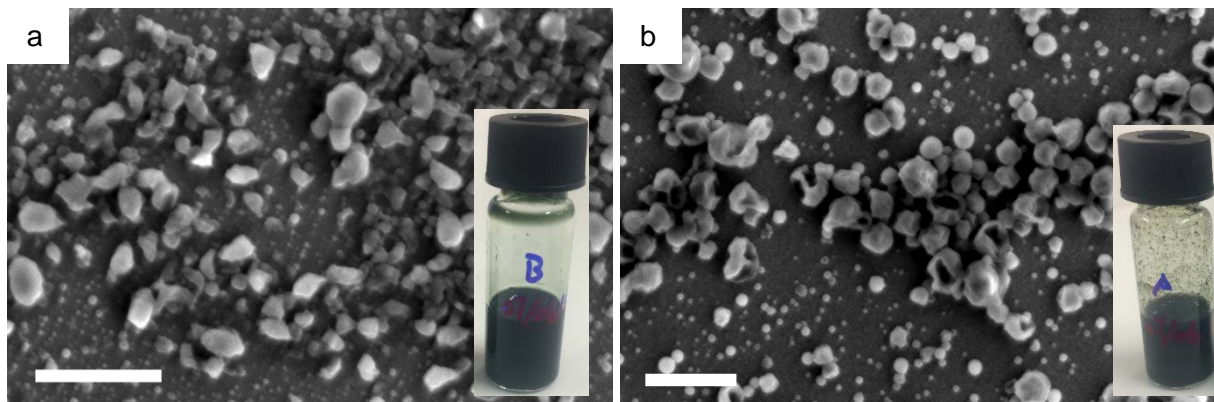


Figure 6.19 SEM images of NPs prepared from (a) TQ1-50A:PC₆₁BM (1:2.5 weight ratio) (b) TQ1-20A:PC₆₁BM (1:2.5 weight ratio) with inserted photos of NP inks. Scale bars are 500 nm.

6.4.3. NPs synthesised from TQ1 and PCSS

NPs based on TQ1 and PCSS were prepared by first dissolving TQ1 in chloroform and PCSS in MilliQ water, respectively, before two phases were mixed by vigorously stirring. The miniemulsion was obtained after ultra-sonication followed by heating to remove chloroform, offering water dispersion with solid content of 0.1wt%. The SEM image (**Figure 6.20**) clearly shows the spherical particles were obtained using PCSS. The solid state spin coated from the water-dispersed NPs gave the size range of approximate 60 nm to 200 nm in diameter. The solubility/dispersity of PCSS was

tested to be maximum of 0.53 mg/mL in aqueous solution, which hinders the realisation of NP ink with higher concentration for photoactive layer deposition. However, NPs containing ternary blend of donor polymer:PCBM:PCSS could be potentially prepared, in which PSCC might stabilize the NPs for OPV device fabrication.

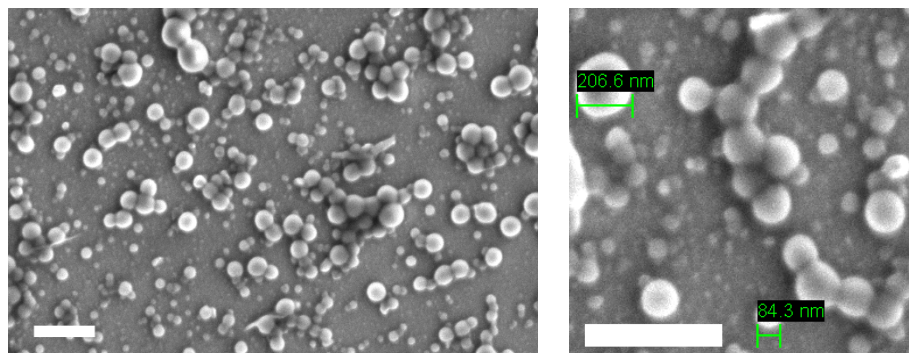


Figure 6.20 SEM images of TQ1:PCSS (1:1 weight ratio) NPs. Scale bars are 500 nm.

6.4.4. Introduction SDS in the preparation of NPs for photovoltaic study

Although NPs without an addition of surfactant could be successfully synthesised by miniemulsion method. The low solid content and unsatisfactory film quality from these water-dispersed NPs cannot meet the requirements for the fabrication of NP based solar cells. The OPVs based on TQ1:TQ1A:PC₆₁BM NPs without using SDS did not show any photovoltaic response. However, with the introducing of amine functionalized polymers, the unsuccessful OPVs could also be resulted from the hole trap formed by amino groups.³³ To exclude the interference from amino groups as the introduced parameter, BHJ solar cells were fabricated with TQ1:TQ1A:PC₇₁BM (4:1:12.5) from *o*-DCB as the active layer. Meanwhile NPs were prepared using TQ1:TQ1A:PC₇₁BM (4:1:12.5) with additional SDS to improve the film quality as well as to reduce the aggregation in NP inks. The device characteristics are shown in **Table 6.7**. Compare to TQ1:TQ1A:PC₇₁BM (4:1:12.5) BHJ devices, which gave 1.79% of PCE, the solar cells based on NPs with SDS presented unsatisfactory performance, reaching only 0.19% of PCE. The low performance could be resulted from the undesirable morphology of NP active layer as well as the insulating surfactant remaining in the devices.

Table 6.7 Device characteristics of TQ1:TQ1A:PC₇₁BM (4:1:12.5) NPs based OPVs and BHJ OPVs with inverted structure ITO/ZnO/active layer/MoO₃/Ag.

Active layer	J_{SC} (mA/cm ²)	FF (%)	V_{OC} (V)	PCE (%)
NPs	1.37	17	0.81	0.19
BHJ	4.71	54	0.70	1.79

Research on the preparation of SDS-free NPs from materials with functionalized groups is still an ongoing process and all parameters in the procedure will be carefully adjusted to realise the fabrication of SDS-free NP based OPVs.

6.5. NPs prepared with ammonium lauryl sulphate (ALS) surfactant

ALS 30% aqueous solution was purchased from Sigma Aldrich. As an ionic surfactant, ALS is also a commonly applied chemical compound in commercially available detergent and has the same alkyl sulphonic structure (**Figure 6.21a**) as in SDS. Using ALS as the surfactant as the alternative of SDS in the preparation of NPs, the ammonium ion remaining in the NP forming film could theoretically be released during the thermal annealing of NP film. Hence, the potential charge traps generated by the ion are eliminated. But the influence of the remaining dodecyl sulphonic acid on the NP device performance needs to be studied.

6.5.1. Thermal property of ALS and ALS assisted NP formation

TGA measurement was performed on ALS 30% water solution to investigate the decomposing property of ALS. Due to that commercially available ALS contains large quantity of water (70%), ALS sample was isothermally treated at 100 °C for 10 min in nitrogen atmosphere to remove water. It can be observed from **Figure 6.21b** that ALS sample experienced continuous weight loss from 100 °C to approximate 140 °C, which is assumed to be the releasing of ammonium and forming of sulphonic acid. A major thermal decomposition occurs beyond 200 °C. The former one was confirmed by testing the pH level of water solution that dissolved 130 °C treated ALS, which shows to be more acidic (pH=1) compared to the pristine ALS solution (pH=6), indicating the conversion from ammonia salt to sulphonic acid.

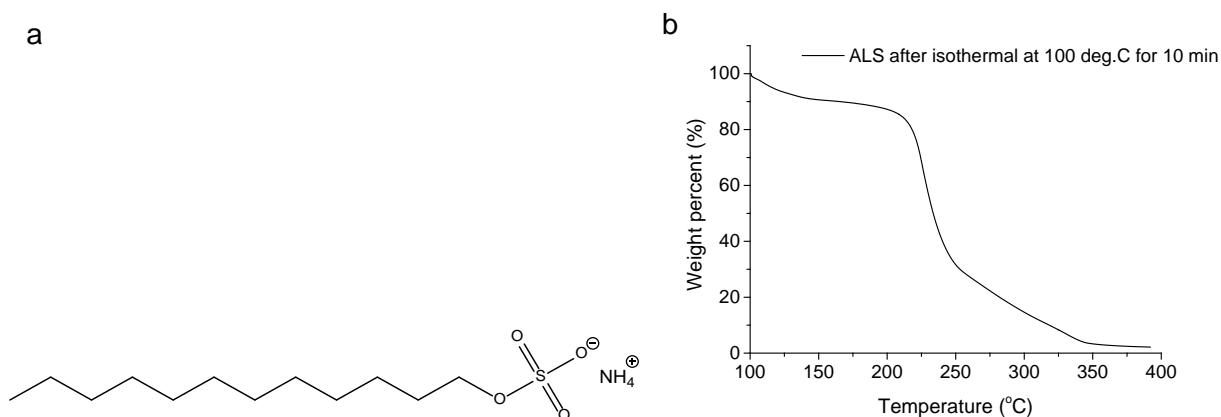


Figure 6.21 (a) Chemical structure of ALS. (b) TGA curve of ALS after isothermal annealing at 100 °C for 10min. Scan rate is 10 °C/min.

To investigate the effectiveness of using ALS in the miniemulsion method to prepare NPs, TQ1 was dissolving in chloroform prior to mixing with diluted ALS aqueous solution, followed by ultrasonication and then the removal of organic solvent. After the excess of free ALS being removed via centrifugal dialysis, stable water dispersed TQ1 NPs were achieved. **Figure 6.22** shows the nanoparticles of neat TQ1 polymer with spherical shape were successfully prepared using ALS.

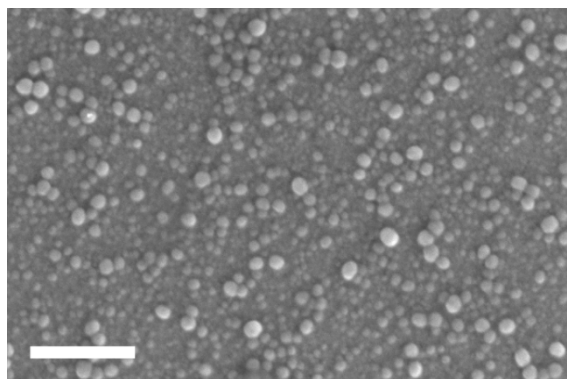


Figure 6.22 SEM image of pure TQ1 NPs prepared with ALS. Scale bar is 400 nm.

6.5.2. Photovoltaic performance

To study the effect of ALS on NP based OPVs with the inverted structure (ITO/ZnO/NPs/MoO₃/Ag), NPs were prepared using TQ1:PC₆₁BM (1:2.5 weight ratio) with surfactant ALS and SDS, respectively. The device characteristics are shown in **Table 6.8**. Thermal annealing at 140 °C was introduced to both NP films and the complete devices. The solar cells based on ALS batch NPs presented very poor photovoltaic performance, only 0.15% of maximum PCE was obtained. Meanwhile, solar cells incorporating SDS stabilized NPs gave 0.86% of PCE, which was fabricated without optimisation. One possible explanation of the poor device performance observed on ALS containing devices could be the sulphonic acid generated after thermal annealing of NP forming layer at 140 °C. The sulphonic acid could possibly interact with the MoO₃ interlayer and change the work function of the hole transport layer. Therefore, using PEDOT:PSS as the alternative of MoO₃ might improve the device performance. Another reason could be the deterioration of the morphology in the active layer after thermal annealing of NP films and post-annealing.

Table 6.8 Device characteristics of OPVs TQ1:PC₆₁BM (1:2.5) NPs using different surfactants with inverted structure ITO/ZnO/NPs/MoO₃/Ag.

Surfactant	Post annealing condition	J_{sc} (mA/cm ²)	FF (%)	V_{oc} (V)	PCE (%)
ALS	No	0.70	23	0.60	0.10
ALS	140 °C, 4 min	1.24	25	0.50	0.15
SDS	No	3.80	32	0.71	0.86
SDS	140 °C, 4 min	3.76	28	0.69	0.73

NP film were thermally annealed at 140 °C for 5 min in the glove-box.

SEM images shown in **Figure 6.23** indicate that after thermal annealing of NP films, which deposited from ALS containing NP ink, large aggregation forming on the top surface. The SDS batch NPs show similar surface topographic change upon annealing. The large aggregation is primarily attributed from the crystallization of PC₆₁BM after thermally heated up to 140 °C. Although the large phase separation observed affect the charge separation in annealed NP active layer, the discrepancies of photovoltaic performance between ALS-NP OPV and SDS-NP OPV cannot be simply imputed to the unsatisfactory morphology. The effect of remaining sulphonic acid in NP active layer needs to be further studied. Otherwise other techniques need to be applied to remove ALS surfactant or sulphonic acid from NP forming active layer to eliminate its negative influence to the photovoltaic performance before ALS can successfully replace SDS in the preparation of NPs using miniemulsion method.

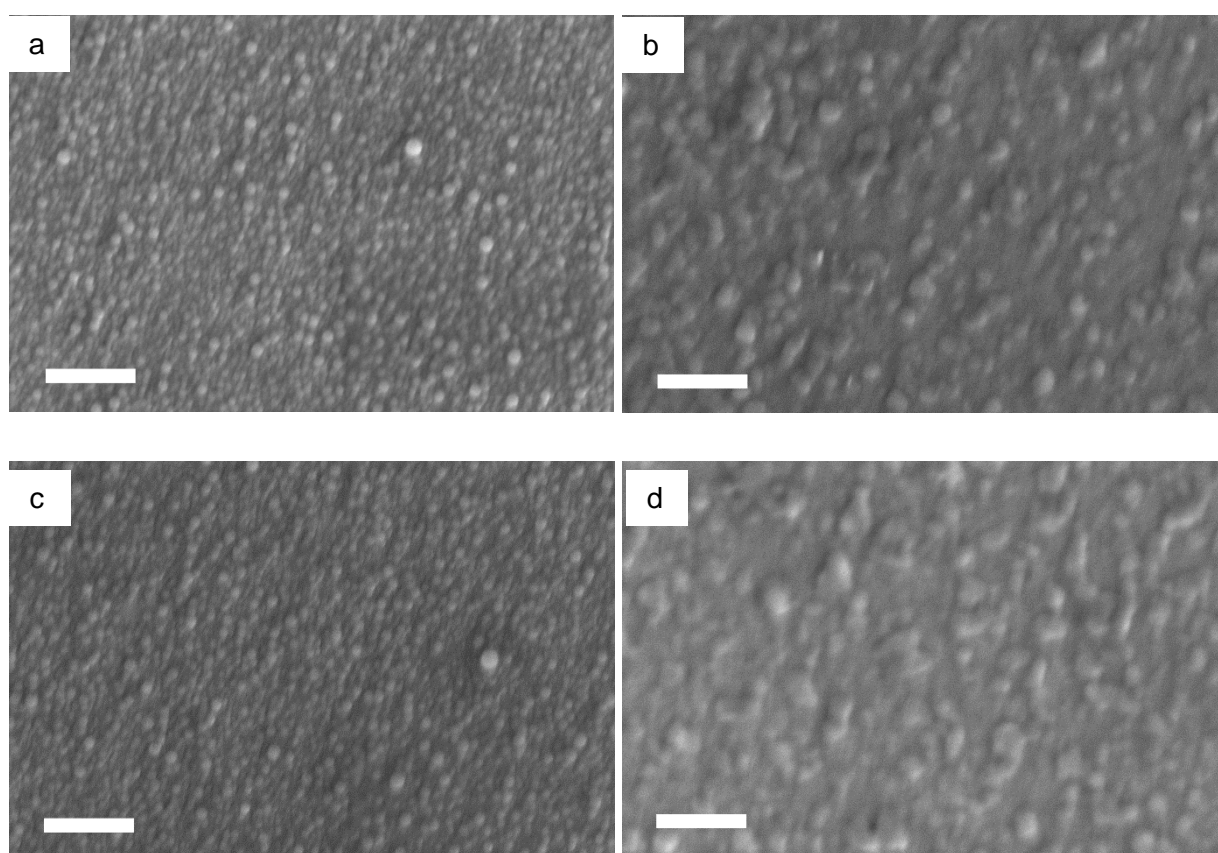


Figure 6.23 SEM images of ALS batch TQ1:PC₆₁BM NP film as-spun (a) and annealed at 140 °C for 5 min (b); SDS batch TQ1:PC₆₁BM NP film as-spun (c) and annealed at 140 °C for 5 min (d). Scale bars are 400 nm.

6.6. Possibility of substituting SDS

Due to the insulating property, SDS used to stabilize NPs remaining in the solar cells was reported to have negative influence on device performance.^{14, 34} The negative influence is mainly resulted from the ions introduced by SDS. Hence, efforts have been made trying to substitute SDS with cleavable and non-ionic surfactants to assist NP formation without the presence of ions in the final

device. In addition, post preparation of NPs incorporating SDS, different materials have been investigated, aiming to reduce SDS content in aqueous NP inks.

6.6.1. Substituted surfactants

Utilisation of cleavable surfactant³⁵ is one possible way to synthesis NPs from conjugated materials for OPVs. As described earlier in this chapter, cleavable surfactant ALS has been used and successfully assisted the formation of TQ1:PCBM NPs. However the decomposed alkyl sulphonic acid couldn't be thermal removed and remained in the complete devices, resulting in poor photovoltaic performance. As far as we know, surfactants that have been applied in the emulsification of water-oil system have chemical structure consisting hydrophobic alkyl or aryl groups and hydrophobic groups. Therefore, an ionic compound octylammonium formate was synthesised from octylamine and formic acid as shown in **Figure 6.24a**. Due to the weak ionic bonding and low boiling point of octylamine (175-177°C) and formic acid (100-101°C), octylammonium formate is hypothesized to be a potential cleavable surfactant that could facilitate the formation of conjugated NPs.

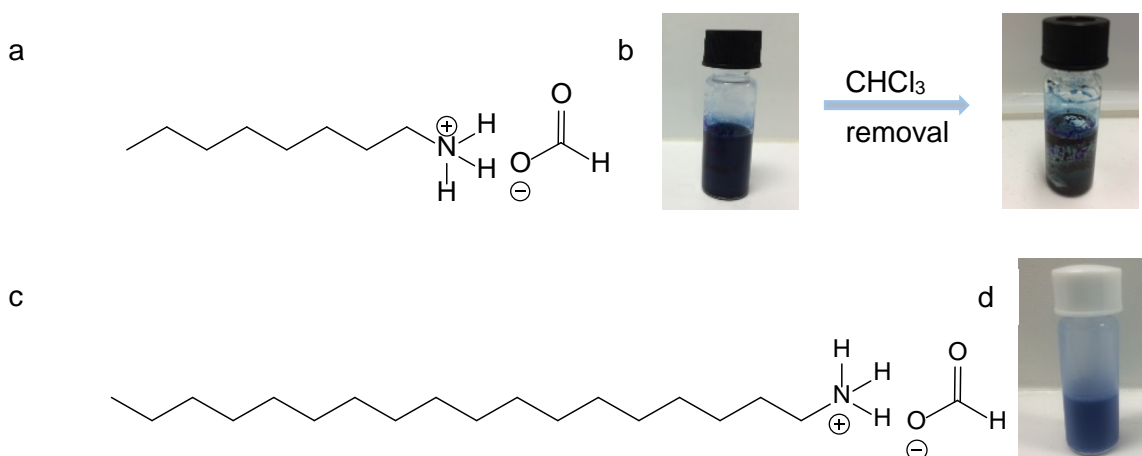


Figure 6.24 (a) Chemical structure of octylammonium formate. (b) Photos depicting miniemulsion formed with octylammonium formate and suspension after chloroform removal. (c) Chemical structure of octadecylammonium formate and (d) forming emulsion.

To investigate its effectiveness of micelle formation, octylammonium formate was used in TQ1:PCBM (1:1) system following general miniemulsion method, but in the absence of SDS. Post ultra-sonication an unstable miniemulsion consisting chloroform dispersed phase TQ1:PCBM was obtained. However, large amount of solid aggregate was formed after the removal of chloroform as depicted in **Figure 6.24b**. The gross aggregation could be a result from the inadequate stability of the miniemulsion, i.e. agglomeration from dispersed droplets in the continuous aqueous phase. Since the alkyl group in octylammonium formate has smaller hydrophobic unit compared to that in SDS, octadecylammonium formate was synthesised from octadecylamine and formic acid as shown in **Figure 6.24c**, and subsequently used to emulsify TQ1:PCBM CHCl_3 solution with water. **Figure 6.24d** presents the TQ1:PCBM miniemulsion being successfully formed assisted by

octadecylammonium formate. Considering the intrinsic high boiling point of octadecylamine (346.8 °C), this surfactant couldn't be removed from NP system post preparation. Therefore continuous research were carried out on investigating other possible non-ionic surfactants.

One challenge of the usage of non-ionic surfactants is their intrinsic low cloud point compared to the ionic counterpart, i.e. SDS. The cloud point is defined as the temperature an aqueous solution of a water-miscible surfactant starts to phase separate, which is a critical characteristic of surfactants.³⁶ When a given non-ionic surfactant is used in the miniemulsion method to prepare semiconductive NPs, the high shearing force during ultra-sonication could increase the temperature of the mixture to be above its cloud point. Furthermore, high temperature used to evaporate miniemulsion dispersed phase solvent can also reach the cloud point of the non-ionic surfactant used. Therefore, the instability of the surfactant used could result in the aggregation of particles. Several non-ionic surfactants tested in the NP preparation are shown in **Figure 6.25**. By checking the clarity of 1% aqueous non-ionic surfactant solution as a function of temperature, the approximate cloud points of the non-ionic surfactants tested to prepare NPs were estimated and shown in **Table 6.9**.

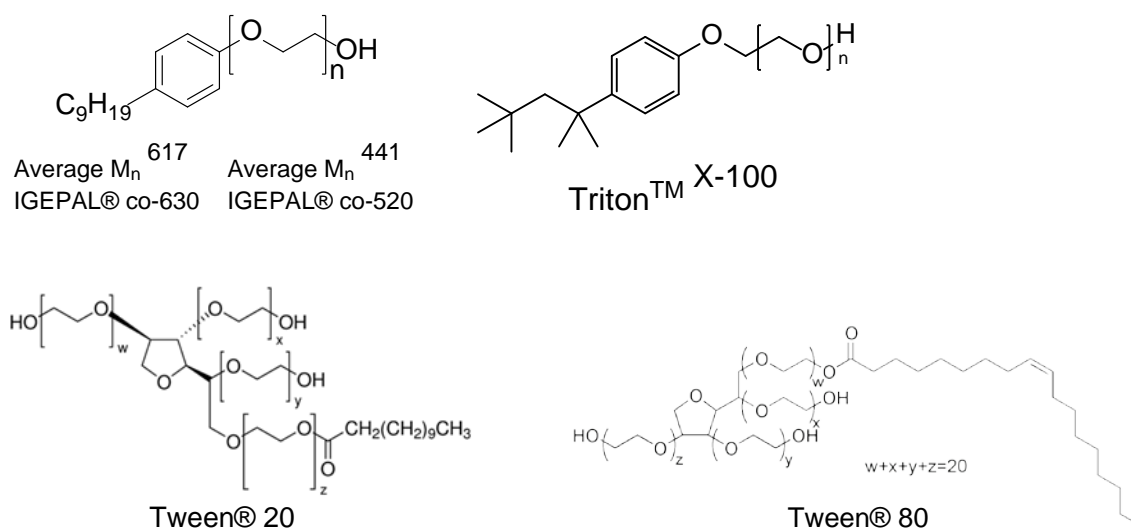


Figure 6.25 Chemical structure of the non-ionic surfactants.

Table 6.9 Estimated cloud points of non-ionic surfactants.

Non-ionic surfactants	Cloud point (°C)
IGEPAL® co-520	<4
IGEPAL® co-630	54
Triton™ X-100	65
Tween® 20	76
Tween® 80	65

It has been reported that IGEPAL® series surfactants can be utilised to assist the formation of metal oxide NPs,³⁷⁻³⁸ but only limited number of publications studied the using of non-ionic surfactants to synthesise NPs from conjugated polymers.^{36, 39} TQ1 NPs (**Figure 6.26a**) were prepared using IGEPAL® co-630 as the surfactant via miniemulsion method. But due to the large amounts of aggregation formation post the removal of miniemulsion dispersed phase solvent, NP ink with very low solid loading was obtained after filtration. **Figure 6.26b** shows the photo of forming emulsion and **Figure 6.26c** for the aqueous TQ1 NP ink, indicating the inadequate stability of semiconducting NPs using IGEPAL® co-630.

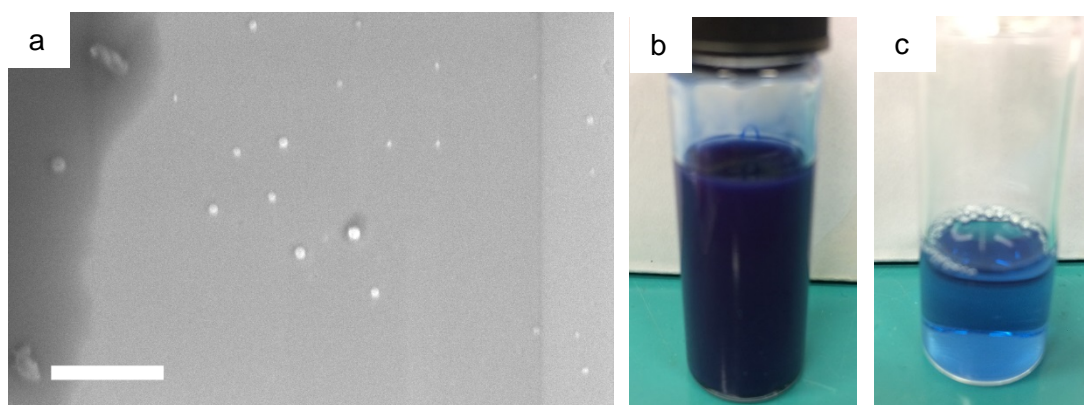


Figure 6.26 (a) SEM image of TQ1 NPs prepared using IGEPAL® co-630. Scale bar is 1 µm. Photos of (b) TQ1 miniemulsion and (c) stable TQ1 NP ink after filtration through 0.45 µm filter.

Furthermore, the other non-ionic surfactants listed in the **Table 6.9** were tested respectively in TQ1 chloroform-water system but unfortunately no successful miniemulsion was achieved.

6.6.2. SDS removal post preparation of NPs

The difficulty of achieving stable NPs using cleavable or non-ionic surfactants impedes the preparation of SDS-free NPs with high solid content for OPVs. Therefore, the removal of residual SDS post NP preparation is another possible way to eliminate/reduce the negative effect from SDS on NP based OPVs. In our typical preparation procedure of NPs using SDS, most of the free surfactant was removed from the aqueous inks by centrifuge assisted dialysis, whereas the surface-bound surfactant couldn't be simply detached from active material NPs without inducing agglomeration. Hence, introducing other stabilizing agent is one possible solution to facilitate the detachment of surface-bound SDS on NPs. To prove this concept, ionic compound octylammonium formate was added to TQ1:PC₆₁BM NP ink prior to the centrifugal dialysis. Unfortunately this experiment was unsuccessful and the aggregation of particles were segregated from water shown in **Figure 6.27**. The severe phase separation was assumed to be resulted from the change of surface charge introduced by additional ionic compound.

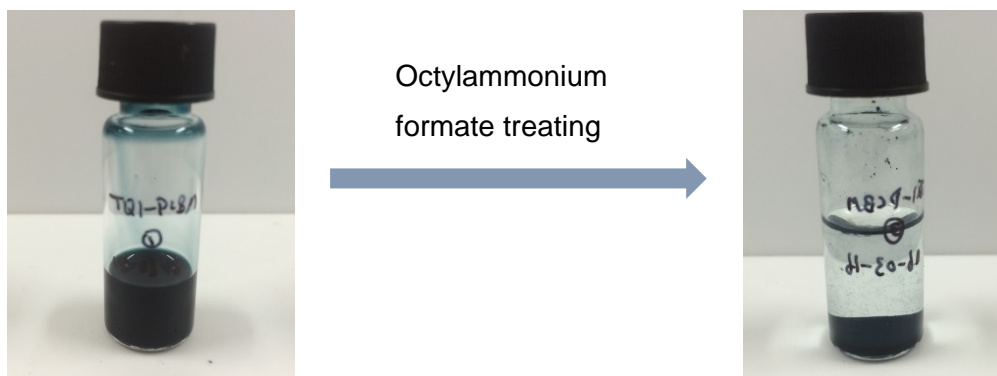


Figure 6.27 Photos showing TQ1:PC₆₁BM NP inks before and after treatment with octylammonium formate.

Unlike SDS, which stabilizes NPs based on the electrical forces between the negative surface charges, non-ionic species assist micelle or particle formation based on the hydrogen bond forming between their hydrophilic groups and water.⁴⁰ Hence, non-ionic surfactants were tested to study whether they can promote the removal of SDS from NP ink. IGEPAL® co-630 was introduced to TQ1:PCBM NPs prepared using SDS for the purpose of replacing bound SDS without severe aggregation of NPs. The experiment was performed by mixing aqueous IGEPAL® co-630 solution with TQ1:PCBM NP dispersion, of which most of the free SDS already being removed by dialysis. The mixture was allowed to stir for 2 hr followed by centrifugal dialysis with IGEPAL® co-630 solution and then pure water. To exclude the interference from extra dialysis steps, a control experiment using pure water instead of IGEPAL® co-630 solution to treat the same batch of NPs was performed in the same approach described.

Energy Dispersive X-ray Spectroscopy (EDS) was performed on solid film of NPs to detect sodium content in NP samples, which was originated from SDS. The EDS analysis reports and corresponding SEM images of NP films are shown in **Figure 6.28**. Before any treatment was introduced to TQ1:PCBM NPs, the Na/C atomic ratio was measured to be 2.8/78.5 (**Figure 6.28a**), which decreased to 0.2/81.3 (**Figure 6.28b**) after NP ink being treated by IGEPAL® co-630. Meanwhile the control sample was measured to have the Na/C atomic ratio of 1.2/89.0 (**Figure 6.28c**), indicating that IGEPAL® co-630 promoted SDS removal post NP preparation. Compared to NP sample without treatment (**Figure 6.28d**) and the one treated with water (**Figure 6.28f**), the SEM image in **Figure 6.28e** shows aggregation of NPs in the solid state, further proving the concept that non-ionic surfactant could replace surface-bound SDS. Although most of the SDS could be detached from TQ1:PCBM NPs using IGEPAL® co-630, the aggregation of NPs deteriorated the morphology of forming film, which is unwanted for OPV fabrication. Hence, further studied need to be implemented on the replacement of SDS without introducing aggregations.

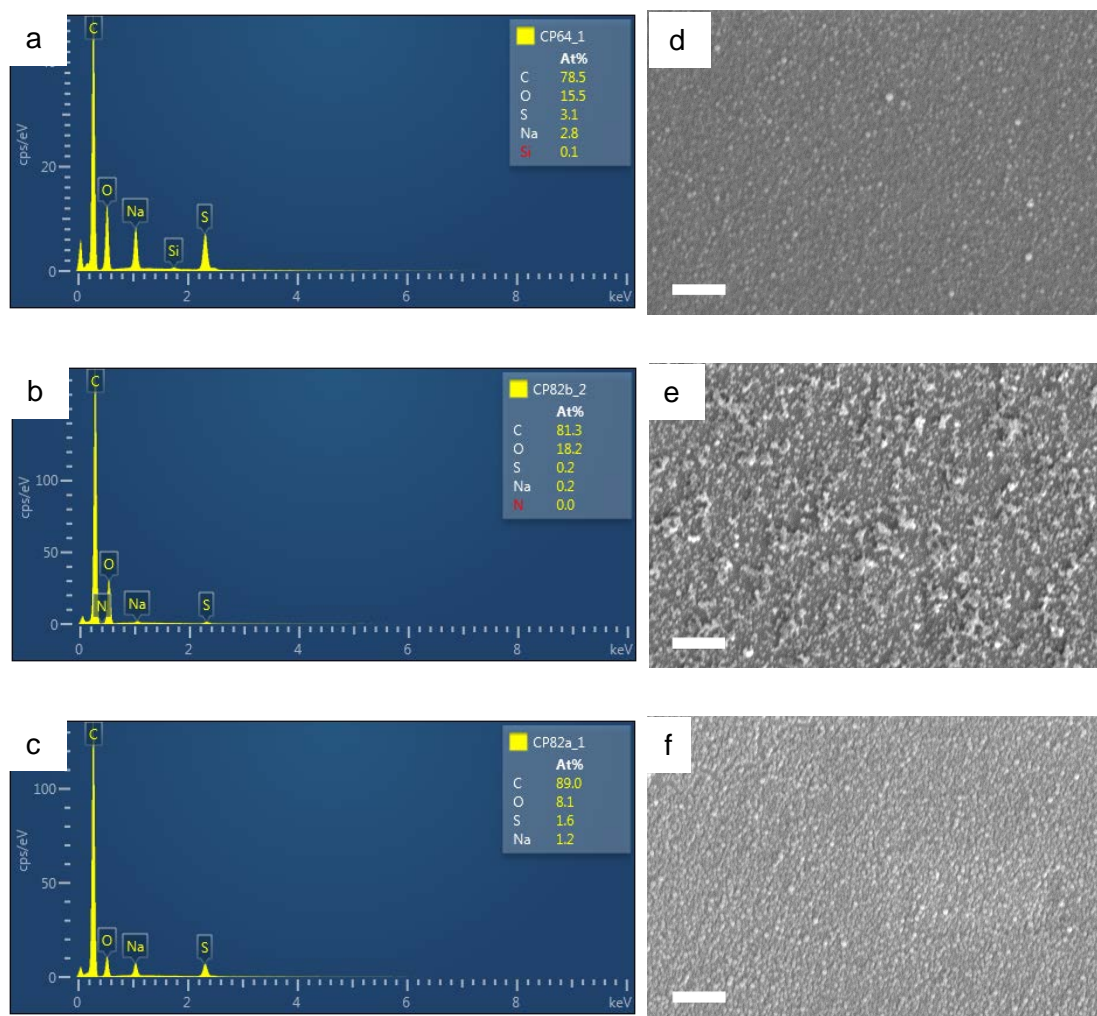


Figure 6.28 EDS element analysis reports (a-c) and SEM images (d-f) of TQ1:PCBM NPs without any treatment (a and d), treated by IGEPAL® co-630 solution (b and e) and treated by pure water as control experiment (c and f). Scale bars are 500 nm.

6.7. Precipitation method

It has been reported that nanoparticles can be successfully made from polymer P3HT and fullerene acceptor using precipitation method described in Chapter 3 without introducing surfactant and ultrasonication process.^{4, 24, 41} However, the inadequate stability of these surfactant-free NPs requires the fabrication of NP solar cells to be done immediately post preparation of NP ink. Moreover, the deposition of NP active layer from this kind of precipitated NP ink with low solid content was commonly performed by multiple spin-coating⁴ or spray coating⁶ to offer ideal thickness. Hence, this type of NP ink published is not suitable for industrial up-scaling in printed solar cells until we find out how to stabilize NPs with different donor:acceptor blends using precipitation method.

6.7.1. Different binary system using precipitation method

The experiments to study the possibility of using precipitation method on different conjugated systems including already published P3HT system have been performed. The preparation was following the procedure reported by Darwis et al.⁴¹ with chloroform as the solvent for active materials

and EtOH as the non-solvent to disperse particles. P3HT, TQ1 and PTNT (structure shown in **Figure 6.29**) were dissolved with PC₆₁BM respectively in chloroform prior to the precipitation in EtOH under vigorously stirring at room temperature to offer EtOH ink with solid load of 0.2wt%. Unfortunately, rapid aggregations were formed immediately post precipitation procedure in samples containing TQ1 and PTNT (**Figure 6.30a, b**). In contrast, P3HT:PCBM NPs precipitated in the same approach exhibited moderate stability in EtOH dispersion shown in **Figure 6.30c**. The SEM images of precipitated samples consisting TQ1:PCBM (**Figure 6.30d**) show large chunks of agglomerates, however, existence of spherical NPs was observed. Similar observation was also found in PTNT:PCBM samples (**Figure 6.30e**). It is assumed that NPs can form in different conjugated system using precipitation method, but the limitation of stability impedes the increase of solid concentration in stable NP inks. Therefore, the procedure of precipitation method needs to be carefully studied in order to achieve stable NPs using other conjugated polymers as an alternative of P3HT for OPVs. Beside the optimisation of the experimental parameters, one possible way to achieve stable NPs using the precipitation method is to modify the polymer structure by replacing the aliphatic side groups with hydrophilic side chains, such as oligoethylene glycol or end-cap the polymer backbone with hydrophilic unit to facilitate the self-assembly.⁴² Another possible method is to introduce additional stabilising agent, such as ionic and non-ionic surfactants to assist the formation of small NPs with the surface stabilised with hydrophilic groups.

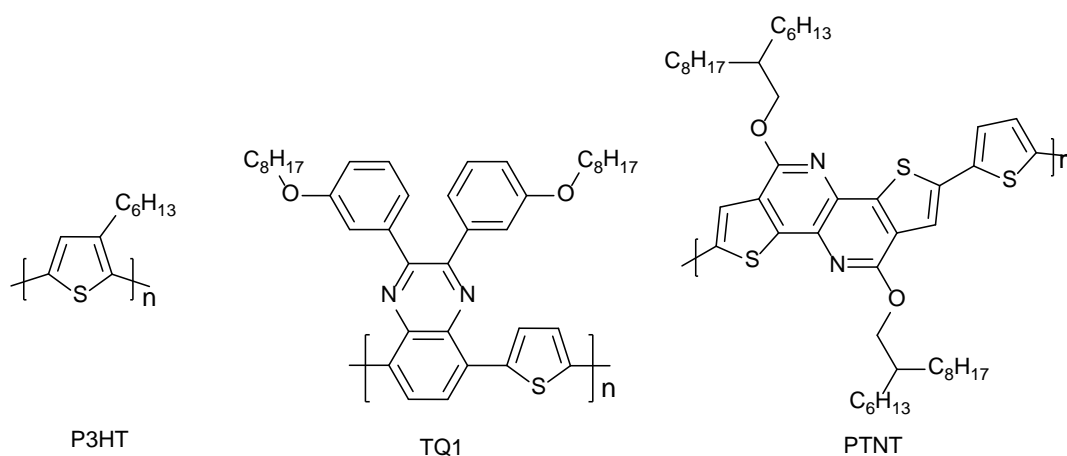


Figure 6.29 Chemical structures of P3HT, TQ1 and PTNT.

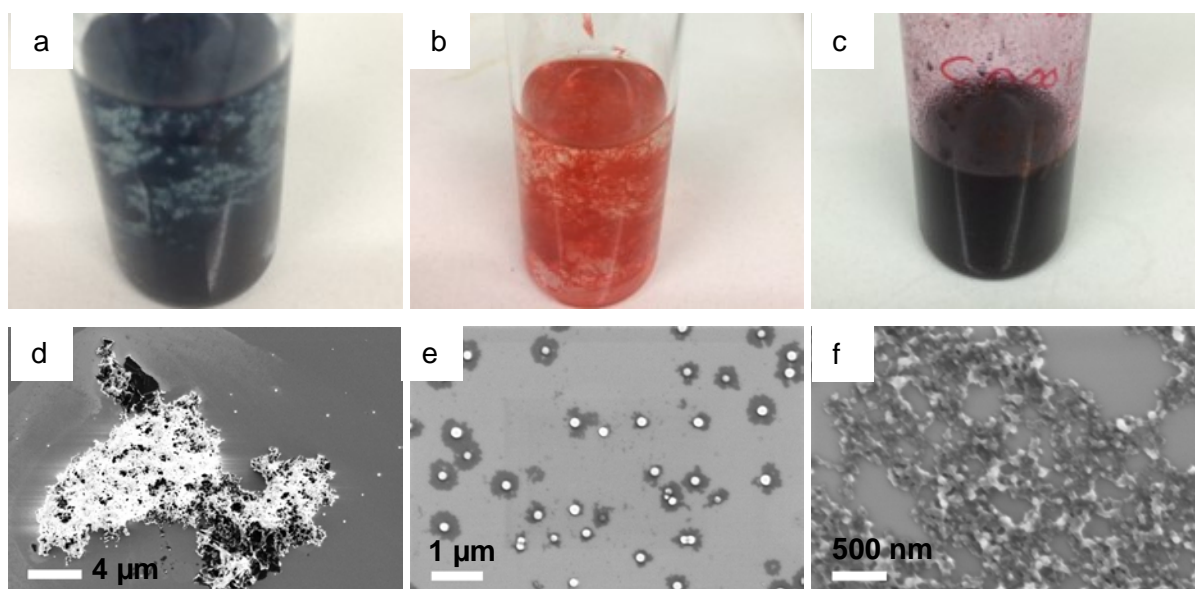


Figure 6.30 Photos (a-c) and SEM images (d-f) of (a, d) TQ1:PC₆₁BM, (b, e) PTNT:PC₆₁BM and (c, f) P3HT:PC₆₁BM particles post preparation via precipitation method.

6.7.2. Study of the experimental parameters in the preparation procedure

The undesirable results presented by TQ1:PC₆₁BM and PTNT:PC₆₁BM particles prepared using precipitation method indicate that the experimental parameters in this precipitation procedure needs to be thoroughly studied and modified. Unlike miniemulsion method, which highly depends on the shearing force of ultra-sonication to form miniemulsion from two immiscible phase, precipitation method form particles by solid precipitating out when two miscible solvents are blended. Therefore performing precipitated NPs could theoretically be achieved by altering the initial solvent and precipitated non-solvent as well as adjusting the concentration of active materials. Furthermore, other factors that influence the stability of NPs should also be considered, such as the surface energy of material used and temperature during precipitation, as high temperature will lead to high mass transfer and high degree of agglomeration. Since different polymers have different physical properties, such as viscosity, crystallinity, solubility or dispersity in different solvent systems, well-studied amorphous polymer TQ1 was thus investigated in the precipitation method to avoid the interference from intrinsic properties of materials. Two batches of TQ1 with different molecular weight ($M_n = 53$ kg/mol and $M_n = 10.8$ kg/mol, respectively) were used to compare the influence of molecular weight to the NPs forming using precipitation method.

It is already known that shearing force introduced by rapid stirring leads to different degrees of mass transfer when different stirring speed is used during mixing of solution.⁶ Moreover, different force distributed in the containers with different size could also result in different particle size, which directly influence the stability of NP ink. To gain better control of NP work presented in this thesis, experiment container, stirrers and stirring plate with temperature control remained constant.

By varying the initial concentration of TQ1:PCBM in CHCl_3 and the final concentration of the blend in EtOH (**Table 6.10**), it was disappointing to realise that even using 0.5 mg/mL CHCl_3 solution, no stable NP ink can be achieved after the removal of chloroform. In the meantime, methanol was also used as a precipitation solvent and LMW-TQ1 was studied as an alternative of HMW-TQ1, but only aggregation was observed. Further diluting the solution to form NPs could be tested, however, the obtained ink cannot fit the purpose of using it for OPVs because of the ultra-low active material content.

Table 6.10 Experimental parameters study in the precipitation method to prepare TQ1:PCBM NPs. All the conditions listed led to aggregation of materials immediately post preparation.

Sample	Initial concentration in CHCl_3 (mg/mL)	Final concentration in EtOH (mg/mL)
1	15	2.010
2		1.005
3	7.5	1.005
4	3.8	0.760
5		0.532
6	0.5	0.100
7		0.067
8		0.050

Considering TQ1:PCBM couldn't be well dispersed in alcohol under the experimental conditions, tetrahydrofuran (THF)-water solvent system were used in precipitation method. By varying the initial and final concentration, stable surfactant-free NPs ink was achieved with solid content of 0.05 mg/mL in aqueous dispersion. It should be noted that post precipitation, THF was removed by rotary evaporation instead of heating to avoid high temperature induced aggregation. Since this low content of active materials cannot meet the requirement for the deposition of active layer by spin-coating or roll-to-roll printing, further concentration steps were performed by centrifugal dialysis to reduce the volume of ink. After one step of dialysis, the solid content was increased to 0.25 mg/mL and no visible aggregation was found, whereas two steps of dialysis resulted in the concentration of 1.25 mg/mL with small amount of aggregation phase-separated from water. Due to the appearance of agglomeration, further concentration step was discontinued. **Figure 6.31** shows the SEM images of TQ1:PCBM NPs before and after dialysis steps. Unlike TQ1:PCBM NPs prepared using miniemulsion method, the nano structure of precipitated particles is not completely spherical, which is possibly attributed to the absence of stabilizing surfactant.

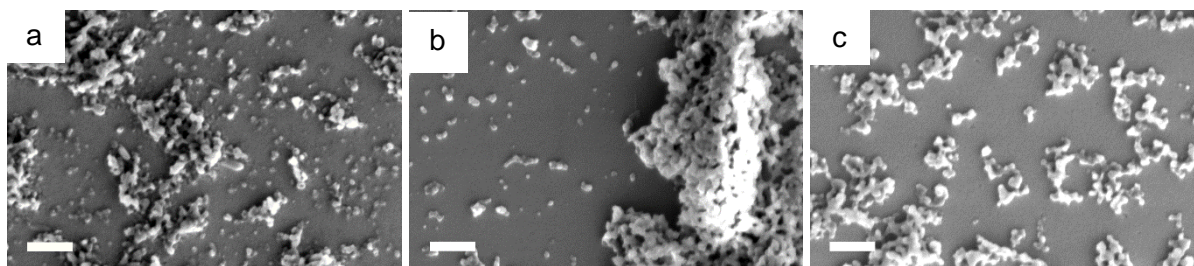


Figure 6.31 SEM images of TQ1:PCBM (1:2.5 weight ratio) NPs (a) without dialysis, (b) with one step dialysis and (c) with two steps of dialysis. Scale bars are 500 nm.

6.7.3. Precipitation method assisted with non-ionic surfactant

Due to the unsuccessful results obtained by using precipitation method to form surfactant-free TQ1:PCBM NPs with high solid content, extra stabilizing agent was subsequently used in the procedure aiming to achieve high concentration of NP inks. The non-ionic surfactants IGEPAL® co-520⁴³ and IGEPAL® co-630 were tested respectively in the precipitation method to investigate their effectiveness of stabilizing NPs in the concentration procedure.

To gain a better control of the experimental parameters in the precipitation procedure, TQ1:PCBM (1:2.5 weight ratio) was dissolved in THF with the initial concentration of 0.5 mg/mL and equal weight of non-ionic surfactant compared to active material was mixed with THF solution. The THF solution was subsequently transferred to water under vigorous stirring to precipitate NPs followed by vacuum assisted rotary evaporation to remove THF, offering aqueous ink with solid content of 0.05 mg/mL. To concentrate the aqueous inks, continuous rotary evaporating was carried out on the dispersion. In the case of using IGEPAL® co-520, aggregation formed when the final concentration reached 0.225 mg/mL. The aggregation could be attributed to the phase separation between this surfactant and water under water evaporation process, which was done at 40 °C and 30 mbar. When IGEPAL® co-630, which has cloud point above 50 °C, was utilised in the process, moderately stable NPs ink with approximate 30 mg/mL concentration was achieved. It should be noted the ink was concentrated from 0.05 mg/mL to 0.32 mg/mL via rotary evaporation followed by centrifugal dialysis to reach final solid content. The SEM image shown in **Figure 6.32** reveals nanoparticles being successfully achieved by non-ionic surfactant assisted precipitation method. The particle size was estimated via dynamic light scattering (DLS) to be 85.2 ± 50.7 nm of the z-average diameter.

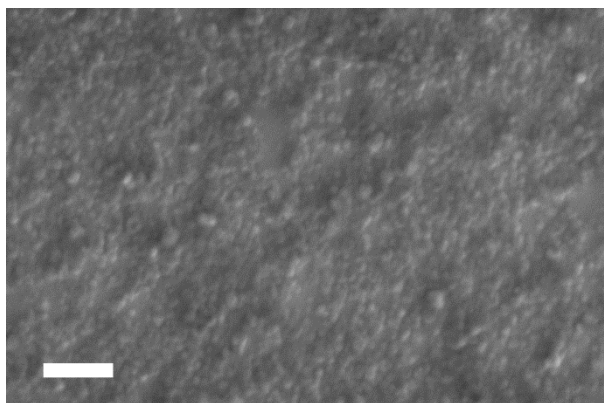


Figure 6.32 SEM image of TQ1:PC₆₁BM (1:2.5 weight ratio) NPs prepared by precipitation method with IGEPAL® co-630. Scale bar is 500 nm.

To evaluate the photovoltaic performance of precipitated NPs containing IGEPAL® co-630, inverted device with the structure of ITO/ZnO/NPs/MoO₃/Ag was fabricated. Due to the insufficient thickness of NP active layer by one step spin-coating, multiple coating process (4 layers) was performed with drying at 90 °C in between to avoid delamination of NPs. The complete active layer was thermally annealed at 120 °C to coalesce NPs prior to the deposition of hole transport layer and Ag electrode. It is found that the intrinsic high boiling point of IGEPAL® co-630 impedes the removal of it under vacuum and the percolation/diffusion of surfactant to the electrode altered the appearance of Ag electrode to be grey. Unfortunately no photovoltaic effect was observed on these NP devices, which could be a result from the large amount of insulating surfactant remaining in the device. Therefore the effect of remaining non-ionic surfactant on OPVs needs to be carefully investigated and methods to remove any insulating compound from photoactive layer needs to developed.

6.7.4. NPs containing functionalized conjugated polymers using precipitation method

It is already experimentally confirmed that conjugated NPs can be successfully prepared using precipitation method with additional non-ionic surfactant to offer high concentration. But the insulating property of introduced surfactant is unwanted in the NP based solar cells. Hence the usage of semiconducting stabilization agent could be one possible way to realise the NP preparation by precipitation method for solar cell fabrication.

In the NP study using miniemulsion method, we already know that TQ1 derivatives functionalized with amino side chains assist the formation of miniemulsion and stabilize NPs in the aqueous dispersion. Hence, tertiary amine functionalized polymers were further studied to understand if they can stabilize NPs using precipitation method. Another consideration of the utilisation of amino polymers is that they can dissolve in alcohol after protonation with acid, offering charged species in the non-solvent used for conjugated NPs, which could possibly realise the preparation of NP alcohol dispersion using precipitation method. TQ1-50A was dissolved in isopropyl alcohol (IPA) with formic acid considering IPA has higher boiling point compared to THF, which was used to dissolve neat PC₆₁BM. The PCBM solution was transferred to IPA solution at 60 °C under vigorously stirring to

precipitate particles followed by continuous heating to remove residual THF solvent. The SEM image shown in **Figure 6.33** reveals TQ1-50A:PC₆₁BM NPs being successfully achieved through this precipitation procedure, though the size is not optimised and macro-scale agglomeration was observed post preparation.

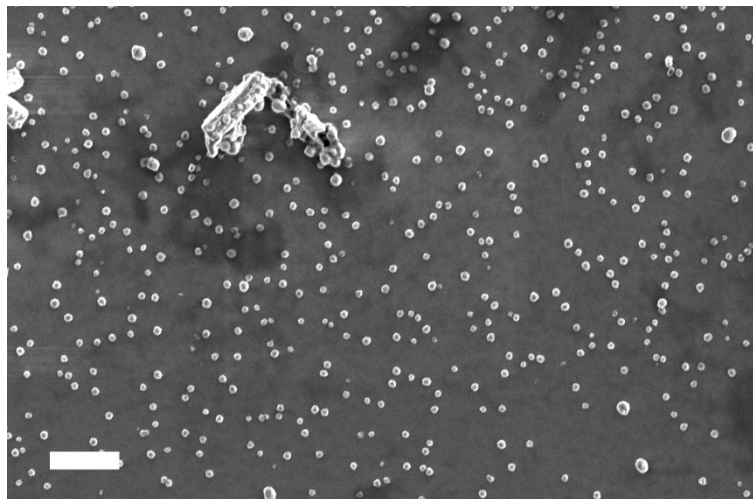


Figure 6.33 SEM images of precipitated TQ1-50A:PC₆₁BM NPs. Scale bar is 2 μ m.

The result opens the possibility to prepare precipitated NPs with amino polymers. TQ1:TQ1A:PC₇₁BM (4:1:12.5) nanocomposite can be achieved via miniemulsion method as described earlier in this chapter, and OPV based on which achieved PCE of 0.19%. Therefore, surfactant free TQ1:TQ1A:PC₇₁BM NPs were prepared via precipitation method following the similar procedure in **7.7.3** and subsequently fabricated as active layer in OPVs. To avoid aggregation during concentrating step, no dialysis was carried out, and the final ink was obtained with 3.5 mg/mL. Since large amount of defects were accumulated by the multiple steps of spin-coating, resulting in deteriorated morphology, no photovoltaic effect was observed on these NP OPVs. The precipitation procedure assisted with amino polymers is still under modification, aiming to achieve stable NP dispersion for efficient organic solar cells.

6.8. Experimental

6.8.1. Materials

TQ1 and PTNT ($M_n=55.7$ kg/mol, $M_w=163.2$ kg/mol) were synthesised in our lab as per previously reported procedures.^{18, 44} The molecular weight was measured by size exclusion chromatography (SEC) using a high temperature SEC at 150 °C in 1,2,4-trichlorobenzene and all values are relative to polystyrene standards. In the case of NP forming investigation, TQ1 used in the study was the high molecular weight batch, with $M_n=53$ kg/mol and PDI of 2.5.

PC₆₁BM, PC₇₁BM, C₆₀ and C₇₀ were purchased from Solenne BV. The surfactants, such as SDS, ALS (30% aqueous solution), IGEPAL® co-520 and IGEPAL® co-630 were purchased from Sigma

Aldrich and were used without further purification. Triton™ X-100, Tween® 20 and Tween® 80 were obtained from collaborators and are commercially available from Sigma Aldrich.

TQ1A, TQ1-50A, TQ1-20A and TQ1P4 were synthesised by Stille coupling polymerisation. The detailed synthetic procedure can be found in **Appendix A**. The fullerene derivative PSCC was synthesised in our lab by Desta.

6.8.2. Preparation of nanoparticles

6.8.2.1. General preparation of NPs using the miniemulsion method

Polymer or polymer-fullerene blends were dissolved in 560 µL of organic solvent (chloroform, *o*-xylene or anisole) at 35 °C with stirring at 500 rpm for 2 hours. Meanwhile the aqueous phase was prepared by dissolving sodium dodecyl sulphate (SDS) (33 mg) in 2.8 mL of MilliQ water. After ensuring complete dissolution of conjugated materials, the aqueous phase was combined with the organic phase under stirring at 1200 rpm. A macroemulsion was then formed by stirring the mixture at 1200 rpm at 30 °C for approximately 1 hr, with the initial concentration of SDS to be 34.1 mM in the mixture. To generate the miniemulsion, Vibra-Cell ultrasonic processor VCX 750 with 1/8" stepped probe was introduced to ultra-sonicate the macroemulsion at 30% amplitude for 3 min. Then the miniemulsion was transferred immediately to a heating block and stirred at 1200 rpm to form a stable water dispersion of NPs after complete removal of the residual organic solvent. For nanoparticles prepared using chloroform, the miniemulsion was heated at 60 °C for 3 hr to ensure the complete removal of chloroform whereas in the case of using *o*-xylene or anisole, a NPs dispersion was achieved by heating at 75 °C for 6 hr. Additional water was added every hour to compensate for the water loss, which otherwise results in aggregation of material and precipitation on the wall of the vials. To minimise unwanted SDS from negatively impacting the device performance,¹⁴ centrifugal dialysis was introduced to remove excess free surfactant in the dispersion as well as concentrate the active materials in the water dispersion.^{20, 45}

The TQ1:PC₇₁BM NPs with low SDS concentration (1.0 mM) were prepared with the weight ratio of 1:2.5 through the miniemulsion method described above. The aqueous phase was prepared by dissolving SDS (1 mg) in 2.8 mL of MilliQ water.

In the shearing force study, TQ1:PC₇₁BM NPs were prepared following the described procedure above using TQ1 (8.6 mg) and PC₇₁BM (21.5 mg) in 560 µL of chloroform and SDS concentration of 34.1 mM in the mixture. In the miniemulsion generation process, Vibra-Cell ultrasonic processor VCX 750 with 1/8" stepped probe was introduced to ultra-sonicate the macroemulsion at 20% amplitude for 2 min, 30% amplitude for 2 min and 30% amplitude for 3 min, respectively.

In the solvent additive study, TQ1:PC₇₁BM blend solution was prepared by dissolving TQ1 (8.7 mg) and PC₇₁BM (21.7 mg) in chloroform (560 µL) with or without 2% CN in the organic solvents. The

TQ1:PC₇₁BM NPs with or without CN additive were achieved following the described procedure above.

TQ1:PC₇₁BM NPs with or without CN additive for STXM study were prepared by initially dissolving TQ1 (8.2 mg) and PC₇₁BM (20.5 mg) in chloroform (1.01 mL) with or without 2% CN in the organic solvents, respectively at 35 °C under stirring at 500 rpm for 2 hours. Meanwhile an aqueous solution of sodium dodecyl sulphate (SDS) ($\rho_{\text{SDS}} \sim 1 \times 10^{-3}$ M) was prepared by dissolving SDS (1 mg) in MilliQ water (2.8 mL). After dissolution of the active materials, the aqueous SDS solution was added to the organic phase under stirring (1200 rpm) at 30 °C, forming a macroemulsion after stirring for ~1 hour. A miniemulsion was generated by ultra-sonicating (Branson Sonifier 450 system equipped with a microtip for 2 min) at 24 Watts. Then, the miniemulsion was transferred immediately to a heating block and stirred (1200 rpm) at 60 °C for 3 hours to completely remove the organic solvent to result in a stable aqueous TQ1:PC₇₁BM NP dispersion. Subsequently, centrifugal dialysis was performed to remove the excess of free surfactant in the dispersion as well as to concentrate the NP dispersion.

PTNT:C₆₀:C₇₀ NPs were prepared using the weight ratio of PTNT:C₆₀:C₇₀ being 2:1:1 and *o*-xylene as the precursor solvent, following the described general procedure above.

The TQ1:TQ-FSG:PCBM and TQ-FSG:PCBM blend NPs without additional surfactant were prepared by firstly dissolve all active materials in chloroform and then mixed with an aqueous solution containing 2% formic acid, followed by ultra-sonication and removal of chloroform as described above. The TQ1:PCSS NPs were prepared by mixing TQ1 chloroform solution and PCSS aqueous solution, followed by ultra-sonication and removal of chloroform as described above. However, no centrifugal dialysis were performed on these NPs to avoid the aggregation.

The TQ1:PC₆₁BM (1:2.5 weight ratio) NPs prepared using ALS as the surfactant were prepared following the described general procedure above. But 0.11 g ALS (30% aqueous solution) dissolved in 2.72 mL MilliQ water was used as the aqueous phase instead of using SDS aqueous solution.

6.8.2.2. General preparation of NPs using the precipitation method

The preparation of NPs using precipitation method was following the procedure reported by Darwis et al.⁴¹ with chloroform as the solvent for active materials and EtOH as the non-solvent to disperse particles, or THF as the solvent for active materials and water as the non-solvent to disperse particles. The detailed experimental parameters are presented in the 6.7 in this Chapter.

6.8.3. Characterisation of nanoparticles

Scanning electron microscopy (SEM) was performed using an ultra-high resolution field-emission gun scanning electron microscope (Zeiss Merlin) at an accelerating voltage of 2 kV with magnification ranges of 50,000-150,000 X. All SEM samples were spin-coated from diluted nanoparticle water dispersion with ~1wt% of solids content on conductive silicon substrate. The size

distribution of NPs prepared using miniemulsion method was characterised from SEM images with a circular Hough transform algorithm.^{20, 46} Thermal annealing was performed by keeping the NP films on a preheated hotplate in ambient condition.

Solvent vapour annealing were performed by keeping PTNT:C₆₀:C₇₀ (2:1:1) NP films or TQ1:PC₇₁BM (1:2.5) NP films in a closed desiccator with saturated chloroform vapour for given durations described in the discussion, then dried in a vacuum oven at r.t. overnight before SEM measurements.

Solvent blend washing were carried out by dropping solvent mixture of ethanol containing 0%, 2%, 5% and 10% CN, respectively, on TQ1:PC₆₁BM (1:2.5) NP film for 10 s, followed by spin-coating to remove remaining solvent.

Atomic Force Microscopy (AFM) measurements were performed using a multimode AFM (supplied by Bruker) in tapping mode with silicon tips.

Near-edge X-ray absorption fine structure (NEXAFS) spectroscopy measurements were performed to determine key absorption energies of TQ1 and PC₇₁BM. Measurements were performed on beamline 5.3.2.2 at the Advanced Light Source.⁴⁷ Pristine films of TQ1 and PC₇₁BM were prepared by spin-coating from chloroform solution (3000 rpm, 1 min, with acceleration of 1596 rpm/s) onto PEDOT:PSS (Clevios P VP AI 4083, H.C. Starck) coated glass substrates, with no thermal treatment. A scalpel was used to score approximately 2 x 2 mm² sections of the film prior to floating off the film sections onto the water surface. The floated film sections were allowed to sit on the water surface for sufficient time for the PEDOT:PSS sacrificial layer to wash away before they were collected onto 300 mesh copper grids (purchased from ProSciTech Pty Ltd, Australia) for NEXAFS measurements. Film thickness of pristine films were measured via a KLA-Tencor Alpha-step 500 surface profilometer (COE, University of Newcastle, Australia) to determine the film thickness, 120 nm for TQ1 and 93 nm for PC₇₁BM. Prominent peaks at 287.4 eV and 284.4 eV were identified in the NEXAFS spectra of TQ1 and PC₇₁BM, respectively (**Figure 6.34**). Therefore, 287.4 eV was chosen to map TQ1, while 284.4 eV was chosen for mapping PC₇₁BM to generate scanning transmission X-ray microscopy (STXM) fractional composition maps.

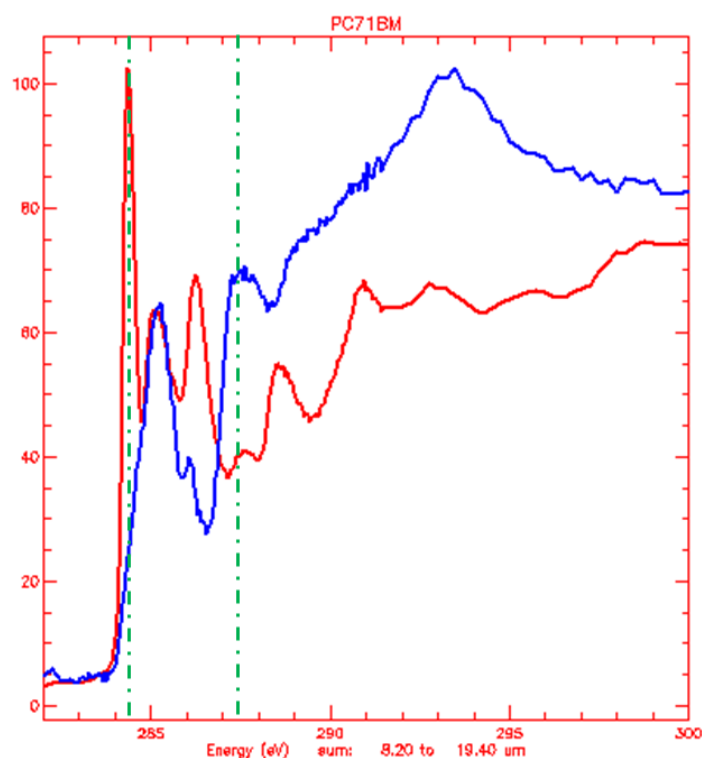


Figure 6.34 NEXAFS spectra of TQ1 (blue) and PC₇₁BM (red) with the photon energy chosen of 284.4 eV for PC₇₁BM and 287.4 eV for TQ1.

The scanning transmission X-ray microscopy (STXM) measurements were performed on beamline 5.3.3.3 at the Advanced Light Source (Berkeley).⁴⁷ Representative and detailed STXM experiment and data analysis are reported elsewhere.^{23, 47-48} Image analysis was performed with the aXis2000 package (<http://unicorn.mcmaster.ca/aXis2000.html>). The samples for STXM were prepared by spin-coating 2.5 μ L NP dispersion (3000 rpm, 1 min, with low acceleration of 112 rpm/s) on silicon nitride window substrates with silicon dioxide coating (cleaned in UV-ozone for 5 min).

Dynamic mechanical thermal analysis (DMTA) samples were prepared by repeatedly drop-casting the TQ1:PC₇₁BM (1:3) NP water dispersion onto a 20-30 mm long, approximately 5 mm wide piece of glass fibre mesh, as described elsewhere²⁹, followed by drying under ambient condition until a uniformly fully covered film on the glass mesh was obtained. The samples were stored in a vacuum oven overnight to remove most of the water before performing DMTA measurements. DMTA measurements were carried out on a TA Q800 DMA in strain-controlled mode at a frequency of 1 Hz and an amplitude of 5 μ m. The samples were measured under a continuous flow of nitrogen gas with a heating rate of 3 $^{\circ}$ C per minute. The first run was performed from room temperature up to 80 $^{\circ}$ C for further drying the sample, followed by a second run from -110 $^{\circ}$ C to 200 $^{\circ}$ C. The data from the second run was utilised to study thermomechanical properties of TQ1:PC₇₁BM NPs with different molecular weight TQ1 in this Chapter.

6.8.4. Device fabrication

6.8.4.1. Conventional structure in additive study

Conventional solar cells with the structure ITO/PEDOT:PSS/NPs/Ca/Al were fabricated using water dispersed TQ1:PC₇₁BM NPs with or without CN additive to coat the active layer. PEDOT:PSS films were spin-coated (5000 rpm, 1 min, 1680 rpm/s) on pre-cleaned patterned ITO-coated glass substrates and annealed at 140 °C for 30 min. TQ1:PC₇₁BM NP active layer TQ1:PC₇₁BM NPs were spin-coated (1750 rpm, 1 min, 1680 rpm/s) from 6 wt% NP dispersions followed by drying in air at 110 °C for 4 min to remove the moisture before being transferred to a glove-box. The NP films were annealed in the nitrogen filled glove-box at various temperatures for 4 min and then transferred to a vacuum deposition chamber. The cathode consists a calcium (Ca) layer (~30 nm) and a aluminium (Al) layer (90 nm), which were thermally evaporated on the active layers in vacuum of 2×10^{-6} torr.

6.8.4.2. Inverted structure

Inverted solar cells with the structure ITO/ZnO/NPs/MoO₃/Ag were fabricated using water dispersed NPs to coat the active layer. Patterned ITO-coated glass substrates (10 Ω/sq, purchased from Xin Yan Technology Ltd) were cleaned using the procedure described elsewhere.¹⁵ ITO-coated glass substrates were first cleaned by soaking in a 5% detergent solution (pyroneg from Johnson Diversey) at 90 °C for 20 minute and then rinsing in deionized (DI) water, before sonicating in DI water, acetone and isopropanol for 10 min each. Substrates were then cleaned in UV-ozone for 20 minute immediately before spin coating the ZnO layer. ZnO sol-gel⁴⁹ on the cleaned ITO substrate was heated at 280 °C for 10 minute in air to yield a 25 nm thick film. NP dispersion was filtered through a PTFE membrane syringe filter (pore size of 0.45 μm) prior to spin coating. Different NP films on ZnO/ITO glass substrates were then dried at 90 °C for 4 minute in air, before transferring to the glove box. Then the NP films were thermally annealed for specific time described in this Chapter inside the glove box with nitrogen atmosphere before a thin layer of MoO₃ (12 nm) was thermally evaporated on top of the active layer to serve as a hole transporting layer. Finally the Ag electrode (80 nm) was deposited by thermally evaporating through a shadow mask, which defined the active area to be 0.1 cm².

6.8.5. J-V characterisation

I-V properties of solar cells were measured in air by an Oriel solar simulator fitted with a 150 W xenon lamp (Newport), filtered to give an irradiation of 100 mW/cm² at AM1.5 and calibrated using a silicon reference cell with NIST traceable certification. The photocurrent-voltage (*I-V*) characteristics of devices were measured through a Keithley 2400 source meter unit.

6.9. Conclusions

The preparation of water or alcohol based NPs consisting donor:acceptor blend realises the fabrication of organic solar cells without using harmful halogenated solvent. The experimental parameters in the preparation procedure were systematically studied. The NPs prepared via miniemulsion method using SDS showed excellent stability and reproducibility, and decent photovoltaic performance was achieved from NP OPVs. To eliminate unwanted effect from SDS on photovoltaic devices, SDS-free NPs were prepared using non-ionic surfactant and functionalized conjugated polymers, respectively, as the stabilizing agent. The SDS-free NPs prepared using either miniemulsion method or precipitation method were not successfully applied as photoactive layer in OPVs, and the modification of NP preparation procedure as well as device fabrication will be continued in the future.

6.10. References

1. Zappia, S.; Scavia, G.; Ferretti, A. M.; Giovanella, U.; Vohra, V.; Destri, S., Water-Processable Amphiphilic Low Band Gap Block Copolymer:Fullerene Blend Nanoparticles as Alternative Sustainable Approach for Organic Solar Cells. *Advanced Sustainable Systems* **2018**, 1700155.
2. Geoffrey, P.; Laurie, P.; Eleni, P.; Gilles, P.; Cyril, B.; Georges, H.; Eric, C., Aqueous PCDTBT:PC71BM Photovoltaic Inks Made by Nanoprecipitation. *Macromolecular Rapid Communications* **2018**, 39 (2), 1700504.
3. D'Olieslaeger, L.; Pirotte, G.; Cardinaletti, I.; D'Haen, J.; Manca, J.; Vanderzande, D.; Maes, W.; Ethirajan, A., Eco-friendly fabrication of PBDTTPD:PC71BM solar cells reaching a PCE of 3.8% using water-based nanoparticle dispersions. *Organic Electronics* **2017**, 42, 42-46.
4. Gärtner, S.; Christmann, M.; Sankaran, S.; Röhm, H.; Prinz, E.-M.; Penth, F.; Pütz, A.; Türel, A. E.; Penth, B.; Baumstümmler, B.; Colsmann, A., Eco-Friendly Fabrication of 4% Efficient Organic Solar Cells from Surfactant-Free P3HT:ICBA Nanoparticle Dispersions. *Advanced Materials* **2014**, 26 (38), 6653-6657.
5. Landfester, K.; Montenegro, R.; Scherf, U.; GÜNTNER, R.; Asawapirom, U.; Patil, S.; Neher, D.; Kietzke, T., Semiconducting polymer nanospheres in aqueous dispersion prepared by a miniemulsion process. *Advanced Materials* **2002**, 14 (9), 651-655.
6. Prunet, G.; Parrenin, L.; Pavlopoulou, E.; Pecastaings, G.; Brochon, C.; Hadziioannou, G.; Cloutet, E., Aqueous PCDTBT:PC71 BM Photovoltaic Inks Made by Nanoprecipitation. *Macromol Rapid Commun* **2017**.
7. Yu, Y.-Y.; Tsai, T.-W.; Yang, C.-C.; Chen, C.-P., Highly Efficient Non-Fullerene Organic Photovoltaics Processed from o-Xylene without Using Additives. *The Journal of Physical Chemistry C* **2017**, 121 (40), 21969-21974.
8. Li, G.; Shrotriya, V.; Yao, Y.; Yang, Y., Investigation of annealing effects and film thickness dependence of polymer solar cells based on poly(3-hexylthiophene). *Journal of Applied Physics* **2005**, 98 (4), 043704.
9. Parrenin, L.; Laurans, G.; Pavlopoulou, E.; Fleury, G.; Pecastaings, G.; Brochon, C.; Vignau, L.; Hadziioannou, G.; Cloutet, E., Photoactive Donor-Acceptor Composite Nanoparticles Dispersed in Water. *Langmuir* **2017**, 33 (6), 1507-1515.
10. Almyahi, F.; Andersen, T. R.; Cooling, N.; Holmes, N. P.; Fahy, A.; Barr, M. G.; Kilcoyne, D.; Belcher, W.; Dastoor, P. C., Optimization, characterization and upscaling of aqueous solar nanoparticle inks for organic photovoltaics using low-cost donor:acceptor blend. *Organic Electronics* **2018**, 52, 71-78.
11. Holmes, N. P.; Ulum, S.; Sista, P.; Burke, K. B.; Wilson, M. G.; Stefan, M. C.; Zhou, X.; Dastoor, P. C.; Belcher, W. J., The effect of polymer molecular weight on P3HT:PCBM nanoparticulate organic photovoltaic device performance. *Solar Energy Materials and Solar Cells* **2014**, 128, 369-377.
12. Mukerjee, P.; Mysels, K. J. *Critical micelle concentrations of aqueous surfactant systems*; National Standard reference data system: 1971.
13. Domínguez, A.; Fernández, A.; González, N.; Iglesias, E.; Montenegro, L., Determination of critical micelle concentration of some surfactants by three techniques. *Journal of Chemical Education* **1997**, 74 (10), 1227.
14. Colberts, F. J. M.; Wienk, M. M.; Janssen, R. A. J., Aqueous Nanoparticle Polymer Solar Cells: Effects of Surfactant Concentration and Processing on Device Performance. *ACS Applied Materials & Interfaces* **2017**, 9 (15), 13380-13389.
15. Sharma, A.; Kroon, R.; Lewis, D. A.; Andersson, G. G.; Andersson, M. R., Poly(4-vinylpyridine): A New Interface Layer for Organic Solar Cells. *ACS Applied Materials & Interfaces* **2017**, 9 (12), 10929-10936.
16. Hansson, R.; Ericsson, L. K. E.; Holmes, N. P.; Rysz, J.; Opitz, A.; Campoy-Quiles, M.; Wang, E.; Barr, M. G.; Kilcoyne, A. L. D.; Zhou, X.; Dastoor, P.; Moons, E., Vertical and lateral morphology effects on solar cell performance for a thiophene–quinoxaline copolymer:PC70BM blend. *Journal of Materials Chemistry A* **2015**, 3 (13), 6970-6979.
17. Fan, B.; Ying, L.; Wang, Z.; He, B.; Jiang, X.-F.; Huang, F.; Cao, Y., Optimisation of processing solvent and molecular weight for the production of green-solvent-processed all-polymer

- solar cells with a power conversion efficiency over 9%. *Energy & Environmental Science* **2017**, *10* (5), 1243-1251.
18. Wang, E.; Hou, L.; Wang, Z.; Hellstrom, S.; Zhang, F.; Inganas, O.; Andersson, M. R., An easily synthesized blue polymer for high-performance polymer solar cells. *Advanced Materials* **2010**, *22* (46), 5240-4.
 19. Tang, Z.; Andersson, L. M.; George, Z.; Vandewal, K.; Tvingstedt, K.; Heriksson, P.; Kroon, R.; Andersson, M. R.; Inganas, O., Interlayer for modified cathode in highly efficient inverted ITO-free organic solar cells. *Advanced Materials* **2012**, *24* (4), 554-8.
 20. Holmes, N. P.; Marks, M.; Kumar, P.; Kroon, R.; Barr, M. G.; Nicolaidis, N.; Feron, K.; Pivrikas, A.; Fahy, A.; Mendaza, A. D. D. Z.; Kilcoyne, A.; Müller, C.; Zhou, X.; Andersson, M. R.; Dastoor, P. C.; Belcher, W. J., Nano-pathways: Bridging the divide between water-processable nanoparticulate and bulk heterojunction organic photovoltaics. *Nano Energy* **2016**, *19*, 495-510.
 21. Pedersen, E. B. L.; Pedersen, M. C.; Simonsen, S. B.; Brandt, R. G.; Böttiger, A. P. L.; Andersen, T. R.; Jiang, W.; Xie, Z. Y.; Krebs, F. C.; Arleth, L.; Andreasen, J. W., Structure and crystallinity of water dispersible photoactive nanoparticles for organic solar cells. *Journal of Materials Chemistry A* **2015**, *3* (33), 17022-17031.
 22. Chen, Y.; Cui, Y.; Zhang, S.; Hou, J., Molecular design toward efficient polymer solar cells processed by green solvents. *Polymer Chemistry* **2015**, *6* (22), 4089-4095.
 23. Holmes, N. P.; Burke, K. B.; Sista, P.; Barr, M.; Magurudeniya, H. D.; Stefan, M. C.; Kilcoyne, A. L. D.; Zhou, X.; Dastoor, P. C.; Belcher, W. J., Nano-domain behaviour in P3HT:PCBM nanoparticles, relating material properties to morphological changes. *Solar Energy Materials and Solar Cells* **2013**, *117*, 437-445.
 24. Schwarz, K. N.; Farley, S. B.; Smith, T. A.; Ghiggino, K. P., Charge generation and morphology in P3HT:PCBM nanoparticles prepared by mini-emulsion and reprecipitation methods. *Nanoscale* **2015**, *7* (47), 19899-904.
 25. Singh, A.; Dey, A.; Iyer, P. K., Influence of molar mass ratio, annealing temperature and cathode buffer layer on power conversion efficiency of P3HT:PC 71 BM based organic bulk heterojunction solar cell. *Organic Electronics* **2017**, *51*, 428-434.
 26. Watts, B.; Belcher, W. J.; Thomsen, L.; Ade, H.; Dastoor, P. C., A Quantitative Study of PCBM Diffusion during Annealing of P3HT:PCBM Blend Films. *Macromolecules* **2009**, *42* (21), 8392-8397.
 27. Gibbs, J. H.; DiMarzio, E. A., Nature of the Glass Transition and the Glassy State. *The Journal of Chemical Physics* **1958**, *28* (3), 373-383.
 28. Fox, T. G.; Flory, P. J., Second - Order Transition Temperatures and Related Properties of Polystyrene. I. Influence of Molecular Weight. *Journal of Applied Physics* **1950**, *21* (6), 581-591.
 29. Sharma, A.; Pan, X.; Campbell, J. A.; Andersson, M. R.; Lewis, D. A., Unravelling the Thermomechanical Properties of Bulk Heterojunction Blends in Polymer Solar Cells. *Macromolecules* **2017**, *50* (8), 3347-3354.
 30. Zhao, G.; He, Y.; Li, Y., 6.5% Efficiency of polymer solar cells based on poly(3-hexylthiophene) and indene-C(60) bisadduct by device optimization. *Advanced Materials* **2010**, *22* (39), 4355-8.
 31. Campoy-Quiles, M.; Ferenczi, T.; Agostinelli, T.; Etchegoin, P. G.; Kim, Y.; Anthopoulos, T. D.; Stavrinou, P. N.; Bradley, D. D.; Nelson, J., Morphology evolution via self-organization and lateral and vertical diffusion in polymer:fullerene solar cell blends. *Nature Materials* **2008**, *7* (2), 158-64.
 32. Zhao, Y.; Xie, Z.; Qu, Y.; Geng, Y.; Wang, L., Solvent-vapor treatment induced performance enhancement of poly(3-hexylthiophene):methanofullerene bulk-heterojunction photovoltaic cells. *Applied Physics Letters* **2007**, *90* (4), 043504.
 33. Duan, C.; Cai, W.; Hsu, B. B. Y.; Zhong, C.; Zhang, K.; Liu, C.; Hu, Z.; Huang, F.; Bazan, G. C.; Heeger, A. J.; Cao, Y., Toward green solvent processable photovoltaic materials for polymer solar cells: the role of highly polar pendant groups in charge carrier transport and photovoltaic behavior. *Energy & Environmental Science* **2013**, *6* (10), 3022-3034.
 34. Xie, C.; Classen, A.; Späth, A.; Tang, X.; Min, J.; Meyer, M.; Zhang, C.; Li, N.; Osvet, A.; Fink, R. H.; Brabec, C. J., Overcoming Microstructural Limitations in Water Processed Organic Solar Cells by Engineering Customized Nanoparticulate Inks. *Advanced Energy Materials* **2018**, 1702857.
 35. Hellberg, P.-E.; Bergström, K.; Holmberg, K., Cleavable surfactants. *Journal of Surfactants and Detergents* **2000**, *3* (1), 81-91.
 36. Muenmart, D.; Foster, A. B.; Harvey, A.; Chen, M.-T.; Navarro, O.; Promarak, V.; McCairn, M. C.; Behrendt, J. M.; Turner, M. L., Conjugated Polymer Nanoparticles by Suzuki–Miyaura Cross-

Coupling Reactions in an Emulsion at Room Temperature. *Macromolecules* **2014**, *47* (19), 6531-6539.

37. Son, V. T.; Phong, L. V.; Islam, N. M.; Hung, T. Q.; Kim, S.-R.; Jeong, J.-H.; Kim, C.-G.; Jeong, J.-R., Effect of Non-ionic Igepal CO-520 in Sonochemical Synthesis of Monodisperse Fe₃O₄ Nanoparticles. *Journal of Magnetism* **2010**, *15* (3), 112-115.

38. Chandradass, J.; Bae, D.-S., Synthesis and Characterization of Alumina Nanoparticles by Igepal CO-520 Stabilized Reverse Micelle and Sol-Gel Processing. *Materials and Manufacturing Processes* **2008**, *23* (5), 494-498.

39. Kuehne, A. J.; Gather, M. C.; Sprakel, J., Monodisperse conjugated polymer particles by Suzuki-Miyaura dispersion polymerization. *Nature Communications* **2012**, *3*, 1088.

40. Schwuger, M. J., Mechanism of interaction between ionic surfactants and polyglycol ethers in water. *Journal of Colloid and Interface Science* **1973**, *43* (2), 491-498.

41. Darwis, D.; Holmes, N.; Elkington, D.; David Kilcoyne, A. L.; Bryant, G.; Zhou, X.; Dastoor, P.; Belcher, W., Surfactant-free nanoparticulate organic photovoltaics. *Solar Energy Materials and Solar Cells* **2014**, *121*, 99-107.

42. Roger, K.; Eissa, M.; Elaissari, A.; Cabane, B., Surface charge of polymer particles in water: the role of ionic end-groups. *Langmuir* **2013**, *29* (36), 11244-50.

43. Clifton, S. N.; Huang, D. M.; Massey, W. R.; Kee, T. W., Femtosecond dynamics of excitons and hole-polarons in composite P3HT/PCBM nanoparticles. *The Journal of Physical Chemistry B* **2013**, *117* (16), 4626-33.

44. Kroon, R.; Diaz de Zerio Mendaza, A.; Himmelberger, S.; Bergqvist, J.; Bäcke, O.; Faria, G. C.; Gao, F.; Obaid, A.; Zhuang, W.; Gedefaw, D.; Olsson, E.; Inganäs, O.; Salleo, A.; Müller, C.; Andersson, M. R., A New Tetracyclic Lactam Building Block for Thick, Broad-Bandgap Photovoltaics. *Journal of the American Chemical Society* **2014**, *136* (33), 11578-11581.

45. Ulum, S.; Holmes, N.; Darwis, D.; Burke, K.; David Kilcoyne, A. L.; Zhou, X.; Belcher, W.; Dastoor, P., Determining the structural motif of P3HT:PCBM nanoparticulate organic photovoltaic devices. *Solar Energy Materials and Solar Cells* **2013**, *110*, 43-48.

46. Wang, Y.; Cheng, G., Application of gradient-based Hough transform to the detection of corrosion pits in optical images. *Applied Surface Science* **2016**, *366*, 9-18.

47. Kilcoyne, A.; Tyliczszak, T.; Steele, W.; Fakra, S.; Hitchcock, P.; Franck, K.; Anderson, E.; Harteneck, B.; Rightor, E.; Mitchell, G., Interferometer-controlled scanning transmission X-ray microscopes at the Advanced Light Source. *Journal of synchrotron radiation* **2003**, *10* (2), 125-136.

48. McNeill, C. R.; Watts, B.; Thomsen, L.; Belcher, W. J.; Greenham, N. C.; Dastoor, P. C., Nanoscale quantitative chemical mapping of conjugated polymer blends. *Nano letters* **2006**, *6* (6), 1202-1206.

49. Sun, Y.; Seo, J. H.; Takacs, C. J.; Seifert, J.; Heeger, A. J., Inverted polymer solar cells integrated with a low-temperature-annealed sol-gel-derived ZnO Film as an electron transport layer. *Advanced Materials* **2011**, *23* (14), 1679-83.

7. Chapter Seven - Environmentally Friendly Preparation of Nanoparticles for Organic Photovoltaics

This chapter is a reformatted version of the paper published in Organic Electronics, Year 2018. DOI: 10.1016/j.orgel.2018.05.040

Author contribution:

Xun Pan: Performed all the preparation and characterisation of nanoparticles (except NEXAFS and STXM measurements), data analysis and interpretation, prepared the first draft of manuscript.

Dr. Anirudh Sharma: Performed device fabrication & testing, contributed to the revision of manuscript.

Dr. Desta Gedefaw & Dr. Renee Kroon: Synthesised polymer PTNT, contributed to the revision of manuscript.

Dr. Amaia Diaz de Zerio: Contributed to the conceptualizing of experiments.

Dr. Natalie P. Holmes & A. L. David Kilcoyne & Matthew Barr & Adam Fahy & Melissa Marks & Prof. Xiaojing Zhou & Prof. Warwick Belcher & Prof. Paul C. Dastoor: Performed NEXAFS and STXM experiments, contributed to the data interpretation and revision of manuscript.

Prof. Mats R. Andersson: Intellectual contribution in conceptualizing experiments & revision of manuscript.

7.1. Abstract

Aqueous nanoparticle dispersions were prepared from a conjugated polymer PTNT and fullerene blend utilising chloroform as well as a non-chlorinated and environmentally benign solvent, *o*-xylene, as the miniemulsion dispersed phase solvent. The nanoparticles (NPs) in the solid-state film were found to coalesce and offered a smooth surface topography upon thermal annealing. Organic photovoltaics (OPVs) with photoactive layer processed from the nanoparticle dispersions prepared using chloroform as the miniemulsion dispersed phase solvent were found to have a power conversion efficiency (PCE) of 1.04%, which increased to 1.65% for devices utilising NPs prepared from *o*-xylene. Physical, thermal and optical properties of NPs prepared using both chloroform and *o*-xylene were systematically studied using dynamic mechanical thermal analysis (DMTA) and photoluminescence (PL) spectroscopy and correlated to their photovoltaic properties. The PL results indicate different morphology of NPs in the solid state were achieved by varying miniemulsion dispersed phase solvent.

7.2. Introduction

Ever increasing global energy consumption has led to a tremendous rise in fossil fuel emissions, resulting in air pollution and global warming.¹ The urgent need for the development of clean and renewable energy sources has attracted immense attention of both scientific and industrial researchers.²⁻³ Undoubtedly, solar energy is one of the best candidates to fulfil the current and future energy needs.⁴⁻⁵ Organic photovoltaics (OPVs) enjoy significant advantages over traditional solar technology due to their lightweight, flexibility, ease of manufacturing, scalability and low cost.⁶⁻⁹ Continued research into OPV technology has led to significant improvements in the device performance with power conversion efficiency (PCE) of up to 13% being reported.¹⁰ However, OPVs are commonly prepared via spin-coating the active materials on small indium tin oxide (ITO) coated glass substrates from non-environmentally friendly halogenated solvents,¹¹ which is counterproductive to achieving scalable and environmentally friendly fabrication of OPVs.

In recent years a number of publications have focussed on developing alternative OPV fabrication methods, which are scalable at low cost such as roll-to-roll printing.^{8, 12-14} Although remarkable success has been achieved in printing OPVs on flexible substrates, most of the best performing materials used for printing are still processed from chlorinated solvents such as *ortho*-dichlorobenzene (*o*-DCB).¹⁵ The large-scale use of chlorinated solvents is harmful to human health and has a detrimental impact on the environment.¹⁶⁻¹⁷ Moreover, the usage of chlorinated solvents increases the cost of large-scale fabrication of OPVs, which results from expensive halogenated solvent recovery systems. The harmfulness and high cost of chlorinated solvents used for processing photoactive materials in OPV fabrication is one of the main hurdles to be overcome before the knowhow of fabricating high performing OPVs can be transferred from a lab-scale to an industrial scale fabrication. Thus, it is of utmost importance to develop green deposition methods by utilising benign and non-chlorinated solvents.¹⁸⁻²⁰

OPVs with active layers processed from a water or alcohol based nanoparticle dispersion has been reported in recent years.²¹⁻²⁴ These nanoparticles are processed from donor-acceptor blends either through a miniemulsion process with the presence of surfactant²⁵⁻²⁸ or a precipitation method.^{21-23, 29} Furthermore, conjugated polymer nanoparticles were also reported to be synthesised by direct Suzuki-Miyaura dispersion polymerisation.³⁰⁻³² In the miniemulsion method, the organic solvent utilised to dissolve the active materials should ideally have high vapour pressure as well as be immiscible with water. Most procedures reported in the literature to date use harmful chlorinated solvents, such as chloroform (CHCl₃),^{21, 33} chlorobenzene³⁴ or *o*-DCB.²⁶ Compared to conventional bulk heterojunction (BHJ) OPV fabrication, the NP method is still environmentally superior considering (a) the volume of chlorinated solvents utilised is comparably less; (b) the roll-to-roll printing of solar cells is free from chlorinated solvents as they can be removed in a closed loop system prior to printing. Considering that the upscaling of OPVs with NP active layers will lead to an

increase in the consumption of solvents used to prepare NPs, it is timely to consider the use of industrially relevant solvents during the preparation of the NPs of the photoactive materials in addition to the subsequent deposition.

In this chapter, we report for the first time the preparation of water-dispersed nanoparticles using a relatively benign and industrially relevant solvent, *o*-xylene, as the miniemulsion dispersed phase solvent, and successfully demonstrate the fabrication of solar cells with comparable device parameters to BHJ OPVs.¹⁹ The nanoparticles were prepared from a wide bandgap semicrystalline conjugated polymer namely poly[thiophene-2,5-diyl-*alt*-5,10-bis((2-hexyldecyl)oxy)dithieno[3,2-*c*:3',2'-*h*][1,5]naphthyridine-2,7-diyl] (PTNT)³⁵ and PC₇₁BM (phenyl C₇₁ butyric acid methyl ester). PTNT polymer was chosen in this study as it was demonstrated to perform well in an active layer thickness of up to 400 nm,³⁵ which makes it a relevant polymer for devices fabricated via printing. To gain a better understanding of the influence of the miniemulsion dispersed phase solvent on the nanoparticle properties, PTNT:PC₇₁BM NPs prepared using chloroform as the miniemulsion dispersed phase solvent were also studied. Size distribution, optical, thermomechanical and photovoltaic properties of PTNT:PC₇₁BM nanoparticles prepared using *o*-xylene (NP-xylene) were systematically studied and compared with those processed from chloroform (NP-chloroform). A maximum PCE of 1.65%, with a short circuit current density (J_{SC}) of 4.75 mA/cm² was achieved from nanoparticles prepared using *o*-xylene as the miniemulsion dispersed phase solvent as compared to a 1.04% PCE and 2.84 mA/cm² of J_{SC} for the dispersions prepared using chloroform as the miniemulsion dispersed phase solvent.

7.3. Experimental

7.3.1. PTNT synthesis

Polymer PTNT (**Figure 7.1**) was synthesised by Stille coupling copolymerisation from monomer 2,7-dibromo-5,10-bis((2-hexyldecyl)oxy)dithieno[3,2-*c*:3',2'-*h*][1,5]naphthyridine (dibromo-NT) and 2,5-bis(trimethylstannyl)thiophene as previously reported.³⁵ The molecular weight was measured by size exclusion chromatography (SEC) in 1,2,4-trichlorobenzene (1,2,4-TCB) at 150 °C. M_r = 55.7 kg/mol, M_w = 163.2 kg/mol were determined relative to polystyrene standards. Through square wave voltammetry, the HOMO and LUMO energy levels of PTNT are estimated to be -5.9 and -3.6 eV, respectively.³⁵ Bulk heterojunction (BHJ) solar cells processed using PTNT:PC₇₁BM (1:2 weight ratio) processed from *o*-DCB solution have been reported to achieve a PCE of 5% in a conventional configuration³⁵ and 5.1% in an inverted structure.³⁶

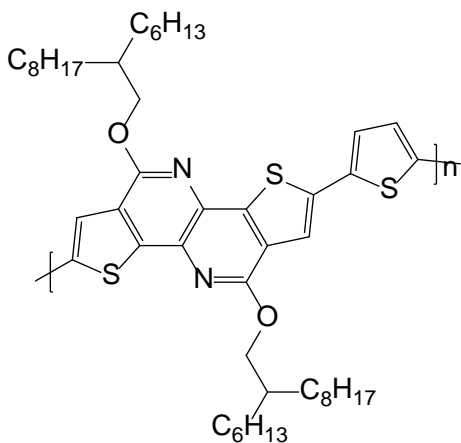


Figure 7.1 Chemical structure of PTNT.

7.3.2. Nanoparticle preparation

7.3.2.1. Preparation of small NPs for device fabrication

PC₇₁BM was purchased from Solenne BV. PTNT:PC₇₁BM nanoparticles were prepared with the weight ratio of 1:2 through the miniemulsion method.^{33, 37} The weight ratio was chosen based on the best performance of BHJ devices from a PTNT:PC₇₁BM blend without solvent additive.³⁵ PTNT (10 mg) and PC₇₁BM (20 mg) were dissolved in 540 μ L of organic solvent (chloroform or *o*-xylene) at 35 °C with stirring at 500 rpm for 2 hours. Meanwhile the aqueous phase was prepared by dissolving sodium dodecyl sulphate (SDS) (33 mg) in 2.8 mL of MilliQ water. After ensuring complete dissolution of PTNT and PC₇₁BM, the aqueous phase was combined with the organic phase under stirring at 1200 rpm. A macroemulsion was then formed by stirring the mixture at 1200 rpm at 30 °C for approximately 1 hr. To generate the miniemulsion, Vibra-Cell ultrasonic processor VCX 750 with 1/8" stepped probe was introduced to ultra-sonicate the macroemulsion at 30% amplitude for 3 min. Then the miniemulsion was transferred immediately to a heating block and stirred at 1200 rpm to form a stable water dispersion of NPs after complete removal of the residual organic solvent. For nanoparticles prepared using chloroform, the miniemulsion was heated at 60 °C for 3 hr to ensure the complete removal of chloroform whereas in the case of using *o*-xylene, a NPs dispersion was achieved by heating at 75 °C for 6 hr. Additional water was added every hour to compensate for the water loss, which otherwise results in aggregation of material and precipitation on the wall of the vials. To minimise unwanted SDS from negatively impacting the device performance,²⁷ centrifugal dialysis was introduced to remove excess free surfactant in the dispersion as well as concentrate the active materials in the water dispersion, giving the final dispersion a solids content of 6 wt% in 0.5 mL water.

7.3.2.2. Preparation of large NPs for morphology study

Due to the resolution limit of scanning transmission X-ray microscopy (STXM), it is difficult to perform measurements on small NPs ($\phi \leq \sim 30$ nm). Hence we prepared large PTNT:PC₇₁BM NPs with a broad

size distribution and measured the particle composition for a range of particle sizes, measuring the same composition over a range of sizes allows us to hypothesise 30 nm nanoparticles prepared via the same method have a comparable interior morphology.

First, a concentrated PTNT:PC₇₁BM blend solution ($\rho_{\text{blend}} \sim 55 \text{ g/L}$) was prepared by dissolving PTNT (10 mg) and PC₇₁BM (20 mg) in chloroform (540 μL) at 35 °C under stirring at 500 rpm for 2 hours. Meanwhile an aqueous solution of sodium dodecyl sulphate (SDS) ($\rho_{\text{SDS}} \sim 1 \times 10^{-3} \text{ M}$) was prepared by dissolving SDS (1 mg) in MilliQ water (2.8 mL). After dissolution of the active materials, the aqueous SDS solution was added to the organic phase under stirring (1200 rpm) at 30 °C, forming a macroemulsion after stirring for ~ 1 hour. A miniemulsion was generated by ultra-sonicating (Branson Sonifier 450 system equipped with a microtip for 2 min) at 24 Watts. Then, the miniemulsion was transferred immediately to a heating block and stirred (1200 rpm) at 60 °C for 3 hours to completely remove the organic solvent to result in a stable aqueous PTNT:PC₇₁BM NP dispersion. Subsequently, centrifugal dialysis was performed to remove the excess of free surfactant in the dispersion as well as to concentrate the NP dispersion. Finally, 0.5 mL of an aqueous PTNT:PC₇₁BM NP dispersion was obtained with $\rho_{\text{NP}} \sim 60 \text{ g/L}$.

7.3.2.3. Preparation of NPs for varied annealing temperature study

QSonica Q125 sonicator equipped with 1/8" microtip probe was introduced to sonicate the macroemulsion at 40% amplitude for 5 min. The other preparing procedures are the same as the preparation of small NPs.

The mean diameter of nanoparticles is $60 \pm 21 \text{ nm}$ for ones prepared from *o*-xylene and $60 \pm 25 \text{ nm}$ in the case of preparing from chloroform. The size of these two batches of nanoparticles was characterised from SEM images with a circular Hough transform algorithm, showing in **Figure 7.2**.

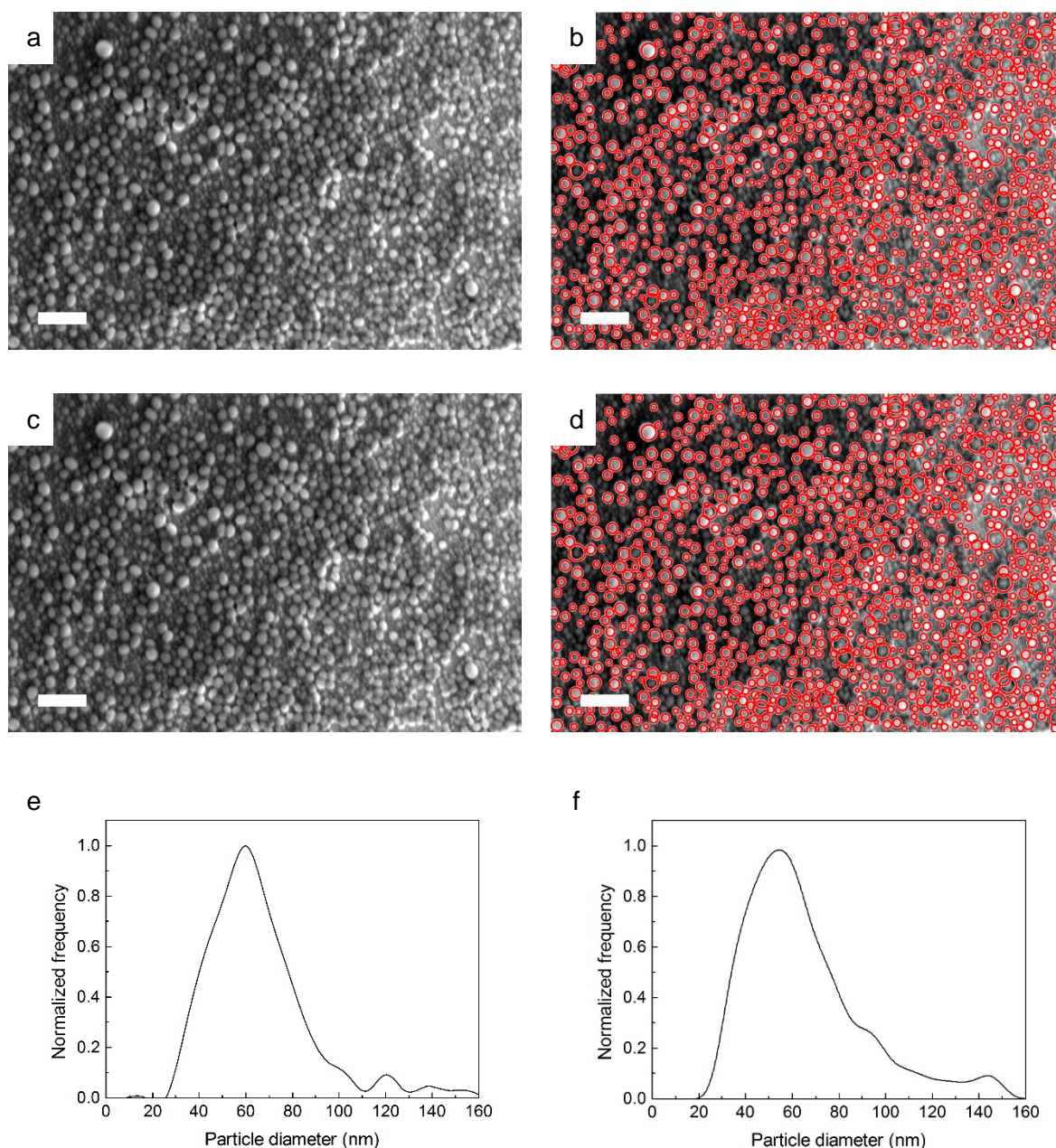


Figure 7.2 SEM images of PTNT:PC₇₁BM (1:2) NPs prepared via QSonica Q125 sonicator from *o*-xylene (a) and chloroform (c). Circle identification by circular Hough transform (b is *o*-xylene batch and d is chloroform batch). Size distribution of PTNT:PC₇₁BM (1:2) NPs prepared from *o*-xylene (e) and chloroform (f). All scale bars are 400 nm.

7.3.3. Nanoparticle characterisation

Scanning electron microscopy (SEM) was performed using an ultra-high resolution field-emission gun scanning electron microscope (Zeiss Merlin) at an accelerating voltage of 2 kV with magnification ranges of 50,000-150,000 X. All SEM samples were spin-coated (3000 rpm for 1 minute) from diluted nanoparticle water dispersion with 1wt% of solids content on conductive silicon substrate. The size distribution of PTNT:PC₇₁BM (1:2 weight ratio) NPs prepared from different organic solvents were characterised from SEM images with a circular Hough transform algorithm.³⁷⁻

³⁸ In the varied annealing temperature study, all films were pre-dried at 90 °C for 4 min immediately after spin-coating for consistency with device fabrication.

The ultraviolet–visible (UV-vis) study was performed on a Perkin Elmer UV-vis-NIR Lambda950 spectrophotometer. The photoluminescence (PL) measurements were performed on a Varian Cary Eclipse fluorescence spectrophotometer at the excitation wavelength of 450 nm. The PL measurements of NP water dispersions were performed on diluted NP-xylene and NP-chloroform dispersion with the same concentration. Measurements of the solid state were performed on spin coated NP films from original NP dispersion. It should be noted that the study of absorbance change of NP film with and without annealing was measured on the same area on the same film for comparison.

Dynamic mechanical thermal analysis (DMTA) samples were prepared by repeatedly drop-casting the PTNT:PC₇₁BM NP water dispersion or neat PTNT chloroform solution onto a 20-30 mm long, approximately 5 mm wide piece of glass fibre mesh, as described elsewhere³⁹, followed by drying under ambient condition until a uniformly fully covered film on the glass mesh was obtained. The samples were stored in a desiccator overnight to remove most of the water before performing DMTA measurements. DMTA measurements were carried out on a TA Q800 DMA in strain-controlled mode at a frequency of 1 Hz and an amplitude of 5 μm. The samples were measured under a continuous flow of nitrogen gas with a heating rate of 3 °C per minute. The first run was performed from room temperature up to 80 °C for further drying the sample, followed by a second run from -110 °C to 200 °C. The data from the second run was utilised to study thermomechanical properties of materials in this study.

Near-edge X-ray absorption fine structure (NEXAFS) spectroscopy measurements were performed to determine key absorption energies of PTNT and PC₇₁BM. Measurements were performed on beamline 5.3.2.2 at the Advanced Light Source.⁴⁰ Pristine films of PTNT and PC₇₁BM were prepared by spin-coating from chloroform solution (3000 rpm, 1 min, with acceleration of 1596 rpm/s) onto PEDOT:PSS (Clevios P VP Al 4083, H.C. Starck) coated glass substrates, with no thermal treatment. A scalpel was used to score approximately 2 x 2 mm² sections of the film prior to floating off the film sections onto the water surface. The floated film sections were allowed to sit on the water surface for sufficient time for the PEDOT:PSS sacrificial layer to wash away before they were collected onto 300 mesh copper grids (purchased from ProSciTech Pty Ltd, Australia) for NEXAFS measurements. Film thickness of pristine films were measured via a KLA-Tencor Alpha-step 500 surface profilometer (COE, University of Newcastle, Australia) to determine the film thickness, 80 nm for PTNT and 93 nm for PC₇₁BM. Prominent peaks at 287.4 eV and 284.4 eV were identified in the NEXAFS spectra of PTNT and PC₇₁BM, respectively (**Figure 7.3**). Therefore, 287.4 eV was chosen to map PTNT, while 284.4 eV was chosen for mapping PC₇₁BM to generate scanning transmission X-ray microscopy (STXM) fractional composition maps.

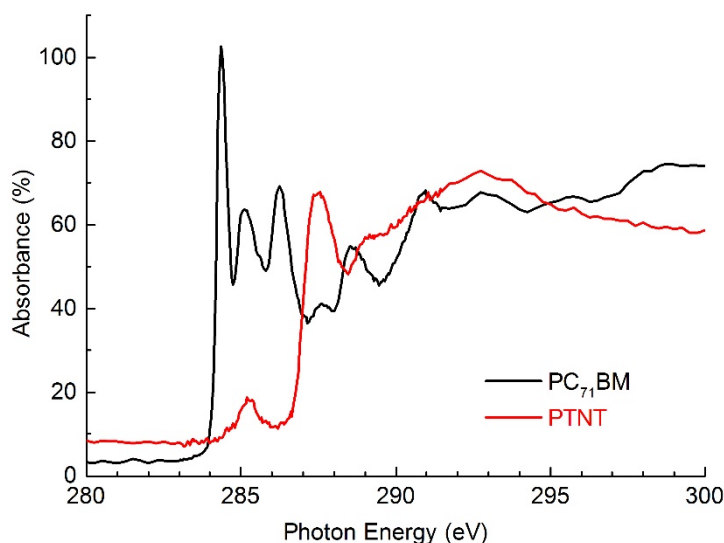


Figure 7.3 NEXAFS spectra of PTNT (red) and PC₇₁BM (black) with the photon energy chosen of 284.4 eV for PC₇₁BM and 287.4 eV for PTNT.

The scanning transmission X-ray microscopy (STXM) measurements were performed on beamline 5.3.3.3 at the Advanced Light Source (Berkeley).⁴⁰ Representative and detailed STXM experiment and data analysis are reported elsewhere.^{25, 40-41} Image analysis was performed with the aXis2000 package (<http://unicorn.mcmaster.ca/aXis2000.html>). The samples for STXM were prepared by spin-coating 2.5 μ L NP dispersion (3000 rpm, 1 min, with low acceleration of 112 rpm/s) on silicon nitride window substrates with silicon dioxide coating (cleaned in UV-ozone for 5 min).

Atomic Force Microscopy (AFM) measurements were performed using a multimode AFM (supplied by Bruker) in tapping mode with silicon tips.

7.3.4. Device fabrication

Inverted solar cells with the structure ITO/ZnO/NPs/MoO₃/Ag were fabricated using water dispersed NPs to coat the active layer. Patterned ITO-coated glass substrates (10 Ω /sq, purchased from Xin Yan Technology Ltd) were cleaned using the procedure described elsewhere.³⁶ ITO-coated glass substrates were first cleaned by soaking in a 5% detergent solution (pyroneg from Johnson Diversey) at 90 °C for 20 minute and then rinsing in deionized (DI) water, before sonicating in DI water, acetone and isopropanol for 10 min each. Substrates were then cleaned in UV-ozone for 20 minute immediately before spin coating the ZnO layer. ZnO sol-gel⁴² on the cleaned ITO substrate was heated at 280 °C for 10 minute in air to yield a 25 nm thick film. The PTNT:PC₇₁BM (1:2 weight ratio) NP dispersion was filtered through a PTFE membrane syringe filter (pore size of 0.45 μ m) prior to spin coating, and resulted in approximate film thickness of 190 nm. The NP films on ZnO/ITO glass substrates were then dried at 90 °C for 4 minute in air, before transferring to the glove box. It should be noted that 4 minute thermal annealing at 90 °C did not induce NPs sintering (**Figure 7.4**), further

supporting the first run of DMTA scan did not alter the NP structure. The NP films were thermally annealed at 160 °C for 4 minute inside the glove box with nitrogen atmosphere before a thin layer of MoO₃ (12 nm) was thermally evaporated on top of the active layer to serve as a hole transporting layer. Finally the Ag electrode (80 nm) was deposited by thermally evaporating through a shadow mask, which defined the active area to be 0.1 cm². To achieve best performing devices, NP solar cells were post-annealed (after the electrode deposition) for 4 minute in the glove box at 140 °C or 160 °C (as specified in the discussion).

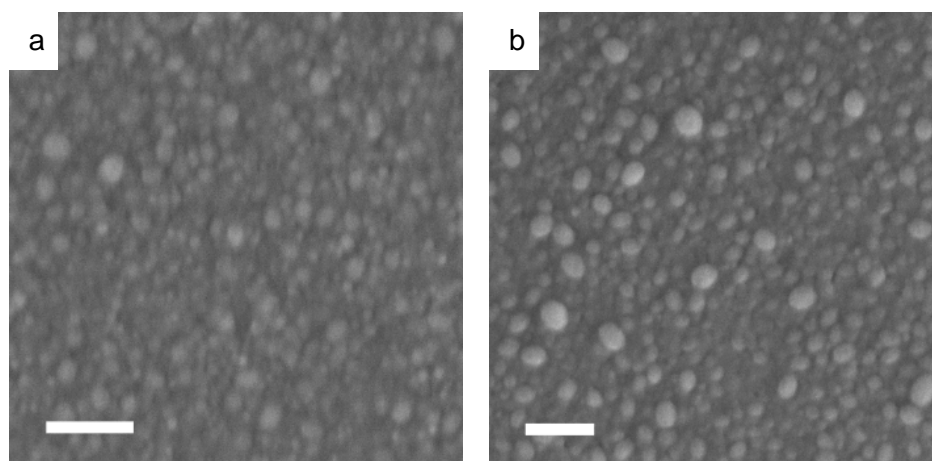


Figure 7.4 SEM images (a) NP-xylene and (b) NP-chloroform, each dried at 90 °C for 4 min, respectively.

7.3.5. *J-V* characterisation

I-V properties of solar cells were measured in air by an Oriel solar simulator fitted with a 150 W xenon lamp (Newport), filtered to give an irradiation of 100 mW/cm² at AM1.5 and calibrated using a silicon reference cell with NIST traceable certification. The photocurrent-voltage (*I-V*) characteristics of devices were measured through a Keithley 2400 source meter unit. External quantum efficiency (EQE) measurements were performed by a Cornerstone 260™ motorized 1/4 m monochromator (model 74125, Newport) and TracQ basic software for data acquisition.

7.4. Results and discussion

7.4.1. Properties of nanoparticles

To evaluate the size of prepared NPs, SEM measurement was performed on NPs in the solid state. SEM images presented in **Figure 7.5** depict the PTNT:PC₇₁BM nanoparticulate films for NPs prepared from chloroform and *o*-xylene, respectively. NPs were as spun from water-based colloidal dispersions without further treatment. The particulate shape of PTNT:PC₇₁BM NPs was found not to be completely spherical, which is typical for NPs made of semicrystalline polymer.^{25, 27, 43-45} The size distribution of NPs (**Figure 7.5e**) was measured by applying a circular Hough transform algorithm to the SEM images of NP films. Since the circular Hough transform algorithm is based on circle calculation, the model resulted in several mismatches (**Figure 7.5c, d**). Nevertheless the mean diameter of PTNT:PC₇₁BM NPs prepared using chloroform (NP-chloroform) was calculated to be 32

± 12 nm whereas the nanoparticles from the *o*-xylene batch (NP-xylene) had a mean diameter of 27 ± 11 nm in the solid state. Compared to NP-chloroform, NP-xylene resulted in a slightly narrower size distribution with the presence of fewer large sized NPs on the surface. This observation indicates that the higher temperature and the longer time required to convert the NP-xylene miniemulsion to an aqueous dispersion does not result in material aggregation or further increase in the particle size.

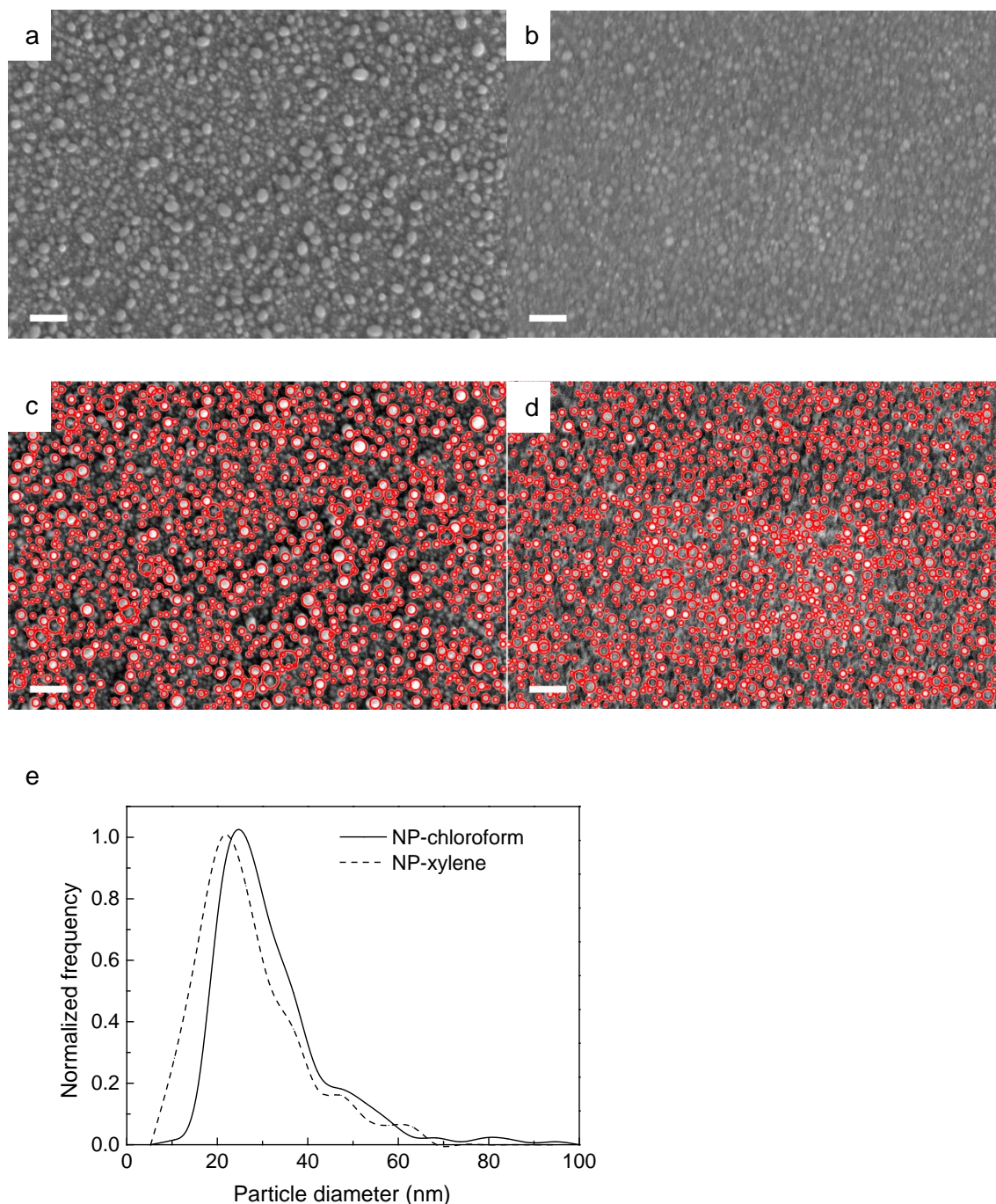


Figure 7.5 SEM image of (a) NP-chloroform and (b) NP-xylene. Circle identification of (c) NP-chloroform and (d) NP-xylene by circular Hough transform. Size distribution of NP-chloroform and NP-xylene (e). Scale bars are 200 nm.

To achieve well performing solar devices using water dispersed NPs, it is imperative to achieve good morphology of the active layer.⁴⁶⁻⁴⁷ Due to the particulate shape and the core-shell structure of NPs prepared through miniemulsion method,^{25, 37} the coalescing of NPs could ideally tune the morphology of the active layer and is thus desirable for better charge transport and extraction.^{21, 48} To coalesce NPs without inducing defects in the film, thermal-annealing was introduced, which is widely applied to both NP and BHJ solar devices to improve the morphology of the active layer, therefore enhancing the performance of devices.⁴⁸⁻⁵⁰ The schematic shown in **Figure 7.6** depicts coalescence of NPs upon annealing in the solid state. SEM and AFM (*presented in 7.4.3*) was thus used to systematically study the changes induced in the surface topography of the NP films as a function of annealing temperatures, and to find the ideal annealing temperature which resulted in best performing devices.

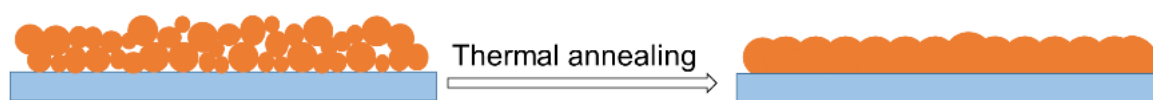


Figure 7.6 Schematic of NP coalescing upon thermal annealing to form continuous film.

The as spun film prepared from NP-chloroform (**Figure 7.5a**) shows that the separate NPs are clearly distinguishable. The near-edge X-ray absorption fine structure (NEXAFS) spectroscopy measurements (**Figure 7.3**) and scanning transmission X-ray microscopy (STXM) results (**Figure 7.7**) reveal the core-shell structure of PTNT:PC₇₁BM NPs without thermal annealing.

Thermal annealing of NP-chloroform films at 100 °C (**Figure 7.8a**) or 120 °C (**Figure 7.8b**) was not found to make any significant changes on the surface features of the films, as a large degree of nanoparticulate structure was still observed by SEM. The particles were found to interconnect with each other (sinter) after the NP-chloroform film was annealed at 140 °C (**Figure 7.8c**), with some residual nanoparticles presented on the surface. When thermally annealed at 160 °C (**Figure 7.8d**), NPs were sintered and the relatively homogenous film was obtained, which could improve the charge transport⁴⁵ and reduce the possibility of charge recombination in the coalesced NP active layer in OPVs.²¹ Upon annealing at 180 °C, large aggregates in the NP-chloroform film were observed (**Figure 7.8e**), which was attributed to the crystallization of PC₇₁BM.⁵¹ The gross phase separation deteriorated the NP film morphology, which is detrimental for the device performance of NP solar devices.^{33, 45, 52} Thus, precise control over the thermal annealing temperature is crucial to achieve a homogenous active layer in OPVs as well as removing the moisture and avoiding large phase separation.³⁷

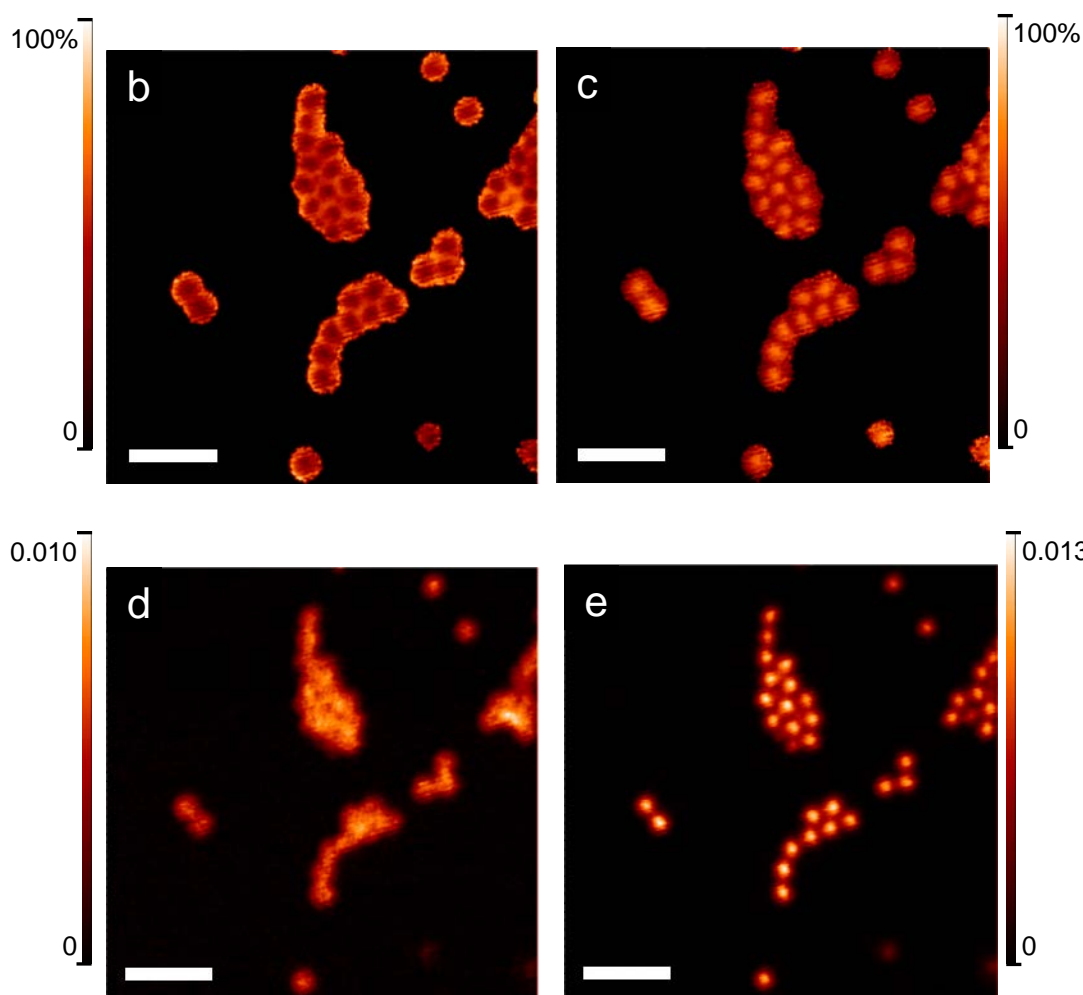
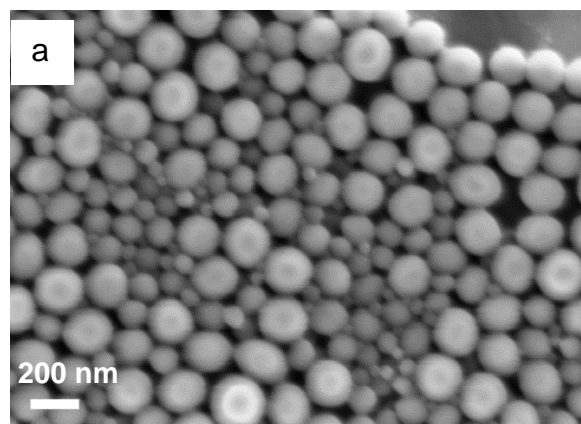


Figure 7.7 (a) SEM image of PTNT:PC₇₁BM NPs without thermal-annealing. STXM fractional composition maps showing the concentration of (b) PTNT and (c) PC₇₁BM, with (d, e) corresponding STXM mass plots of PTNT:PC₇₁BM nanoparticles as cast (no thermal treatment). The colour contrast is scaled such that light colours correspond to higher component concentrations. Minima and maxima for the colour scale bar in (b) and (c) are black = 0 and white = 100%. For (d) and (e) the colour scale bars indicate concentration of component in mg cm⁻². Scale bars are 1 μm in STXM plots.

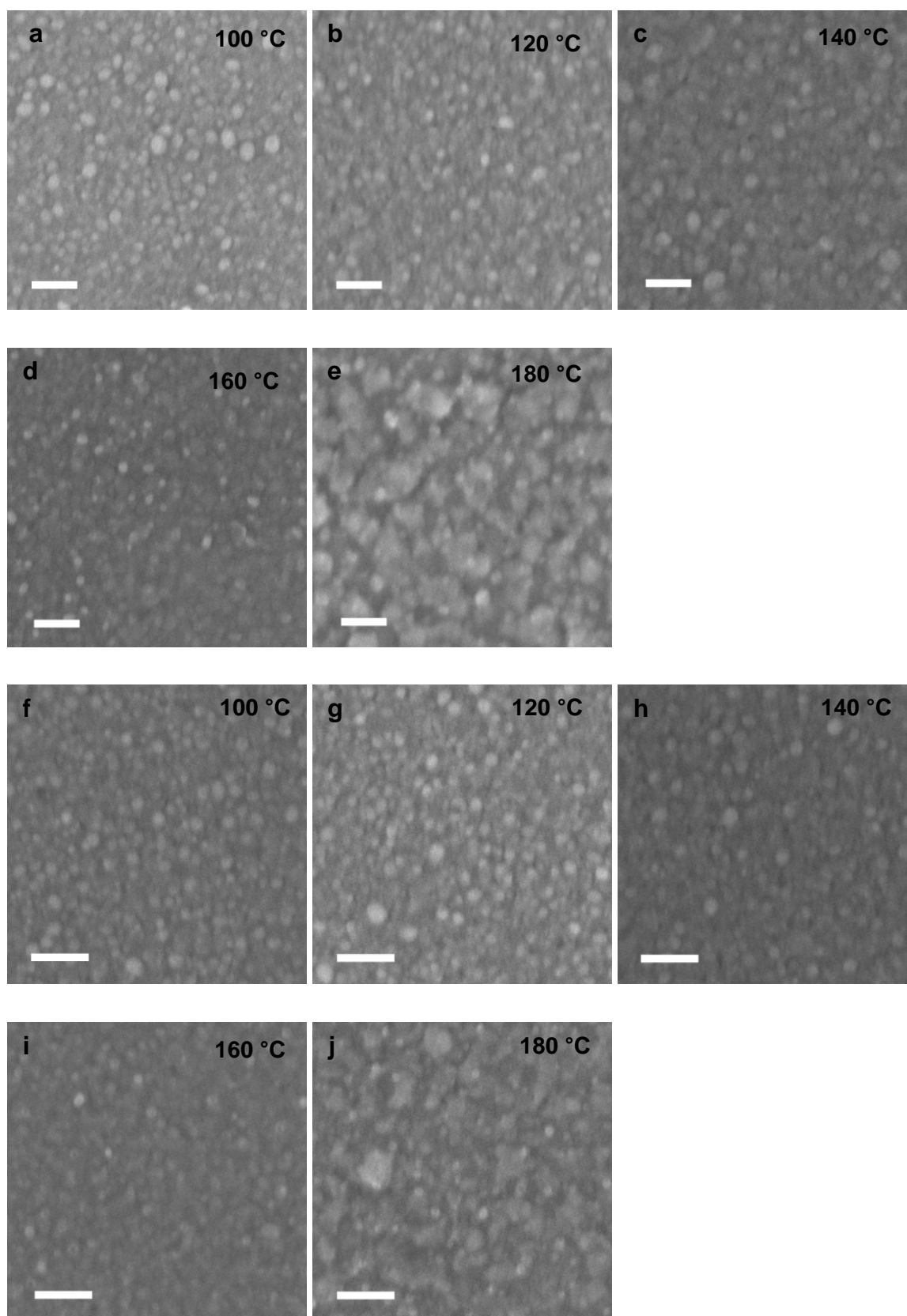


Figure 7.8 SEM images of PTNT:PC₇₁BM (1:2) NP films cast from NP-chloroform (a-e) and NP-xylene (f-j) thermally annealed at varied temperature for 4 min. Scale bars are 200 nm.

Similar behaviour was also found in the case of NP-xylene films, when annealed at different temperatures (**Figure 7.8f-j**). Compared to the reported P3HT:PCBM NPs,⁵³ which require lower

annealing temperature to form coalescent film, the slightly harsh annealing performed to sinter PTNT:PC₇₁BM NPs could be explained by the difference in the thermal properties of the polymers used to form NPs as P3HT is reported to have a glass transition temperature (T_g) of 38 °C.³⁹

To further probe the morphological changes and thermomechanical behaviour of PTNT:PC₇₁BM NP films, DMTA measurements³⁹ were performed on thin films cast from NP-xylene and NP-chloroform as well as pure PTNT (**Figure 7.9**). Since DMTA measures the thermal properties of materials with high sensitivity,^{39, 54-55} it further compliments the SEM study which only probes the surface topography. **Figure 7.9a** shows the storage modulus (E') in the DMTA scan of the NP-xylene sample. E' was found to drop around 100 °C with a significant loss at 160 °C, indicating the softening of the amorphous part of the PTNT-rich phase.⁵⁶ Based on the STXM results (**Figure 7.7**), it is known that the nanoparticles have a core-shell structure with a PTNT-rich NP shell and a PC₇₁BM-rich NP core. As such, the nanoparticles should start to coalesce only when PTNT in the polymer-rich shell reaches the rubbery state⁵⁷ similarly to P3HT:PCBM NPs.²⁵ Thus, the significant drop in the E' observed using DMTA agrees well with the coalescence of the nanoparticles in thin films observed using SEM. Beyond 160 °C, the stiffness (E') of the DMTA sample was again found to increase, which is attributed to the crystallization of PC₇₁BM in the PC₇₁BM-rich phase after the coalescence of the NPs, revealing the maximum temperature before detrimental crystallization occurs. This behaviour was also observed in SEM as drastic phase separation and coarsening of the film (**Figure 7.8j**). The DMTA temperature scan of the NPs prepared using chloroform (**Figure 7.9b**) shows a similar thermomechanical behaviour, whereas the neat PTNT DMTA scan (**Figure 7.9c**) did not show the increase of E' above 160 °C, which further confirms the increase in stiffness being attributed to the PC₇₁BM thermal transition. Since PTNT is a conjugated polymer with large side chains and more rigid backbones than P3HT, the onset of the decrease in storage modulus at -40 °C is attributed to the relaxation of the side chains, i.e. β transition. The higher β transition temperature (T_β) of PTNT compared to the T_β P3HT^{39, 58} also indicates higher T_g of PTNT, which further supports the higher temperature required to coalesce PTNT:PC₇₁BM NPs compared to the P3HT:PCBM NPs.⁵³

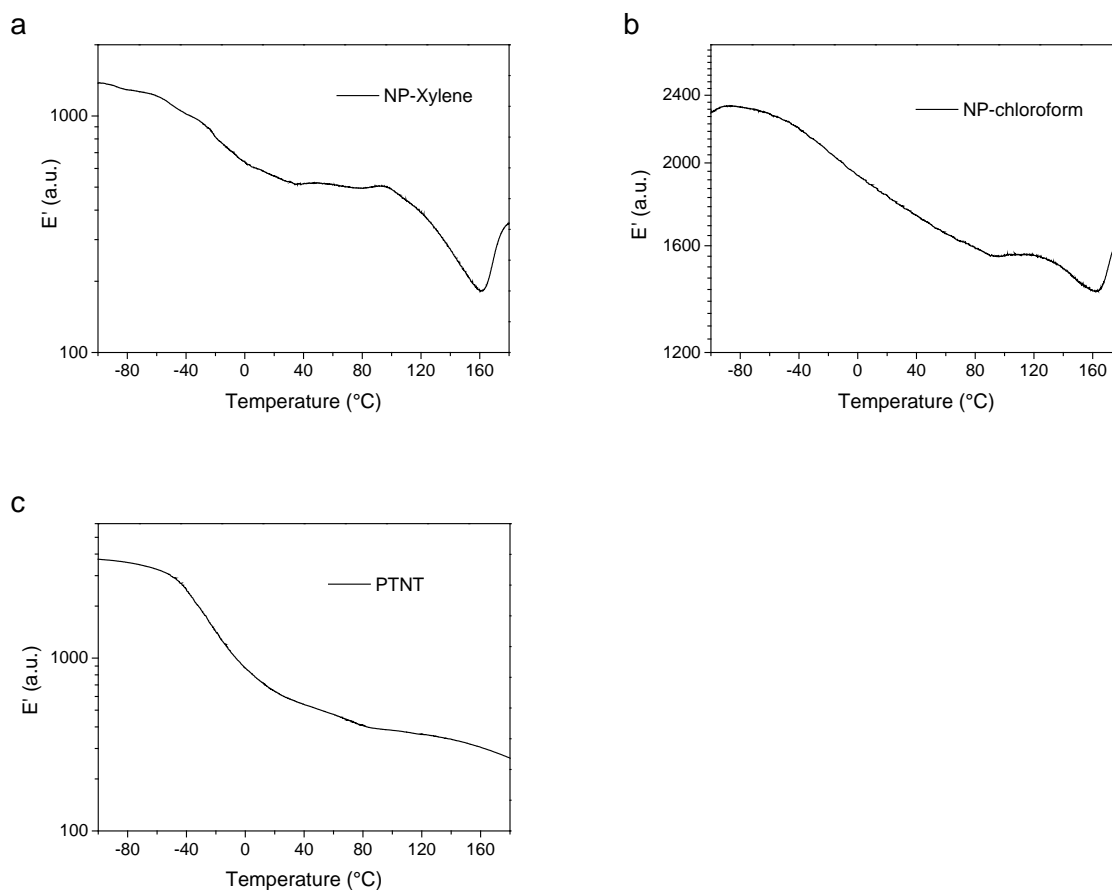


Figure 7.9 Storage modulus (E') as a function of temperature in a DMTA temperature scan of (a) NP-xylene, (b) NP-chloroform and (c) neat PTNT supported by a glass fibre mesh.

7.4.2. Optical properties of nanoparticles

To probe the optical properties of NPs prepared using different solvents, UV-vis and photoluminescence (PL) measurements were carried out on NP films as well as NP dispersions. **Figure 7.10** shows the UV-vis absorption spectra of solid state films from both batches of NPs as well as the PTNT:PC₇₁BM BHJ films processed from chloroform or *o*-xylene. The broad absorption band beyond 400 nm is attributed to the intramolecular charge transfer between donor and acceptor segments in the PTNT polymer backbones.³⁵ The absorption peak below 400 nm is primarily attributed to the absorbance of PC₇₁BM, while the vibronic peaks at 522 nm in the absorption spectra are attributed to the π - π stacking of polymer backbone³⁵ (**Figure 7.10a**). It can be observed that after thermal annealing the absorbance of PTNT:PC₇₁BM NP film was increased (**Figure 7.10b, c**). The increased absorption upon annealing could be due to the increased crystallinity and enhanced ordering of PTNT in the annealed films,^{22, 59} which was also observed in annealed PTNT:PC₇₁BM BHJ films (**Figure 7.10d, e**). The thermal annealing at 160 °C for 4 min did not lead to blue-shifted onset or decrease of the light absorbance of the PTNT:PC₇₁BM NP films, revealing no thermal degradation of materials in the NP film during short-term thermal annealing.

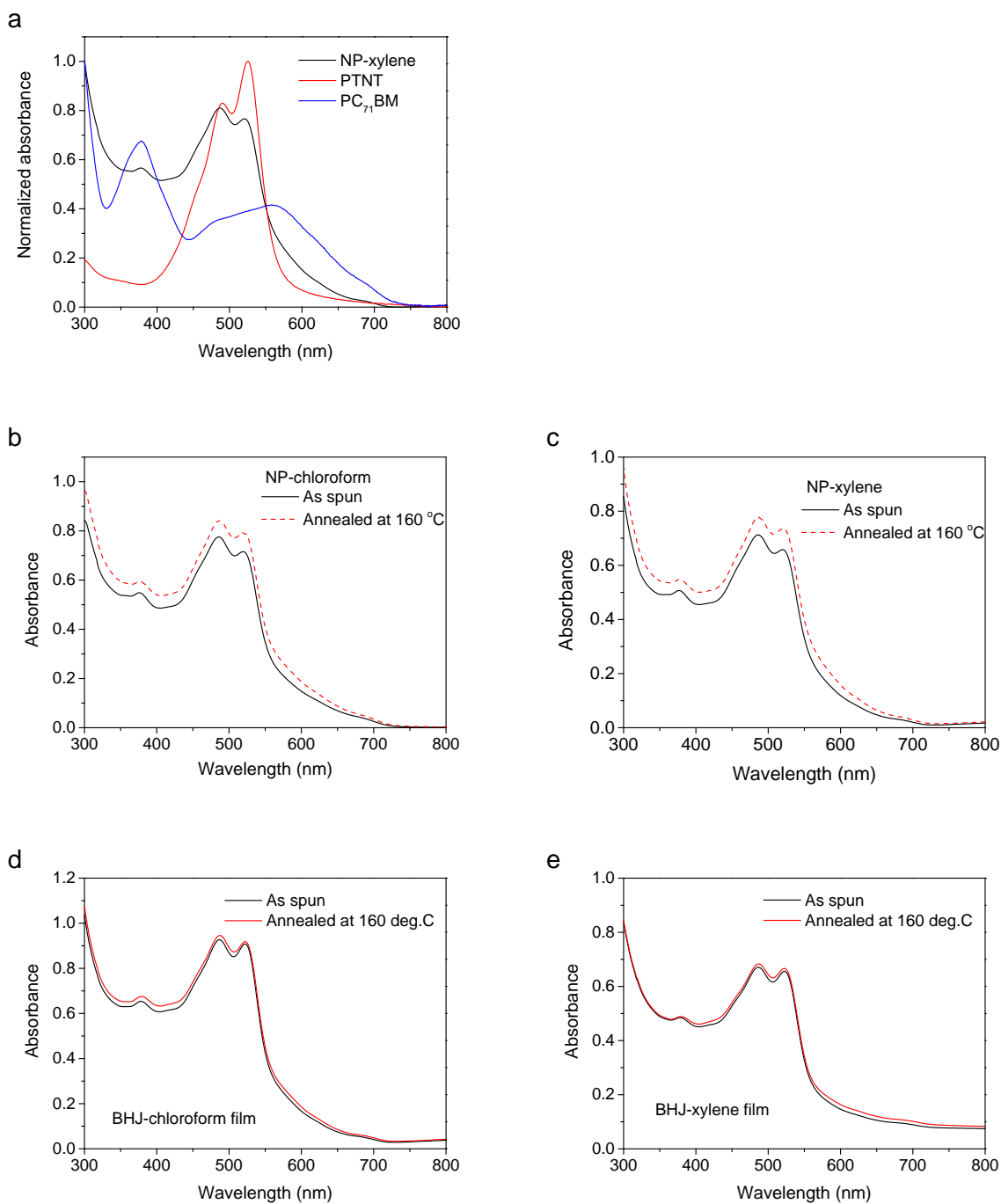


Figure 7.10 UV-vis absorption spectra of pristine PTNT, PC₇₁BM and annealed NP-xylene films (a), PTNT:PC₇₁BM NP-chloroform film (b) and NP-xylene film (c) as spun and thermally annealed at 160 °C for 4 min. UV-vis absorption spectra of PTNT:PC₇₁BM BHJ films spin coated from chloroform solution (BHJ-chloroform) (d) and *o*-xylene solution (BHJ-xylene) (e) as spun and thermally annealed at 160 °C for 4 min.

Figure 7.11 shows the PL spectra from both batches of NPs as well as the neat PTNT film and PTNT:PC₇₁BM BHJ film processed from *o*-xylene. The PL spectra shown in **Figure 7.11a** compare the quenching of PL signal in NP-chloroform and NP-xylene water dispersion. A higher PL intensity is observed for the NP-xylene dispersion (**Figure 7.11a**), which was attributed to a higher degree of donor-acceptor material phase separation within the NPs,^{22, 52, 60} suggesting that larger and/or purer

polymer domains already existed post NP preparation. Similar to the result found in the PL of the aqueous dispersions, NP-xylene film as spun (**Figure 7.11b**) also shows lower PL quenching in the emission band of PTNT compared to NP-chloroform film as spun, indicating the difference in nanomorphology of the NPs prepared from different solvents. However, upon thermal annealing a lower PL signal was found in NP-xylene film compared to the annealed NP-chloroform film, indicating a finer intermixed morphology was achieved. The increase in PL intensity of NP films after annealing (**Figure 7.11b**) indicates an increase in crystallinity of polymer domains or a higher degree of phase separation, generated by PC₇₁BM diffusion from amorphous PTNT-rich domains, resulting in lower PL quenching of PTNT emission upon annealing.^{33, 61} It must be noted that compared to the PL of PTNT pristine film, annealed NP film shows high degree of quenched PL signal (**Figure 7.11c**), indicating efficient photo-induced charge transfer between PTNT and PC₇₁BM.⁶²

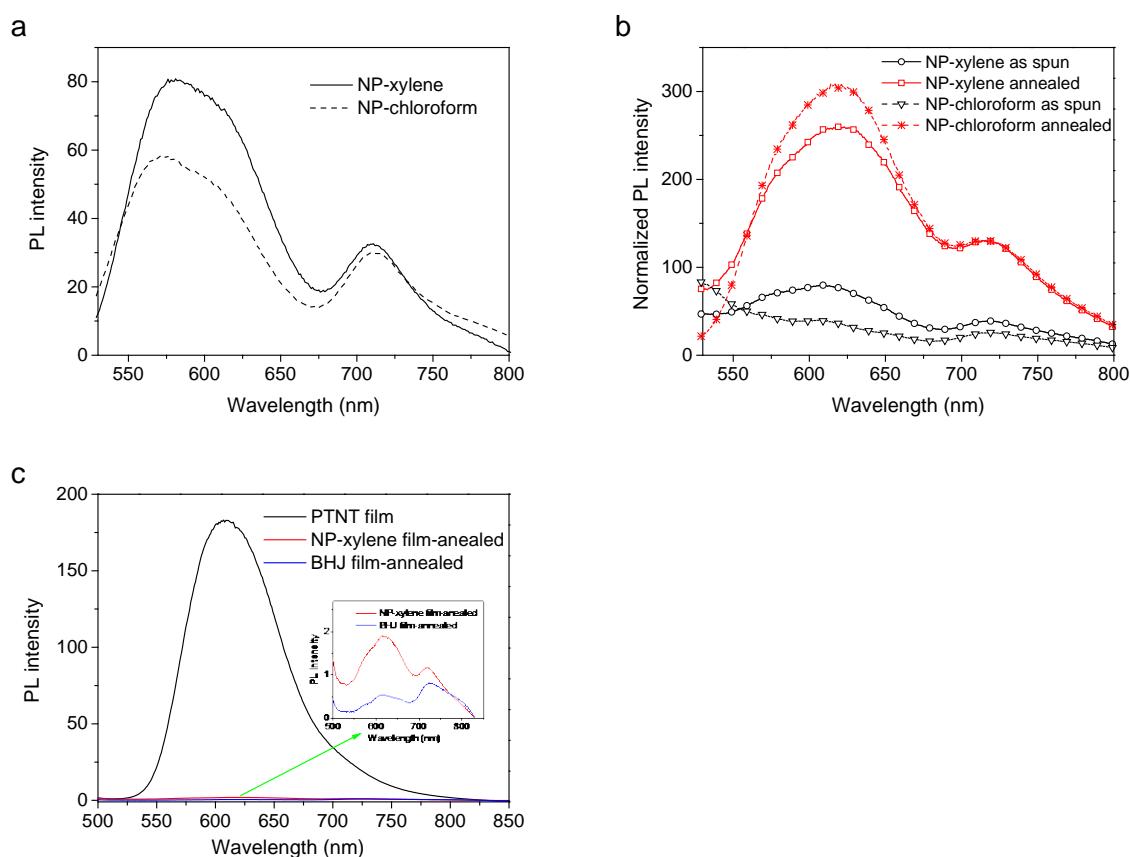


Figure 7.11 PL spectra of (a) NP-xylene and NP-chloroform dispersions, (b) NP-xylene and NP-chloroform films as spun and annealed at 160 °C and (c) neat PTNT film, NP-xylene film and PTNT:PC₇₁BM (1:2 weight ratio) BHJ film annealed at 160 °C. It should be noted that the PL results shown in (c) were measured using lower detecting voltage on fluorescence spectrophotometer compared to the voltage used in the measurements shown in main text.

7.4.3. Photovoltaic characterisations

7.4.3.1. Varied annealing temperature study

In order to test the photovoltaic properties of NPs, solar cells were fabricated and tested with the active layer spin-coated from NP dispersion, which has larger size of NPs (**Figure 7.2**) followed by annealing at different temperatures (**Figure 7.12**).

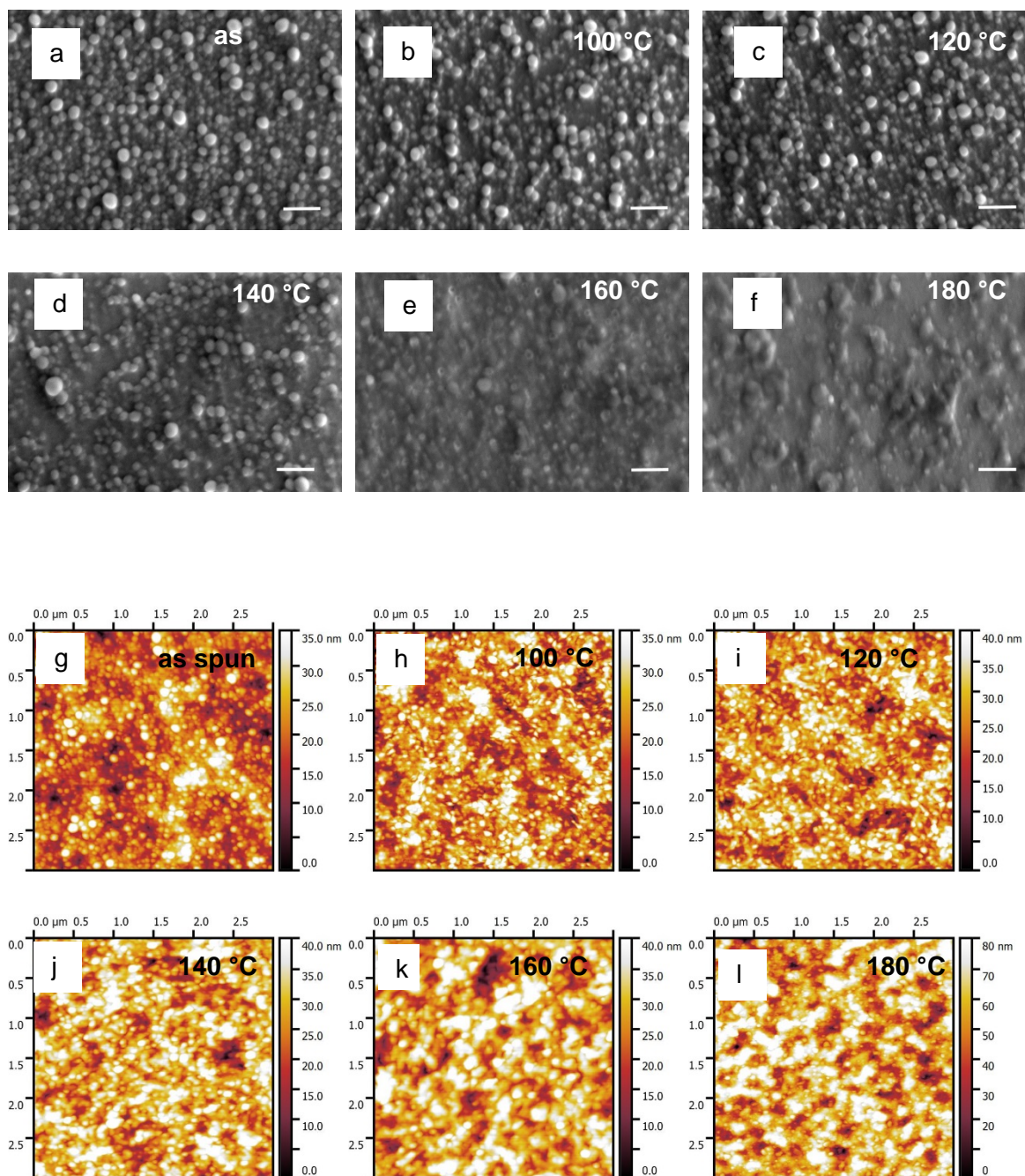


Figure 7.12 SEM images of (a) PTNT:PC₇₁BM NP (prepared with *o*-xylene) film without thermal annealing, (b-f) NP films thermal annealed at 100 °C, 120 °C, 140 °C, 160 °C, 180 °C for 4 min, respectively. Scale bars are 300 nm. AFM image of (g) PTNT:PC₇₁BM NPs film without thermal annealing, (h-l) NP films thermal annealed at 100 °C, 120 °C, 140 °C, 160 °C, 180 °C for 4 min, respectively.

The spherical structure of the NP film persists for progressively higher annealing temperatures ($t_{anneal} = 4$ min. for all experiments), until a thermal annealing temperature of 140 °C is employed. Then, the

sintering of nanoparticles can be observed in the SEM (**Figure 7.12d**) and AFM (**Figure 7.12j**), while the surface of the NP film still exhibits some particle-like features. Upon employing an annealing temperature of 160 °C, NPs were coalescing into a largely homogeneous film. Gross phase separation appeared when annealing the NP film at 180 °C, evidenced by the larger features in SEM image (**Figure 7.12f**) and increased height in AFM image (**Figure 7.12l**). The value of root-mean-squared roughness (R_{RMS}) of NP films measured via AFM is shown in **Table 7.1**. It should be noted that the NPs shown here have larger size compared to NP-xylene and NP-chloroform.

Table 7.1 R_{RMS} value of NP films annealed at varied temperatures.

Thermal annealing condition	No annealing	100 °C	120 °C	140 °C	160 °C	180 °C
R_{RMS} (nm)	6.18	7.27	7.76	7.47	7.94	16.2

The device performance was found to be strongly dependant on the annealing temperature of the NP films (**Figure 7.12, Table 7.2**), with best performing devices being the ones sintered at 160 °C which is in good agreement with the observations made in the morphological studies with SEM and DMTA.

Table 7.2 Device characteristics of PTNT:PC₇₁BM NPs prepared using CHCl₃, best device for varied NP film annealing temperature with average \pm standard deviation in parentheses. Device structure: ITO/ZnO/NPs/MoO₃/Ag. It should be noted that the devices were fabricated using NPs with larger size (60 nm).

Annealing temperature	J_{sc} (mA/cm ²)	FF (%)	V_{oc} (V)	PCE (%)
NPs annealed at 100 °C	1.48 (1.41 \pm 0.06)	34 (33 \pm 3)	0.93 (0.91 \pm 0.02)	0.46 (0.41 \pm 0.04)
NPs annealed at 120 °C	1.54 (1.55 \pm 0.10)	36 (35 \pm 2)	0.91 (0.87 \pm 0.06)	0.50 (0.46 \pm 0.06)
NPs annealed at 140 °C	2.08 (2.04 \pm 0.05)	41 (40 \pm 1)	0.94 (0.93 \pm 0.01)	0.79 (0.76 \pm 0.03)
NPs annealed at 160 °C	2.27 (2.22 \pm 0.04)	49 (48 \pm 1)	0.97 (0.96 \pm 0.01)	1.08 (1.02 \pm 0.03)
NPs annealed at 180 °C	1.74 (1.69 \pm 0.06)	43 (41 \pm 2)	0.97 (0.96 \pm 0.02)	0.73 (0.69 \pm 0.04)

7.4.3.2. Photovoltaic performance of NP-chloroform and NP-xylene

The device characteristics of solar cells fabricated with NP-chloroform and NP-xylene films annealed at 160 °C are listed in **Table 7.3**. NP-chloroform films after thermal annealing at 160 °C were found to result in solar cells with a maximum PCE of 0.76%, a J_{SC} of 2.60 mA/cm² and fill factor (FF) of 32%. The PCE of these devices was further increased up to 1.04% accompanied by slight increase in J_{SC} to 2.84 mA/cm² and a significant increase in FF to 43% upon post-annealing the complete devices at 160 °C. Thermal treatment after the deposition of electrode is known to enhance the performance of NP based solar cells.^{37, 63} Although post-annealing at 160 °C resulted in a slightly higher PCE of 1.04% as compared to the PCE of 0.98% when post-annealed at 140 °C, the standard deviation in the device characteristics in the case of devices post-annealed at 160 °C was higher than that at 140 °C. The increase in the standard deviation could be a result of the uneven distribution of gross phase separation happening during post-annealing at high temperature. The representative J - V curves of NP-chloroform based devices with and without post-annealing are shown in **Figure 7.13a**. It must be noted that the open circuit voltage (V_{OC}) of these devices was found to be as high as 0.90 V, which is comparable to their BHJ counterparts processed from organic solvents (**Table 7.4**).³⁵⁻³⁶ This suggests that the performance of PTNT:PC₇₁BM NP solar cells is mainly limited by the lower current and lower FF , both of which can be highly dependent on the NP film morphology and the nature of the donor/acceptor interface.²⁷ Furthermore, compared to solution-processed BHJ solar cells³⁵, the lower performance of NP devices could be explained by the relatively isolated polymer and PC₇₁BM domains with insufficient connection of fullerene-rich core, which impedes the charge separation⁶⁴ as well as increasing the possibility of non-geminate recombination⁶⁵.

OPVs fabricated from NP-xylene films thermally annealed at 160 °C were found to have higher J_{SC} of 3.91 mA/cm² and comparable V_{OC} of 0.88 V, resulting in a PCE of 1.3%. Post-annealing at 140 °C after the deposition of electrode further increased the PCE up to 1.65 % with the highest J_{SC} of 4.73 mA/cm², 0.89 V in V_{OC} and 39 % in FF . Clearly, the higher performance of the NP-xylene based devices as compared to the NP-chloroform devices is largely due to the higher current in these devices, which is indicative of a relatively more favourable donor-acceptor morphology of NP-xylene film after thermal annealing and is consistent with the observation in the PL measurement. The representative J - V curves of NP-xylene based devices are presented in **Figure 7.13b**. External quantum efficiency (EQE) of NP device post-annealed at 140 °C was found to increase in both PTNT and PC₇₁BM photon absorption range as compared to the non post-annealed devices (**Figure 7.13c**). This could possibly be explained due to better exciton dissociation or reduced charge recombination resulted from the phase separation between polymer and PC₇₁BM.⁶⁶ When a higher post-annealing temperature (i.e. 160 °C) was applied to the device, a decline in the mean value of J_{SC} was observed as well as V_{OC} compared to the device performance without post-annealing. However, an improvement in FF compensated the decrease in J_{SC} and V_{OC} , and resulted in slightly improved efficiency, which is 1.33% on average, compared to the values in device without post-

annealing. The EQE of NP-xylene based device post-annealed at 160 °C showed the contribution of photon harvesting property in PC₇₁BM region (below 400 nm) was increased compared to the contribution from PTNT region (above 400 nm), which can be revealed from the decline of EQE between 450 nm to 600 nm photon wavelength (**Figure 7.13c**). Considering 160 °C is approaching the crystallization temperature of PC₇₁BM,⁵¹ the increase in EQE in the wavelength below 400 nm could be attributed to the crystallization appearing in the pure PC₇₁BM domains, which also agrees with the storage modulus increasing beyond 160 °C (**Figure 7.9**).

Table 7.3 PTNT:PC₇₁BM (1:2 weight ratio) NP device characteristics of best devices for varied post-annealing condition, with average ± standard deviations over 8 devices in parentheses. (All the NP films were thermally annealed at 160 °C before the deposition of electrode.)

Active layer	Annealing condition	J_{sc} (mA/cm ²)	FF (%)	V_{oc} (V)	PCE (%)
NP-chloroform	No post-annealing	2.60 (2.48 ± 0.10)	32 (33 ± 2)	0.90 (0.88 ± 0.03)	0.76 (0.73 ± 0.01)
	140 °C post-annealing	2.75 (2.72 ± 0.10)	39 (39 ± 1)	0.90 (0.88 ± 0.01)	0.98 (0.94 ± 0.02)
	160 °C post-annealing	2.84 (2.59 ± 0.23)	43 (42 ± 1)	0.86 (0.86 ± 0.02)	1.04 (0.93 ± 0.09)
NP-xylene	No post-annealing	4.00 (3.91 ± 0.13)	36 (36 ± 1)	0.89 (0.88 ± 0.02)	1.30 (1.24 ± 0.05)
	140 °C post-annealing	4.73 (4.58 ± 0.13)	39 (39 ± 1)	0.89 (0.87 ± 0.02)	1.65 (1.56 ± 0.06)
	160 °C post-annealing	4.15 (3.76 ± 0.22)	42 (42 ± 1)	0.86 (0.84 ± 0.02)	1.51 (1.33 ± 0.10)

Either with or without post-annealing, the NP solar devices fabricated from *o*-xylene batch PTNT:PC₇₁BM (1:2 weight ratio) NPs achieved higher J_{sc} and efficiency compared to the NP devices produced from NP-chloroform. However, there is no significant difference in FF and V_{oc} between different batches of NPs as long as they were thermally treated in the same way. The increase in J_{sc} is attributed to a finer intermixed nanomorphology in annealed NP-xylene film, which is also suggested by the PL of annealed NP films. The difference in the morphology of NP active layer indicates that post-preparation of NPs, the internal morphology of NPs was changed by altering the miniemulsion dispersed phase solvent from chloroform to *o*-xylene. The difference of the internal

morphology between NP-xylene and NP-chloroform was revealed from the varied PL intensity observed in different batches of NP dispersions.

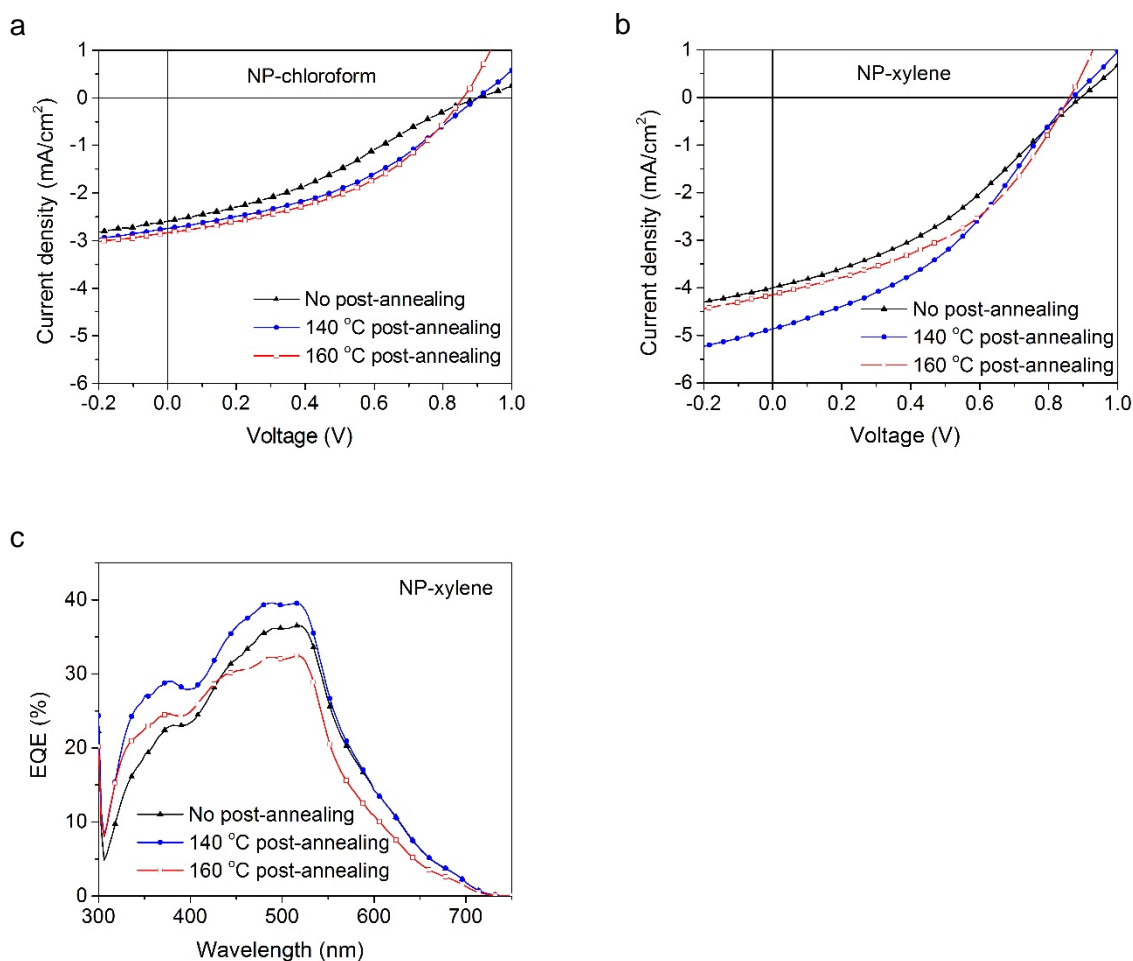


Figure 7.13 Representative J-V curves of devices based on (a) NP-chloroform and (b) NP-xylene without post-annealing and post-annealed at different temperatures. (c) EQE of NP-xylene devices without post-annealing and post-annealed at different temperatures.

BHJ solar cells were also fabricated from PTNT:PC₇₁BM (1:2 weight ratio) blends using chloroform and *o*-xylene as the processing solvents, with the same device geometry. The BHJ devices gave highest PCE of 1.20% with chloroform and 0.84% using *o*-xylene (**Table 7.4**), due to the unfavourable film quality induced by the processing solvents. The NP-OPVs based on aqueous NP-xylene achieved comparable photovoltaic performance without using any harmful solvent during the device fabrication, though the efficiency of PTNT:PC₇₁BM BHJ devices could be improved by altering the processing solvent and using additives.³⁵⁻³⁶

Table 7.4 Device characteristics of PTNT:PC₇₁BM (1:2 weight ratio) BHJ solar cells fabricated using chloroform and *o*-xylene.

BHJ solvent	J_{SC} (mA/cm ²)	FF (%)	V_{OC} (V)	PCE (%)
chloroform	2.55 (2.11 ± 0.27)	53 (51 ± 5)	0.89 (0.90 ± 0.01)	1.20 (0.98 ± 0.19)
<i>o</i> -xylene	1.96 (1.94 ± 0.10)	51 (52 ± 1)	0.84 (0.82 ± 0.01)	0.84 (0.82 ± 0.02)

Device structure: ITO/ZnO/BHJ/MoO₃/Ag.

7.5. Conclusions

Water-dispersed NPs have been prepared from the conjugated polymer PTNT for the first time and non-chlorinated solvent, *o*-xylene, has been used in the miniemulsion method to prepare photoactive NPs for the first time in the NP-OPV research. The NP solar devices fabricated from aqueous PTNT:PC₇₁BM nanoparticles using *o*-xylene as the miniemulsion dispersed phase solvent achieved higher PCE of 1.65%, after optimal thermal-annealing conditions were applied to both the NP layer and the complete device, compared to the chloroform batch counterparts. By introducing *o*-xylene as the miniemulsion dispersed phase solvent to prepare nanoparticles, a water dispersion minimized the amount of organic solvent required in device fabrication and eliminated the utilisation of harmful chlorinated solvents in the solar cell ink preparation. The study of PTNT:PC₇₁BM NPs can potentially be beneficial for the up-scaling of OPV fabrication in future. Furthermore, the preparation procedure presented opens the possibility of using other environment-friendly solvents to achieve aqueous NPs for OPVs.

7.6. References

1. Nejat, P.; Jomehzadeh, F.; Taheri, M. M.; Gohari, M.; Abd. Majid, M. Z., A global review of energy consumption, CO₂ emissions and policy in the residential sector (with an overview of the top ten CO₂ emitting countries). *Renewable and Sustainable Energy Reviews* **2015**, *43*, 843-862.
2. Luderer, G.; Krey, V.; Calvin, K.; Merrick, J.; Mima, S.; Pietzcker, R.; Van Vliet, J.; Wada, K., The role of renewable energy in climate stabilization: results from the EMF27 scenarios. *Climatic Change* **2014**, *123* (3-4), 427-441.
3. Eisenberg, R.; Nocera, D. G., Preface: Overview of the forum on solar and renewable energy. *Inorganic chemistry* **2005**, *44* (20), 6799-6801.
4. Li, S.; Lei, M.; Lv, M.; Watkins, S. E.; Tan, Z. a.; Zhu, J.; Hou, J.; Chen, X.; Li, Y., [6,6]-Phenyl-C61-Butyric Acid Dimethylamino Ester as a Cathode Buffer Layer for High-Performance Polymer Solar Cells. *Advanced Energy Materials* **2013**, *3* (12), 1569-1574.
5. Kalogirou, S. A., *Solar energy engineering: processes and systems*. Academic Press: 2013.
6. Xiao, B.; Wu, H.; Cao, Y., Solution-processed cathode interfacial layer materials for high-efficiency polymer solar cells. *Materials Today* **2015**.
7. Burgués-Ceballos, I.; Machui, F.; Min, J.; Ameri, T.; Voigt, M. M.; Luponosov, Y. N.; Ponomarenko, S. A.; Lacharmoise, P. D.; Campoy-Quiles, M.; Brabec, C. J., Solubility Based Identification of Green Solvents for Small Molecule Organic Solar Cells. *Advanced Functional Materials* **2014**, *24* (10), 1449-1457.
8. Angmo, D.; Larsen-Olsen, T. T.; Jørgensen, M.; Søndergaard, R. R.; Krebs, F. C., Roll-to-Roll Inkjet Printing and Photonic Sintering of Electrodes for ITO Free Polymer Solar Cell Modules and Facile Product Integration. *Advanced Energy Materials* **2013**, *3* (2), 172-175.
9. Noh, J.; Jeong, S.; Lee, J. Y., Ultrafast formation of air-processable and high-quality polymer films on an aqueous substrate. *Nature Communications* **2016**, *7*, 12374.
10. Zhao, W.; Li, S.; Yao, H.; Zhang, S.; Zhang, Y.; Yang, B.; Hou, J., Molecular Optimization Enables over 13% Efficiency in Organic Solar Cells. *Journal of the American Chemical Society* **2017**, *139* (21), 7148-7151.
11. Gedefaw, D.; Sharma, A.; Pan, X.; Bjuggren, J. M.; Kroon, R.; Gregoriou, V. G.; Chochos, C. L.; Andersson, M. R., Optimization of the power conversion efficiency in high bandgap pyridopyridinedithiophene-based conjugated polymers for organic photovoltaics by the random terpolymer approach. *European Polymer Journal* **2017**, *91*, 92-99.
12. Stapleton, A.; Vaughan, B.; Xue, B.; Sesa, E.; Burke, K.; Zhou, X.; Bryant, G.; Werzer, O.; Nelson, A.; David Kilcoyne, A. L.; Thomsen, L.; Wanless, E.; Belcher, W.; Dastoor, P., A multilayered approach to polyfluorene water-based organic photovoltaics. *Solar Energy Materials and Solar Cells* **2012**, *102*, 114-124.
13. Andersen, T. R.; Larsen-Olsen, T. T.; Andreasen, B.; Bottiger, A. P.; Carle, J. E.; Helgesen, M.; Bundgaard, E.; Norrman, K.; Andreasen, J. W.; Jørgensen, M., Aqueous processing of low-band-gap polymer solar cells using roll-to-roll methods. *ACS nano* **2011**, *5* (5), 4188-4196.
14. Krebs, F. C., Fabrication and processing of polymer solar cells: A review of printing and coating techniques. *Solar Energy Materials and Solar Cells* **2009**, *93* (4), 394-412.
15. Krebs, F. C.; Tromholt, T.; Jorgensen, M., Upscaling of polymer solar cell fabrication using full roll-to-roll processing. *Nanoscale* **2010**, *2* (6), 873-86.
16. Brautbar, N.; Williams, J., 2nd, Industrial solvents and liver toxicity: risk assessment, risk factors and mechanisms. *International Journal of Hygiene and Environmental Health* **2002**, *205* (6), 479-91.
17. Moran, M. J.; Zogorski, J. S.; Squillace, P. J., Chlorinated Solvents in Groundwater of the United States. *Environmental Science & Technology* **2007**, *41* (1), 74-81.
18. Chen, X.; Liu, X.; Burgers, M. A.; Huang, Y.; Bazan, G. C., Green-solvent-processed molecular solar cells. *Angewandte Chemie International Edition* **2014**, *53* (52), 14378-81.
19. Zhang, S.; Ye, L.; Zhang, H.; Hou, J., Green-solvent-processable organic solar cells. *Materials Today* **2016**, *19* (9), 533-543.
20. Fan, B.; Ying, L.; Wang, Z.; He, B.; Jiang, X.-F.; Huang, F.; Cao, Y., Optimisation of processing solvent and molecular weight for the production of green-solvent-processed all-polymer solar cells with a power conversion efficiency over 9%. *Energy & Environmental Science* **2017**, *10* (5), 1243-1251.

21. Schwarz, K. N.; Farley, S. B.; Smith, T. A.; Ghiggino, K. P., Charge generation and morphology in P3HT:PCBM nanoparticles prepared by mini-emulsion and reprecipitation methods. *Nanoscale* **2015**, 7 (47), 19899-904.
22. Darwis, D.; Holmes, N.; Elkington, D.; David Kilcoyne, A. L.; Bryant, G.; Zhou, X.; Dastoor, P.; Belcher, W., Surfactant-free nanoparticulate organic photovoltaics. *Solar Energy Materials and Solar Cells* **2014**, 121, 99-107.
23. Gärtner, S.; Christmann, M.; Sankaran, S.; Röhm, H.; Prinz, E.-M.; Penth, F.; Pütz, A.; Türel, A. E.; Penth, B.; Baumstümmler, B.; Colsmann, A., Eco-Friendly Fabrication of 4% Efficient Organic Solar Cells from Surfactant-Free P3HT:ICBA Nanoparticle Dispersions. *Advanced Materials* **2014**, 26 (38), 6653-6657.
24. Landfester, K.; Montenegro, R.; Scherf, U.; GüNTNER, R.; Asawapirom, U.; Patil, S.; Neher, D.; Kietzke, T., Semiconducting polymer nanospheres in aqueous dispersion prepared by a miniemulsion process. *Advanced Materials* **2002**, 14 (9), 651-655.
25. Holmes, N. P.; Burke, K. B.; Sista, P.; Barr, M.; Magurudeniya, H. D.; Stefan, M. C.; Kilcoyne, A. L. D.; Zhou, X.; Dastoor, P. C.; Belcher, W. J., Nano-domain behaviour in P3HT:PCBM nanoparticles, relating material properties to morphological changes. *Solar Energy Materials and Solar Cells* **2013**, 117, 437-445.
26. D'Olieslaeger, L.; Pfannmöller, M.; Fron, E.; Cardinaletti, I.; Van Der Auweraer, M.; Van Tendeloo, G.; Bals, S.; Maes, W.; Vanderzande, D.; Manca, J.; Ethirajan, A., Tuning of PCDTBT:PC71BM blend nanoparticles for eco-friendly processing of polymer solar cells. *Solar Energy Materials and Solar Cells* **2017**, 159, 179-188.
27. Colberts, F. J. M.; Wienk, M. M.; Janssen, R. A. J., Aqueous Nanoparticle Polymer Solar Cells: Effects of Surfactant Concentration and Processing on Device Performance. *ACS Applied Materials & Interfaces* **2017**, 9 (15), 13380-13389.
28. Parrenin, L.; Laurans, G.; Pavlopoulou, E.; Fleury, G.; Pecastaings, G.; Brochon, C.; Vignau, L.; Hadziioannou, G.; Cloutet, E., Photoactive Donor-Acceptor Composite Nanoparticles Dispersed in Water. *Langmuir* **2017**, 33 (6), 1507-1515.
29. Prunet, G.; Parrenin, L.; Pavlopoulou, E.; Pecastaings, G.; Brochon, C.; Hadziioannou, G.; Cloutet, E., Aqueous PCDTBT:PC71 BM Photovoltaic Inks Made by Nanoprecipitation. *Macromol Rapid Commun* **2017**.
30. Kuehne, A. J.; Gather, M. C.; Sprakel, J., Monodisperse conjugated polymer particles by Suzuki-Miyaura dispersion polymerization. *Nature Communications* **2012**, 3, 1088.
31. Anwar, N.; Willms, T.; Grimme, B.; Kuehne, A. J. C., Light-Switchable and Monodisperse Conjugated Polymer Particles. *ACS Macro Letters* **2013**, 2 (9), 766-769.
32. Parrenin, L.; Brochon, C.; Hadziioannou, G.; Cloutet, E., Low Bandgap Semiconducting Copolymer Nanoparticles by Suzuki Cross-Coupling Polymerization in Alcoholic Dispersed Media. *Macromolecular Rapid Communications* **2015**, 36 (20), 1816-21.
33. Ullum, S.; Holmes, N.; Darwis, D.; Burke, K.; David Kilcoyne, A. L.; Zhou, X.; Belcher, W.; Dastoor, P., Determining the structural motif of P3HT:PCBM nanoparticulate organic photovoltaic devices. *Solar Energy Materials and Solar Cells* **2013**, 110, 43-48.
34. D'Olieslaeger, L.; Pirotte, G.; Cardinaletti, I.; D'Haen, J.; Manca, J.; Vanderzande, D.; Maes, W.; Ethirajan, A., Eco-friendly fabrication of PBDTPD:PC71BM solar cells reaching a PCE of 3.8% using water-based nanoparticle dispersions. *Organic Electronics* **2017**, 42, 42-46.
35. Kroon, R.; Diaz de Zerio Mendaza, A.; Himmelberger, S.; Bergqvist, J.; Bäcke, O.; Faria, G. C.; Gao, F.; Obaid, A.; Zhuang, W.; Gedefaw, D.; Olsson, E.; Inganäs, O.; Salleo, A.; Müller, C.; Andersson, M. R., A New Tetracyclic Lactam Building Block for Thick, Broad-Bandgap Photovoltaics. *Journal of the American Chemical Society* **2014**, 136 (33), 11578-11581.
36. Sharma, A.; Kroon, R.; Lewis, D. A.; Andersson, G. G.; Andersson, M. R., Poly(4-vinylpyridine): A New Interface Layer for Organic Solar Cells. *ACS Applied Materials & Interfaces* **2017**, 9 (12), 10929-10936.
37. Holmes, N. P.; Marks, M.; Kumar, P.; Kroon, R.; Barr, M. G.; Nicolaidis, N.; Feron, K.; Pivrikas, A.; Fahy, A.; Mendaza, A. D. D. Z.; Kilcoyne, A.; Müller, C.; Zhou, X.; Andersson, M. R.; Dastoor, P. C.; Belcher, W. J., Nano-pathways: Bridging the divide between water-processable nanoparticulate and bulk heterojunction organic photovoltaics. *Nano Energy* **2016**, 19, 495-510.
38. Wang, Y.; Cheng, G., Application of gradient-based Hough transform to the detection of corrosion pits in optical images. *Applied Surface Science* **2016**, 366, 9-18.

39. Sharma, A.; Pan, X.; Campbell, J. A.; Andersson, M. R.; Lewis, D. A., Unravelling the Thermomechanical Properties of Bulk Heterojunction Blends in Polymer Solar Cells. *Macromolecules* **2017**, *50* (8), 3347-3354.
40. Kilcoyne, A.; Tyliczszak, T.; Steele, W.; Fakra, S.; Hitchcock, P.; Franck, K.; Anderson, E.; Harteneck, B.; Rightor, E.; Mitchell, G., Interferometer-controlled scanning transmission X-ray microscopes at the Advanced Light Source. *Journal of synchrotron radiation* **2003**, *10* (2), 125-136.
41. McNeill, C. R.; Watts, B.; Thomsen, L.; Belcher, W. J.; Greenham, N. C.; Dastoor, P. C., Nanoscale quantitative chemical mapping of conjugated polymer blends. *Nano letters* **2006**, *6* (6), 1202-1206.
42. Sun, Y.; Seo, J. H.; Takacs, C. J.; Seifert, J.; Heeger, A. J., Inverted polymer solar cells integrated with a low-temperature-annealed sol-gel-derived ZnO Film as an electron transport layer. *Advanced Materials* **2011**, *23* (14), 1679-83.
43. Hu, Z.; Gesquiere, A. J., PCBM concentration dependent morphology of P3HT in composite P3HT/PCBM nanoparticles. *Chemical Physics Letters* **2009**, *476* (1-3), 51-55.
44. Hu, Z.; Tenery, D.; Bonner, M. S.; Gesquiere, A. J., Correlation between spectroscopic and morphological properties of composite P3HT/PCBM nanoparticles studied by single particle spectroscopy. *Journal of Luminescence* **2010**, *130* (5), 771-780.
45. Vaughan, B.; Williams, E. L.; Holmes, N. P.; Sonar, P.; Dodabalapur, A.; Dastoor, P. C.; Belcher, W. J., Water-based nanoparticulate solar cells using a diketopyrrolopyrrole donor polymer. *Physical Chemistry Chemical Physics* **2014**, *16* (6), 2647-53.
46. Benanti, T.; Venkataraman, D., Organic Solar Cells: An Overview Focusing on Active Layer Morphology. *Photosynth Res* **2006**, *87* (1), 73-81.
47. Treat, N. D.; Chabynyc, M. L., Phase separation in bulk heterojunctions of semiconducting polymers and fullerenes for photovoltaics. *Annu Rev Phys Chem* **2014**, *65*, 59-81.
48. Ulum, S.; Holmes, N.; Barr, M.; Kilcoyne, A. L. D.; Gong, B. B.; Zhou, X.; Belcher, W.; Dastoor, P., The role of miscibility in polymer:fullerene nanoparticulate organic photovoltaic devices. *Nano Energy* **2013**, *2* (5), 897-905.
49. Dam, H. F.; Holmes, N. P.; Andersen, T. R.; Larsen-Olsen, T. T.; Barr, M.; Kilcoyne, A. L. D.; Zhou, X.; Dastoor, P. C.; Krebs, F. C.; Belcher, W. J., The effect of mesomorphology upon the performance of nanoparticulate organic photovoltaic devices. *Solar Energy Materials and Solar Cells* **2015**, *138*, 102-108.
50. Xia, Y.; Musumeci, C.; Bergqvist, J.; Ma, W.; Gao, F.; Tang, Z.; Bai, S.; Jin, Y.; Zhu, C.; Kroon, R.; Wang, C.; Andersson, M. R.; Hou, L.; Inganäs, O.; Wang, E., Inverted all-polymer solar cells based on a quinoxaline–thiophene/naphthalene-diimide polymer blend improved by annealing. *Journal of Materials Chemistry A* **2016**, *4* (10), 3835-3843.
51. Leman, D.; Kelly, M. A.; Ness, S.; Engmann, S.; Herzing, A.; Snyder, C.; Ro, H. W.; Kline, R. J.; DeLongchamp, D. M.; Richter, L. J., In Situ Characterization of Polymer–Fullerene Bilayer Stability. *Macromolecules* **2015**, *48* (2), 383-392.
52. Holmes, N. P.; Ulum, S.; Sista, P.; Burke, K. B.; Wilson, M. G.; Stefan, M. C.; Zhou, X.; Dastoor, P. C.; Belcher, W. J., The effect of polymer molecular weight on P3HT:PCBM nanoparticulate organic photovoltaic device performance. *Solar Energy Materials and Solar Cells* **2014**, *128*, 369-377.
53. Pedersen, E. B. L.; Pedersen, M. C.; Simonsen, S. B.; Brandt, R. G.; Böttiger, A. P. L.; Andersen, T. R.; Jiang, W.; Xie, Z. Y.; Krebs, F. C.; Arleth, L.; Andreasen, J. W., Structure and crystallinity of water dispersible photoactive nanoparticles for organic solar cells. *Journal of Materials Chemistry A* **2015**, *3* (33), 17022-17031.
54. Li, D.; Brisson, J., DMTA and FTIR Investigation of the Phase Behavior of Poly(methyl methacrylate)–Poly(4-vinylphenol) Blends. *Macromolecules* **1996**, *29* (3), 868-874.
55. Goertzen, W. K.; Kessler, M. R., Dynamic mechanical analysis of carbon/epoxy composites for structural pipeline repair. *Composites Part B: Engineering* **2007**, *38* (1), 1-9.
56. Matsuoka, S., *Relaxation phenomena in polymers*. Hanser Munich etc.: 1992.
57. Karagiannidis, P. G.; Stergiou, A. C.; Karayannidis, G. P., Study of crystallinity and thermomechanical analysis of annealed poly(ethylene terephthalate) films. *European Polymer Journal* **2008**, *44* (5), 1475-1486.
58. Kuila, B. K.; Nandi, A. K., Structural Hierarchy in Melt-Processed Poly(3-hexyl thiophene)–Montmorillonite Clay Nanocomposites: Novel Physical, Mechanical, Optical, and Conductivity Properties. *The Journal of Physical Chemistry B* **2006**, *110* (4), 1621-1631.

59. Kim, K.; Liu, J.; Namboothiry, M. A. G.; Carroll, D. L., Roles of donor and acceptor nanodomains in 6% efficient thermally annealed polymer photovoltaics. *Applied Physics Letters* **2007**, *90* (16), 163511.
60. Kim, Y.; Cook, S.; Tuladhar, S. M.; Choulis, S. A.; Nelson, J.; Durrant, J. R.; Bradley, D. D. C.; Giles, M.; McCulloch, I.; Ha, C.-S.; Ree, M., A strong regioregularity effect in self-organizing conjugated polymer films and high-efficiency polythiophene:fullerene solar cells. *Nature Materials* **2006**, *5* (3), 197-203.
61. Van Bavel, S. S.; Bärenklau, M.; de With, G.; Hoppe, H.; Loos, J., P3HT/PCBM Bulk Heterojunction Solar Cells: Impact of Blend Composition and 3D Morphology on Device Performance. *Advanced Functional Materials* **2010**, *20* (9), 1458-1463.
62. Wang, J.; Wang, D.; Moses, D.; Heeger, A. J., Dynamic quenching of 5-(2'-ethyl-hexyloxy)-p-phenylene vinylene (MEH-PPV) by charge transfer to a C60 derivative in solution. *Journal of Applied Polymer Science* **2001**, *82* (10), 2553-2557.
63. Bag, M.; Gehan, T. S.; Renna, L. A.; Algaier, D. D.; Lahti, P. M.; Venkataraman, D., Fabrication conditions for efficient organic photovoltaic cells from aqueous dispersions of nanoparticles. *RSC Advances* **2014**, *4* (85), 45325-45331.
64. Al-Mudhaffer, M. F.; Griffith, M. J.; Feron, K.; Nicolaidis, N. C.; Cooling, N. A.; Zhou, X.; Holdsworth, J.; Belcher, W. J.; Dastoor, P. C., The origin of performance limitations in miniemulsion nanoparticulate organic photovoltaic devices. *Solar Energy Materials and Solar Cells* **2018**, *175*, 77-88.
65. Xie, C.; Classen, A.; Späth, A.; Tang, X.; Min, J.; Meyer, M.; Zhang, C.; Li, N.; Osvet, A.; Fink, R. H.; Brabec, C. J., Overcoming Microstructural Limitations in Water Processed Organic Solar Cells by Engineering Customized Nanoparticulate Inks. *Advanced Energy Materials* **2018**, 1702857.
66. Kesava, S. V.; Fei, Z.; Rimshaw, A. D.; Wang, C.; Hexemer, A.; Asbury, J. B.; Heeney, M.; Gomez, E. D., Domain Compositions and Fullerene Aggregation Govern Charge Photogeneration in Polymer/Fullerene Solar Cells. *Advanced Energy Materials* **2014**, *4* (11), 1400116.

Conclusion

The development of OPVs has been under rapid growth in the past four years, and remarkably high efficiency over 13% has been achieved. The design of novel low bandgap conjugated materials realised the efficient photon harvesting, as well as the device engineering optimizing the device structure to improve the photovoltaic performance. However, the large consumption of organic, especially halogenated solvents impedes the commercial application of the OPVs, due to their health-hazard to organic life and high cost associated with solvent recovery systems. Hence, it is urgent to develop the green fabrication of OPVs.

This thesis presents two approaches to achieve the green deposition of active layer in OPVs by (1) design and synthesis of p-type conjugated polymers that exhibit green solvent solubility; (2) preparation of water dispersed nanoparticles from donor-acceptor material blend for water processable application of photoactive materials.

The design of water/ethanol soluble conjugated polymers is based on the modification of substituent on well-studied TQ1 polymer. Instead of hydrophobic aliphatic side groups, tertiary amine, pyridine and oligoethylene glycol (OEG) functionalized groups were introduced to the quinoxaline structure, yielding TQ1 derivatives with respective functionalities. The amine or pyridine functionalized polymers showed water/ethanol solubility upon the nitrogen with lone-pair electrons being protonated by volatile acid, which is a reversible process without influencing the thermal stability of polymers. Whereas, the highly hydrophilic OEG functionalized polymer TQ-OEG realise the process of neutral polymer using ethanol.

To study the effect of introduced solubilizing side groups on photovoltaic performance, Chapter 4 presents a systematic study of tertiary amine functionalized polymers and pyridine functionalized polymers. The lack of green solvent soluble n-type materials impedes the evaluation of photovoltaic performance of tertiary amine/pyridine-functionalized polymers using water/alcohol, and organic solvent is used as a compromise to fabricate OPVs with fullerene acceptor. It was found that the amine/pyridine functionalized polymers altered the work function of MoO₃ interlayer in an energetic unfavourable direction, and the device performance was successfully improved by interface engineering using a TPD buffer layer. For the optimized device structure, OPVs based on ethanol soluble amino polymer TQ1-50A presented PCE of 0.82%, which was further improved to 1.33% upon replacing TQ1-50A with pyridine-modified polymer TQ1-50P4. In general, the photovoltaic performance of pyridine polymers showed more promising results compared to the amino polymers, revealing pyridine groups being better candidature for side-chain engineering.

In Chapter 5, more polymers functionalised with tertiary amine, pyridine or OEG side groups are presented. The solvent used for Stille-coupling polymerisation to synthesise polymer with pyridine

polar side groups was studied, and higher molecular weight was achieved by carefully choosing the solvent system. TQ1A and its analogues were designed as the electron-donor material for OPVs, which were also successfully applied in electrochromic devices using green solvent. Whereas, QFA, QFA-Br and QFA-Si, which are polymerised from tertiary amine substituted quinoxaline and fluorene, were designed as the green-solvent processable cathode interface materials. Effective photovoltaic response was achieved based on TQ1A as an electron donor in the BHJ OPVs, although the efficiency is remaining lower compared to reported TQ1 devices. The loss mechanism that results in inferior performance is still under investigation. The evaluation of meta-substituent pyridine polymer TQ1P3 showed different photovoltaic performance compared to the para-substituent TQ1P4, revealing that the delocalization of lone-pair electrons could suppress the interface interaction between pyridine and MoO₃ interlayer. The OEG modified polymer TQ-OEG showed effective photovoltaic response when combined with PCBM to form active layer. The low glass transition temperature of TQ-OEG revealed from DMTA study indicates that the thermal properties of conjugated polymers can be tuned by side chain modification.

In Chapter 6, the approach to realise water processable active layer was presented by the preparation of water-dispersed nanoparticles (NPs). Two methods, i.e. miniemulsion and precipitation technique, to make NPs have been performed on different conjugated materials and the experimental parameters in each procedure have been systematically studied. Amino and pyridine functional polymer as well as the functionalized fullerene derivative have been used to facilitate the stabilization of particles in water and to eliminate the usage of ionic surfactant, and nanoparticles have been successfully achieved in the absence of an additional surfactant. However, the procedure to make NPs without SDS by miniemulsion method is still under optimization and NP-OPVs in the absence of SDS will be fabricated in the future.

Due to the nature of core-shell nanostructure occurred to NPs prepared by miniemulsion method, precipitation method was developed aiming to achieve finer blended morphology in single particles. It was found that the stability of NPs is highly sensitive to the final concentration of solid in the aqueous ink post precipitation, and non-ionic surfactant was introduced in the procedure to facilitate the particle stabilization. However, the intrinsic limited stability of NPs prepared using precipitation method has to be overcome to achieve highly performing OPVs based on these NP active layers.

In Chapter 7, an environmentally benign preparation of nanoparticles was presented by using *o*-xylene as the precursor solvent. In this study, a conjugated donor polymer PTNT and PC₇₁BM was used to form water processable nanoparticle inks for OPV fabrication. It was found that by altering the precursor solvent, the thermally annealed NP films showed different nanomorphology. The devices based on *o*-xylene batch NPs achieved the PCE of 1.65%, after optimal thermal-annealing conditions were applied to both the NP layer and the complete device. Furthermore, DMTA has been applied to study the thermal mechanical property of NP systems to correlate the behaviour of

coalescence with the thermal transition of conjugated materials. The introduction of DMTA to NPs compliments the commonly used technique, i.e. AFM and SEM, which only probe the surface topography.

In summary, it is a long journey to achieve completely green fabrication of organic photovoltaics. The substituent engineering is proven to be an effective and efficient tool to tune the solubility of conjugated polymers being water/ethanol soluble. However, the ratio between introduced polar substituents and aliphatic side groups requires to be well balanced to achieve both green solvent solubility and decent photovoltaic performance. In addition, the substituent needs to be carefully chosen to avoid the charge traps created by functional groups. The conversion from organic solution of conjugated materials to water-dispersed conjugated nanoparticles shows very promising results, as the PCE achieved from NP inks is comparable with their organic solvent processed counterparts.

Appendix A

1. Detailed synthesis procedure of small molecules

3,6-dibromobenzene-1,2-diamine (4-1): 4,7-dibromobenzo[c][1,2,5]thiadiazole (13.0 g, 44.2 mmol) was added in a 1000 mL flask with EtOH (330 mL). After being stirred at 0 °C in an ice bath for half an hour, NaBH₄ was added to the solution in portions. Then the reaction mixture was stirred at r.t. for 20 h. Through checking thin-layer chromatography (TLC), there was no starting material left, the reaction was quenched by adding water and then stirred for 20 min at r.t.. After that, the mixture was extracted with diethyl ether. The organic phase was washed with saturated NaCl (aq.) and water subsequently prior to being dried via NaSO₄. After filtration, the solvent in filtrate was removed by rotary evaporation, crude product was obtained as light yellow solid. In this reaction process, the generated gas in the mixture caused a small explosion, and some of the mixture was lost due to the spilling. After recrystallisation with ethanol and water, the product was dried in a vacuum oven, resulting grey solid (5.7 g, 48.5%). ¹H-NMR (300 MHz, CDCl₃) δ 3.90(b, 4H, NH₂), 6.85(s, 2H, ArH).

2-hydroxy-1,2-bis(3-methoxyphenyl)ethanone (4-2): Thiamine hydrochloride (10 g, 29.6 mmol) was added to a 500 mL roundbottom flask with 200 mL EtOH, resulting a white suspension. Water was added under stirring until a colorless transparent solution was obtained. Then NaOH (aq. 20 mL, 2 M, 60 mmol) was added dropwise to the solution. The color of solution turned to yellow from colorless, and after stirring for 2 min changed to pale yellow. Then 3-methoxybenzaldehyde (**3**) (50 g, 367.2 mmol) was added and the reaction mixture was stirred at 40 °C for 20 h. Through checking TLC, the mixture was cooled to r.t to stop reaction. Then mixture was poured into water, and extracted with dichloromethane (DCM). The organic phase was washed with brine and water subsequently. After dried via NaSO₄, filtered and removed solvent through rotary evaporator, crude product was obtained as orange oil (55.9 g), which was used in the next step without further purification.

1,2-bis(3-methoxyphenyl)ethane-1,2-dione (4-3): The crude product (**4-2**) (55.9 g) from benzoin condensation was dissolved in 200 mL DMSO, then 115 mL HBr (48%) was added gradually under stirring during the period of around 50 min at r.t. After all the HBr had been added, the mixture turned to be less transparent and was stirred under 50 °C for 4 hours before stirred under 90 °C for 16 hours. Then the brown reaction suspension was cooled in an ice bath, and after filtration, brown crystals was got as crude product. The crude product was recrystallised with EtOH and water, and then dried in a vacuum oven to yield product (35.6g, 64.2%), which were light yellow crystals. ¹H NMR (300 MHz, CDCl₃) δ 7.62 (t, 2H), 7.50 (m, 2H), 7.39 (t, 2H), 7.23 (dd, 2H), 3.69 (s, 6H).

1,2-bis(3-hydroxyphenyl)ethane-1,2-dione (4-4): HBr (385 mL, 48%), acetic acid (60 mL) and 1,2-bis(3-methoxyphenyl)ethane-1,2-dione (**4-3**) (35.6 g, 131.7 mmol) were added to a 1000 mL

roundbottom flask. After heated under reflux for 4 hours, the reaction mixture turned to dark green brown. Through checking TLC, the reaction was stopped by cooling to r.t and then put in an ice bath under stirring for 1 h prior to filter. The filter cake was washed with cold water several time, then dried in the vacuum oven under 40 °C, affording slight green solid product (30.2g, 94.67%). ¹H NMR (300 MHz, DMSO-*d*₆) δ 10.03 (s, 2H), 7.41 (ddd, *J* = 8.1, 7.4, 0.6 Hz, 2H), 7.30 – 7.22 (m, 4H), 7.15 (ddd, *J* = 8.1, 2.5, 1.1 Hz, 2H).

1,2-bis(3-(3-(dimethylamino)propoxy)phenyl)ethane-1,2-dione (4-5): To a 500 mL roundbottom, flask, 1,2-bis(3-hydroxyphenyl)ethane-1,2-dione (**4-4**) (5.0 g, 20.6 mmol), K₂CO₃ (20.7 g, 150.0 mmol), KI (0.342 g, 2.06 mmol) was added with 200 mL DMSO. The mixture was heated up to 90 °C under stirring. Then 3-dimethylamino-1-propylchloride hydrochloride (15.8 g, 100 mmol) was added in portions and the reaction mixture was stirred under 90 °C for 2 days. The reaction was stopped by cooling to r.t. before 200 mL of water was added. After stirring for 20 min, the mixture was extracted with ethyl acetate, and organic phase was separated, washed with brine and water, dried via NaSO₄, filtered and solvent was removed under rotary evaporation to afford a brown oily crude product. The crude product was purified through column chromatography with DCM : methanol : trimethylamine = 20 : 1 : 1 as the eluent and 1.2 g product was obtained (14.1%). ¹H NMR (300 MHz, DMSO-*d*₆) δ 7.50 (t, *J* = 8.0 Hz, 2H), 7.42 – 7.37 (m, 4H), 7.37 – 7.32 (m, 2H), 4.06 (t, *J* = 6.4 Hz, 4H), 2.34 (t, *J* = 7.1 Hz, 4H), 2.13 (s, 12H), 1.90 – 1.78 (m, 4H).

3,3'-(((5,8-dibromoquinoxaline-2,3-diyl)bis(3,1-phenylene))bis(oxy))bis(N,N-dimethylpropan-1-amine) (4-6): 1,2-bis(3-(3-(dimethylamino)propoxy)phenyl)ethane-1,2-dione (**4-5**) (1.1 g, 2.67 mmol), 3,6-dibromobenzene-1,2-diamine (**4-1**) (0.645 g, 2.42 mmol) was added in a 25 mL round-bottom flask with 10 mL acetic acid. The reaction mixture was stirred under 60 °C overnight before checking TLC and was found no starting materials left. Then the reaction mixture was cooled to r.t. and transferred into K₂CO₃ (aq. pH=12) solution, resulting a yellow emulsion (pH=9). The emulsion was extracted with chloroform, and separated organic phase was washed with brine, dried with NaSO₄. After filtration and removal of solvent, brown oily crude product was purified through column chromatography with DCM : hexane : methanol : trimethylamine = 20 : 10 : 1 : 1 as eluent to afford yellow solid. Then the yellow solid was further purified through recrystallisation with acetone and water, and pale yellow crystals were obtained (1.5 g, 87.4%). ¹H NMR (300 MHz, DMSO-*d*₆) δ 8.14 (s, 2H), 7.34 – 7.26 (m, 2H), 7.11 (dd, *J* = 7.1, 1.3 Hz, 4H), 7.01 – 6.96 (m, 2H), 3.88 (t, *J* = 6.5 Hz, 4H), 2.28 (t, *J* = 7.0 Hz, 4H), 2.11 (s, 12H), 1.75 (p, *J* = 6.7 Hz, 4H).

3,3'-(5,8-dibromoquinoxaline-2,3-diyl)diphenol (4-7): 1,2-bis(3-hydroxyphenyl)ethane-1,2-dione (**4-4**) (0.735 g, 3.03 mmol), 3,6-dibromobenzene-1,2-diamine (**4-1**) (0.807 g, 3.03 mmol) were mixed with 30 mL acetic acid. After the mixture was stirred at room temperature for one hour, reaction temperature was increased to 60 °C. And the reaction mixture was stirred for one hour at 60 °C. After checking TLC to confirm there is no reactants remaining, the reaction was quenched by adding

80 mL water to the reaction mixture. Then the mixture was cooled down to room temperature to offer a grey suspension. After filtering the suspension, the filter cake was washed with water several time, then dried in the vacuum oven under 30 °C overnight. 1.34 g grey solid product was obtained (93.7%). ¹H NMR (300 MHz, DMSO-*d*₆) δ 9.60 (s, 2H), 8.12 (s, 2H), 7.16 (t, 2H), 7.05-7.08 (m, 2H), 6.85-6.91 (m, 2H), 6.79-6.85 (m, 2H).

4-(3-bromopropyl)pyridine hydrobromide (4-8): 4-pyridinepropanol (3.35 g, 24.4 mmol) was added to a 50 mL round-bottom flask with 30 mL of hydrobromic acid (48 wt. % in H₂O). The reaction mixture was heated under reflux overnight. Then the reaction was stopped by cooling to room temperature and neutralized with potassium carbonate solution (38.2 g in 100 mL water). The neutralized crude was extracted with diethyl ether and washed with water several times. After collecting the organic phase, Mg₂SO₄ was added into the solution for drying. The dried solution was filtered and stirred with adding 2.76 mL HBr (48 wt. % in H₂O) before diethyl ether was removed under rotary evaporator. Then 40 mL of acetonitrile was added to the mixture to assist the evaporation of water before removing solvents again. This procedure was repeated two times. Then 25 mL DCM was added to the mixture before removing solvents. This procedure was repeated two times to yield solid product. After keeping in the vacuum oven overnight at 30 °C, pale yellow solid product was obtained (5.2 g, 75.8%). ¹H NMR (300 MHz, D₂O) δ 8.51 (d, 2H), 7.81 (d, 2H), 3.49 (t, 2H), 2.99 (t, 2H), 2.17-2.29 (m, 2H).

5,8-dibromo-2,3-bis(3-(3-(pyridin-4-yl)propoxy)phenyl)quinoxaline (4-9): 3,3'-(5,8-dibromoquinoxaline-2,3-diyl)diphenol (**4-7**) (0.865 g, 1.83 mmol), potassium carbonate (1.85 g, 13.4 mmol), 18-crown-6 (30 mg) were added with 40 mL acetonitrile into a round-bottom flask. The mixture was heated up to 80 °C under N₂ for 1 hour. Then 4-(3-bromopropyl)pyridine hydrobromide (**4-8**) (2.571 g, 9.15 mmol) was dissolved in 7 mL acetonitrile and the solution was slowly transferred to the reaction mixture in portions. After all 4-(3-bromopropyl)pyridine hydrobromide was transferred, reaction temperature was increased to 87 °C to let the solvent reflux under N₂ overnight. After the mixture was reacted for 24 hours, TLC was checked (ethyl acetate: DCM: methanol=12: 12: 1) to confirm no starting material (**4-7**) remaining in the reaction mixture. The reaction was stopped by cooling to r.t. and then removing acetonitrile under rotary evaporation. The residue was re-dissolved by adding chloroform and water. The organic phase was separated and washed with water for several times before drying with MgSO₄. Then the solvent in filtered solution was removed by rotary evaporation to offer a brown viscous liquid crude product. The crude product was purified through column chromatography with ethyl acetate: DCM: methanol=14: 14: 1 as the eluent. Yellow solid product was obtained (0.55 g, 42.3%). ¹H NMR (300 MHz, DMSO-*d*₆) δ 8.44 (d, 4H), 8.15 (s, 2H), 7.25-7.32 (m, 2H), 7.20 (d, 4H), 7.01-7.14 (m, 4H), 6.91-6.99 (m, 2H), 3.84(t, 4H), 2.68 (t, 4H), 1.92-1.99 (m, 4H).

3-(3-bromopropyl)pyridine hydrobromide (5-2): 3-pyridinepropanol (5.19 g, 37.8 mmol) was added to a 100 mL round-bottom flask with 50 mL of hydrobromic acid (48 wt. % in H₂O). The reaction mixture was heated under reflux overnight. Then the reaction was stopped by cooling to room temperature and neutralized with potassium carbonate solution (40 g in 100 mL water). The neutralized crude was extracted with diethyl ether and washed with water several times. After collecting the organic phase, Mg₂SO₄ was added into the solution for drying. The dried solution was filtered and stirred with adding 4.3 mL HBr (48 wt. % in H₂O) before diethyl ether was removed under rotary evaporator. Then 40 mL of acetonitrile was added to the mixture to assist the evaporation of water before removing solvents again. This procedure was repeated two times. Then 30 mL DCM was added to the mixture before removing solvents. This procedure was repeated two times to yield solid product. After keeping in the vacuum oven overnight at 30 °C, pale yellow solid product was obtained (8.33 g, 78.4%). ¹H NMR (300 MHz, DMSO-*d*₆) δ 8.65 (d, 2H), 8.50 (d, 1H), 7.95 (t, 1H), 3.48 (t, 2H), 2.99 (t, 2H), 2.17-2.27 (m, 2H).

5,8-dibromo-2,3-bis(3-(3-(pyridin-3-yl)propoxy)phenyl)quinoxaline (5-3): 3,3'-(5,8-dibromoquinoxaline-2,3-diyl)diphenol (**4-7**) (1.328 g, 2.82 mmol), potassium carbonate (2.92 g, 21 mmol), 18-crown-6 (40 mg) were added with 40 mL acetonitrile into a round-bottom flask. The mixture was heated up to 80 °C under N₂ for 1 hour. Then 3-(3-bromopropyl)pyridine hydrobromide (**5-2**) (3.96 g, 14.1 mmol) was dissolved in 7 mL acetonitrile and the solution was slowly transferred to the reaction mixture in portions. After all 3-(3-bromopropyl)pyridine hydrobromide was transferred, reaction temperature was increased to 87 °C to let the solvent reflux under N₂ overnight. After the mixture was reacted for 24 hours, TLC was checked (ethyl acetate: DCM: methanol=12: 12: 1) to confirm no starting material (**4-7**) remaining in the reaction mixture. The reaction was stopped by cooling to r.t. and then removing acetonitrile under rotary evaporation. The residue was re-dissolved by adding chloroform and water. The organic phase was separated and washed with water for several times before drying with MgSO₄. Then the solvent in filtered solution was removed by rotary evaporation to offer a brown viscous liquid crude product. The crude product was purified through column chromatography with ethyl acetate: DCM: methanol=12: 12: 1 as the eluent. Pale yellow solid product was obtained (0.2672 g, 13.3%).

2. Polymerisation procedure

2.1. Stille coupling polymerisation

Poly[3,3'-(((5,8-dibromoquinoxaline-2,3-diyl)bis(3,1-phenylene))bis(oxy))bis(N,N-dimethylpropan-1-amine)-alt-thiophene] (TQ1A)

3,3'-(((5,8-dibromoquinoxaline-2,3-diyl)bis(3,1-phenylene))bis(oxy))bis(N,N-dimethylpropan-1-amine) (**4-6**) (200.9 mg, 0.3127 mmol) and 2,5-bis(trimethylstannyl)thiophene (128.1 mg, 0.3127 mmol) were added to a dry 25 mL flask, vacuumed and then protected with Nitrogen before 10 mL of degassed dry toluene was added to the flask. The solution was stirred at 90 °C under N₂ protection

for 30 min. Then catalysts, tris(dibenzylideneacetone)dipalladium(0) (6 mg) and tri(o-tolyl)phosphine (12 mg) was dissolved in 2 mL degassed toluene and resulting solution was added to the monomer solution. The colour of the mixture turned to deep blue after stirring for half an hour. Depending on the viscosity of the solution, the reaction mixture was stirred at 90 °C for 2 days. Then the solution was precipitated in hexane and filtered to collect solid. The dark blue solid was re-dissolved in 100 mL chloroform and a solution of sodium diethyldithiocarbamate trihydrate (10%, 10 g in 100 mL H₂O) was added to the resulting CHCl₃ solution. The mixture was stirred vigorously at 60 °C for 1 h. Then the organic phase was separated and washed with deionized water for 5 times to remove most of the residual complex agent. The organic phase was concentrated to approximately 10 mL before precipitated in methanol. The polymer was collected by filtration through an extraction thimble, and Soxhlet-extracted subsequently with hexane, acetone, diethyl ether, ethyl acetate and finally chloroform. The chloroform fraction was concentrated to about 10 mL, and precipitated in methanol. The solid was collected by filtration and dried in a vacuum oven under 36 °C to afford 168.7 mg polymer (95.4%). ¹H NMR (600 MHz, CDCl₃) δ 7.81-8.31 (m, 4H), 7.31-7.49 (m, 2H), 7.11-7.23 (m, 4H), 6.87 (s, 2H), 3.79 (bs, 4H), 2.19-2.30 (m, 4H), 2.10-2.12 (m, 12H), 1.75 (bs, 4H).

TQ1-20A

3,3'-(((5,8-dibromoquinoxaline-2,3-diyl)bis(3,1-phenylene))bis(oxy))bis(N,N-dimethylpropan-1-amine) (**4-6**) (37.4 mg, 0.0582 mmol), 5,8-dibromo-2,3-bis(3-(octyloxy)phenyl)quinoxaline (153.4 mg, 0.2328 mmol), 2,5-bis(trimethylstannyl)thiophene (119.3 mg, 0.2910 mmol), tris(dibenzylideneacetone)dipalladium(0) (8 mg), tri(o-tolyl)phosphine (16 mg), toluene (8 mL). Reaction resulted in 112.3 mg (63.5%) polymer as dark blue solid. ¹H NMR (600 MHz, CDCl₃) δ 7.79-8.22 (m, 10H), 7.31-7.44 (m, 5H), 7.10-7.23 (m, 10H), 6.85 (bs, 5H), 3.70 (bs, 10H), 2.19-2.24 (m, 2H), 2.12 (bs, 6H), 1.72 (bs, 2H), 1.51 (bs, 8H), 1.12-1.26 (m, 40 H), 0.80 (bs, 12H).

TQ1-50A

3,3'-(((5,8-dibromoquinoxaline-2,3-diyl)bis(3,1-phenylene))bis(oxy))bis(N,N-dimethylpropan-1-amine) (**4-6**) (99.8 mg, 0.1553 mmol), 5,8-dibromo-2,3-bis(3-(octyloxy)phenyl)quinoxaline (102.3 mg, 0.1553 mmol), 2,5-bis(trimethylstannyl)thiophene (127.3 mg, 0.3017 mmol), tris(dibenzylideneacetone)dipalladium(0) (8 mg), tri(o-tolyl)phosphine (16 mg), toluene (8 mL). Reaction resulted in 108.9 mg (59.2%) polymer as dark blue solid. ¹H NMR (600 MHz, CDCl₃) δ 7.80-8.22 (m, 4H), 7.32-7.49 (m, 2H), 7.11-7.23 (m, 4H), 6.85 (bs, 2H), 3.70-3.78 (m, 4H), 2.19-2.26 (m, 2H), 2.10-2.12 (m, 6H), 1.78 (bs, 2H), 1.12-1.27 (m, 12 H), 0.79 (bs, 3H).

TQ1P4

5,8-dibromo-2,3-bis(3-(3-(pyridin-4-yl)propoxy)phenyl)quinoxaline (**4-9**) (278.5 mg, 0.392 mmol), 2,5-bis(trimethylstannyl)thiophene (160.6 mg, 0.392 mmol),

tris(dibenzylideneacetone)dipalladium(0) (11 mg), tri(o-tolyl)phosphine (22 mg), toluene (4 mL), DMF (4 mL). Reaction afforded 194.5 mg (78.2%) polymer as dark blue/purple solid. ¹H NMR (600 MHz, CDCl₃) δ 8.30-8.55 (m, 6H), 7.97 (bs, 2H), 7.44-7.60 (m, 2H), 7.01-7.20 (m, 4H), 6.77-6.98 (m, 6H), 3.63 (bs, 4H), 2.77-2.98 (m, 2H), 2.11-2.48 (m, 6H).

TQ1-20P4

5,8-dibromo-2,3-bis(3-(3-(pyridin-4-yl)propoxy)phenyl)quinoxaline (**4-9**) (58.5 mg, 0.082 mmol), 5,8-dibromo-2,3-bis(3-(octyloxy)phenyl)quinoxaline (229.4 mg, 0.329 mmol), 2,5-bis(trimethylstannyl)thiophene (168.6 mg, 0.411 mmol), tris(dibenzylideneacetone) dipalladium(0) (10 mg), tri(o-tolyl)phosphine (20 mg), toluene (6 mL), DMF (1.5 mL). Reaction afforded 183 mg (71.4%) polymer as dark blue/purple powder. ¹H NMR (600 MHz, CDCl₃) δ 8.36 (s, 2H), 7.89 (bs, 6H), 7.29-7.50 (m, 4H), 7.05-7.25 (m, 14H), 6.89 (bs, 6H), 3.74 (bs, 10H), 2.43 (bs, 4H), 1.10-1.39 (m, 48 H), 0.82-0.98 (m, 12 H).

TQ1-50P4

5,8-dibromo-2,3-bis(3-(3-(pyridin-4-yl)propoxy)phenyl)quinoxaline (**4-9**) (108.8 mg, 0.153 mmol), 5,8-dibromo-2,3-bis(3-(octyloxy)phenyl)quinoxaline (106.7 mg, 0.153 mmol), 2,5-bis(trimethylstannyl)thiophene (125.5 mg, 0.306 mmol), tris(dibenzylideneacetone) dipalladium(0) (8 mg), tri(o-tolyl)phosphine (16 mg), toluene (4 mL), DMF (4 mL). Reaction resulted in 154.0 mg (80.4%) polymer as dark blue solid. ¹H NMR (600 MHz, CDCl₃) δ 8.34 (bs, 2H), 7.90 (bs, 2H), 7.40-7.52 (m, 2H), 7.08-7.25 (m, 6H), 6.87 (m, 4H), 3.68 (bs, 4H), 2.38 (bs, 4H), 1.12-1.39 (m, 12H), 0.82-0.96 (m, 4H).

TQ1-5A

3,3'-(((5,8-dibromoquinoxaline-2,3-diyl)bis(3,1-phenylene))bis(oxy))bis(N,N-dimethylpropan-1-amine) (**4-6**) (18.5 mg, 0.0288 mmol), 5,8-dibromo-2,3-bis(3-(octyloxy)phenyl)quinoxaline (360.0 mg, 0.5466 mmol), 2,5-bis(trimethylstannyl)thiophene (235.9 mg, 0.5754 mmol), tris(dibenzylideneacetone)dipalladium(0) (10 mg), tri(o-tolyl)phosphine (20 mg), toluene (10 mL). Reaction afforded 271 mg (76.3%) polymer as dark blue/purple fibers.

TQ6A

5,8-dibromo-2,3-bis(3-(diethylamino)hexyloxy)phenyl)quinoxaline (**5-1**) (505.1 mg, 0.645 mmol), 2,5-bis(trimethylstannyl) thiophene (264.4 mg, 0.645 mmol), tris(dibenzylideneacetone)dipalladium(0) (10 mg), tri(o-tolyl)phosphine (20 mg), toluene (8 mL). Reaction afforded 321 mg (70.4%) polymer as dark blue solid.

TQ1P3

5,8-dibromo-2,3-bis(3-(3-(pyridin-3-yl)propoxy)phenyl)quinoxaline (**5-3**) (266.2 mg, 0.375 mmol), 2,5-bis(trimethylstannyl)thiophene (153.5 mg, 0.375 mmol), tris(dibenzylideneacetone)dipalladium(0) (10 mg), tri(o-tolyl)phosphine (20 mg), toluene (4 mL), DMF (4 mL). Reaction afforded 213.4 mg (89.6%) polymer as dark blue/purple solid.

TQ-OEG

The monomer **5-4** (154.8 mg, 0.126 mmol), 2,5-bis(trimethylstannyl)thiophene (51.4 mg, 0.126 mmol), tris(dibenzylideneacetone) dipalladium(0) (2.3 mg), tri(o-tolyl)phosphine (3.1 mg), toluene (3 mL), DMF (0.6 mL). Reaction resulted in 85.1 mg (84.2%) polymer as dark blue solid.

2.2. Suzuki coupling polymerisation

QFA

3,3'-(((5,8-dibromoquinoxaline-2,3-diyl)bis(3,1-phenylene))bis(oxy))bis(N,N-dimethylpropan-1-amine) (**4-6**) (403.7 mg, 0.628 mmol), 9,9-dioctylfluorene-2,7-diboronic acid bis(pinacol) ester (403.8 mg, 0.628 mmol) and 10 mL of degassed toluene were added to a 25 mL flask. Then tris(dibenzylideneacetone)dipalladium(0) (10 mg), tri(o-tolyl)phosphine (20 mg) and aliquat® 336 (583 mg, 1.44 mmol) were added to the monomer solution. The solution was stirred at 90 °C under N₂ protection for 30 min before adding a potassium carbonate (0.43 g, 3.14 mmol) aqueous solution (1 mL). Depending on the viscosity of the solution, the reaction mixture was stirred at 90 °C for 1 day. The reaction was stopped by cooling to r.t., then removing toluene by rotary evaporation. The crude polymers were re-dissolved in 100 mL chloroform and a solution of sodium diethyldithiocarbamate trihydrate (10%, 10 g in 100 mL H₂O) was added to the resulting CHCl₃ solution. The mixture was stirred vigorously at 60 °C for 1 h. Then the organic phase was separated and washed with brine and deionized water several times to remove most of the residual complex agent. The organic phase was concentrated to approximately 10 mL before precipitated in hexane. The resulted suspension was allowed to store in a fridge for 2 days. Then the polymer was collected by filtration through an extraction thimble, and Soxhlet-extracted subsequently with diethyl ether and chloroform. The chloroform fraction was concentrated to about 10 mL, and precipitated in hexane. The solid was collected by filtration and dried in a vacuum oven under 36 °C to afford 240.8 mg polymer (43.9%) as green powder.

QFA-Si

3,3'-(((5,8-dibromoquinoxaline-2,3-diyl)bis(3,1-phenylene))bis(oxy))bis(N,N-dimethylpropan-1-amine) (**4-6**) (179.1 mg, 0.279 mmol), 9,9-dioctyl-9H-9-silafluorene-2,7-bis(boronic acid pinacol) ester (183.6 mg, 0.279 mmol), tris(dibenzylideneacetone)dipalladium(0) (6 mg), tri(o-tolyl)phosphine (12 mg), toluene (8 mL), aliquat® 336 (260 mg, 0.64 mmol), potassium carbonate (193 mg, 1.4 mmol) aqueous solution (1 mL). Reaction resulted in 24.3 mg (9.8 %) polymer as green solid.

Quaternisation of the copolymer QFA-Br

Polymer **QFA** (110.8 mg) was dissolved in 20 mL THF in a 100 mL flask. Excess bromoethane (200 μ L) was dissolved in 10 mL DMF, and the resulted solution were added to polymer THF mixture. The solution was stirred at r.t. for 2 days in darkness. Then THF and extra bromoethane were removed by rotary evaporation. The polymer was precipitated in ethyl acetate, collected by centrifugation (4400 rpm, 30 min). The collected solid was then washed with THF, dried in a vacuum oven overnight to afford dark green solid polymer (90 mg, yield: 65%).

Appendix B

NMR spectra of quinoxaline monomers and polymers presented in Chapter 4

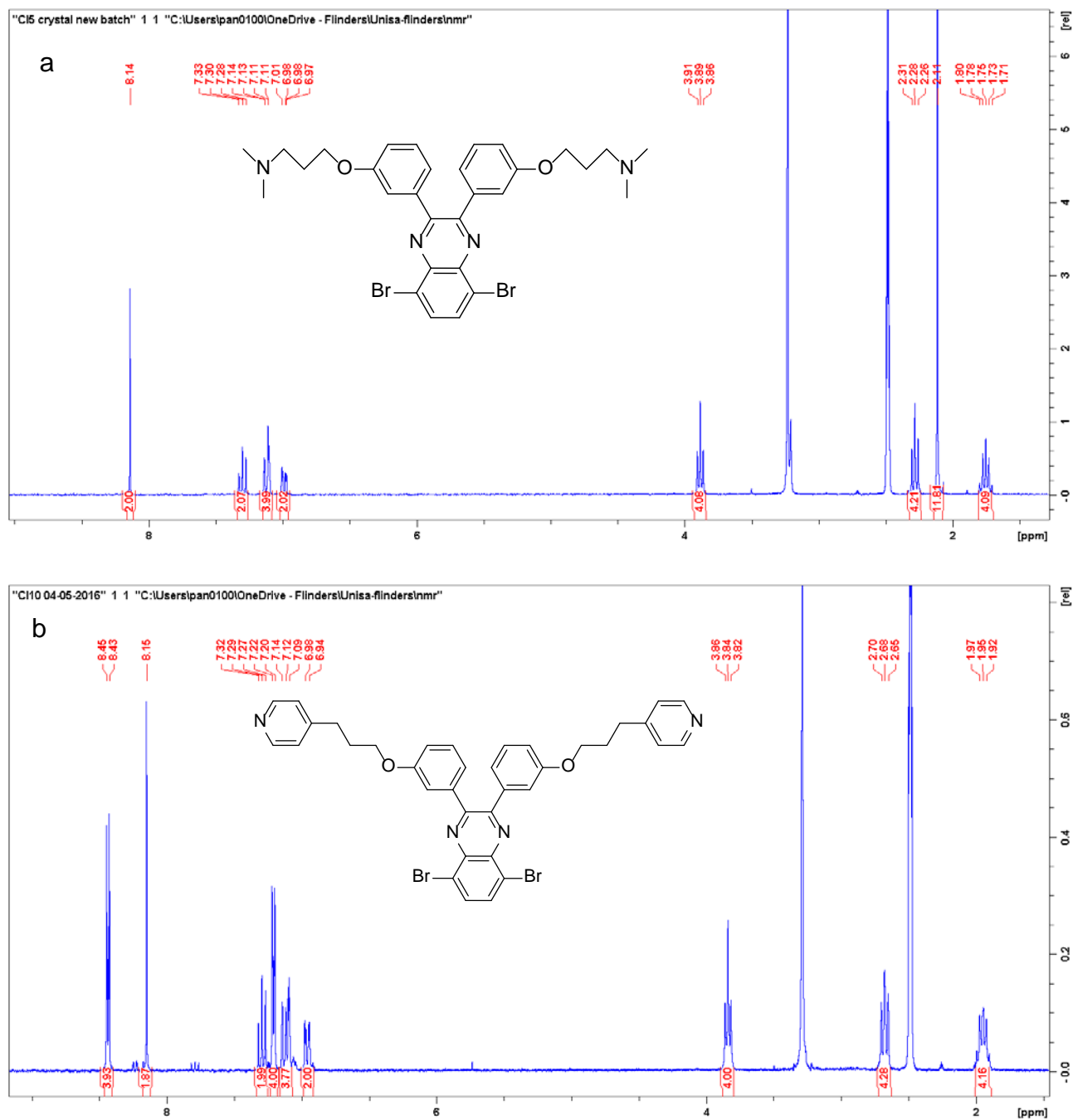
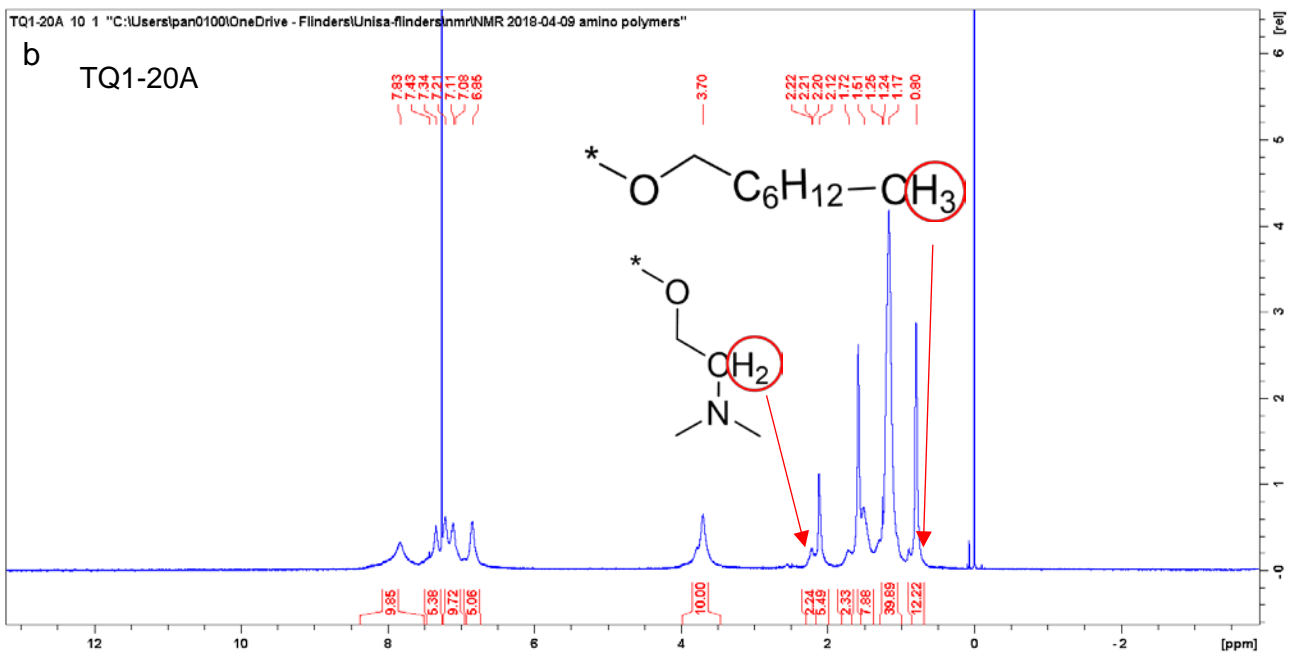
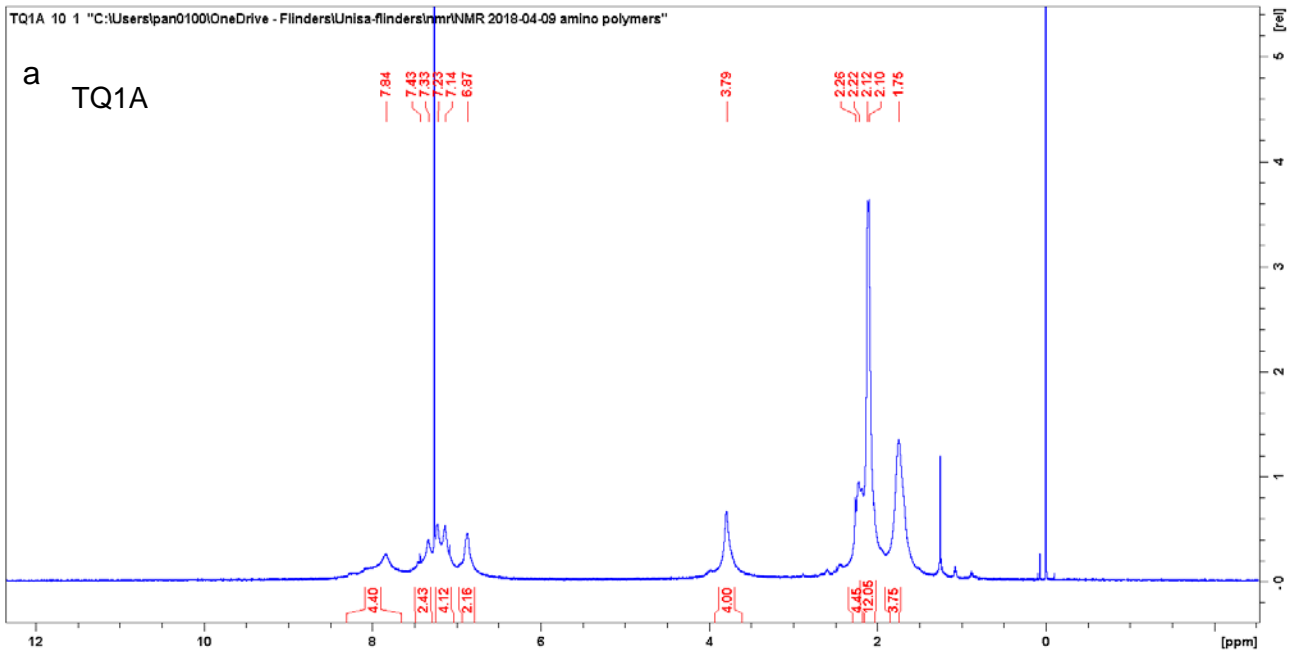
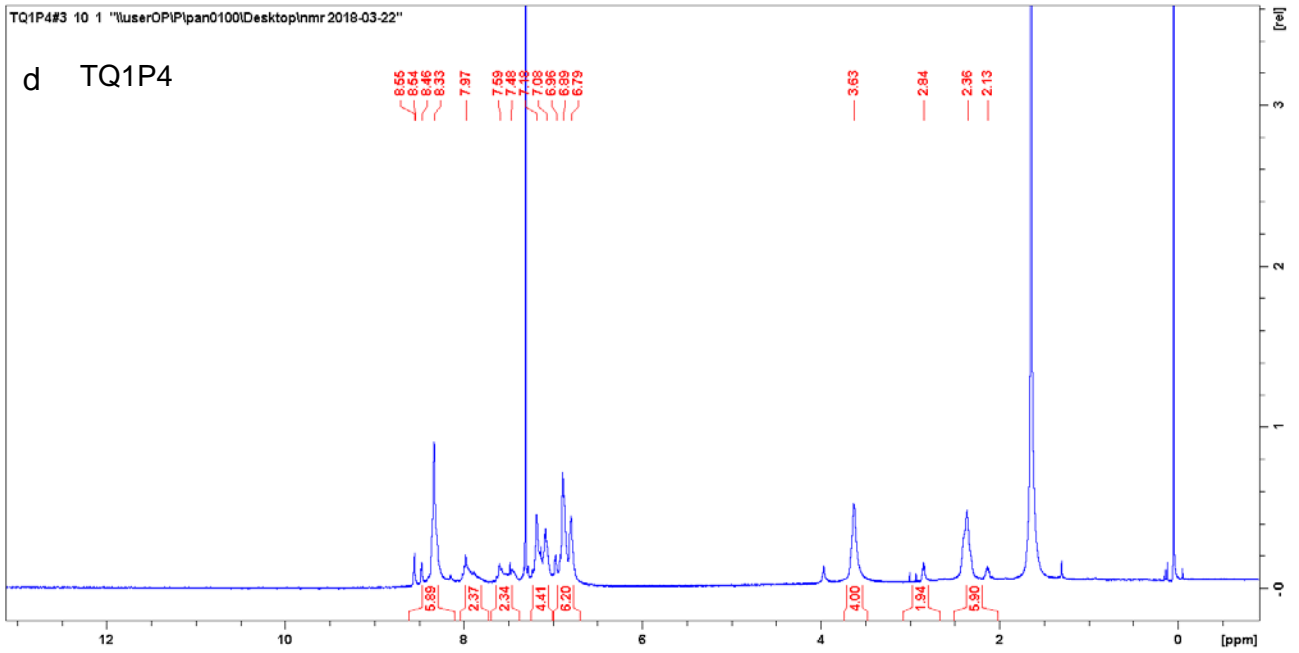
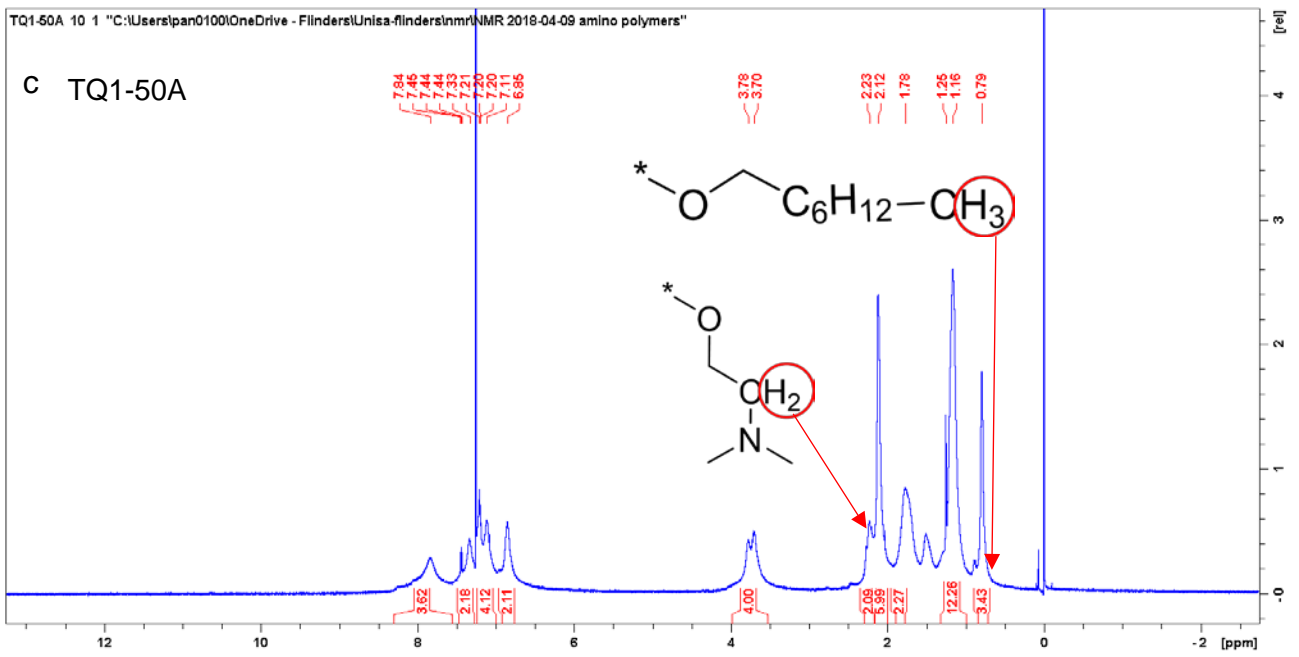


Figure B1 ¹H NMR (300 MHz) spectra of (a) TQ1A monomer and (b) TQ1P4 monomer in deuterated DMSO.





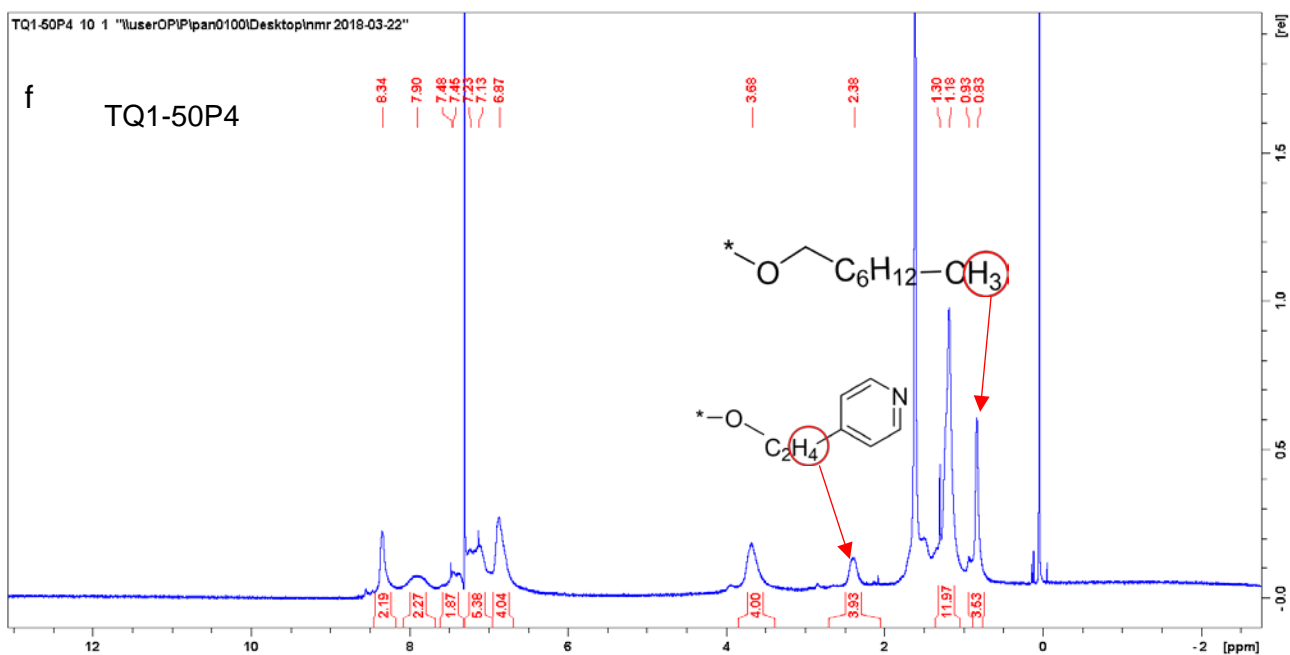
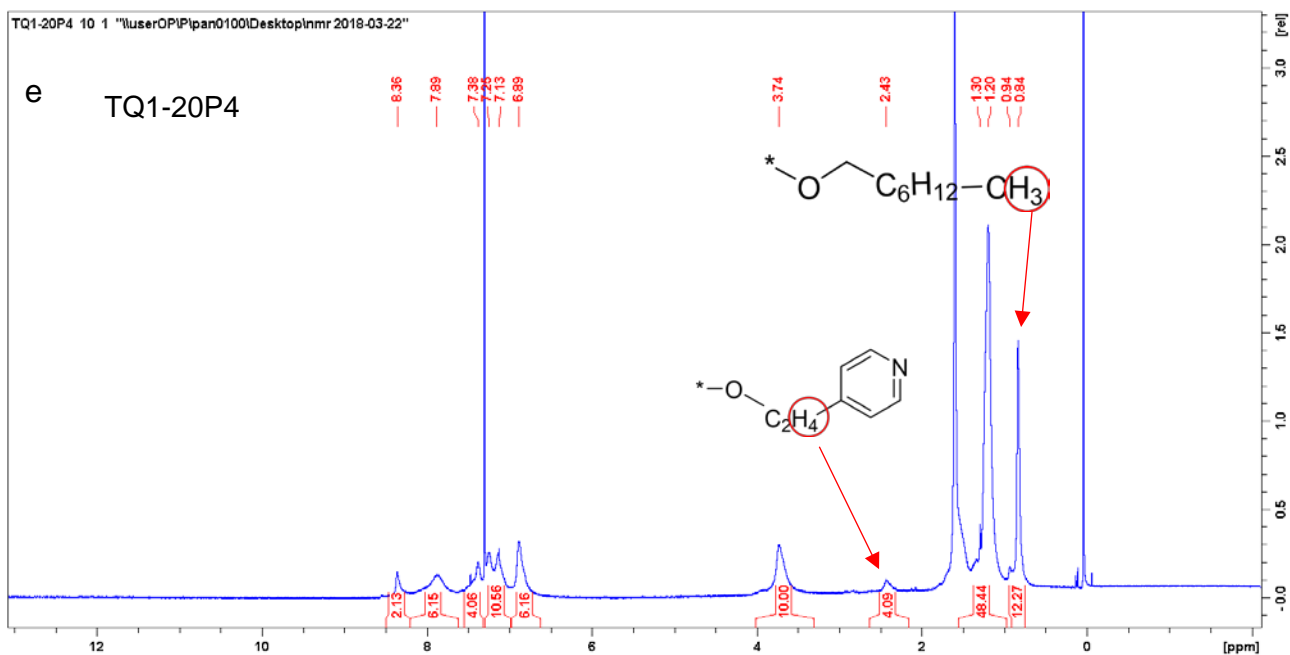


Figure B2 ¹H NMR (600 MHz) spectra of (a) TQ1A, (b) TQ1-20A, (c) TQ1-50A, (d) TQ1P4, (e) TQ1-20P4 and (f) TQ1-50P4 in deuterated chloroform. The side groups and arrows inserted illustrate the specific proton signals.

The ratios of side groups on random polymers TQ1-20A, TQ1-50A, TQ1-20P4 and TQ1-50P4 are calculated based on the specific proton signal integrals as illustrated in **Figure B2**.

Table B1. Ratio of polar functional side groups to octyl side groups calculated by NMR spectra and estimated from monomer feed ratios.

	TQ1-20A	TQ1-50A	TQ1-20P4	TQ1-50P4
Calculated from NMR spectra	1.12:4.07 (21.6% amine)	1.05:1.14 (47.9% amine)	1.02:4.09 (20.0% pyridine)	0.98:1.18 (46.3% pyridine)
Estimated from monomer ratio	2:8 (20% amine)	5:5 (50% amine)	2:8 (20% pyridine)	5:5 (50% pyridine)